AD-A043 457 TECHNOLOGY INC SAN ANTONIO TEX LIFE SCIENCES DIV F/G 6/18
RESEARCH ON THE OCULAR EFFECTS OF LASER RADIATION.(U)
AUG 77 J A ZUCLICH, J T YATES, A D NAWROCKI F41609-73-C-0017
UNCLASSIFIED TI-77-0561-03 NL

1 OF 3
AD A043457

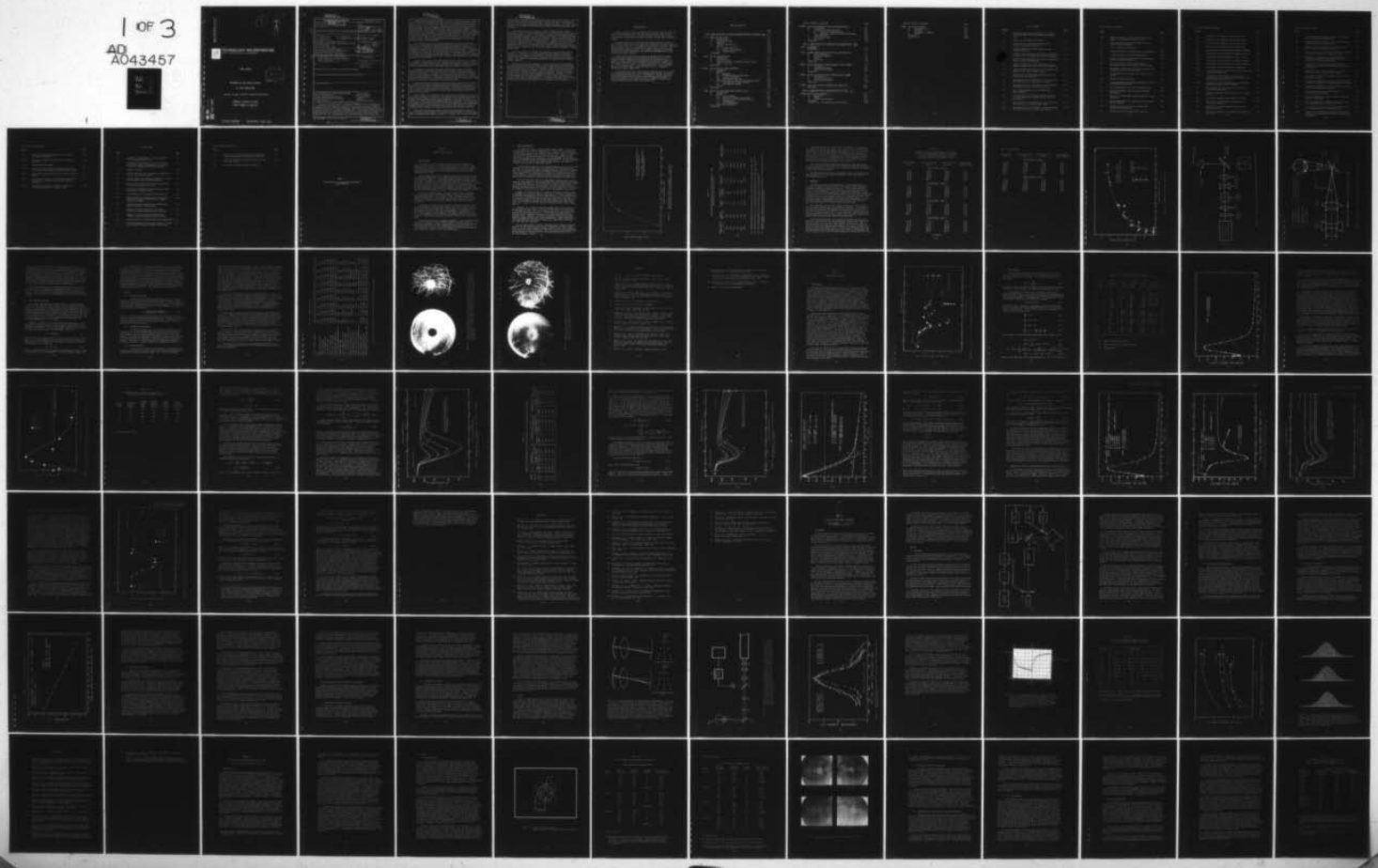

AD A043457

(4)

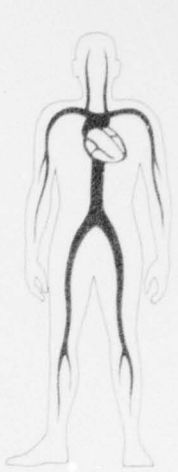

TECHNOLOGY INCORPORATED

LIFE SCIENCES DIVISION

FINAL REPORT

DDC
RECEIVED
AUG 25 1977
A

RESEARCH ON THE OCULAR EFFECTS OF LASER RADIATION

Approved for public release; distribution unlimited.

CONTRACT F41609-73-C-0017
REPORT NUMBER 77-0561-03

AU NO.
DDC FILE COPY

511 WEST RHAPSODY - SAN ANTONIO, TEXAS 78216

UNCLASSIFIED

SECURITY CLASSIFICATION OF THIS PAGE (When Data Entered)

REPORT DOCUMENTATION PAGE	READ INSTRUCTIONS BEFORE COMPLETING FORM
1. REPORT NUMBER (14) TI-77-0561-03 / Technology Incorporated	2. GOVT ACCESSION NO.
	3. RECIPIENT'S CATALOG NUMBER (9)
4. TITLE (and Subtitle) (6) RESEARCH ON THE OCULAR EFFECTS OF LASER RADIATION.	5. TYPE OF REPORT & PERIOD COVERED FINAL REPORT. 16 Feb 1975 - 30 Nov 1976,
	6. PERFORMING ORG. REPORT NUMBER
7. AUTHOR(s) J. A. Zuclich, Ph.D. / J.T. Yates, Ph.D. / A.D. Nawrocki, Ph.D. / W. H. Bowie, M.S. / R. Lemberger, B.S.E.E.	8. CONTRACT OR GRANT NUMBER(s) (15) F41609-73-C-0017
9. PERFORMING ORGANIZATION NAME AND ADDRESS Technology Incorporated, Life Sciences Division 511 West Rhapsody San Antonio, Texas 78216	10. PROGRAM ELEMENT, PROJECT, TASK AREA & WORK UNIT NUMBERS 62202F (17) 92 (16) 7757-02-34
11. CONTROLLING OFFICE NAME AND ADDRESS USAF School of Aerospace Medicine (RZL) Aerospace Medical Division (AFSC) Brooks Air Force Base, Texas 78235	12. REPORT DATE (11) 5 August 1977 / 13. NUMBER OF PAGES
14. MONITORING AGENCY NAME & ADDRESS (if different from Controlling Office) (10) Joseph A./Zuclich, J. Terry/Yates, A. David/Nawrocki, William H./Bowie Ronald F./Lemberger	15. SECURITY CLASS. (of this report) Unclassified
	15a. DECLASSIFICATION/DOWNGRADING SCHEDULE

16. D

(12) 207p.

Approved for public release; distribution unlimited.

17. DISTRIBUTION STATEMENT (of the abstract entered in Block 20, if different from Report)

18. SUPPLEMENTARY NOTES

19. KEY WORDS (Continue on reverse side if necessary and identify by block number)

Laser-induced ocular damage, rhesus monkey	Corneal damage
Retinal Photochemistry	Oxygen dependence
Retinal temperature measurement	Action spectrum
Histopathology/electron microscopy	Cataract
Ultraviolet laser	Physiological optics

20. ABSTRACT (Continue on reverse side if necessary and identify by block number)

This final technical report for Contract F41609-73-C-0017, USAF School of Aerospace Medicine, summarizes research on ocular effects of laser radiation conducted by the Life Sciences Division of Technology Incorporated during the period 15 February 1975 through 30 November 1976. The various research projects conducted during this period are categorized as: Ocular Effects of Visible and Near-Infrared Laser Radiation (Part I); Ocular Effects of Ultraviolet Laser Radiation (Part II); and Neurophysiology and Physiological Optics (Part III).

DD FORM 1 JAN 73 1473 EDITION OF 1 NOV 65 IS OBSOLETE

UNCLASSIFIED

SECURITY CLASSIFICATION OF THIS PAGE (When Data Entered)

401 650

LB

Techniques were developed (Chapter 1) for the accurate placement of laser-induced lesions of specified sizes (175-1100 μm) in the macular area of the rhesus retina. Such lesions were induced in the retinae of trained primates so that the recovery of visual acuity following laser insult could be monitored. The experiments indicated apparent recovery of visual acuity (Landolt "C") to the 20/20 level within 75 to 110 days for subjects exhibiting retinal lesions smaller than ∿200 μm diameter. For lesion sizes between 250 and 750 μm, acuities of 20/40 and 20/50 were measured within the same time frame. Only those subjects with lesions greater than ∿900 μm failed to show acuities of 20/100 or better within 110 days. Whether these results are indicative of true recovery of visual acuity or due to a learned response which compensates for the central scotomas remains to be determined.

The theoretical basis for certain experimental retinal threshold data indicative of photochemical damage mechanisms is examined in Chapter 2. It is shown that it is possible to explain the dependence of retinal threshold on interpulse separation for fixed configurations of identical pulses in terms of a sequence of consecutive, irreversible first-order rate processes. Alternatively the experimental data can also be explained by a model based upon competing first-order rate processes of different species. In either case, the correlation of the hypothesized rate processes with in vivo retinal photochemical processes has yet to be established.

A series of in vivo retinal probe experiments was conducted in an attempt to validate a thermal model of laser induced retinal injury. Progress in the development of surgical techniques and of the experimental apparatus required to carry out thermal and optical probe experiments is presented in Chapter 3.

An attempt to elucidate the apparent photochemical nature of retinal damage produced by repetitive visible pulses and short visible wavelengths is described in Chapter 4. The effect of laser radiation on retinal lipids was examined under conditions thought to be optimum for the induction of retinal lesions by photochemical processes while minimizing the possibility of involvement of thermal processes. Preliminary experiments did not indicate any obvious effects of such laser irradiations on the retinal lipids.

Chapter 5 describes comparative light and electron microscopy of a series of retinal lesions induced by mode-locked visible laser pulses. Tissue preparation and sectioning techniques developed for obtaining alternate thick and thin sections for light and electron microscopy, respectively are discussed. The electron microscopy revealed in greater detail morphology observed at the light microscopy level.

Ocular effects of ultraviolet laser radiation are discussed in Part II of this report (Chapters 6 through 10). Following a short introduction (Chapter 6), corneal damage induced by near-UV laser radiation is examined in detail in Chapter 7. Corneal epithelial damage thresholds in the rhesus eye are reported for exposures to krypton, argon and nitrogen laser radiation. The results for pulsewidths ranging from 250 μsec to 10^4 sec are consistent with a photochemical damage mechanism. Ocular hazards of near-UV lasers are discussed in terms of existing safety standards for laser radiation (see also Chapters 9 and 10).

Additional experimental evidence regarding the photochemical nature of near-UV induced corneal damage is discussed in Chapter 8 where an oxygen dependence of the damage threshold is reported. A factor of two increase in corneal

threshold was found for eyes flushed with nitrogen gas prior to exposure compared to those flushed with oxygen under similar conditions. The observed oxygen effect and the magnitude of the threshold dose required to induce corneal lesions are consistent with observations of near-UV effects on bacterial cell cultures.

Yet another aspect of the nature of near-UV induced corneal damage is presented in Chapter 9 where determination of an action spectrum for the near-UV wavelength range is reported. The corneal threshold increases monotonically with wavelength throughout the near-UV range but exhibits a pronounced shoulder in the 340-350 nm region. Again, this behavior is consistent with studies of effects of near-UV radiation on bacterial cells. However, the action spectrum reported in Chapter 9 as well as the results of Chapters 7 and 8 are unique in that they examine the nature of near-UV induced photochemical processes in mammalian cells *in situ* as opposed to most earlier studies which have examined bacterial cell cultures or, in a few cases, mammalian cells suspended in various buffer media.

Lenticular effects of near-UV laser radiation are discussed briefly in Chapter 10. Induction of lenticular opacities which appear to represent a permanent form of damage are described for instances where the lenticular thresholds are lower than the corneal thresholds for identical exposure parameters. The lenticular thresholds appeared to be consistent with a thermal damage mechanism.

Part III of this report (Chapters 11 and 12) discusses the development of neurophysiological and physiological optics procedures for evaluating the spatial visual system's response to transient changes in adaptation resulting from high intensity laser radiation. Chapter 11 describes a preliminary set of experiments designed to analyze pattern information and extract response features from a variety of visual system perturbations. Chapter 12 presents an assessment of the wavelength dependence of focus in the rhesus eye. A sensitive method for *in vivo* evaluation of chromatic images was devised and used to obtain data for the rhesus eye. The results were found to be in close agreement with data obtained under similar conditions for the human eye.

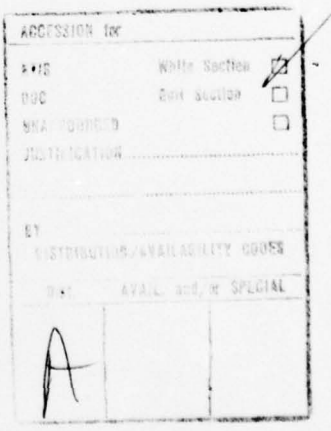

ACKNOWLEDGEMENTS

John S. Connolly, Ph.D., was Research Director for Contract F41609-73-C-0017 during the period covered by this report and supervised research activities for the contract. His advice and guidance as well as specific contributions to the material presented in Part I of the report are acknowledged.

Technical support in the form of animal preparation and handling, experimental setup, laser beam diagnostics, photography and animal surgery was provided by Mr. John E. McGlothan and Mr. Gregory L. Sweeney. Additional animal surgery as well as histopathologic support for all projects was provided by Mr. William H. Bowie. Mr. Ronald F. Lemberger designed and fabricated electronic components and assisted with programming and data analysis for several projects.

A total of seven visiting scientists participated in the contract effort during the summers of 1975 and 1976 under the auspices of the National Science Foundation Faculty Research Participation Program. In addition to those participants designated as co-authors of chapters of this report, the efforts of the following researchers are acknowledged: Drs. Fred M. Loxsom, James R. Crawford and Michael K. Garrity (In Vivo Reginal Probe Experiments, summer 1975) and Dr. Bill S. Yamanashi (Lenticular Effects, summer 1976).

In addition to the Laser Effects Branch, Radiobiology Division, USAF School of Aerospace Medicine, which supported this research, assistance was rendered by numerous personnel in the Radiation Biology, Radiation Physics and Weapons Effects Branches of the Radiobiology Division, as well as personnel of the Biometrics, Clinical Sciences, Epidemiology, Support Services and Veterinary Sciences Divisions.

TABLE OF CONTENTS

		PAGE
PART I	OCULAR EFFECTS OF VISIBLE AND NEAR-INFRARED LASER RADIATION	1
1.	LARGE RETINAL LESIONS	1-1
	A. Introduction	1-1
	B. Model Calculations	1-2
	C. Apparatus	1-5
	D. Ray-Trace Calculations	1-11
	E. Results	1-12
	E-1. Retinal Image Sizes	1-12
	E-2. Retinal Laser Exposures	1-12
	E-3. Retinal Lesions	1-12
	References	1-17
2.	RETINAL PHOTOCHEMISTRY	2-1
	A. Introduction	2-1
	B. Empirical Model	2-3
	C. Comparative Effects of Repetitive Laser Pulses: 1064 vs. 514.5 nm	2-17
	References	2-26
3.	IN VIVO RETINAL PROBE EXPERIMENTS	3-1
	A. Background	3-1
	B. Methods	3-2
	B-1. Apparatus	3-2
	B-2. Microthermocouple Calibrations	3-5
	B-3. Surgical Techniques	3-6
	B-4. Experimental Procedures	3-8
	C. Ray-Tracing Applications and Beam Deflector Design	3-10
	C-1. Description of Computer Software	3-10
	C-2. Beam Deflector Design	3-11
	D. Results	3-12
	References	3-21
4.	EFFECTS OF LASER RADIATION ON RETINAL LIPIDS, and	4-1
	A. Introduction	4-1
	B. Methods	4-3
	B-1. Laser Exposures	4-3
	B-2. Removal of Retinal Tissue Samples	4-8
	B-3. Preparation of Tissue Lipids for Gas Chromatography	4-8
	B-4. Gas Chromatography	4-9
	C. Results and Discussion	4-10
	References	4-16

TABLE OF CONTENTS (continued)

		PAGE
5.	OCULAR HISTOPATHOLOGY AND ELECTRON MICROSCOPY	5-1
	A. Introduction	5-1
	B. Preliminary Electron Microscopy	5-2
	B-1. Previously Prepared Tissues	5-2
	B-2. Comparative Light and Electron Microscopy	5-4
	C. Light Microscopy	5-6
	D. Electron Microscopy	5-9
	E. Conclusions	5-17
	References	5-18
PART II	OCULAR EFFECTS OF ULTRAVIOLET LASER RADIATION	
6.	BACKGROUND	6-1
	References	6-4
7.	CORNEAL DAMAGE INDUCED BY NEAR-UV LASER RADIATION	7-1
	A. Early Experiments	7-1
	B. Experimental Methods	7-2
	C. Results	7-11
	D. Discussion	7-17
	References	7-23
8.	OXYGEN DEPENDENCE OF NEAR-UV INDUCED CORNEAL DAMAGE	8-1
	A. Introduction	8-1
	B. Experimental Methods	8-2
	C. Results and Discussion	8-4
	References	8-7
9.	ACTION SPECTRUM FOR NEAR-UV INDUCED CORNEAL DAMAGE, and	9-1
	A. Introduction	9-1
	B. Experimental Methods	9-1
	C. Results and Discussion	9-3
	References	9-13
10.	LENTICULAR EFFECTS OF NEAR-UV LASER RADIATION;	10-1
	References	10-9
PART III	NEUROPHYSIOLOGY AND PHYSIOLOGICAL OPTICS	
11.	VISUAL EVOKED RESPONSE, and	11-1
	A. Background	11-1
	B. Method	11-3
	C. Results and Discussion	11-5
	References	11-8
	Appendix 11-A Counterphase Grating Stimulator	11-A-1

TABLE OF CONTENTS (continued)

		PAGE
12.	PHYSIOLOGICAL OPTICS	12-1
	A. Introduction	12-1
	B. Apparatus	12-2
	C. Experimental Procedures	12-2
	D. Results	12-5
	References	12-9
	Appendix 12-A	12-A-1

LIST OF FIGURES

FIGURE		PAGE
1-1	Observed Retinal Lesion Development as a Function of Retinal Energy Dose for Various Retinal Image Sizes.	1-3
1-2	Summary of IITRI Model Calculations.	1-8
1-3	Block Diagram of Experimental Apparatus for Inducing Large Retinal Lesions.	1-9
1-4	Schematic Diagram of Optical System for Large Retinal Image Sizes.	1-10
1-5	Ordinary Fundus Photograph and Fluorescein Angiogram of Subject 572 (OS) Taken at Two Hours Post-exposure.	1-15
1-6	Ordinary Fundus Photograph and Fluorescein Angiogram Taken at 75 Days Post-exposure.	1-16
2-1	Retinal Threshold vs. Pulse Separation for Fixed Numbers of Repetitive 10 μsec, 514.5 nm Laser Pulses.	2-2
2-2	Relative Retinal Sensitivity vs. Pulse Separation for Double 10 μsec, 514.5 nm Laser Pulses.	2-5
2-3	Empirical Fit of Relative Retinal Sensitivity as a Function of Pulse Separation.	2-7
2-4	Semi-empirical Fit of Threshold vs. Pulse Separation for Multiple 10 μsec, 514.5 nm Laser Pulses.	2-11
2-5	Semi-empirical Fit of Threshold vs. Pulse Separation for Multiple 10 μsec, 514.5 nm Laser Pulse.	2-14
2-6	Least Squares Analysis of $z = \pm\sqrt{\ln[C_0/(S-1)]}$ vs. Pulse Separation.	2-15
2-7	Semi-empirical Fit of Relative Retinal Sensitivity vs. Pulse Separation for Double 10 μsec, 514.5 nm Laser Pulses.	2-18
2-8	Semi-empirical Fit of Threshold vs. Pulse Separation for Double 10 μsec, 514.5 nm Laser Pulses.	2-19
2-9	Semi-empirical Fit of Threshold vs. Pulse Separation for Multiple 10 μsec, 514.5 nm Laser Pulses.	2-20

LIST OF FIGURES (continued)

FIGURE		PAGE
2-10	Retinal Threshold vs. Pulse Separation for Fixed Numbers of Q-switched Nd:YAG Laser Pulses.	2-22
3-1	Block Diagram of Experimental System for In Vivo Retinal Probe Measurements.	3-3
3-2	Static Thermocouple Calibration.	3-7
3-3	Predicted Responses to Beam Deflector in Average Eye.	3-13
3-4	Schematic Diagram of Experimental Apparatus.	3-14
3-5	Results of Three Sequential Scans of Laser-Induced Retinal Temperature Increase.	3-15
3-6	Oscilloscope Trace of Laser-Induced Retinal Temperature Increase Near Center of Retinal Image.	3-17
3-7	Dependence of Peak Retinal Temperature Increase with Pulsewidth at Various Corneal Powers.	3-19
3-8	Representative In Vivo Optical Scan Data of Rhesus Retina.	3-20
4-1	Diagram of Retinal Exposures.	4-4
4-2	Fundus Photographs of Presumed Photochemical Lesions at One Week Post-exposure.	4-7
4-3	Gas Chromatogram of Fatty Acids of Monkey Retina.	4-14
5-1	Electron Micrograph Showing Swollen, Distended Mitochondria.	5-3
5-2	EM View of a Longitudinal Section Through the Pigment Epithelium.	5-3
5-3	Electron Micrograph of a Transverse Section Through Bruch's Membrane.	5-5
5-4	EM View of a Transverse Section Through Inner Segments of Photoreceptors.	5-5
5-5	Diagram of Retinal Exposure Area in 511C OD.	5-7

LIST OF FIGURES (continued)

FIGURE		PAGE
5-6	Probable Lesion Produced by 832 mW Peak Power.	5-8
5-7	Definite Lesion Produced by 1092 mW Peak Power.	5-8
5-8	Definite Lesion Produced by 1587 mW Peak Power.	5-8
5-9	Definite Lesion Produced by 1261 mW Peak Power.	5-8
5-10	Longitudinal Section Through the Pigment Epithelium.	5-10
5-11	Longitudinal Section Through the Pigment Epithelium.	5-10
5-12	Longitudinal Section Through a Rod Outer Segment.	5-11
5-13	Longitudinal Section Through the Pigment Epithelium.	5-11
5-14	Longitudinal Section Through the Pigment Epithelium.	5-13
5-15	Longitudinal Section Through Bruch's Membrane.	5-13
5-16	Longitudinal Section Showing Muller Cell Proliferation Around a Damaged Nucleus.	5-14
5-17	Longitudinal Section Showing Cross-section of Photoreceptor Axons Between the Outer Nuclear Layer and the Outer Plexiform Layer.	5-14
5-18	Longitudinal Section Showing Phagocytized Material Vitread to the Outer Plexiform Layer.	5-16
7-1	Block Diagram of Laser Apparatus for Corneal and Lenticular Irradiations.	7-4
7-2	Horizontal Beam Scan of Near-UV Emission of Krypton Laser.	7-5
7-3	Experimental Apparatus for Nitrogen Laser Study.	7-6
7-4	Beam Scan of Focused Output of Nitrogen Laser; Horizontal Direction.	7-8
7-5	Beam Scans of Focused Output of Nitrogen Laser; Vertical Direction.	7-9
7-6	Experimental Apparatus for Simultaneous Exposure of Four Eyes.	7-10

LIST OF FIGURES (continued)

FIGURE		PAGE
7-7	Slit Lamp Photograph Showing Corneal Lesion Induced by Near-UV Output of Krypton Laser.	7-12
7-8	Photomicrograph of Corneal Tissue in Region Exposed to Near-UV Output of Krypton Laser.	7-13
7-9	Photomicrograph of Corneal Tissue Showing Central Area of Lesion Illustrated in Figure 7-8.	7-14
7-10	Dose-response Plot for 120-second Continuous Exposures to the Near-UV Output of a Krypton-ion Laser.	7-15
7-11	Comparison of Experimentally Determined Corneal Thresholds with Present ANSI Maximum Permissible Exposures for 315-400 nm Radiation.	7-19
7-12	Comparison of Experimentally Determined Corneal Threshold Data with ANSI Maximum Permissible Exposure for Near-UV.	7-21
8-1	Schematic Diagram of Laser Apparatus for Corneal Irradiation Under a Controlled Atmosphere.	8-3
9-1	Experimental Apparatus for Inducing Corneal Lesions with Xenon Arc Lamp.	9-2
9-2	Experimental Thresholds for Corneal Epithelial Lesions Induced by Monochromatic, Noncoherent Near-UV Radiation.	9-5
9-3	Experimental Threshold for Corneal Epithelial Lesions Induced by Noncoherent UV Radiation.	9-6
9-4	Relative Sensitivity of Corneal Epithelium to Absorbed Near-UV Radiation.	9-12
10-1	Slit Lamp Photograph of Cataract Induced by Near-UV Output of Argon Laser.	10-2
10-2	Slit Lamp Photograph of Cataracts Induced by Trains of 10 Nanosecond Pulses from Nitrogen Laser.	10-4
10-3	Slit Lamp Photograph of Cataracts Induced by Trains of 10 Nanosecond Pulses from Nitrogen Laser.	10-5
10-4	Comparison of Experimentally Determined Lenticular Thresholds with Thresholds Predicted by Thermal Model Calculations.	10-8

LIST OF FIGURES (continued)

FIGURE		PAGE
11-1	Summed Evoked Response Amplitude vs. Contrast for Two Spatial Frequencies.	11-6
11-A-1	Diagram of a Spatial Sinusoidal Grating Stimulus Generator.	11-A-2
12-1	Schematic Optical System.	12-3
12-2	Comparison of Two Methods of Determining Best Focus for a Line Target Imaged on the Rhesus Monkey Fundus.	12-6
12-3	Normalized Chromatic Aberration for the Eye of Rhesus Monkey.	12-7
12-4	Comparison of Primate vs. Human Chromatic Aberration as Measured by Similar Electro-optical Scanning Techniques.	12-8
12-A-1	Schematic Lens System for the Major Components of the Continuous Dioptric Corrector System.	12-A-2

LIST OF TABLES

TABLE		PAGE
1-1	Experimental Observations of Lesion Development for Large Retinal Image Sizes.	1-4
1-2	Summary of Calculated Lesion Sizes (IITRI Model) for Various Retinal Image Diameters as Functions of Retinal Irradiance and Retinal Energy Dose.	1-6
1-3	Summary of Results.	1-14
2-1	Retinal Thresholds for Fixed Numbers of Repetitive 10 μsec, 514.5 nm Laser Pulses.	2-4
2-2	Threshold Powers and Energies for Repetitive 10 μsec, 514.5 nm Laser Pulses at Optimum Spacing.	2-8
2-3	Predicted and Experimental Thresholds for Multiple 10 μsec Laser Pulses at 514.5 nm.	2-12
3-1	Peak Retinal Temperatures Induced by Various Laser Pulsewidths and Corneal Powers.	3-18
4-1	Laser Exposures of Experimental and Control Eyes.	4-5
4-2	Comparison of Fatty Acid Patterns of Control and Laser-treated Areas of Monkey Retina + Pigment Epithelium + Choroid.	4-12
4-3	Comparison of Fatty Acid Patterns of Retina with Pigment Epithelium + Choroid Layers.	4-13
7-1	Summary of Threshold Irradiances for Corneal Epithelial Lesions Induced by Krypton-ion Laser.	7-16
7-2	Summary of Threshold Irradiances for Corneal Epithelial Lesions Induced by Krypton-ion Laser.	7-18
8-1	Corneal Epithelial Thresholds Under Various Atmospheres.	8-5
9-1	Wavelength Dependence of Thresholds (ED_{50}) for Corneal Lesions Induced by Noncoherent Near-UV Radiation.	9-4

LIST OF TABLES (continued)

TABLE		PAGE
9-2	Molecular Extinction Coefficients for Absorption of Near-UV Radiation by the Corneal Epithelium.	9-9
9-3	Wavelength Dependence of Relative Sensitivity (R) of Corneal Tissue.	9-11
10-1	Lenticular Thresholds for 350 nm Radiation.	10-7

PART I

OCULAR EFFECTS OF VISIBLE AND NEAR-INFRARED LASER RADIATION

CHAPTER 1

LARGE RETINAL LESIONS

A. INTRODUCTION

This study was a joint effort of the Laser Effects Branch and Weapons Effects Branch of the USAF School of Aerospace Medicine. The purpose of this project was to place large lesions (150-1200 μm diameter) in the retinae of trained primates (Macaca mulatta) in order to make quantitative measurements of visual acuity as a function of lesion size and post-exposure time.

Previous measurements[1] of long-term recovery of visual acuity from the immediate effects of laser-induced retinal lesions have been sparse and the results ambiguous. These efforts were hampered primarily by the difficulty of centering the laser exposures precisely and reproducibly on the fovea. The inability of a primate to recover its visual acuity[1], even to the 20/200 level, six months after receiving a lesion approximately 900 μm in diameter is not a surprising result. The lesions in this case had been induced near the center of the macula and almost certainly totally disrupted the fovea centralis, which in the rhesus has a diameter of ∿75 μm[2].

However, a different animal, in which a ∿250 μm lesion had been induced, showed apparent recovery to 20/200 visual acuity within eight days after exposure[1]. This result, if real, is highly significant. However, other exposures made during this earlier study had clearly not overlapped the fovea completely and, hence, further experiments were required.

The primary task was to place lesions in the retina so that in each case the damage was centered on the fovea. The second problem, that of predicting final lesion dimensions, arose because of the apparent trend of recovery of visual acuity with lesion diameter. Accordingly, an experimental regimen was developed in which lesions ranging from ∿150 μm to ∿1200 μm diameter would be induced in primates trained to respond to Landolt "C" projections ranging from 20/20 to 20/200 on the visual acuity scale.

To minimize variations in exposure parameters, it was deemed advisable to maintain a constant retinal irradiance and pulse duration for all exposures, regardless of retinal image diameter. An added benefit of this requirement was that the lesion development, expressed as a ratio of lesion diameter to retinal image size, appears to be essentially constant over the selected range of lesion sizes (see below).

B. MODEL CALCULATIONS

The theoretical basis of laser-induced thermal damage in the retina has been discussed in detail elsewhere[3-8]. Briefly, it is assumed that a large fraction of the laser radiation focused onto the retina is absorbed in the pigment epithelium (PE) and dissipated as heat. When the local temperature is elevated above the norm for sufficient periods of time, irreversible damage occurs, presumably via rate-dependent injury mechanisms such as enzyme inactivation and protein denaturation[7]. At supra-threshold exposures, retinal lesions are characterized by massive disruption of cellular layers as well as edema and lysis[6].

For laser pulse durations in the range of 100 μsec to 10 sec, excellent agreement is found between theory and experiment[8,9], thereby lending validity to the assumption that the damage mechanisms are primarily thermal. Thus, for the exposure parameters of interest in this project, the IITRI thermal model[3] can be considered as an entirely adequate predictive tool for the purpose of correlating retinal lesion sizes with laser beam parameters such as wavelength, exposure time, beam-divergence and power level.

The first indication that lesion development, expressed as a ratio of lesion to image diameters, can be predicted from retinal energy dose appears in the data obtained in an earlier study[10] on large retinal lesions. This work, which was carried out using the 647.1 nm line of a krypton-ion laser, had been completed before the IITRI model was fully operational, and, hence, no systematic investigation was made of lesion development on this basis.

However, as shown in Figure 1-1, there is an obvious trend of lesion development with increasing retinal energy dose; a trend which appears to be reasonably independent of retinal image diameter or laser pulse duration at least for this limited range of relatively long pulses (see Table 1-1). The asymptotic behavior at high retinal energy doses can be understood in terms of an approach to thermal equilibrium, at which point the rate of heat input is equal to the rate of heat dissipation and no further damage occurs.

Evidently, this trend of lesion development would not be expected to be maintained for very short ($\leq$ 10 μsec) or very long ($\geq$ 10 sec) pulses. In the former instance, the rate of heat production is much greater than the rate of heat dissipation; i.e., in this short-pulse approximation, the peak retinal temperature increase is directly proportional to the absorbed energy. However, even with this assumption, lesion development remains a complicated function of peak temperature, retinal image size, laser beam geometry, and change of state (e.g., vaporization of water), if any, induced by the exposures.

For very long pulses ($\geq$ 10 sec), the power level (retinal irradiance) required to reach thermal equilibrium will depend on the retinal image size; for larger image diameters, thermal equilibrium will be achieved at lower levels of retinal irradiance. Thus, for a given retinal energy dose, the development of large lesions will be quantitatively greater than in the case of smaller lesions.

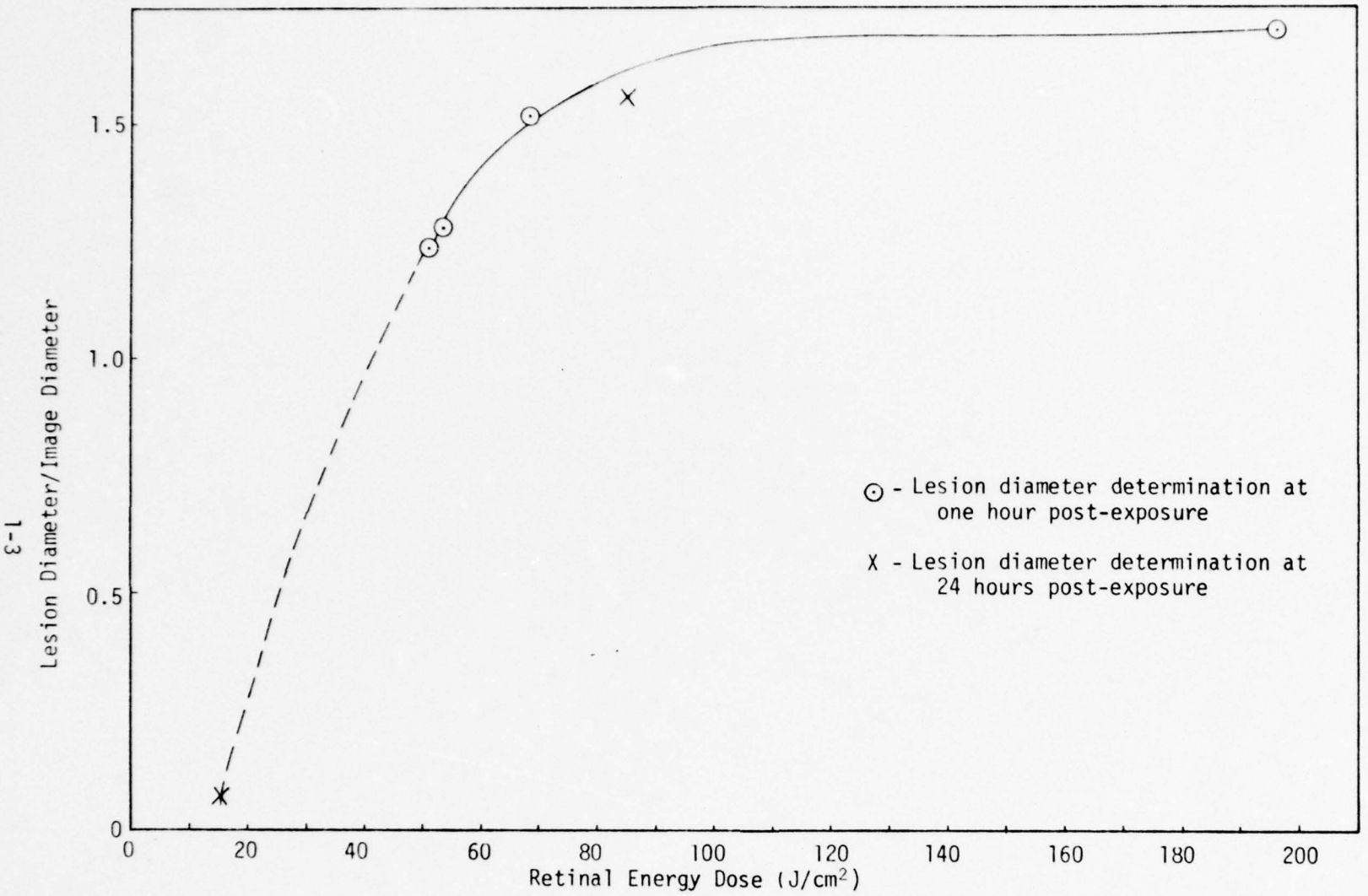

FIGURE 1-1. Observed Retinal Lesion Development as a Function of Retinal Energy Dose for Various Retinal Image Sizes.

TABLE 1-1.

EXPERIMENTAL OBSERVATIONS OF LESION DEVELOPMENT FOR LARGE RETINAL IMAGE SIZES (647.1 nm)[10].

Image Diameter $1/e^2$ (μm)	Corneal Power (mW)	Exposure (sec)	Retinal[a] Irradiance (W/cm^2)	Retinal Dose (J/cm^2)	Final Lesion Diameter (μm)	Lesion Diameter / Image Diameter
180	200	0.1	536	53.6	231[b]	1.28
450	320	0.5	137	68.6	683[b]	1.52
450	400	0.5	171	85.7	700[c]	1.56
850	425	1.0	51.1	51.1	1050[b]	1.24
1050	425	4.0	49.1	196	1790[b]	1.70
(280)	(39)	(0.25)	(43.2)	(10.8)	(∿10)[d]	(∿0.03)

(a) Assuming transmission through the anterior ocular media to be 0.682 at 647.1 nm[11].

(b) Mean values of ten lesions observed ophthalmoscopically at one hour post-exposure[10].

(c) One lesion measured at 24 hours post-exposure by histopathology[5].

(d) Threshold (ED_{50}) determined from ophthalmoscopic observation of "minimum visible lesions" (∿10 μm diameter) at one hour post-exposure[5].

Nevertheless, over the limited range of pulsewidths of interest in this experiment, the trend (Figure 1-1) is encouraging. Moreover, it can be seen that for an incident retinal energy dose of ∿75 J/cm^2 the lesion growth factor (∿1.6) is approaching its asymptotic limit. Taking the transmission of the ocular media[11] to be 0.682 at this wavelength (647.1 nm), a retinal dose of 75 J/cm^2 is equivalent to a corneal power of ∿100 W for an exposure of 1.1 sec. Using these values as a starting point, IITRI model[3] calculations were carried out. The results of these computer calculations are summarized in Table 1-2 and Figure 1-2.

The striking agreement between model predictions and experimental results is significant in that the calculated points represent the model's actual predictions of lesion sizes; i.e., none of these points was normalized to agree with experimental data.

The remaining problems, precise placement of the lesion and accurate determination of the laser beam profile on the retina, are discussed in the following sections.

C. APPARATUS

The apparatus used in these experiments is shown diagrammatically in Figure 1-3 and a schematic diagram of the optical system employed to vary beam divergence is shown in Figure 1-4. The principal variations from the usual arrangement[4-6,10] consisted of replacing the swing-away mirror with a dichroic beam splitter and redesigning the holder for the external lenses to permit independent alignment of complex lens configurations. In addition, a pair of mirrors was placed in the laser path to provide beam alignment in the direction normal to the plane shown in Figure 1-3. This modification permitted alignment of the laser beam along the optic axis of the fundus camera, independent of the movable beam splitter which was mounted on the holder of the fundus camera objective lens.

The reflectivity of the dichroic beam splitter was ∿94% for 647.1 nm light polarized perpendicular to the plane of incidence. This component had very high transmission throughout the visible spectrum, especially in the blue, thus providing the capability of viewing the fundus through the beam splitter while preparing for the laser exposure. Last minute checks of animal movement or optical misalignment could, therefore, be made immediately prior to exposing the retina to the laser beam.

It was found empirically, from the results of more than 50 retinal exposures, that the center of the lesion had a circular error probability (CEP) of about 10% of the laser image diameter at the retina. That is, for large image sizes (∿750 μm), the center of the lesion was generally within ∿75 μm of the intended target location. For smaller retinal images (∿200 μm), the CEP was about 20-25 μm. The principal limiting factor was not the alignment of the dichroic mirror, but rather the alignment of the external lenses used to vary the beam divergence of the laser at the cornea.

TABLE 1-2.

SUMMARY OF CALCULATED LESION SIZES (IITRI MODEL) FOR VARIOUS RETINAL IMAGE DIAMETERS AS FUNCTIONS OF RETINAL IRRADIANCE AND RETINAL ENERGY DOSE. (Wavelength: 647.1 nm, Pulsewidth: 1.1 sec).

Corneal Power (mW)	Retinal Irradiance (W/cm^2)	Retinal Energy Dose (J/cm^2)	Lesion Diameter / Image Diameter
	Image Diameter = 180 μm		
6.19	16.58	18.24	0.00
10.76	28.83	31.71	0.67
24.84	66.55	73.21	1.33
25.00	66.98	73.68	1.34
45.12	120.9	133.0	2.00
72.53	194.3	213.8	2.67
	Image Diameter = 300 μm		
12.70	12.25	13.47	0.00
15.20	14.66	16.13	0.33
22.20	21.41	23.55	0.67
34.80	33.57	36.92	1.00
54.90	52.95	58.25	1.33
70.00	67.52	74.27	1.55
148.0	142.8	157.0	2.21
	Image Diameter = 450 μm		
20.10	8.62	9.48	0.00
24.70	10.59	11.65	0.31
34.20	14.66	16.13	0.62
53.60	22.98	25.28	0.93
91.40	39.18	43.10	1.24
160.0	68.59	75.45	1.64
266.0	114.0	125.4	1.99
	Image Diameter = 550 μm		
26.20	7.52	8.27	0.00
31.70	9.10	10.01	0.33
46.00	13.20	14.52	0.65
77.10	22.13	24.34	0.98
142.0	40.75	44.83	1.31
240.0	68.87	75.76	1.64
451.0	129.4	142.4	2.05

continued...

TABLE 1-2 (continued)

Corneal Power (mW)	Retinal Irradiance (W/cm^2)	Retinal Energy Dose (J/cm^2)	Lesion Diameter / Image Diameter
	Image Diameter = 650 μm		
31.90	6.55	7.21	0.00
39.20	8.05	8.86	0.34
59.30	12.18	13.40	0.68
110.0	22.60	24.86	1.02
210.0	43.15	47.46	1.35
330.0	67.80	74.58	1.62
700.0	143.8	158.2	2.08
	Image Diameter = 750 μm		
38.00	5.86	6.45	0.00
47.50	7.33	8.06	0.35
74.50	11.50	12.65	0.69
147.0	22.69	24.95	1.04
302.0	46.61	51.27	1.39
440.0	67.90	64.69	1.60
1050.0	162.0	178.2	2.09

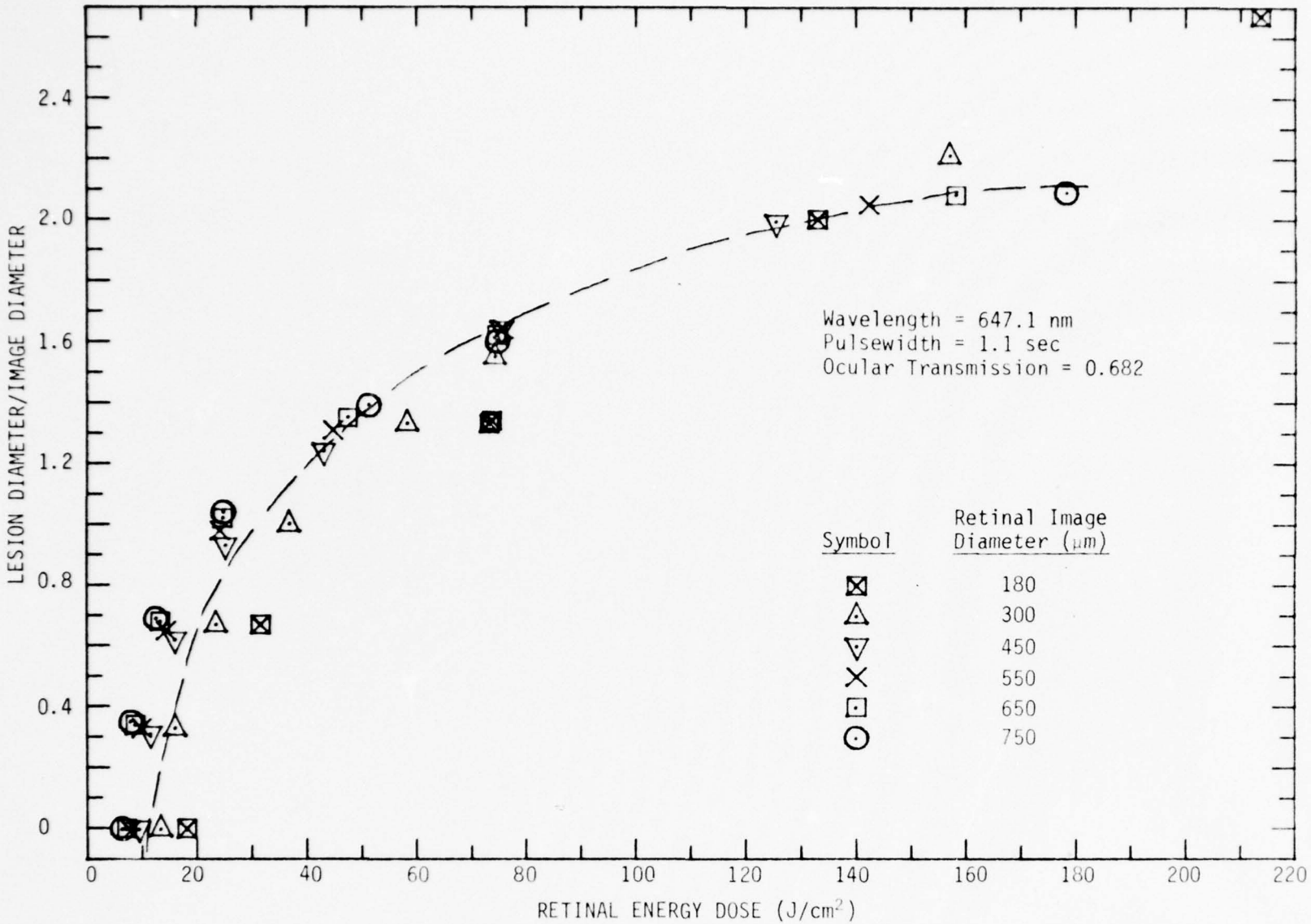

FIGURE 1-2. Summary of IITRI Model Calculations.

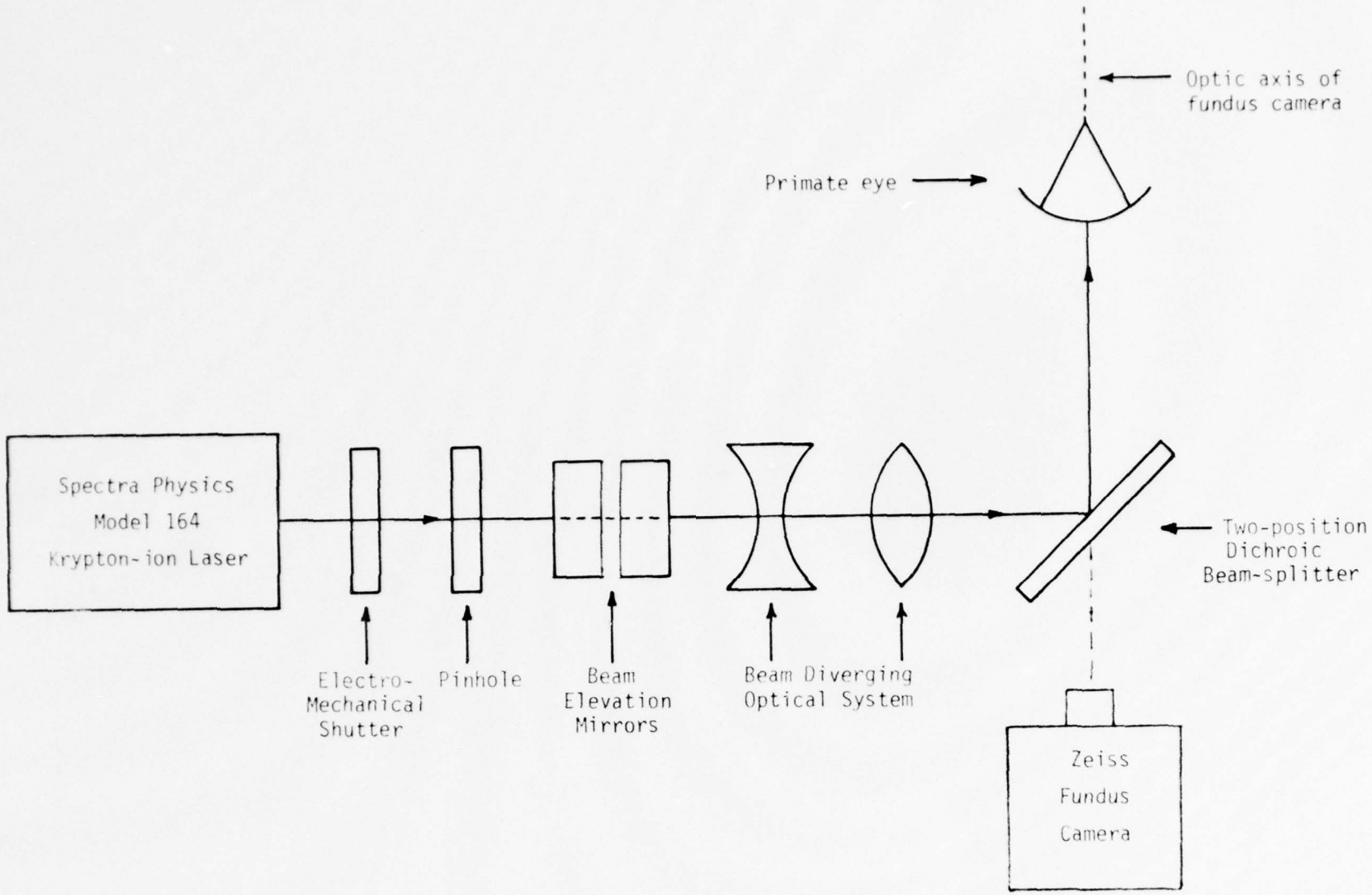

FIGURE 1-3. Block Diagram of Experimental Apparatus for Inducing Large Retinal Lesions.

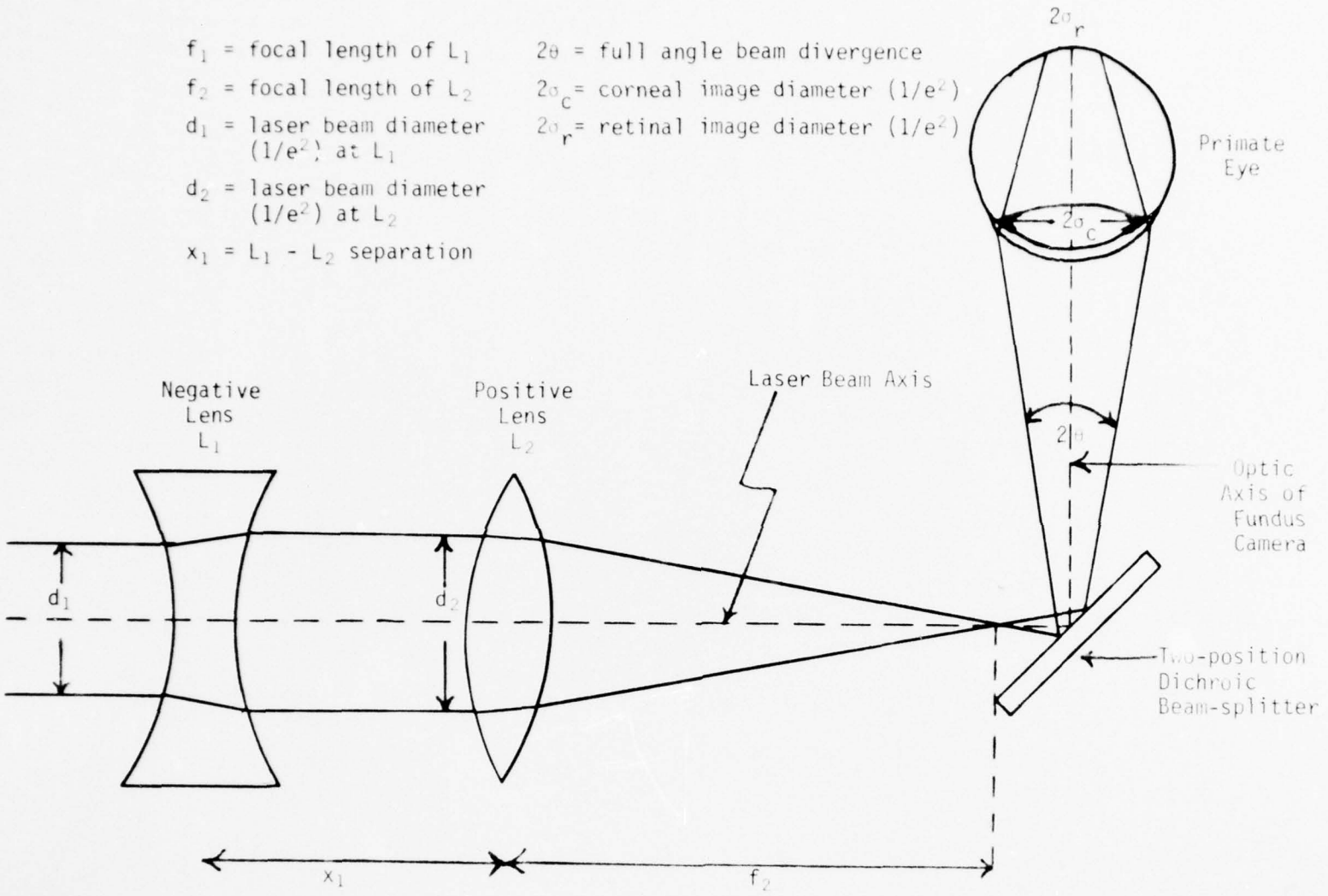

FIGURE 1-4. Schematic Diagram of Optical System for Large Retinal Image Sizes.

Thus, the center of the beam must coincide with both the optic and geometric axes of the lens system. To accomplish this, a pinhole (~80 μm diameter) was interposed on an X-Y micrometer translation stage between the shutter and the beam elevation mirrors. This arrangement, together with external bench marks for laser alignment, permitted fine adjustment of all optical components in order to achieve beam symmetry and precise beam alignment, both before and after the external lens system. Finally, the capability of translating the external lens assembly along the laser beam axis assured that the beam did not come to a focus on the beam splitter itself (Figure 1-4) and allowed a fixed beam diameter of ~2.5 mm to be maintained at the cornea, irrespective of divergence angle.

The trial-and-error process required to achieve high accuracy and precision in lesion placement was prolonged and tedious, since each of the nine optical components of the system had at least two degrees of freedom. However, the results achieved were quite satisfactory and the apparatus, thus configured, was used to expose the retinae of six trained primates.

D. RAY-TRACE CALCULATIONS

The retinal image diameters listed in Table 1-2 were selected to provide the best range of lesion sizes for the first series of exposures. In practice, actual retinal image diameters were extremely difficult to measure, in part because the dichroic beam splitter reflected light polarized perpendicular to the plane of incidence. Thus, even though the laser light scattered from the fundus was largely depolarized, about 50% of this intensity was rejected by the beam splitter. In addition, subjective estimates of beam daimeters at the retina vary widely according to laser wavelength and beam intensity, degree of dark adaptation of the observer, and individual judgments of the $1/e^2$ limits.

Therefore, in order to set the beam parameters (divergence, power level and pulsewidth) desired to induce a given retinal lesion, it was preferable to calculate, rather than to attempt to measure, the $1/e^2$ image diameter at the retina. Using the terminology shown in Figure 1-4, the full-angle beam divergence, 2θ, at the cornea is given by:

$$2\theta \simeq \frac{d_1(f_1 + x_1)}{f_1 f_2} \qquad (1\text{-}1)$$

where 2θ is in milliradians (mrad), d_1 is the laser beam diameter (mm) at lens L_1, x_1 is the spearation (m) of lenses L_1 and L_2, and f_1 and f_2 are the respective focal lengths (m) of the lenses. Therefore, the retinal image diameter, $2\sigma_r$, is given by:

$$2\sigma_r \simeq 2\theta \times f_e \qquad (1\text{-}2)$$

where f_e is the effective focal length of the primate eye. With 2θ given in milliradians and f_e in millimeters, $2\sigma_r$ has units of micrometers (μm).

For initial estimates of laser beam parameters and the concomittant choice of external optics, a value for f_e ≈13.35 mm may be used as determined by Sanders[10], although this value will evidently vary with the psysiological optical parameters of an individual primate eye. In addition, ray-trace calculations[12,13] suggest that a Gaussian beam profile at the cornea will be severely distorted at the retina, especially in the case of large divergence angles. To overcome these problems, keratometry, phakometry and ultrasonographic distance measurements were carried out on the eyes of all trained animals used in the visual acuity studies. Unfortunately, the trained animals were not available for phakometric measurements before receiving retinal laser exposures. Since accurate ray-tracing calculations require knowledge of lenticular curvatures, absolute calculations had to be undertaken well after the fact. The results are summarized below.

E. RESULTS

E-1. Retinal Image Sizes

The experimental conditions (beam divergence, laser power and pulsewidth) used to expose the trained subjects were selected to induce retinal lesions ranging from 300 to 1100 μm diameter. Initial estimates of the $1/e^2$ retinal image diameters were made using Equations (1-1) and (1-2) with individual estimates of the effective focal length of each subject eye calculated from the relationship:

$$f_e = \frac{(\text{Total Axial Length})^2}{1.336\ (A+V) + 1.416\ (L)}\ \text{mm} \qquad (1\text{-}3)$$

where A, V and L are the respective thicknesses of the anterior chamber, vitreous, and lens obtained by ultrasonography, and 1.336 and 1.416 are the refractive indices[14] of water and the rhesus lens, respectively. This method was employed in lieu of absolute ray-tracing and the calculated image sizes are tabulated below.

E-2. Retinal Laser Exposures

The trained subjects were irradiated on a schedule such that there was a minimum of two weeks between exposures of the two eyes of a given subject. Lesion sizes were measured ophthalmoscopically (fundus camera) immediately after the exposures (2-3 min) and at ∿30 min post-exposure. In addition, fluorescein angiography on each eye was performed by collaborators[15,16], although in some cases not until 75 days post-exposure. Nevertheless, cross-calibration of funduscopic photographs permitted measurement of lesion sizes from the angiograms to within ±5%.

E-3. Retinal Lesions

In the earlier sections of this chapter, it was shown that a constant energy dose of 80-90 J/cm^2 should induce lesions approximately 60% larger than the respective retinal image sizes. Thus, both computer

calculations and experiments on young (2-3 years) rhesus subjects indicated that the ratio of final (1-24 hour post-exposure) lesion diameter to retinal image size should be sensibly constant at ∿1.6. Accordingly, in the initial exposures on the trained primates the retinal energy dose was maintained between 78 and 85 J/cm^2, using a fixed exposure time of 1.1 sec and varying only the laser power. Results on the first four eyes demonstrated quite conclusively that the trend observed for younger animals (see Figure 1-1) did not apply to these trained subjects. Specifically, the observed lesion diameters were considerably smaller (by ∿20%) than the calculated values. The only apparent explanation is that the subjects used in the present experiments ranged in age from 6 to 9 years compared to ages of 2-3 years for the subjects used in the trial exposures. It is conceivable that age-dependent variations in the nature and/or content of the macular pigment are responsible for this marked departure from theoretical and previous experimental results.

In any case, the actual lesion sizes achieved (175-1100 μm) cover the range desired for the follow-up visual acuity measurements. A comprehensive summary of the results of this study is listed in Table 1-3, which includes lesion measurements taken from fluorescein angiograms[16]. Figures 1-5 and 1-6 show comparative fundus photographs and fluorescein angiograms of subject 572 (OS). These photographs were taken at 2 hours post-exposure (Fig. 1-5) and at 75 days post-exposure (Fig. 1-6). The magnifications in both cases are the same, and it can be seen that the apparent lesion dimensions in the angiograms are somewhat smaller than those shown in the fundus photographs.

The correlation between lesion size and short-term (6-41 days) visual acuity[15] shows the expected trend of acuity decrement with increasing lesion size. However, long-term visual acuity data following laser exposure show two distinct transition stages. Measurements taken at 75 to 110 days post-exposure[16] show that for lesions smaller than ∿200 μm, there is apparent recovery of visual acuity (Landolt "C") to the 20/20 level. For lesion sizes between 250 and 750 μm, acuities of 20/40 to 20/50 were measured. Visual acuities of 20/100 or worse were measured only for lesion sizes greater than ∿900 μm.

Whether these results are indicative of true recovery of visual acuity or, for example, a learned response which compensates for the central scotomas, remains to be determined. In any case, it seems clear that more meaningful interrogation of the visual response following laser exposures is required. In particular, chromatic visual acuity tests should be investigated in order to probe the foveal response. Such tests should distinguish between true recovery of visual acuity and a learned response[17].

A more complete description of the psychophysical aspects of this study, including the temporal histories of post-exposure acuity tests will be found elsewhere[15].

TABLE 1-3. SUMMARY OF RESULTS

Subject No. (Age, years)*	3824 (9)	741 (6)	3797 (9)	3797 (9)	572 (6)	572 (6)	741 (6)	3926 (8)	3926 (8)
Eye	OS	OD	OS	OD	OD	OS	OS	OD	OS
Beam Divergence (mrad)	13.6	13.6	22.9	22.2	30.8	43.3	49.0	47.6	43.1
Corneal Image (mm)	2.04	2.04	2.670	2.600	1.86	2.88	3.53	3.43	3.10
Anterior Chamber (mm)	3.802	3.456	3.687	3.744	3.168	3.111	3.456	3.514	3.514
Lens Thickness (mm)	3.401	2.771	3.464	3.464	3.149	3.464	2.771	3.464	3.464
Length of Vitreous (mm)	11.097	10.521	11.961	12.019	10.694	10.406	10.694	11.615	11.558
Total Axial Length (mm)	18.300	16.748	19.112	19.227	17.011	16.981	16.921	18.593	18.536
Effective Focal Length (mm)	13.547	12.413	14.152	14.238	12.593	12.557	12.542	13.763	13.721
Calc. Retinal Image Diameter (μm)	184	169	324	316	388	544	615	655	591
Corneal Power (mW)	36	36	76	87	141	259	322	351	378
Retinal Energy Dose (J/cm^2)	101.3	120.6	69.1	83.2	89.5	83.7	81.4	78.1	103.2
Calc. Lesion Growth Factor	1.73	1.92	1.48	1.6	1.75	1.72	1.65	1.63	1.86
Calc. Final Lesion Diameter (μm)*	319	324	480	506	679	935	1014	1068	1100
Immed. Lesion Dimensions (μm)	150	(No Lesion)	275±25	350	700	700	750×800	600	600
Lesion Dimensions at 30 min	175	---	300	400	700	1100	700×900	850	700
Lesion Dimensions at 20 days	---	---	375±25	---	---	1250	700×900	825±25	---
Lesion Dimensions: Angiography (μm)	---	---	250	280	540±20	680×760	740×1030	920	500×600
Date of Exposure (1975)	29 May	2 July	29 May	18 Jun	17 Jun	28 May	28 May	18 Jun	1 July
Date of Angiography (1975)	29 May	11 Aug	11 Aug	11 Aug	11 Aug	11 Aug	11 Aug	11 Aug	11 Aug
Visual Acuity(1) as of 8 July 1975	20/20	20/20	20/20	20/200	20/100	20/100	20/100	20/200	20/100

* Subjects are listed in order of increasing calculated final lesion diameters.

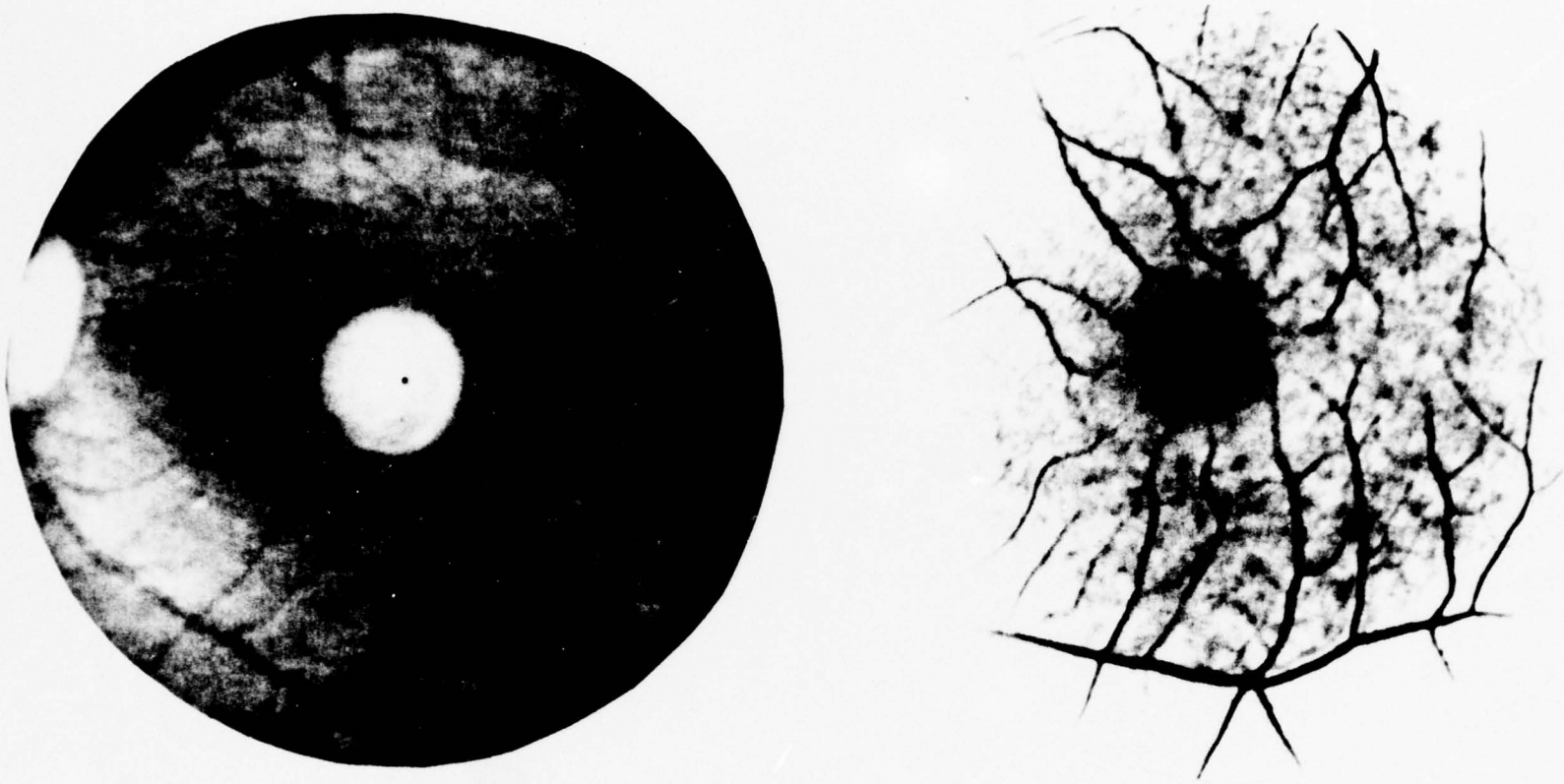

FIGURE 1-5. Ordinary Fundus Photograph (left) and Fluorescein Angiogram (right) of Subject 572 (OS) Taken[16] at Two Hours Post-exposure. Calculated laser image diameter at retina, 544 μm; corneal power, 259 mW; exposure time, 1.1 sec; calculated average retinal dose, 83.7 J/cm^2. Measured lesion diameter (funduscopic) 1100 μm. See Table I-3.

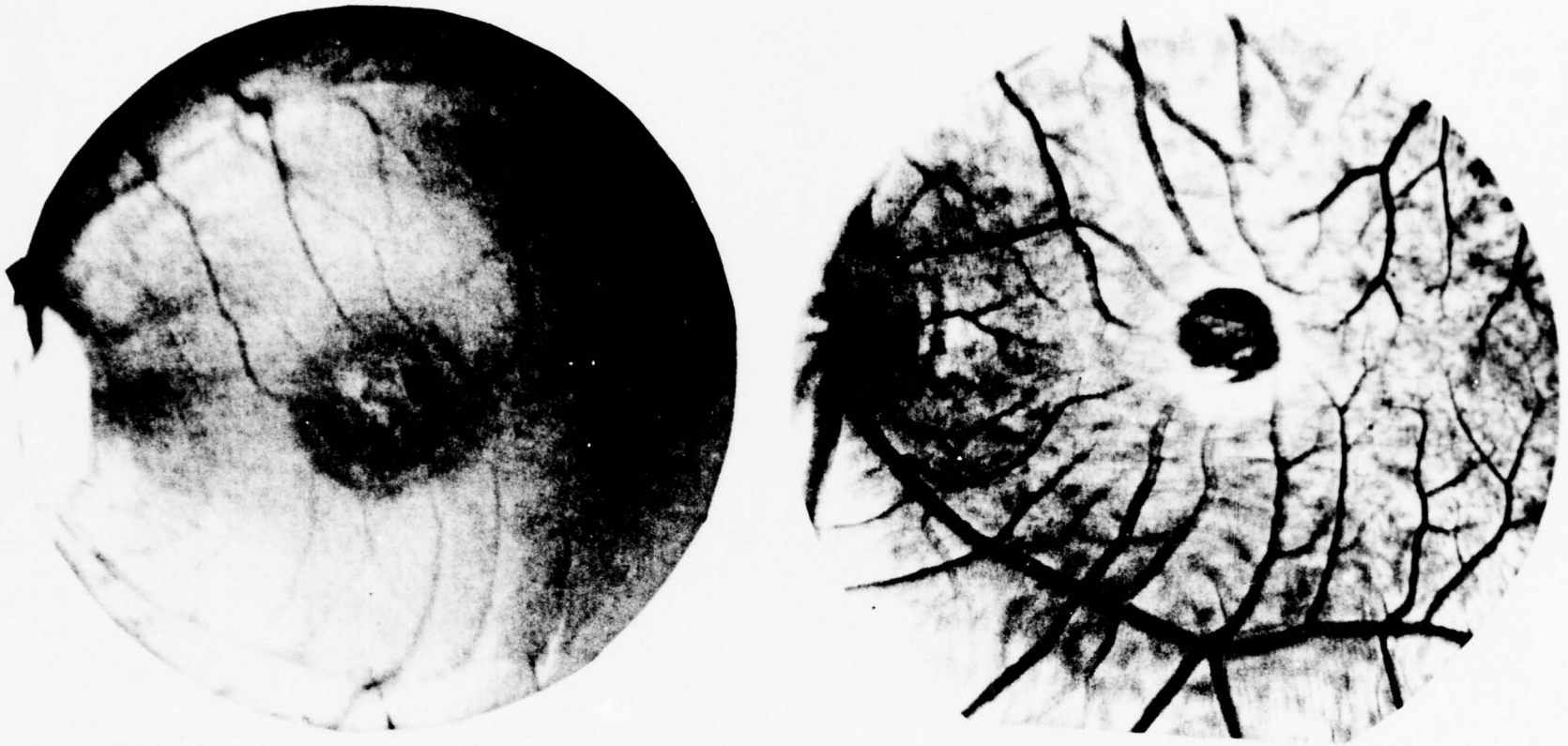

FIGURE 1-6. Ordinary Fundus Photograph (left) and Fluorescein Angiogram (right) Taken[16] at 75 Days Post-exposure. Funduscopic lesion diameter is seen to be ~1250 μm, whereas measurement of the angiogram gives approximate lesion dimensions of 680 x 760 μm (see Table 1-3).

REFERENCES

1. Farrer, D. E. and P. V. Garcia, personal communication.

2. Wolff, E., "Anatomy of the Eye and Orbit", 6th Ed., W.B. Saunders Co., San Francisco, 1968.

3. Takata, A.N., et al., "Thermal Model of Laser-Induced Eye Damage", Illinois Institute of Technology Research Institute, Final Technical Report, Contract F41609-74-C-0005, USAF School of Aerospace Medicine, October 1974.

4. Connolly, J.S. and H.W. Hemstreet, Jr., in "Research on the Ocular Effects of Laser Radiation", Technology Incorporated, Second Annual Report, Part I, Contract F41609-73-C-0017, USAF School of Aerospace Medicine, February 1975.

5. Sanders, V.E. and H.W. Hemstreet, Jr., ibid., Part V.

6. Nawrocki, A.D., et al., This report, Chapter 3.

7. Geeraets, W.J. and D. Ridgeway, "Retinal Damage from High Intensity Light", Acta Ophthl. Suppl. 76:109, 1963.

8. Hemstreet, H.W., Jr., J.S. Connolly and D.E. Egbert, "Ocular Hazards of Picosecond and Repetitive Pulsed Lasers, Volume I. Nd:YAG Laser (1064 nm)", Technology Incorporated, Final Report, Contract F41609-73-C-0016, USAF School of Aerospace Medicine, January 1977.

9. Connolly, J.S., H.W. Hemstreet, Jr. and D.E. Egbert, ibid., Volume II. "Argon-ion Laser (514.5 nm)", January 1977.

10. Sanders, V.E., in "Research on the Ocular Effects of Laser Radiation", Technology Incorporated, First Annual Report, Part I, Contract F41609-73-C-0017, USAF School of Aerospace Medicine, February 1974.

11. Boettner, E.A., "Spectral Transmission of the Eye", University of Michigan, Final Technical Report, Contract AF41(609)-2966, USAF School of Aerospace Medicine, July 1967.

12. Nawrocki, A.D., et al., in "Research on the Ocular Effects of Laser Radiation", Technology Incorporated, Second Annual Report, Part III, Contract F41609-73-C-0017, USAF School of Aerospace Medicine, February 1975.

13. Nawrocki, A.D. and R.F. Lemberger, unpublished results, 1975.

14. Gallagher, J.T., "Optical Components", USAF School of Aerospace Medicine (SAM/RZL), unpublished report, 1975.

15. Garcia, P.V., et al., "Assessment of Functional Vision", University of Texas at El Paso, Draft Final Technical Report, Contract F41609-75-C-0002, USAF School of Aerospace Medicine, July 1975.

16. Garcia, P.V. and D.N. Farrer, to be putlished (1977). Permission to cite these results is gratefully acknowledged.

17. Yates, J.T., personal communication.

CHAPTER 2

RETINAL PHOTOCHEMISTRY

A. INTRODUCTION

Involvement of photochemical processes in laser-induced retinal damage mechanisms has been inferred from results of two widely disparate kinds of threshold experiments. Ham, et al.[1] observed a strong wavelength dependence of damage threshold for long-term (1-1000 sec), low power exposures over the range from 441.6 to 1064 nm. The results were compared against calculated temperature increases from which it was inferred that thermal mechanisms predominate in the case of near-IR exposure with a gradual progression to photochemical mechanism(s) with decreasing wavelengths. Ham[2] has recently attributed the latter primarily to coagulation of pigment granules in the pigment epithelium (PE). The macula lutea appears to be less sensitive than the paramacula to blue wavelengths, presumably due to protective absorption by xanthophyll[2]. We have observed a similar effect and tend to concur with this explanation (see Chapter 4).

Another case of presumed photochemical damage was reported by Connolly, et al.[3,4]. Short (10 μsec), repetitive pulses of visible and near-IR laser radiation demonstrate distinct cumulative effects that are optimal for certain pulse separations. Figure 2-1 shows this pattern for fixed configurations of 2, 3, 5 and 10 identical pulses of 514.5 nm radiation. The distinct minima in the damage thresholds for interpulse separations of 0.5 to 2.5 sec cannot be understood in terms of strictly thermal processes. Accordingly, we hypothesize involvement of photochemical or photobiological effects in the retina, possibly involving the photoreceptor pigments[3]. The distinction between photochemistry and photobiology in this particular case is necessarily ambiguous. For the purpose of this discussion, however, we can consider that photochemical processes involve relatively rapid (msec or less) molecular changes due to chemical reactions of excited electronic states. In contrast, photobiological processes may be defined as alterations of biological activity, usually on a much longer time scale. However, in both cases, the initial event is quantum conversion of the absorbed electric-dipole radiation, as opposed to thermal conversion in which the absorbed light is degraded as heat.

In an earlier report[3], we discussed initial results of empirical computer modeling. These efforts were undertaken for the dual purpose of predicting relative damage thresholds for multiple-pulse configurations and to provide insight regarding possible damage mechanisms. Thus, if the available data could be described by a set of simple analytical functions, one or more working hypotheses could be constructed and experiments designed to test them.

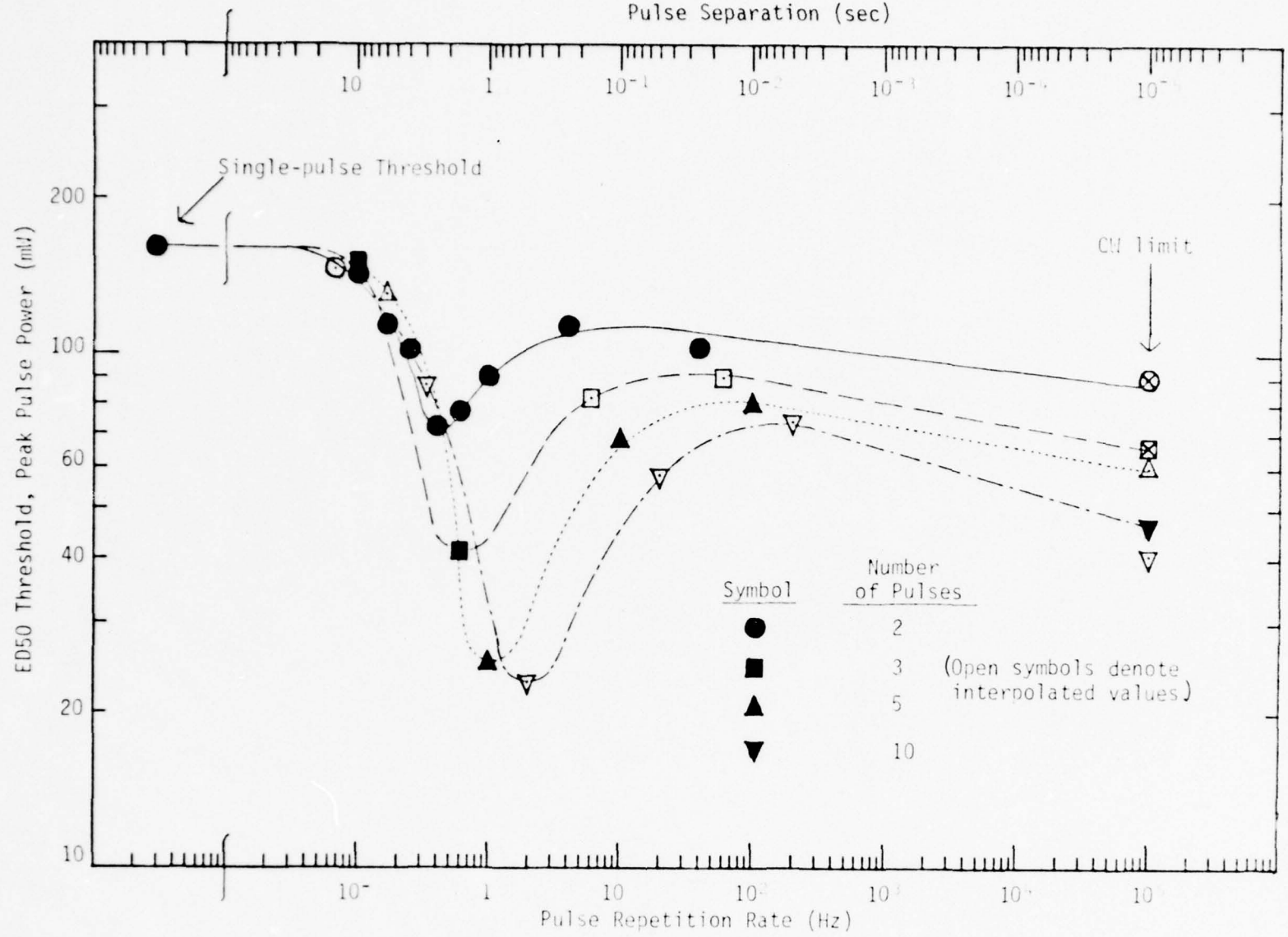

FIGURE 2-1. Retinal Threshold vs. Pulse Separation for Fixed Numbers of Repetitive 10-μsec, 514.5 nm Laser pulses.

B. EMPIRICAL MODEL

The multiple-pulse data displayed in Figure 2-1 are listed in Table 2-1. Double-pulse threshold data are re-plotted in Figure 2-2 as "relative sensitivity" vs. time. This sensitivity function is defined by:

$$S(t) = \frac{161}{ED_{50}(t)} \tag{2-1}$$

where 161 is the single-pulse threshold (in mW incident at the cornea) and $ED_{50}(t)$ is the threshold for double pulses separated by t sec.

In attempting to fit these curves to analytic functions, the principal criteria were: (a) to minimize the number of adjustable parameters, and (b) to restrict the choice of trial functions to those with some reasonable biophysical interpretation. The rate equations for the consecutive, irreversible first-order rate processes:

$$A \xrightarrow{k_1} B \xrightarrow{k_2} C \xrightarrow{k_3} D \tag{2-2}$$

meet both criteria. Moreover, consecutive, irreversible first-order processes are well established in the photochemistry of the retinal pigment rhodopsin[5,6]. The differential equations describing the time dependence of these species are:

$$\frac{dA}{dt} = -k_1 A \tag{2-3}$$

$$\frac{dB}{dt} = k_1 A - k_2 B \tag{2-4}$$

$$\frac{dC}{dt} = k_2 B - k_3 C \tag{2-5}$$

$$\frac{dD}{dt} = k_3 C = -\left(\frac{dA}{dt} + \frac{dB}{dt} + \frac{dC}{dt}\right) \tag{2-6}$$

The solutions of these equations can be found in any standard text[7]:

$$A(t) = A_0 e^{-k_1 t} \tag{2-7}$$

$$B(t) = \frac{A_0}{k_1 - k_2}\left(e^{-k_2 t} - e^{-k_1 t}\right) \tag{2-8}$$

$$C(t) = A_0 k_1 k_2 \left\{ \frac{e^{-k_1 t}}{(k_1-k_2)(k_1-k_3)} - \frac{e^{-k_2 t}}{(k_1-k_2)(k_2-k_3)} + \frac{e^{-k_3 t}}{(k_2-k_3)(k_1-k_3)} \right\} \tag{2-9}$$

$$D(t) = A_0 - \{A(t) + B(t) + C(t)\} \tag{2-10}$$

where A_0 represents the initial concentration (i.e., at t = 0) of species A.

TABLE 2-1. RETINAL THRESHOLDS FOR FIXED NUMBERS OF REPETITIVE 10-μsec, 514.5-nm LASER PULSES[3]

No. of Pulses	Pulse Repetition Frequency (Hz)	Inter-Pulse Spacing (sec)	ED50[a] Peak Pulse Power (mW)	ED50[a] Energy/ Pulse (μJ)	90%[b] Confidence Interval Power (mW)	No. of Eyes
2	40	0.025	103	1.03	98.5 - 108	10
	4	0.25	113	1.13	108 - 118	9
	1	1	90.5	0.90	83.7 - 8.0	5
	0.6	1.667	77.3	0.77	67.8 - 88.1	3
	0.4	2.5	72.3	0.72	69.8 - 74.3	11
	0.25	4	102	1.02	97.0 - 108	4
	0.167	6	114	1.14	105 - 124	4
	0.10	10	143	1.43	133 - 155	4
	0.067	15	≈146	≈1.46	---	(c)
3	60	0.017	≈90	≈0.9	---	(c)
	6	0.167	≈82	≈0.82	---	(c)
	0.6	1.667	41.3	≈0.41	39.6 - 43.1	10
	0.1	10	151	1.51	144 - 157	10
5	100	0.01	79.8	0.80	77.8 - 81.8	10
	10	0.10	67.8	0.68	66.5 - 69.2	6
	1	1	25.0	0.25	23.9 - 26.1	11
	0.167	6	≈130	≈1.3	---	(c)
10	200	0.005	≈74	0.74	---	(c)
	20	0.05	≈58	0.58	---	(c)
	2	0.5	≈23	0.23	---	(c)
	0.333	3	≈87	0.87	---	(c)

(a) Powers and energies at cornea.

(b) Lower and upper 95% confidence limits.

(c) Interpolated.

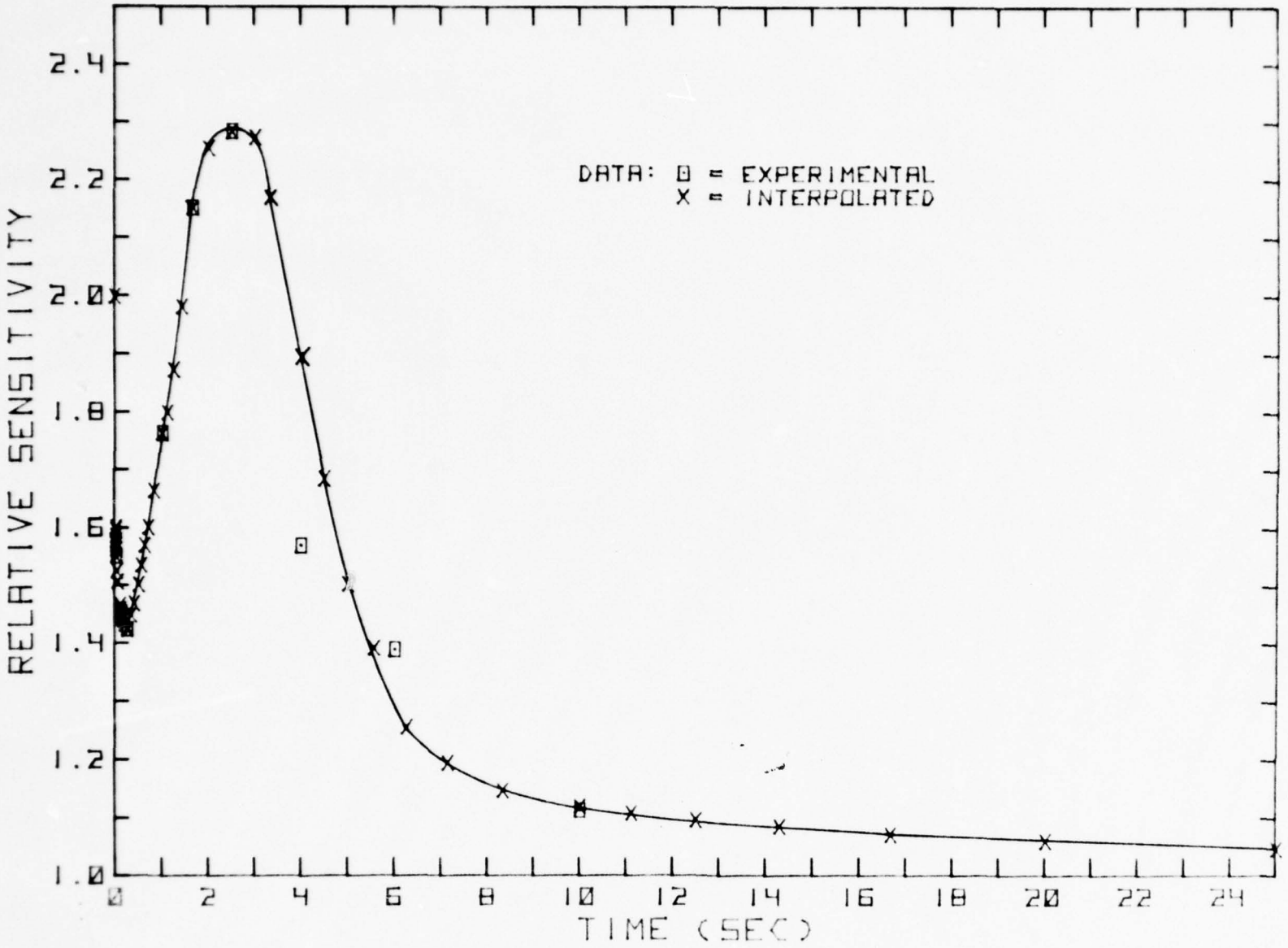

FIGURE 2-2. Relative Retinal Sensitivity vs. Pulse Separation for Double 10 μsec, 514.5 nm Laser Pulses.

By trial and error, we found that the data, expressed as retinal sensitivity (Fig. 2-2), could be fit satisfactorily by Equation (2-9) with $A_0 = 2.85$, $k_1 = 1.6\ sec^{-1}$, $k_2 = 0.8\ sec^{-1}$ and $k_3 = 0.48\ sec^{-1}$, as shown in Figure 2-3.

It is not essential to assume that retinal damage induced by repetitive laser pulses results from a molecular scheme exactly as depicted by Equation (2-2). Rather, the immediate purpose of this modeling effort was to determine whether the same time-dependent function (e.g., Eq. 2-9) could adequately describe not only the double-pulse threshold data, but also multiple-pulse ($n > 2$) threshold data.

The treatment for double pulses is relatively straightforward since pulse separation is identical to real time. Furthermore, the presumed roles of the two pulses are separate and discrete: the first pulse is considered to sensitize the retina either by the formation of a transient intermediate species or by inducing a time-dependent alteration in the condition of the retina (e.g., high local concentrations of Na^+ or Ca^{++}[8]). The second pulse then induces damage which is considered to be reversible up to some as yet undetermined level (i.e., threshold) and irreversible beyond that point. As discussed previously[3], the data in Figure 2-1 suggest that there is a different threshold for each pulse. Specifically, the threshold power for the first pulse appears to be in the neighborhood of 20-25 mW, since no damage was observed at lower peak powers, even for 10 or more pulses. The threshold of the second pulse appears to be ~70 mW, i.e., the lowest power at which damage could be induced with double pulses.

For three or more pulses, the picture is more complex. First, pulse separation and real time are not identical. Secondly, in an n-pulse train, the middle (n-2) pulses are considered to have the dual roles of inducing damage and sensitizing the retina for the next pulse. Finally, inspection of the data for 2, 3, and 5 pulses (Table 2-2) suggests that the effect of the last (n-1) pulses is energy- rather than power-dependent.

Thus, in order to apply Equation (2-9) to the case of three or more pulses, it is necessary to make some explicit assumptions.

(1) It is assumed that the cumulative effects of visible laser pulses are due to photobiological (or photochemical) processes rather than to thermal effects. The basis for this assumption is that thermal relaxation processes in the retina have been shown, both experimentally[9-11] and theoretically[12], to be much faster than the observed 0.5-2.5 sec optimum interpulse spacing.

(2) It is further assumed that the primary light absorbing species responsible for the observed phenomenon is the photoreceptor pigment. It has been amply demonstrated that brief, intense flashes saturate the photoreceptors at 50% conversion of rhodopsin to its bleached photoproducts[5]. Since the time scale for recovery of bleaching (~30 min)[13] is much longer than the time span of interest here, recovery of the light absorbing species

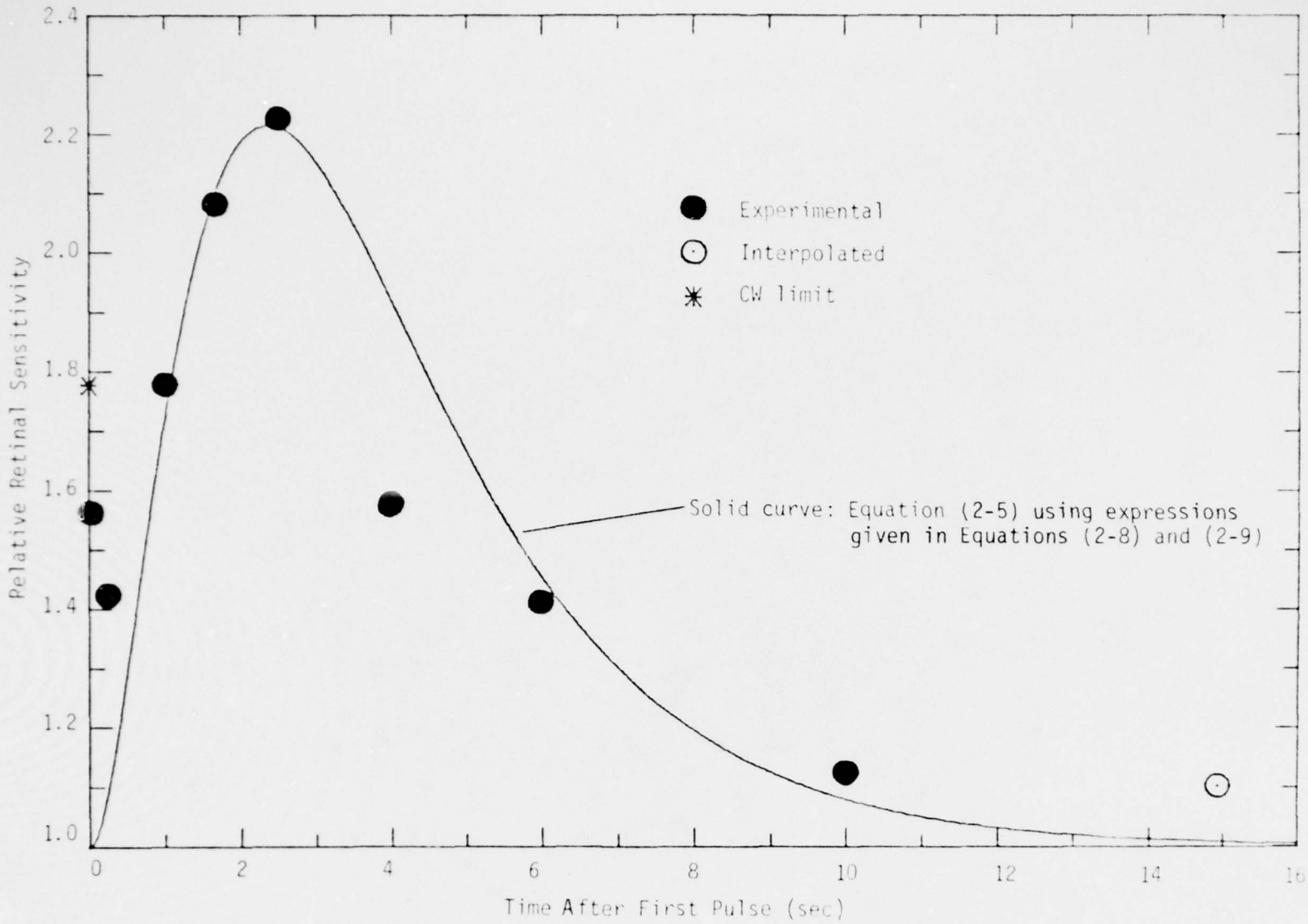

FIGURE 2-3. Empirical Fit of Relative Retinal Sensitivity as a Function of Pulse Separation. (The Sensitivity is defined as the ratio of single- to double-pulse thresholds).

TABLE 2-2.

THRESHOLD POWERS AND ENERGIES FOR REPETITIVE 10 μsec, 514.5 nm LASER PULSES AT OPTIMUM SPACING

No. of Pulses (n)	Interpulse Spacing (sec)	ED50* Threshold Power (mW)	ED50* Energy per Pulse (μJ)	Total Energy n Pulses (μJ)	Total Energy (n-1) Pulses (μJ)
2	2.5	∿72	0.72	1.44	0.72
3	1.67	∿41	0.41	1.23	0.82
5	1.0	∿25	0.25	1.25	1.00
10	∿0.5	∿23	0.23	∿2.3	2.07

* Incident at the cornea.

can be considered negligible. Thus, the contribution of each pulse to the retinal sensitivity is assumed to decrease by successive factors of two. Equation (2-9), which expresses the time dependence of retinal sensitivity only for the first pulse, can then be rewritten for each pulse in a train of n pulses:

$$F_n(t) = \frac{A_0' \, f_n(t)}{2^n} \qquad (2\text{-}11)$$

$$= 0 \text{ if } t \leq ns$$

where $f_n(t)$ is given by Equation (2-9), s is the interpulse spacing, and A_0' becomes the new normalization factor.

(3) For a train of n pulses we consider only the effects of the last (n-1) pulses. In other words, it is implicitly assumed that the sensitization effect is independent of laser intensity[14]. This assumption is consistent with the double-threshold hypothesis[3] and has some interesting consequences which are discussed below.

(4) It is necessary to make some assumption regarding the fate or role of the presumed transient intermediate state. It may be assumed that state "C" represents a real intermediate species, which itself is subject to whole or partial destruction by absorption of subsequent laser pulses. Alternatively, state "C" may represent an intermediate species (or a transient condition of the retina) which, once formed, is unaffected by subsequent laser pulses. In the former case, the pool would be depleted by successive pulses and the cumulative effect would be expected to saturate at fewer pulses than in the latter case where no destruction is assumed. Both cases have been treated and the results are discussed below.

No attempt has yet been made to calculate absolute threshold powers or energies, primarily because there exist insufficient experimental data on which to base a "damage integral". However, if the two-threshold hypothesis discussed previously for double pulses[3] is verified experimentally, it will be a relatively simple matter to define a numerical damage criterion and calculate the power (energy) required to induce retinal lesions.

From Equation (2-11), it is seen that the cumulative effect of n successive pulses can be written as:

$$G(n,t) = \frac{f(t)}{2} + \frac{f(t-s)}{4} + \frac{f(t-2s)}{8} + \ldots + \frac{f\{t-(n-1)s\}}{2^n}$$

$$= \sum_{k-1}^{n} \frac{f\{t-(k-1)s\}}{2^k} \qquad (2\text{-}12)$$

where s is the interpulse spacing and, as before, $f(t-ns) = 0$ if $t \leq ns$.

If it is first assumed that the damage probability for the n^{th} pulse is proportional to the population of species "C" induced by the previous (n-1) pulses where "C" is not subject to destruction by the laser radiation, then for any given pulse separation the "damage integral" is simply the sum of the appropriately normalized values of G(n,t) at the time each successive pulse is delivered. For two pulses, the optimum interpulse spacing is calculated to be ~2.4 sec and the damage threshold is higher than in the case of three or more pulses.

For multiple-pulse exposure trains (n>2), the optimum retinal sensitivity will occur at a spacing, s, such that the sum of the values of G(n,t) evaluated at each time interval (t=ns) is a maximum. Thus, multiplying Equation (2-12) by the normalization factor (A_0'), the sum to be evaluated is:

$$A_0' \sum_{j=1}^{n} G(j,js) = \frac{A_0'}{2}\left[\sum_{j=1}^{n} f(js) + \sum_{j=2}^{n}\sum_{k=1}^{j-1} \frac{f(js-ks)}{2^k}\right] \qquad (2\text{-}13)$$

A BASIC language computer program was written for the Hewlett-Packard 9830 system to carry out these calculations. The resulting equation used to fit the data is:

$$P = \frac{161}{1+A_0' \sum_{n} G(n,ns)} \times \frac{1}{T} \qquad (2\text{-}14)$$

where P is the threshold power per pulse (mW at the cornea), the summation is defined by Equations (2-13) and (2-9), and T is an empirical correction term to take into account cumulative effects of strictly thermal mechanisms[15]. The correction would only be important at very high frequencies (i.e., short interpulse spacings). The results are shown in Figure 2-4 for A_0' = 5.7.

It can be seen that the fit of Equation (2-14) is rather satisfactory for 2, 3, and 5 pulse configurations. However, this version of the model does not yield a saturation of the cumulative effect at n ≥ 5 pulses. Instead, this model predicts that repetitive laser pulses continue to demonstrate a cumulative effect even beyond 10 pulses. This feature is a logical consequence of assumption (3) above, namely that the magnitude of retinal sensitization is independent of laser intensity which is evidently not the case.

The results in Figure 2-4 suggest that if the intensity of the first pulse is sufficiently high, subsequent pulses at low power can induce damage if enough of them are delivered to the retina at a spacing of 0.4 to 0.5 sec. In other words, this version of the model adequately describes the two-threshold hypothesis[3] discussed above. This is shown more clearly in Table 2-3, which compares the predicted and experimentally observed results. These results suggest that in addition to the interpulse power dependence for two pulses, experiments should be undertaken to test the equal energy relation predicted for the last n-1 pulses for multiple-pulse exposures. The results would immediately confirm or deny the validity of both the two-threshold hypothesis and this version of the multiple-pulse

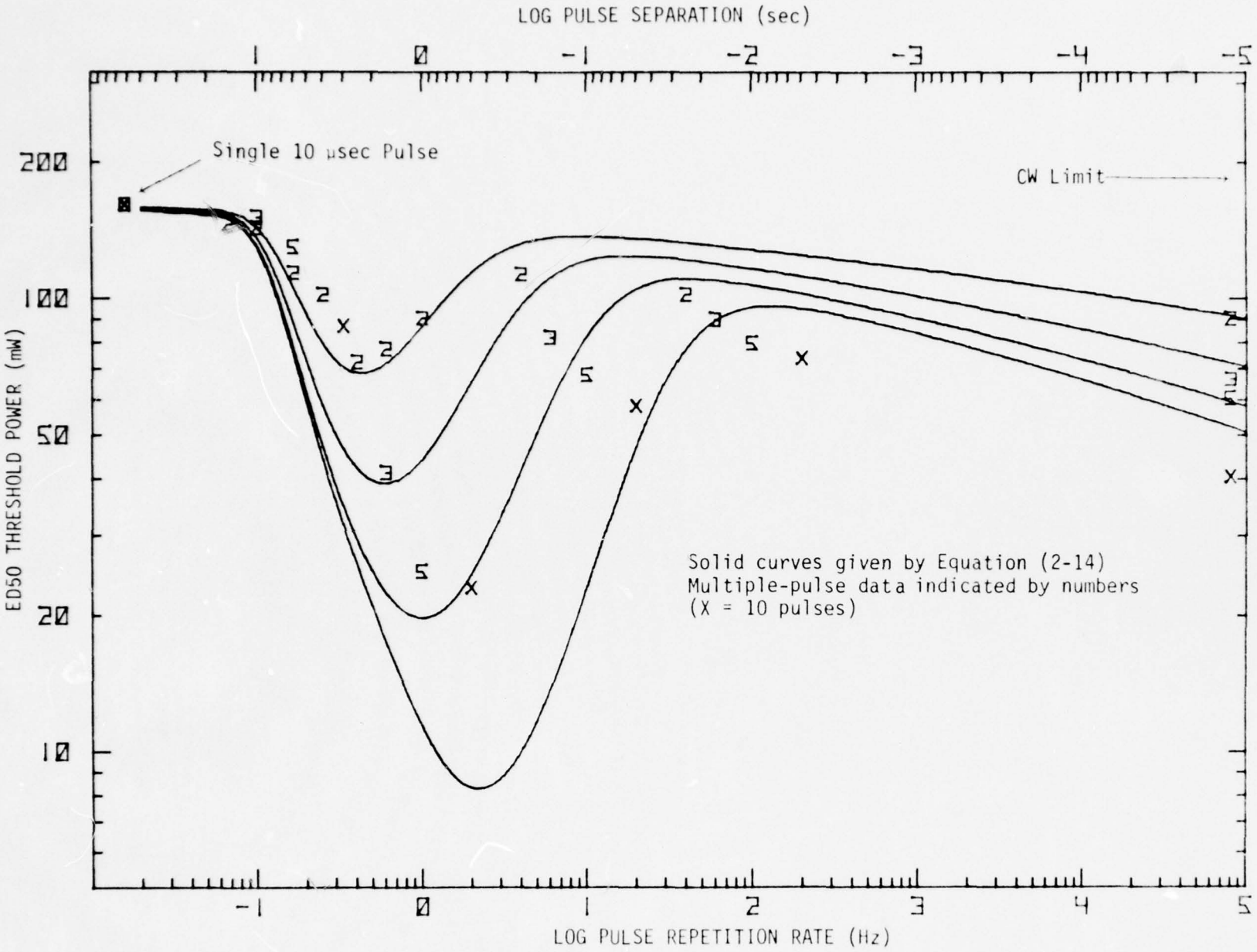

FIGURE 2-4. Semi-empirical Fit of Threshold vs. Pulse Separation for Multiple 10 μsec, 514.5 nm Laser Pulses.

TABLE 2-3.

PREDICTED AND EXPERIMENTAL THRESHOLDS FOR MULTIPLE 10 μsec LASER PULSES AT 514.5 nm.

Total No. of Eyes	EXPERIMENTAL			PREDICTED (Eq. 2-14)			PREDICTED (Eq. 2-16)		
	ED_{50} (mW)	Optimum Spacing (sec)	Energy of Last (n-1) Pulses (μJ)	Threshold (mW)	Optimum Spacing (sec)	Energy of Last (n-1) Pulses (μJ)	Threshold (mW)	Optimum Spacing (sec)	Energy of Last (n-1) Pulses (μJ)
2	72.3	2.5	0.72	68.3	2.3	0.68	68.3	2.3	0.68
3	41.3	1.67	0.83	39.1	1.7	0.78	45.3	1.9	0.92
5	25.0	1.0	1.00	19.7	1.0	0.79	33.0	1.6	1.32
10	∿23.0	∿0.5	2.07	8.3	0.5	0.75	29.3	1.4	2.64

model. In addition, if the results validate the model, then the hypothesis of a photochemical damage mechanism will be proved.

Next, consider the case where state "C" is presumed to be a real intermediate chemical species formed by the first n-1 pulses and destroyed, wholly or in part, by the last n-1 pulses. It is assumed that of the amount of "C" (formed by the first pulse), available when the second pulse arrives (t = s), 50% is destroyed while the second pulse simultaneously converts 50% of the remaining absorber pool to state "C". The third pulse then destroys half the amount of the intermediate available at t = 2s, and so forth. The net effect is that the maximum amount of the pool that can be destroyed is 50% and the overall retinal sensitivity (Eq. 2-13) is reduced by half. Thus, an equation similar to (2-13) is employed except that the double summation will be missing a term of the form f(s)/2. The operable equation for depletion or destruction of species "C" is described by Equations (2-15) and (2-16):

$$P = \frac{161}{1+A_0' \sum_n G'(n,ns)} \times \frac{1}{T} \qquad (2\text{-}15)$$

$$A_0' \sum_n G'(n,ns) \equiv A_0' \sum_{j=1}^{n} G'(j,js)$$

$$= \frac{A_0'}{2}\left[\sum_{j=1}^{n} f(js) + \sum_{j=3}^{n}\sum_{k=2}^{j-1} \frac{f(js-ks)}{2^k}\right] \qquad (2\text{-}16)$$

As before, f(ns) is given by Equation (2-9). The results for 2, 3, 5 and 10 pulse exposures are shown in Figure 2-5.

The symmetry displayed in Figure 2-2 suggests an alternative modeling approach; namely, that either a Gaussian or Lorentzian function might yield a more satisfactory fit. Both functions require only three arbitrary parameters although the biophysical significance of the results would clearly be open to question. In any case, neither of these functions alone gave a satisfactory fit to the data, although the Gaussian analysis did provide some useful insight regarding the form of the equation corresponding to the smooth curve in Figure 2-2.

A Gaussian function of the form:

$$Y = C_0 \exp\left(-\{(t-a)/b\}^2\right) \qquad (2\text{-}17)$$

has a linear transform expressed by:

$$\pm \sqrt{\ln(C_0/Y)} = \frac{t-a}{b} \qquad (2\text{-}18)$$

A set of data can be fit to a Gaussian profile using a simple least squares analysis. Taking the positive root of Equation (2-18) for t > a and the negative root for t < a extends the region of the linear fit. Figure 2-6

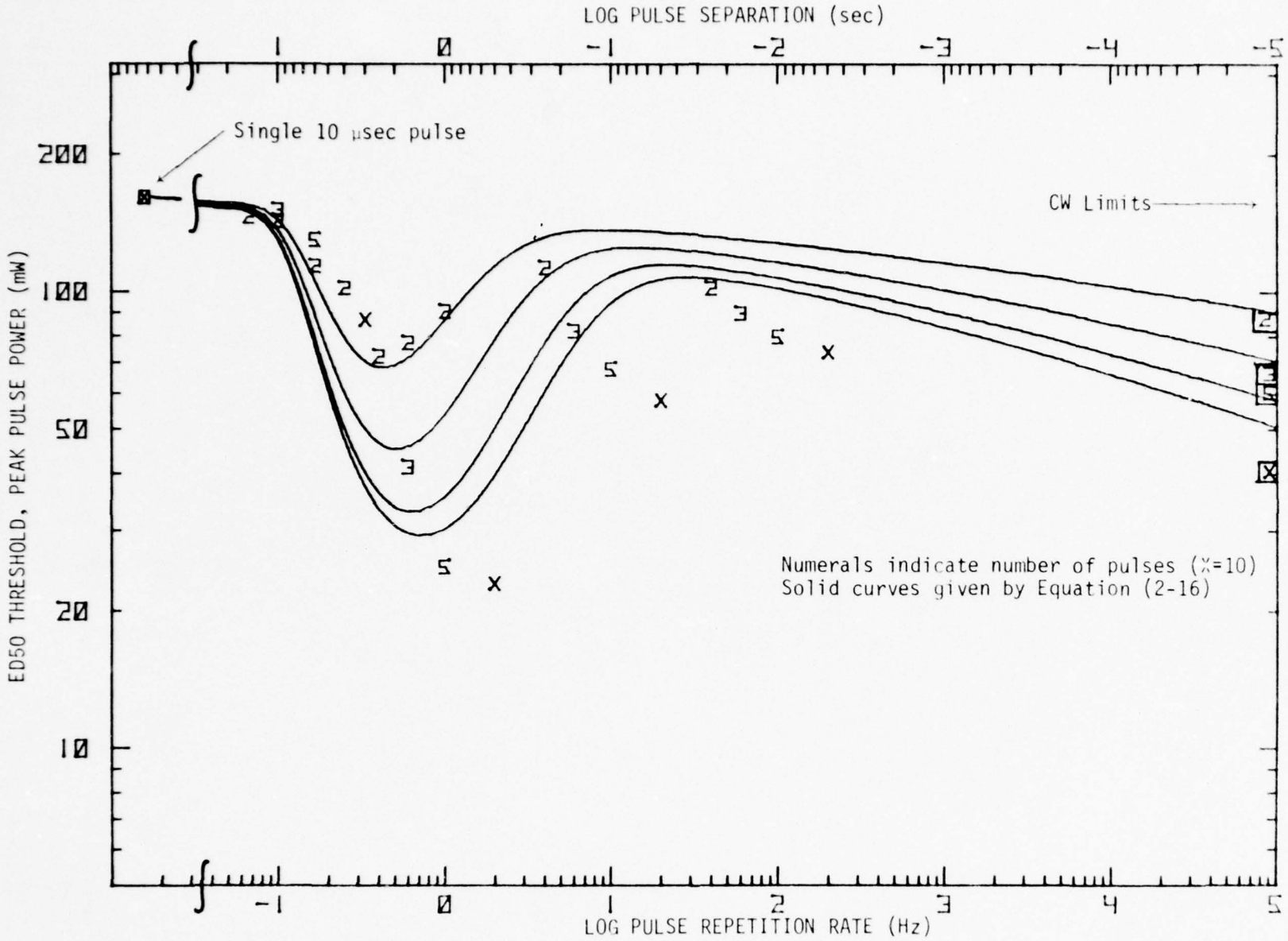

FIGURE 2-5. Semi-empirical Fit of Threshold vs. Pulse Separation for Multiple 10 μsec, 514.5 nm Laser Pulse.

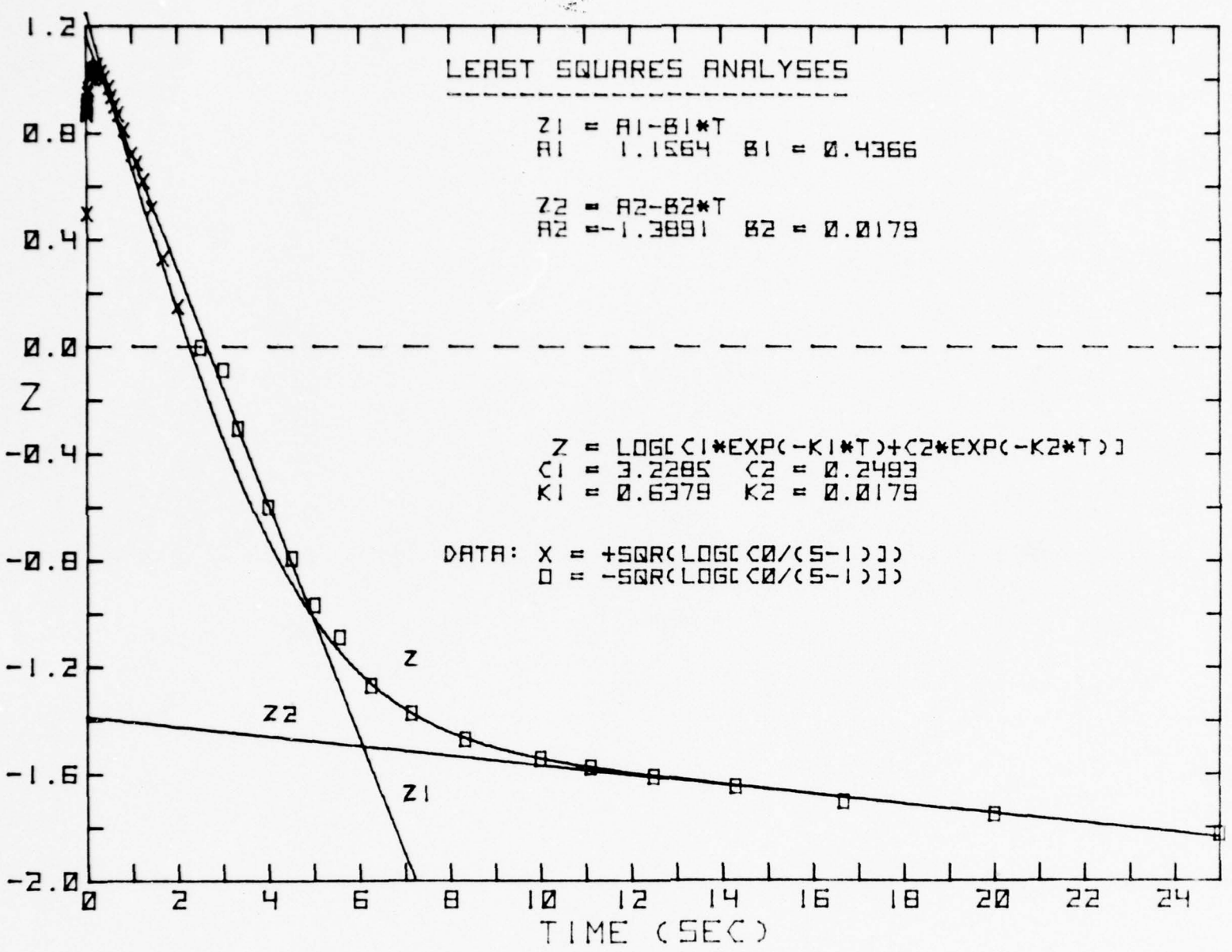

FIGURE 2-6. Least Squares Analysis of $Z = \pm \sqrt{\ln[C_0/(S-1)]}$ vs. Pulse Separation.

displays the results* for the (interpolated) data shown in Figure 2-2. The ordinate is simply:

$$Z = \sqrt{\ln\{C_0/(S-1)\}} \qquad (2\text{-}19)$$

where S is the retinal sensitivity (Eq. 2-1) and C_0 is a normalization factor. There appear to be two linear regions:

(a) $0 \leq t \leq 5$ sec: $Y_1 = A_1 - B_1 t$ (2-20)

and (b) $10 \leq t \leq 25$ sec: $Y_2 = A_2 - B_2 t$ (2-21)

The values of the four coefficients obtained by least squares analysis are indicated on the figure. These results suggest that the sensitivity curve is composed of overlapping Gaussian profiles: e.g.,

$$S-1 = C_1 \exp\left(-\{(t-a)/b_1\}^2\right) + C_2 \exp\left(-\{(t-a)/b_2\}^2\right) \qquad (2\text{-}22)$$

in which case the two linear regions in Figure 2-6 would represent non-overlap between the two expressions on the right side of Equation (2-22). Physical meaning can be attributed to this analysis if the sensitivity curve is viewed in terms of the kinetics of competing first-order processes of different species. For example, consider the case of two transient species, S_1 and S_2, which disappear by first-order rate processes:

$$\begin{aligned} S_1 &\xrightarrow{k_1} P_1 \\ S_2 &\xrightarrow{k_2} P_2 \end{aligned} \qquad (2\text{-}23)$$

If, at a given wavelength, both S_1 and S_2 absorb light more strongly than their respective products, P_1 and P_2, an overall decay of the total absorbance, D_T, would be observed. Since D_T is simply the sum of the absorbance changes of the two species, D_1 and D_2, attempts to analyze the observed absorbance decay in terms of first-order kinetics would yield a result quite similar to Figure 2-6. That is, a semi-logarithmic plot of D_T vs. t would yield a plot of $\ln(D_1^0 e^{-k_1 t} + D_2^0 e^{-k_2 t})$ where D_1^0 and D_2^0 refer to absorbance changes at $t = 0$. Assuming that $k_1 > k_2$, the usual treatment[6] in such cases is to determine D_2^0 and k_2 by linear least squares techniques at times sufficiently long that contributions from the other term are negligible. At shorter times, contributions of the second term are computed, converted to absorbance and subtracted from the overall absorbance, D_T. The logarithm of the residual is in turn subjected to least squares analysis, thereby giving good estimates of all four parameters. Computer analysis of such kinetic processes is commonplace in photochemistry, radiation chemistry, and biochemistry.

*NOTE: The experimental data shown in Figure 2-6 and the following figures were taken from earlier calculations of the ED_{50} thresholds using a combined probit analysis[15]. The points shown are only slightly different from those listed in Table 2-1.

The time dependence of the function Z (Eq. 2-19) was analyzed in this way. Thus,

$$Z = \sqrt{\ln(C_0/S-1)} = \ln(C_1e^{-k_1t}+C_2e^{-k_2t}) \qquad (2\text{-}24)$$

Equation (2-24) yields a new computed retinal sensitivity function:

$$S(t) = 1+C_0/\exp\{\left[\ln(C_1e^{-k_1t}+C_2e^{-k_2t})\right]^2\} \qquad (2\text{-}25)$$

This function is shown on a linear time scale in Figure 2-7 and the agreement with the experimental data appears to be rather satisfactory.

This function can be used to compute relative threshold values by a transformation of Equation (2-1):

$$ED_{50}(t) = \frac{161}{S(t)} \qquad (2\text{-}26)$$

The result is plotted on a log-log scale in Figure 2-8. Again, the fit is satisfactory although a somewhat better fit can be obtained by small adjustments in the parameters, especially C_1 and k_1.

As shown in Figure 2-9, the fit achieved by successive application of Equations (2-25) and (2-26) is less than satisfactory for all but the double-pulse case. These computations were carried out as described previously (Eqs. 2-13 and 2-14) and incorporated the assumption that of the available pool of light absorbing species, only 50% are affected by each pulse. The principal differences between these computations and those described earlier are the choice of the functional form of the sensitivity of the retina and the neglect of thermal corrections in the latter case. In addition, the new function (Eq. 2-25) requires a different normalization factor in order to fit the double-pulse data at optimum pulse separation ($\sim$2.5 sec).

It is worth repeating that the double-pulse retinal sensitivity curve was chosen simply as a convenient way to represent the threshold data on a linear time scale in order to derive an analytic expression applicable to other multiple-pulse configurations. If it is assumed that the function, Z, (Eq. 2-24) is a measure of retinal sensitivity, then the overall kinetics represent formation of two transient species (or other retinal changes) with relaxation times of $\sim$1.6 and $\sim$55 sec, respectively. This may prove to have more mechanistic significance than any other aspect of this model.

C. COMPARATIVE EFFECTS OF REPETITIVE LASER PULSES: 1064 vs. 514.5 nm

The preceding discussion of presumed photochemical or photobiological damage in the retina, resulting from cumulative effects of successive laser pulses, offers no serious conceptual difficulties for the case of visible radiation. The photoreceptor pigment, rhodopsin, absorbs very strongly in the mid-visible region of the spectrum[5,6], and quantum conversion of

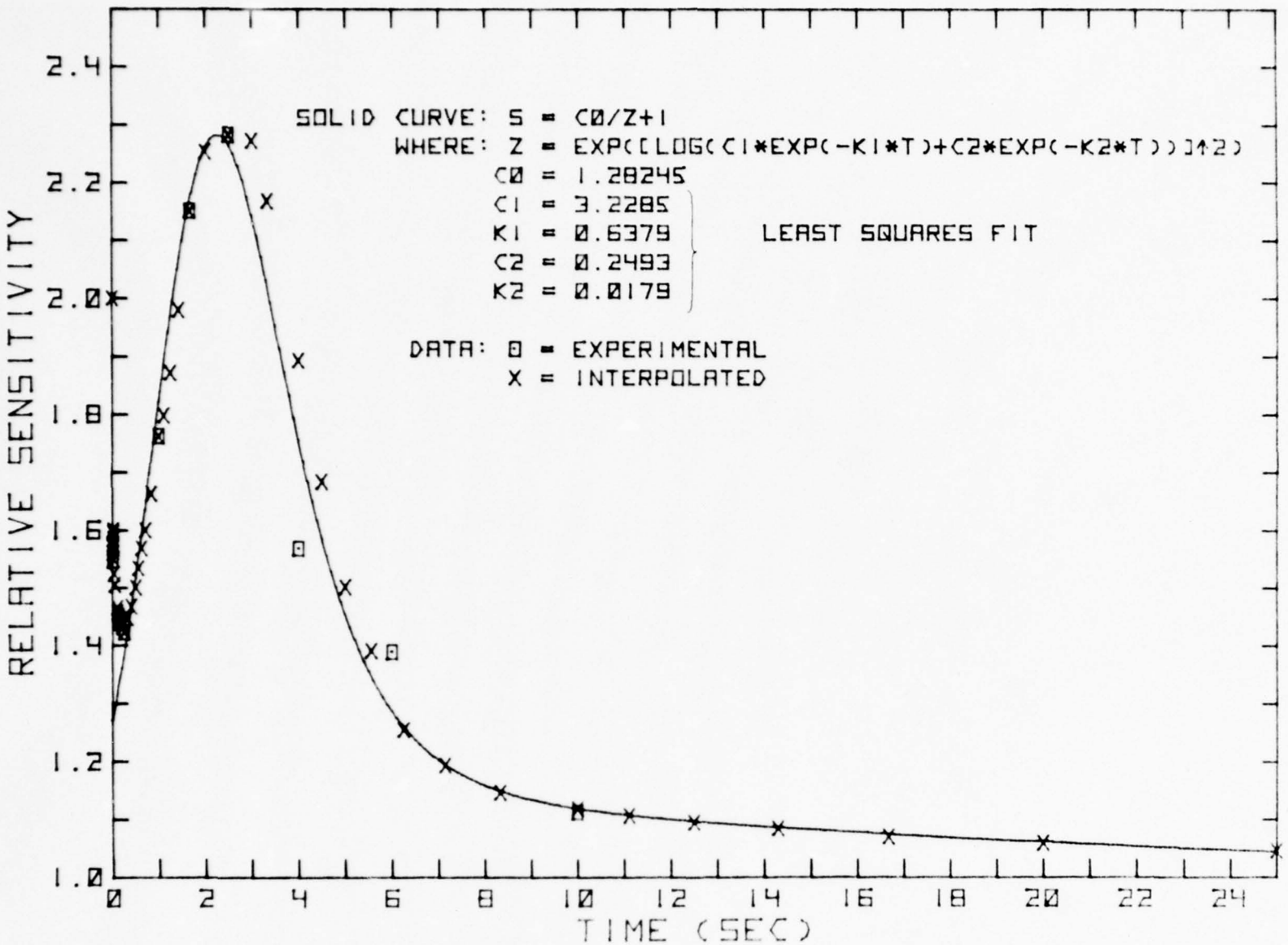

FIGURE 2-7. Semi-Empirical Fit of Relative Retinal Sensitivity vs. Pulse Separation for Double 10 μsec, 514.5 nm Laser Pulses.

BEST AVAILABLE COPY

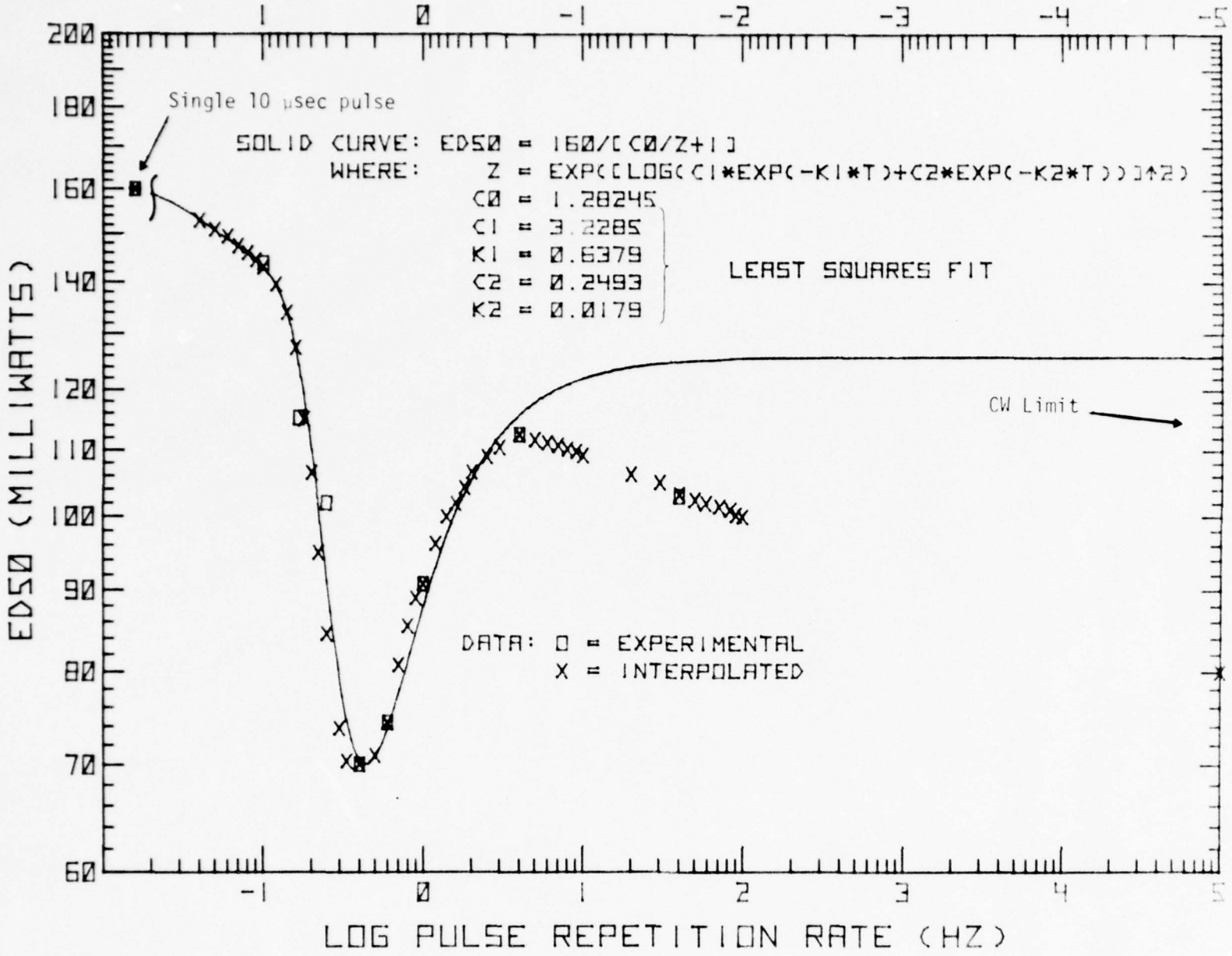

FIGURE 2-8. Semi-empirical Fit of Threshold vs. Pulse Separation for Double 10 μsec, 514.5 nm Laser Pulses. (Thermal corrections neglected).

BEST AVAILABLE COPY

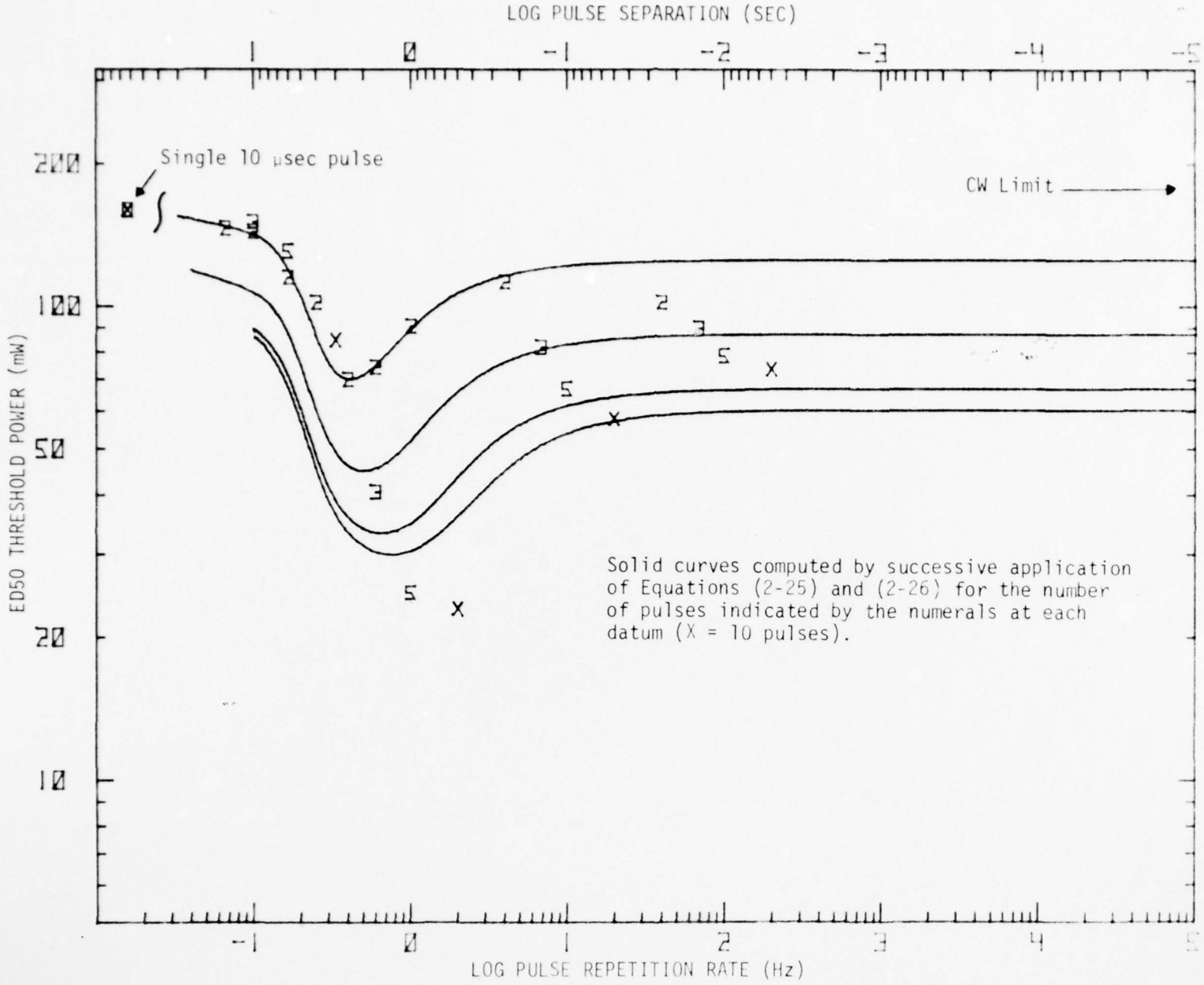

FIGURE 2-9. Semi-Empirical Fit of Threshold vs. Pulse Separation for Multiple 10 μsec, 514.5 nm Laser Pulses. (Thermal corrections neglected.)

BEST AVAILABLE COPY

visible light initiates the complex sequence of chemical and biochemical reactions involved in the visual process[17,18].

Moreover, excess or prolonged photic stimulation of the retina with visible light has been demonstrated to induce retinal degeneration in vertebrates[19-21]. The damage mechanism may involve high concentrations[22,23] of unbound retinol (i.e., all-trans vitamin A alcohol) or free opsin[24,25], both of which are end products of the rhodopsin cycle[17-26]. The visual protein, opsin, has been shown[22] to be more thermally labile when in the free state than when bound either to the chromophore, retinal (i.e., 11-cis vitamin A aldehyde), or to outer-segment membranes. In addition, prolonged or intense exposure of the retina to visible light can induce high localized gradients of Na^+ or Ca^{++} ions[8], which may either damage the retinal membranes or sensitize the exposed area to damage by subsequent radiation. Cation gradients are also implicated by the kinetics involved in multiple-pulse retinal damage. The optimum interpulse spacings of 1-2.5 sec for 10 μsec visible pulses[3] and 0.2 to 0.5 sec for 300 nsec near-IR pulses[4] are much longer than the lifetimes of the various transient intermediates in the rhodopsin cycle[5,6,17,18,22-25,27,28]. However, Bonting[29] has calculated that the recovery time for the light-induced cation gradient in a single rod sac is 0.55 sec at saturating intensities. This compares favorably with the molecular diffusion rates ($\sim 2 \times 10^{-3}$ cm sec^{-1}) calculated by Hagins[30] for frog cones and primate foveal cones.

In the near-infrared (IR) region, however, cumulative effects of repetitive laser pulses are difficult to interpret in terms of either photic or thermal effects. Figure 2-10 shows retinal damage thresholds determined by Hemstreet, et al.[4] for repetitive Q-switched (~300 nsec) 1064 nm laser pulses. The remarkable similarity between these threshold profiles and those measured using 10 μsec, 514.5 nm pulses (see Fig. 2-1) led these workers to speculate that either frequency-doubling or two-photon absorption of 1064 nm laser radiation was involved.

Quantum conversion of the incident laser pulse is considered essential only for the first pulse. That is, for double-pulse threshold damage, the effect of the first pulse is considered to be photic, whereas thermal effects induced by the second pulse (e.g., thermal degradation of free opsin) are not ruled out. From the relative intensities of visible and near-IR radiation required to induce threshold damage at optimum interpulse spacing (viz., ~25 mW at 514.5 nm vs. ~20 W at 1064 nm), a frequency-doubling efficiency of ~0.1% was estimated[3,4] to be sufficient to convert near-IR laser pulses to the necessary intensity of visible light.

Frequency doubling, or second-harmonic generation (SHG), results from a complex interaction between coherent light and the bound electrons in a non-linear medium[31] such as an anisotropic crystal. The efficiency of SHG depends on a variety of factors, including the wavelength, mode purity and power density of the incident laser beam and the thickness of the non-linear medium. SHG in biological tissues has been observed by Fine and Hansen[32] for stretched, Q-switched pulses (60-90 nsec) of ~694.3 nm laser light. For whole cornea (rabbit and dog) and other collagenous tissues

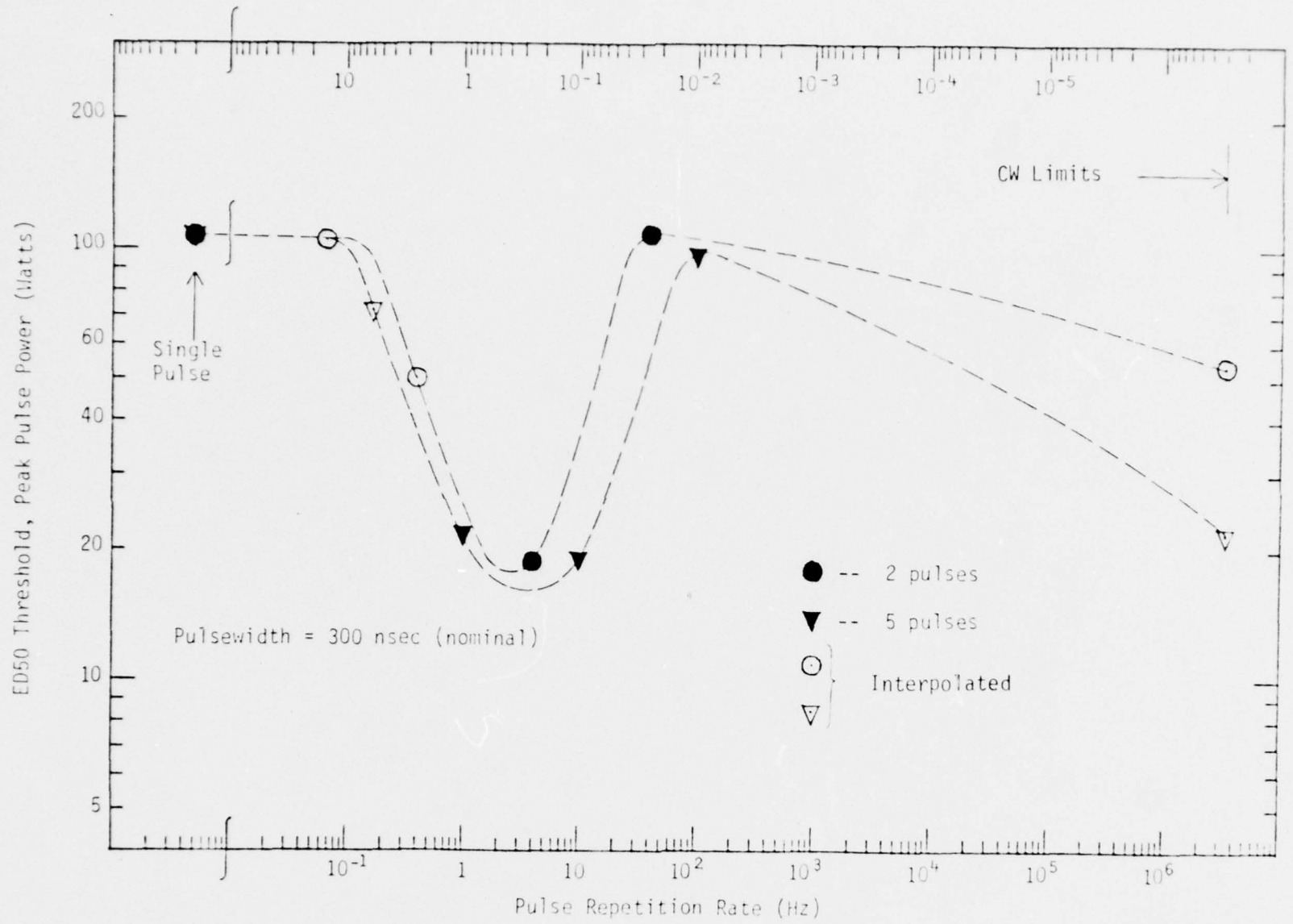

FIGURE 2-10. Retinal Threshold vs. Pulse Separation for Fixed Numbers of Q-switched Nd:YAG Laser Pulses.

BEST AVAILABLE COPY

they measured an SHG efficiency of $\geq 10^{-10}$ at incident peak power densities of $\sim$20 MW cm^{-2}. They noted, however, that the actual conversion efficiency might be substantially higher if light scattering could have been accounted for quantitatively. Thus, a doubling efficiency as high as 10^{-3} (0.1%) for 1064 nm light (1-2 kW cm^{-2}) passing through a highly non-linear[33] crystalline medium as thick as the rhesus lens ($\sim$3.5 mm) is conceivable, but remains to be observed experimentally.

An alternative mechanism for inducing the hypothetical reversible photo-trigger by near-IR laser pulses is biphotonic absorption in the photoreceptor pigment. This effect has been observed in a number of hydrocarbons, both in the crystalline state and in fluid solution, and two-photon absorption cross-sections for 694.3 nm laser radiation have been determined[34]. Based on these values, one can estimate the probability of two-photon absorption in rhodopsin for the laser intensities of interest.

The molecular cross-section (Lambertian) for single-photon absorption (σ_1) is related to the decadic molar extinction coefficient (ε) by[34]:

$$\sigma_1 = \frac{2303\varepsilon}{N} = 3.824\times10^{-21}\varepsilon \qquad (2\text{-}27)$$

where N is the Avogadro number (6.023×10^{23}); ε has units of liter mole^{-1}cm^{-1}, and σ_1 has units of cm^2 molecules^{-1}. The Beer-Lambert equation for intensity of light, I, transmitted through path length, l (cm) is:

$$I = I_0 e^{-\sigma_1 n l} \qquad (2\text{-}28)$$

where I_0 is the intensity of the incident light (photons sec^{-1}) and n is the concentration of the absorbing molecules (molecules/cm^3).

For bovine rod-outer-segment rhodopsin, the decadic molar extinction coefficient[24] at 498 nm (ε_{498}) is 4.1×10^4 liter mole^{-1}, which from Equation (2-27) gives a value of $\sim1.6\times10^{-16}$ cm^2 molecule^{-1} for the single-photon absorption cross-section. For an optically thin absorbing medium, the rate of single-photon absorption (R_1) is:

$$R_1 = I_0\sigma_1 n l = I_0'\sigma_1 n' \text{ photon sec}^{-1} \qquad (2\text{-}29)$$

where n' is the total number of absorbing molecules in a cylindrical volume element of area A and length l (i.e., n = n'/Al) and I_0' is the irradiance (I_0/A) in photons cm^{-2} sec^{-1}.*

---

* It follows from Equation (2-28) that the fraction of light absorbed in a path length, l(cm) by a concentration n(molecules cm^{-3}) is $1-\exp(-\sigma_1 n l)$. To the extent that this term can be approximated by $\sigma_1 n l$, the sample is said to be optically thin. The actual number of absorbing molecules, n' (e.g., $\sim5\times10^{14}$ molecules cm^{-3} for bovine rod outer segments – ref. 31) need not be included in these calculations since it is assumed to be constant for the two cases considered here.

The minimum multiple-pulse threshold for 500 nm laser radiation is 25 mW at the cornea. If this intensity is focused to a 25 μm radius spot at the retina, then the retinal irradiance, I_0', is given by:

$$I_0' = \frac{25\times10^{-3}\,J\ sec^{-1}\times2.5\times10^{18}\ photons\ J^{-1}\times0.6}{\pi(25\times10^{-4})^2\,cm^2} \qquad (2\text{-}30)$$

$$\approx 2\times10^{21}\ photons\ cm^{-2}\ sec^{-1}$$

where the factor of 0.6 is the approximate transmission of the anterior ocular media at this wavelength[35]. Substituting this value together with the single-photon absorption cross-section into Equation (2-29) gives the rate of absorption:

$$R_1 = 3.2\times10^{5}\ n'\ photon\ sec^{-1} \qquad (2\text{-}31)$$

The rate of simultaneous biphotonic absorption (R_2) is proportional to the square of the light intensity[34] and the two-photon absorption cross-section. By analogy to Equation (2-29),

$$R_2 = (I_0'')^2\sigma_2 n' \qquad (2\text{-}32)$$

where I_0'' is expressed in units of photon cm^{-2} sec^{-1} and the double prime denotes the longer wavelength, ∿1000 nm, which is also assumed for σ_2. By way of comparison, σ_2 for polycyclic aromatic hydrocarbons (e.g., anthracene, tetracene, etc.) ranges from about 10^{-50} to 10^{-48} cm^4 sec $photon^{-1}$ $molecule^{-1}$ for ruby laser (694.3 nm) excitation[34]. Thus, for the same density of absorbers (n'), comparison of Equation (2-32) with (2-31) shows that to achieve equal absorption rates by one- and two-photon processes at ∿500 and ∿1000 nm, respectively, the irradiance in the latter case must be on the order of 10^{27} photons cm^{-2} sec^{-1} at the retina. Assuming as before, a retinal image radius of 25 μm and a transmission (at 1060 nm) of 0.8 through the anterior ocular media[35], this photon density at the retina corresponds to a power of ∿5 kW at the cornea. Thus, it would appear that the minimum multiple-pulse threshold, 25 W, for Q-switched 1064 nm laser radiation[4] is too low a factor of about 200 for two-photon absorption processes to account for the observed damage.

The value of 10^{27} photon cm^{-2} sec^{-1} should be regarded as an upper limit since the visible light intensity actually required to induce the presumed photo-trigger may be considerably less than the value calculated (Eq. 2-30) using the multiple-pulse damage threshold. This, in turn, would imply that a lower intensity of 1064 nm radiation would be sufficient to induce the photo-trigger via two-photon absorption. Therefore, until a reasonable estimate of the photo-trigger threshold can be obtained, involvement of biphotonic absorption in retinal damage induced by repetitive near-IR laser pulses should not be ruled out.

In summary, more retinal threshold data are required to explain the parallel results of retinal damage induced by 514.5 nm and 1064 nm laser

pulses. Both hypotheses invoked in the latter case, viz., second-harmonic generation in the anterior ocular media and biphotonic absorption in rhodopsin, can be verified readily by in vitro experiments using a Q-switched Nd:YAG or Nd:glass laser on the extracted ocular components. Preliminary experiments designed to obtain multiple-pulse threshold data using a 100 kW pulsed nitrogen laser (Avco) with a dye laser attachment were unsuccessful due to insufficiency of the peak power output of the system. Other experiments involving laser-induced retinal lesions, possibly of photochemical origin[1,2] are discussed in Chapter 4.

REFERENCES

1. Ham, W.T., Jr., H.A. Mueller and D.N. Sliney, "Retinal Sensitivity to Damage from Short Wavelength Light", Nature 260:153, 1976.

2. Ham, W.T., Jr., Presentation at Laser Bioeffects Meeting, Bureau of Radiological Health, U.S. Food and Drug Administration, Rockville, Md., 13 July 1976.

3. Connolly, J.S., H.W. Hemstreet, Jr. and D.E. Egbert, "Ocular Hazards of Picosecond and Repetitive Pulse Lasers. Volume II: Argon-ion Laser (514.5 nm)", Technology Incorporated, Final Report, Contract F41609-73-C-0016, USAF School of Aerospace Medicine, January 1977.

4. Hemstreet, H.W., Jr., J. S. Connolly and D.E. Egbert, ibid., Volume I: "Nd:YAG Laser (1064 nm)", January 1977.

5. Williams, T.P., "Dynamics of Opsin, a Visual Protein", Accts. Chem. Res. 8:107, 1975.

6. Ostroy, S.E., "Protein Configuration Changes in the Photolysis of Cattle Rhodopsin", Dissertation, Case Institute of Technology, 1966.

7. Rodiguin, N.M. and E.N. Rodiguina, "Consecutive Chemical Reactions, Mathematical Analysis and Development", (English Translation). D. van Nostrand and Co., New York, 1964.

8. Robinson, G.W., "Rhodopsin Cooperativity in Visual Response", Vision Res. 15:35, 1975.

9. Welch, A.J., C.P. Cain and L.A. Priebe, "Investigation of Temperature Rise in the Fundus Exposed to Laser Radiation", The University of Texas at Austin, Final Report, Contract F41609-73-C-0031, USAF School of Aerospace Medicine, May 1974.

10. Welch, A.J. and L.A. Priebe, "Model of Thermal Injury Based on Temperature Rise in the Fundus Exposed to Laser Radiation", The University of Texas at Austin, Interim Technical Report, Contract F41609-74-C-0025, USAF School of Aerospace Medicine, September 1974.

11. Welch, A.J., et al., "Limits of Applicability of Thermal Inury", The University of Texas at Austin, Interim Technical Report, Contract F41609-76-C-0005, USAF School of Aerospace Medicine, May 1976.

12. Takata, A.N., et al., "Thermal Model of Laser-Induced Eye Damage", IIT Research Institute, Final Report, Contract F41609-74-C00005, USAF School of Aerospace Medicine, October 1974. (This report contains a comprehensive survey of the literature on thermal effects in biological systems as well as a review of earlier computer models of thermal injury).

13. Kliger, D.S. and E.L. Menger, "Vision: An Overview", Accts. Chem. Res. 8:81, 1975.

14. Williams, T.P., "Photoreversal of Rhodopsin Bleaching", J. Gen. Physiol. 47:679, 1964.

15. Connolly, J.S., in "Research on the Ocular Effects of Laser Radiation", Technology Incorporated, Twelfth Interim Report, Part I, Contract F41609-73-C-0017, USAF School of Aerospace Medicine, March 1976.

16. Connolly, J.S., D.S. Gorman and G.R. Seely, "Laser Flash Photolysis of Chlorin and Porphysin Systems", Ann. N.Y. Acad. Sci. 206:649, 1973.

17. Wald, G., "Molecular Basis of Visual Excitation", Science 162:230,1968.

18. Abrahamson, E.W., "Dynamic Processes in Vertebrate Rod Visual Pigments and Their Membranes", Accts. Chem. Res. 8:101, 1975.

19. Kuwabara, T. and R.A. Gorn, "Retinal Damage by Visible Light: An Electron Microscope Study", Arch. Ophthalmol. 79:69, 1968.

20. Noell, W.K., et al., "Retinal Damage by Light in Rats", Invest. Ophthalmol. 5:450, 1966.

21. Friedman, E. and T. Kuwabara, "The Retinal Pigment Epithelium: IV - The Damaging Effects of Radiant Energy", Arch. Ophthalmol. 80:265, 1968.

22. Mainster, M.A., "Destructive Light Adaptation", Ann. Ophthalmol. 2:44, 1970.

23. Mainster, M.A., "Retinal Transport and Regeneration of Human Cone Photopigment", Nature (New Biology) 238:223, 1972.

24. Abrahamson, E.W. and J.R. Wiesenfeld, in "Handbook of Sensory Physiology", H.J.A. Dartnell, ed., Vol. VII/1, Chapter 3 (and references cited therein), Springer-Verlag, Berlin, 1972.

25. Cone, R.A. and W.H. Cobbs, III, "Rhodopsin Cycle in the Living Eye of the Rat", Nature 221:820, 1969.

26. Dowling, J.E. and R.L. Sidman, "Inherited Retinal Dystrophy in the Rat", J. Cell. Biol. 14:73, 1962.

27. Mainster, M.A., T. J. White and C. C. Stevens, "Mathematical Analysis of Rhodopsin Kinetics", Vision Res. 11:435, 1971.

28. Williams, T.P., "Upper Limits to the Bleaching of Rhodopsin by High Intensity Flashes", Vision Res. 14:603, 1974.

29. Bonting, S.J., "Current Topics in Bioenergetics", D.R. Sanadi, ed., Vol. 3, Academic Press, NY, 1969.

30. Hagins, W.A., "The Visual Process: Excitatory Mechanisms in the Primary Receptor Cells", Ann. Rev. Biophys. Bioeng. 1:131, 1972.

31. Marcuse, D., "Engineering Quantum Electrodynamics", Harcourt, Brace and World, New York, 1970.

32. Fine, S. and W.P. Hansen, "Optical Second Harmonic Generation in Biological Systems", Appl. Opt. 10:2350, 1971.

33. Schachar, R.A. and S.A. Solin, "The Microscopic Protein Structure of the Lens with a Theory for Cataract Formation as Determined by Raman Spectroscopy in Intact Bovine Lenses", Invest. Ophthalmol. 14:380, 1975.

34. Birks, J.B., "Photophysics of Aromatic Molecules", pp. 62-83, Wiley-Interscience, London, 1970.

35. Boettner, E.A. and J.R. Wolter, "Transmission of the Ocular Media", Invest. Ophthalmol. 1:776, 1962.

CHAPTER 3

IN VIVO RETINAL PROBE EXPERIMENTS

A. David Nawrocki, J. Terry Yates
and Ronald F. Lemberger

A. BACKGROUND

Of the various sensory organs in man, the most susceptible to injury by laser irradiation is the eye. The increasing use of lasers has necessitated the implementation of safety standards based upon experimental measurements and, where possible, clinical data. As understanding of laser-induced injury and dysfunction has increased, these standards have been revised periodically.

At the present time, it appears that the complex chemistry which underlies laser-induced injury can be predicted reasonably well as classical (macroscopic) heat diffusion and first-order kinetics. However, recent results[1,2] indicate that the retinal effects of multiple laser pulses at repetition rates typical of field applications are not cumulative in a way that is consistent with strictly thermal processes. In addition, present thermal models ignore possible changes of state such as vaporization in which heat is absorbed incrementally without contributing to rising temperature. Thus, both from first principles and direct experiment, thermal modeling cannot be expected to predict effects of all possible laser parameters, in particular of certain short, intense or repetitive pulses.

Clearly, experimental validation of thermal modeling in such applications is necessary to establish limits of its overall utility as well as to provide possible corroborating evidence as to the significance or predominance of other mechanisms. The advantage of such a model, once validated, is its ability to predict ophthalmoscopic damage -- and by extension with other physiological and psychophysical correlates, visual dysfunction -- without the expense and time of generating large masses of experimental data for each new set of exposure parameters.

Briefly, thermal effects of visible laser irradiation in the retina may be understood as follows: with the exception of the pigment epithelium (PE) and choroid, the retina and underlying tissue are essentially transparent, and the PE and choroid may be considered as a double-layered, wavelength-dependent heat sink. When a highly collimated source or a sufficiently bright, diffuse source impinges on the eye, the PE and choroid can rapidly absorb and conduct heat. For laser pulse durations less than about 10 sec and greater than 100 μsec, the associated temperature increases apparently cause rate-dependent injury mechanisms such as deactivation of enzymes and protein denaturation[3] as well as pathological signs such as edema, lysis, and at suprathreshold exposures, massive disruption of cellular layers.

Experimental temperature measurements with probes whose tip diameters exceed 50 μm have been suspected of recording artifacts[4,5]. Metal-vapor coated, quartz microthermocouples developed by Reed[6] and modified by Cain[7] appear to be more suitable; tip diameters of 10-30 μm and time constants of about 200 μsec have been reported[5]. Experimental measurements with such probes have been conducted by Welch, et al.[5,8] and have been compared with thermal models originally devised by White, et al.[9] and Henriques[10].

Research efforts under this contract utilized thermocouple probes developed by Reed and Cain (cited above) in conjunction with an advanced computational scheme for predicting chorioretinal spatio-temporal temperature profiles[11]. The recording/control systems for performing these measurements were based, in part, on equipment assembled by Crum[12]. The chief objective of the project was to measure spatial distributions and temporal histories of temperature changes induced in the posterior portion of the vertebrate eye by laser radiation. The approach involved visually guided, surgical insertion of the microthermocouple probes through the sclera in the region of the posterior pole.

B. METHODS

B-1. Apparatus

The experimental apparatus developed for in vivo retinal probe measurements has been described in detail elsewhere[12,13]. A block diagram of the system, as originally configured[13], is shown in Figure 3-1. Major modifications which were subsequently incorporated into the system are discussed below.

Briefly, the laser beam passes through converging optics to a pellicle driven by an incremental, hydraulically driven beam deflector which directs the beam into the eye. The beam is gated and scanned across the retina by control logic and clock circuitry. Analog signals representing the temperature changes monitored by the microthermocouple probe are amplified and displayed on a strip-chart recorder or stored on magnetic tape for off-line computer processing.

A binocular ophthalmoscope, originally utilized for retinal observation, was replaced by a Zeiss fundus camera. Although an acceptable image could be obtained with the ophthalmoscope, frequent and tedious realignment of the condenser optics was needed to rid the image of corneal reflections each time the eye was rotated slightly. A split filament lamp and black dots on the ophthalmic lens of the fundus camera served to block corneal reflections.

The fundus camera has sufficient magnification to permit the probe tip to be seen when it penetrates the retina, and thus facilitates location of the tip and alignment of the probe with the laser beam projected into the eye at low intensity. Also, landmarks referenced to the optic disc are more easily identified through a fundus camera.

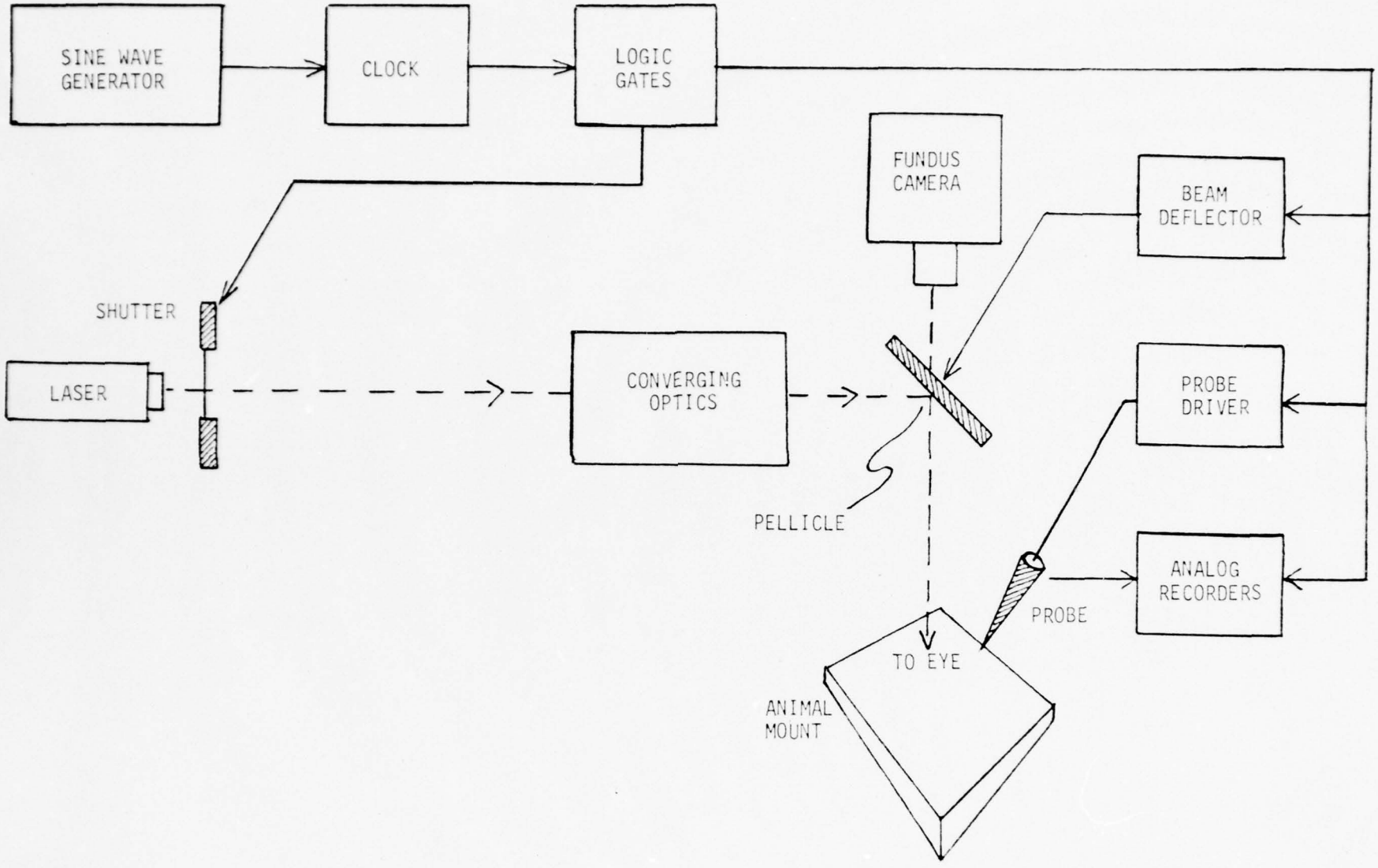

FIGURE 3-1. Block Diagram of Experimental System for In Vivo Retinal Probe Measurements.

The Kopf stereotaxic manipulator previously used to drive the probes did not have sufficient mechanical rigidity and flexibility for the task at hand. It was replaced by a Narishige micromanipulator consisting of three translational stages which was mounted to a rigid vertical post attached to a movable plate on the animal platform. By adjusting the position of the plate and the angle of the manipulator, a preliminary alignment of the manipulator drive axis relative to the posterior orbit can be achieved. Fine adjustment of the translational stages permits precise probe adjustment in less time then previously required with the Kopf manipulator.

The apparatus was modified to allow a satisfactory method of aligning the animal eye with respect to the pivot axes of the animal mount. This method consisted of attaching a platform and pointer at the base of the animal mount. The tip of this pointer is positioned to intersect the horizontal and vertical rotational axes of the animal mount. When an animal was placed on this mount for in vivo measurements, the ear pins and bite bar for the animal head could be adjusted so that the center of the pupil of the right eye could be aligned to within 0.5 mm of this intersection point. This method of centering greatly improved experimental efficiency since the fundus camera image tended to stay in focus when the animal was rotated.

Rapid alignment of the fundus camera with the laser beam was provided by a pointer mounted on the camera such that its tip, located at the center of the filament image, was directed upward. In turn, the pointer on the animal mount was directed downward. By bringing these pointers into coincidence with the laser beam, one could effect a fairly precise initial alignment. Fine adjustment was then accomplished with a set of orthogonal mirrors.

Major modifications in the original beam deflector system were based upon ray-tracing considerations and are discussed in Section C. Development of a series of calibration procedures was required in order to assess the accuracy of the beam steering device. After overhauling the stepping motor to eliminate occasional skipping, the hydraulic drive system was calibrated. A measuring microscope was focused on a reference mark on the slave cylinder of the device while the drive cylinder was advanced manually. After advancing the latter by 100 μm, the system was found to have a +2 μm error; i.e., the counter showed 100 μm increments when the actual movement, as viewed through the microscope, was, on the average, 102 μm. Although this accuracy is reasonable for this type of device, some improvement could be obtained by replacing the rolling diaphragms in the master and slave cylinders.

Evaluation of the pellicle displacement system uncovered another source of error. Small angular excursions produced positive errors (overshoot) whereas larger movements undershot and produced negative errors. The net effect was that the two errors tended to cancel each other when a large excursion was executed. The largest error seen would translate into a 20 μm displacement error on the retina of a rhesus monkey. Errors of this magnitude would be unacceptable in some experiments, especially when using small

probes. The problem was traced to the mechanical linkage between pellicle and piston, and the required adjustments were made.

In order to determine the locus of beam rotation, a small pinhole was positioned on a translation stage at various distances beyond the pellicle. By sweeping the beam to and fro, it was possible to visually estimate the beam "cross-over", i.e., the point at which the amount of light passing through the pinhole was invariant.

During the course of these measurements, another potential problem was unveiled. While scanning the beam of a helium-neon alignment laser, it was discovered that changes in apparent brightness occurred as a function of the incident angle of the input beam. It was determined that this was due to the interference fringe pattern resulting from the pellicle behaving as an optical wedge. The problem was subsequently circumvented by use of a small front surface mirror in place of the pellicle.

A new differential amplifier system with high input impedance, low noise and low drift, and variable gain was fabricated and tested. Also, a proportionally controlled oven chamber was acquired. The thermocouple amplifier was housed in the temperature stabilized chamber along with a reference thermocouple. This new system provided the necessary gain to permit FM tape recording of signals as well as providing increased noise immunity from common-mode rejection due to differential amplification procedures. The reference oven permitted greater amplifier stability than the ambient environment and also provided the capability of absolute (i.e., referred to core temperature) rather than relative temperature measurements.

B-2. Microthermocouple Calibrations

The electrical resistances of the thermal probes were measured no more than a day before their use in an animal experiment, thus screening out probes whose resistances had changed to unacceptable values ($<100\Omega$ or $>500\Omega$). On the day of an experiment, acceptable probes were calibrated by immersing the probe tip in a water bath and varying the temperature. A Yellow Springs Instruments thermistor bridge and probe were used to monitor the bath temperature, and the combined voltage response (in mV) of the microthermocouple-preamplifier system was recorded. The bath temperature was gradually raised over a range from room temperature to values exceeding $45^{0}C$. This range provided an acceptable end point for animal experiments which theoretically would generate retinal temperature changes less than $\sim 5^{0}C$, yet it was broad enough to allow assessment of detector linearity. From preliminary calibration data, it was found that convection currents produced by heating in the comparatively large water bath could cause noise and drifts. Therefore, a small container filled with water was placed around the probe, and both were immersed in the water bath.

In the preliminary calibrations, temperature increments of less than $5^{0}C$ were used so that departures from linearity could be detected readily

by a linear least squares fit of the data. Calibration data were sufficiently linear so that only 3-5 calibration points were needed for each probe.

A system was designed to allow simultaneous temperature calibration of up to five microthermocouples. The device consisted of a large diameter, shallow glass cylinder into which was inserted a Lucite plate containing five glass cuvettes. The large cylinder was fitted with inlet and outlet ports to allow circulation of water around the cuvettes by means of a peristaltic pump. A calibrated reference thermocouple was sealed into the base of each cuvette. The microthermocouples were immersed in water in the cuvettes and the plate containing the cuvettes set in the warm water (45-50^{0}C) which filled the large cylinder. When the cuvette temperatures reached steady-state, the entire system was rapidly cooled by immersion into a large ice bath. Cuvette temperatures were monitored by the reference thermocouples, and a double-pole, rotary stepping switch used to sequentially sample the thermocouple and probe voltages. Cuvette temperatures declined at a rate of $\sim$0.25-2.0^{0}C per minute, so that calibration data could be collected in one hour or less.

Computer software to plot the calibration data and to fit a least squares straight line of voltage vs. temperature was written for the Hewlett-Packard 9830 system. An example of a calibration curve exhibiting typical linearity is shown in Figure 3-2. The value of the slope is a function of probe resistance, since this determines the value of the input impedance which, in turn, influences the effective gain of the probe and preamplifier as a unit. The intercept of the curve represents a good approximation to the temperature of the reference thermocouple.

B-3. Surgical Techniques

The subjects were preanesthetically atropinized and tranquilized with ketamine hydrochloride. Sodium pentobarbital was administered through an indwelling catheter in a saphenous vein. Throughout the surgery and subsequent experimentation, surgical levels of anesthesia were maintained by continuous infusion of pentobarbital (7 mg/Kg/hr).

After a midline incision was made and a temporal flap of scalp was removed, the temporal muscle was incised at its insertion. The muscle was reflected and hemisected in the rostral-caudal plane and temporal bone was removed to aid in visualization of the temporal-zygomatic foramen. The extrinsic eye muscles (except for the superior oblique) were excised as were the attendant fat pad and lacrimal tissue. After the lids were removed, a scleral ring was sutured in place at the limbus and a corneal contact lens inserted. Keratometry prior to experimentation ensured a proper fit of the lens. Examination of the fundus before and after suturing and lens insertion assured minimal distortion of the globe.

Following removal of orbital fascia and connective tissue, the sclera was visualized at the posterior pole. A hand-held ophthalmoscope directed at the fovea gave enough trans-scleral illumination so that a

FIGURE 3-2. Static Thermocouple Calibration.

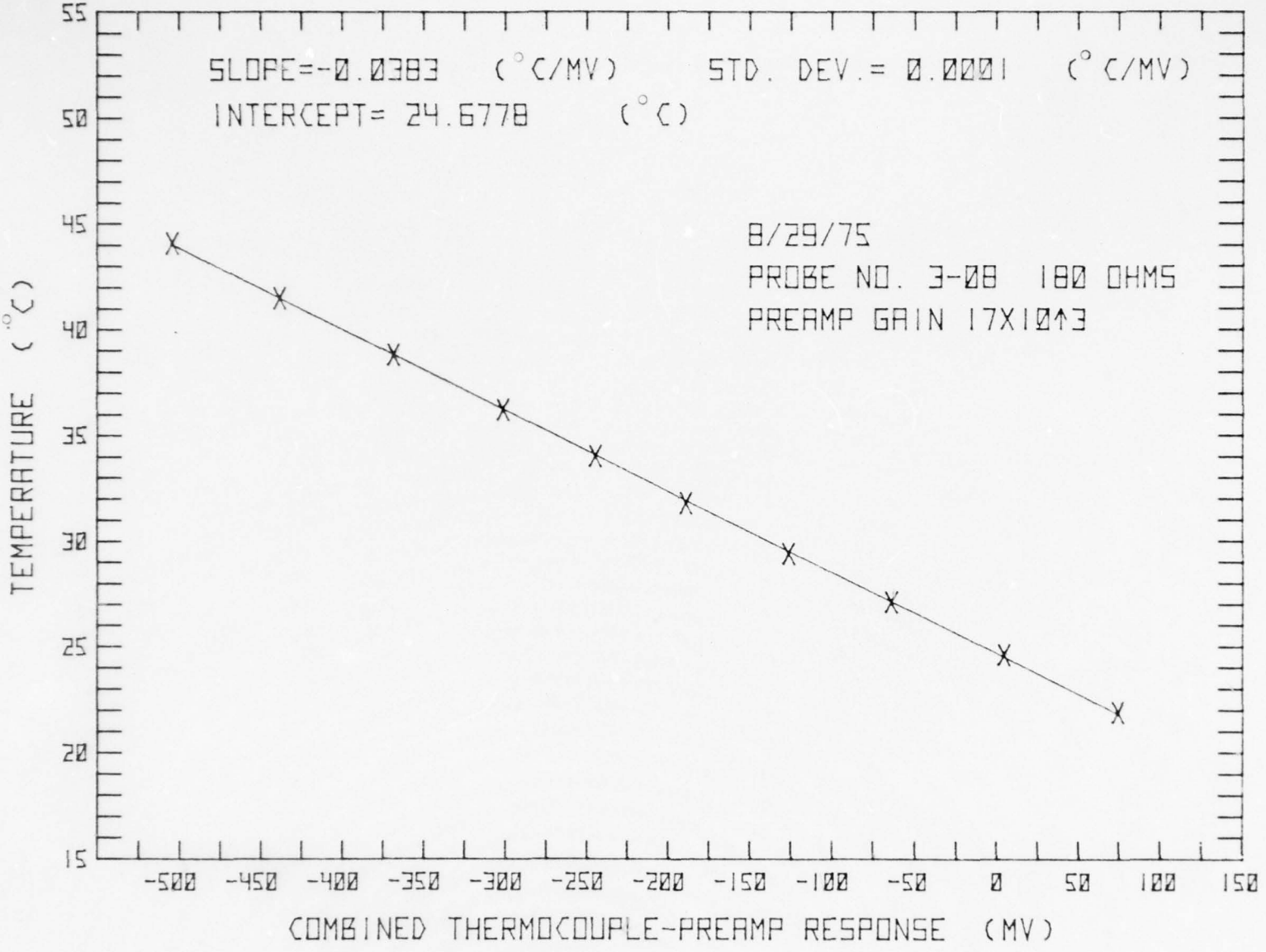

reference point could be located when an assistant viewed the posterior wall of the eye through an operating microscope. Alternatively, this reference point can be defined by the actual laser spot on the macula as viewed through a fundus camera. In either case, a small scleral incision was made at this point to facilitate penetration of the probe. In small animals, considerable difficulty was encountered when an attempt was made to rotate the eye so that the macular region was positioned in the surgical field. Extreme rotation resulted and considerable difficulty in using the fundus camera was encountered.

An alternative approach, one in which less rotation of the globe is required, could also be accomplished. Removal of a segment of temporal bone and the underlying fronto-temporal cerebral cortex by sub-pial aspiration would provide a larger operating field. If done carefully, this procedure is relatively atraumatic. Control of bleeding from dural and surface vessels can be easily accomplished by conventional means (cold saline lavage, gelatin foam packing, etc.). The greater ease of scleral fenestration for probe insertion and the reduced ocular rotation required make this procedure desirable.

B-4. Experimental Procedures

Details of the experimental procedures used in obtaining the results presented in Section D are given below. The procedures were continuously adjusted and updated as modifications were made in the apparatus and surgical techniques. The details reported here are representative of experiments conducted toward the end of the contract period.

The incident source was the 647.1 nm line of a Spectra-Physics Model 164 krypton-ion laser. The beam was attenuated with a fixed neutral density filter near the laser output mirror and laser powers were varied by adjusting the tube current. Output was measured using a calibrated Scientech 3600 power meter. Readings were taken at the corneal plane before and after each experiment and the values compared with readings taken midway in the optical path before, during and after the run.

Beam scans were taken at appropriate distances on either side of the corneal plane to determine beam divergence, quality and stability of alignment, and the cross-over point of the micrometer-driven deflector[12]. In order to maintain a Maxwellian view of the fundus, it is necessary that the focal point of the beam-expanding optics coincide with the deflector cross-over point. In order to view the fundus, both must be within ~45 mm of the fundus camera objective. Because of geometric constraints imposed by the size of the deflection system components, the closest achievable distance between the deflection mirror and the fundus camera objective is ~20 mm. In practice cross-over points of ~35 and ~25 mm were used. Although the former did not provide an optimum view of the fundus, it offered other advantages which relieved some of the rigid constraints imposed by the overall geometry of the system.

The low reflectivity pellicle used in the previous experiments[13] as well as in the original design[12] was replaced with a pellicle which had been vapor deposited with a thin film of aluminum. However, the laser intensity at the near-focused spot on the mirrored surface induced permanent depressions in the film which gave rise to interference patterns in the projected beam. Therefore, the pellicle was replaced by a ∿2 mm x 2 mm chip of a first-surface mirror cemented to a small pedestal machined to fit the pellicle holder. The dimensions of the pedestal were such that it was possible to obtain a relatively unobstructed view of the laser spot on the fundus when the fundus camera, deflector and subject eye were properly aligned.

Signal capture was accomplished with a strip chart recorder (Clevite-Brush) with either two or six channels. In the former instance, one channel was used to record the delivered light pulses as detected with a beamsplitter-photodiode arrangement and the other, to record the output of the intra-ocular probe. When a six channel recorder was used, two channels were used to record each signal, usually at different amplifications to preclude loss of data due to the trace going off scale. The laser output channel was calibrated against powers measured at the corneal plane.

Retinal beam sizes were estimated by visual inspection through the fundus camera prior to surgical rotation of the eye. The retinal image diameter ($1/e^2$) was also calculated using a ray-trace software package written for the Hewlett-Packard 9830A calculator (see Section C). For the experiments discussed in Section D, the full-angle beam divergence was 19.2 mrad which yielded a calculated retinal image diameter ($1/e^2$) of 250 μm. The effects of beam deflector displacement are included in the computer program. For the conditions employed in these experiments, a linear displacement of the micrometer drive by ∿500 μm resulted in a calculated beam displacement at the retina of ∿169 μm. It should be noted that the physiological optics parameters employed in these calculations were taken from a "model eye"[14] and not from measurements (e.g., ultrasonography) made on each experimental eye. However, the experimental retinal scans are consistent with the calculations.

The microthermocouple used was supplied by A.J. Welch (University of Texas at Austin) and was quite similar to those used in experiments conducted in his laboratory[5,8]. The tip diameter was ∿30 μm. A linear least squares analysis of the temperature calibration data gave a slope of 0.0452°C/mV and intercept of 37.7°C at a reference temperature of 37.9°C.

Laser powers (at the cornea) were 34-35 mW for retinal scans and were varied from ∿8 to 28 mW for subsequent measurements of peak temperature increases for pulsewidths ranging from 50 msec to 10 sec. The laser beam was gated by a synchronous signal from the timing clock to an electromechanical shutter (Gerbrand) with a shutter speed (both opening and closing) of ∿2msec. For retinal scan runs the laser pulsewidths were 100 msec and the pulse repetition rate was fixed at 0.1 Hz. The micrometer drive was incremented at a rate of 1 μm/sec and, thus, a laser pulse was delivered to the retina every 10 μm of linear drive, which corresponded to ∿3.4 μm translational increments across the retina.

The laser spot on the macula could be viewed fairly well by translating the animal toward the fundus camera (z-axis); the probe was then inserted at the reference point defined on the sclera by the transmitted laser beam. Subsequent microscopic examination of this eye showed that the probe had indeed been inserted in the macula and that the trauma was relatively minor.

Following probe insertion, the subject was moved back along the z-axis so that the focal and cross-over points of the optical system were coincident near the front nodal plane of the eye. The laser beam was manually deflected across the probe insertion site and minor adjustments were made in the position of the subject (angle, elevation and z-axis) until the thermocouple output was maximized. Subsequent scans revealed that a Maxwellian view had apparently been achieved.

Several hundred μm of probe insertion were required before a thermal response could be detected from 100 msec pulses at laser powers set somewhat below calculated[11] retinal damage thresholds (viz., ∿21 mW). Full insertion (i.e., through the pigment epithelium to the point of radiometric response) was avoided since one cannot be assured that laser-induced temperature increases measured within the PE after it has been damaged by the probe are necessarily representative of actual temperatures experienced in the rhesus eye under non-invasive conditions. Thus, the actual depth of the probe in the PE was unknown. Temperature scans of the retina were obtained at a depth of ∿600 μm anterior to the point of initial scleral contact. However, the major uncertainty remains the angle of probe insertion, so that estimates of retinal depth along the probe axis do not yield particularly meaningful estimates of probe depth in the PE.

C. RAY-TRACING APPLICATIONS AND BEAM DEFLECTOR DESIGN

Computer simulation of the combined optical performance of the monkey eye and beam deflector system, using two dimensional ray-tracing in the horizontal meridian, was employed to effect a rapid analysis of various possible beam deflector modifications designed to correct a sampling error inherent in the original system[12], and to estimate performance of the possible modifications with respect to translational invariance of the scanned distribution. Specific results are discussed in more detail following a brief description of the ray-tracing program.

C-1. Description of Computer Software

Briefly, the ray-tracing software applies Snell's Law to an arbitrary number of refracting surfaces intersected by rays which are projected from an idealized virtual or real point source, either inside or outside of the eye. In the first case, light is focused into the eye; in the second, it is diverging toward the eye from a virtual image point in front of the eye. In both cases, a reflecting beam deflector is inserted along the axis of the laser beam to simulate the operating

conditions of the beam deflector system (hence, the virtual image in the second case). The input rays are assumed to have a Gaussian spatial distribution. After each ray passes through the optical system, it is intersected with an observation plane or an assumed spherical surface which simulates the retina, using values of the physiological optics parameters obtained by Gallagher[14] for the "average" rhesus eye.

A number of options exist: one can vary (a) the (odd) number of rays, depending upon the amount of detail needed; (b) laser convergence or divergence angle and corneal spot size; (c) linear movement of the pellicle drive; (d) the horizontal distance between center position of the pellicle and the front of the eye; (e) horizontal tilt angle between the axis defined by the above two points and the optical axis of the eye. Also, since the assumed surfaces are arbitrary, a tear layer or a contact lens plus a layer of methyl cellulose can be added between the pellicle and cornea.

Scattering and diffraction are necessarily ignored. Fresnel reflection and transmission coefficients, although desirable, are not needed; likewise, intensity is not calculated at observation points, although it can readily be reconstructed graphically from the computer output. The output consists of ray plots, which have been particularly useful in analyzing and sorting through predicted performances of a large number of trial designs, and of printed output, which has been used chiefly to analyze the translational invariance of the deflected beam. Typically three plots and printouts are obtained in each simulation, one set for the center position of the pellicle, the other two for the extreme positions of the pellicle.

C-2. Beam Deflector Design

Initially, the optical responses of the system devised by Crum[12], using an extended laser source, were ray-traced. Results indicated that a significant non-linearity in the retinal scans would occur. This situation was not improved significantly when the eye-to-pellicle distance was optimized by moving the eye ~4 mm closer to the pellicle. Hence, it was clear that design of a different contact lens was needed, or incorporation of additional external optics, or a combination of the two. The only other choice was to re-design the entire beam deflector head or to adopt the simpler but more cumbersome technique of rotating the animal[5,8].

The non-linearity in the retinal scan was due chiefly to angular dependence in the corneal refractive power. Thus, optical responses to contact lens configurations, having larger than normal front surface radii of curvature, were simulated in an attempt to by-pass the cornea. Although the scan linearity improved, it was clear that the corneal spot size would have to be reduced considerably, which would involve considerable investment in a micro-reducing collimator.

Therefore, a different approach was utilized. By letting the eye focus the beam toward an idealized point far enough behind the eye, the intersection

of the converging beam with the retina could be configured, by proper choice of an external lens, so as to produce a retinal spot size of roughly several hundred μm at the $1/e^2$ points. Thus, in effect, the light source would be placed at an idealized point somewhere between the near-point for vision and the front surface of the unaccomodated eye. A preliminary calculation indicated that a good place to accomplish this would be ∿100 mm in front of the eye. Subsequent ray-traced simulation of this system indicated that fairly good retinal scan linearity could be obtained in this fashion, provided that the tolerance in the eye-to-pellicle distance could be held to ±1 mm. This system had the advantage that a special corneal contact lens was not necessary; thus, it appeared that the closer the source was to the eye, the less significant the influence of corneal and other aberrations.

Hence, borrowing from the principle of a Maxwellian view, ray-tracing software was extended to simulate optical responses to light focused to an arbitrary point within an eye fitted with a neutral power contact lens. With the beam deflector in its center position, the best position for this point was roughly mid-way between the first unit plane and second nodal plane. In spite of the fact that when the pellicle was translated to one of its extreme positions -- causing this focal point to migrate anywhere from nearly outside of the eye to the back surface of the crystalline lens -- the retinal scan linearity was surprisingly good. In fact, although simulated spatial profiles of beams at the retina changed somewhat when the center position of this focal point was shifted from its optimum by amounts up to ∿2 mm along the deflector optical axis, the beam profiles at the center and two pellicle extremes, were in good agreement. Thus, this particular design was incorporated into the experimental system.

Sample ray plots under conditions of such optimal alignment are shown in Figure 3-3. Figure 3-4 is a schematic drawing of the experimental setup showing optimal alignment of the eye and the pellicle in its center position. In practice, the eye was rotated nasally so that the visual axis coincided with the beam axis and the beam came to a focus within 2 mm of the front nodal plane of the eye.

D. RESULTS

Figure 3-5 shows typical results of the reproducible scans of laser-induced retinal temperature increases obtained in one experiment. Three sequential runs were carried out under the conditions indicated. The average retinal irradiance in this experiment can be estimated from the corneal power, ocular transmission at this wavelength and calculated retinal image diameter (250 μm). Assuming that 95% of the intensity is within the $1/e^2$ intensity limits, the retinal irradiance is estimated to be ∿61 W/cm^2. If, instead of the calculated image diameter, the $1/e^2$ limits of the temperature scan (∿180 μm diameter, Figure 3-5) are used, the average retinal irradiance is ∿118 W/cm^2. The measured peak temperature increase was ∿19^{0}C. This may be compared with the results of Welch, et al.[15], who measured a peak temperature increase of 19.8^{0}C for 29 mW (cornea),

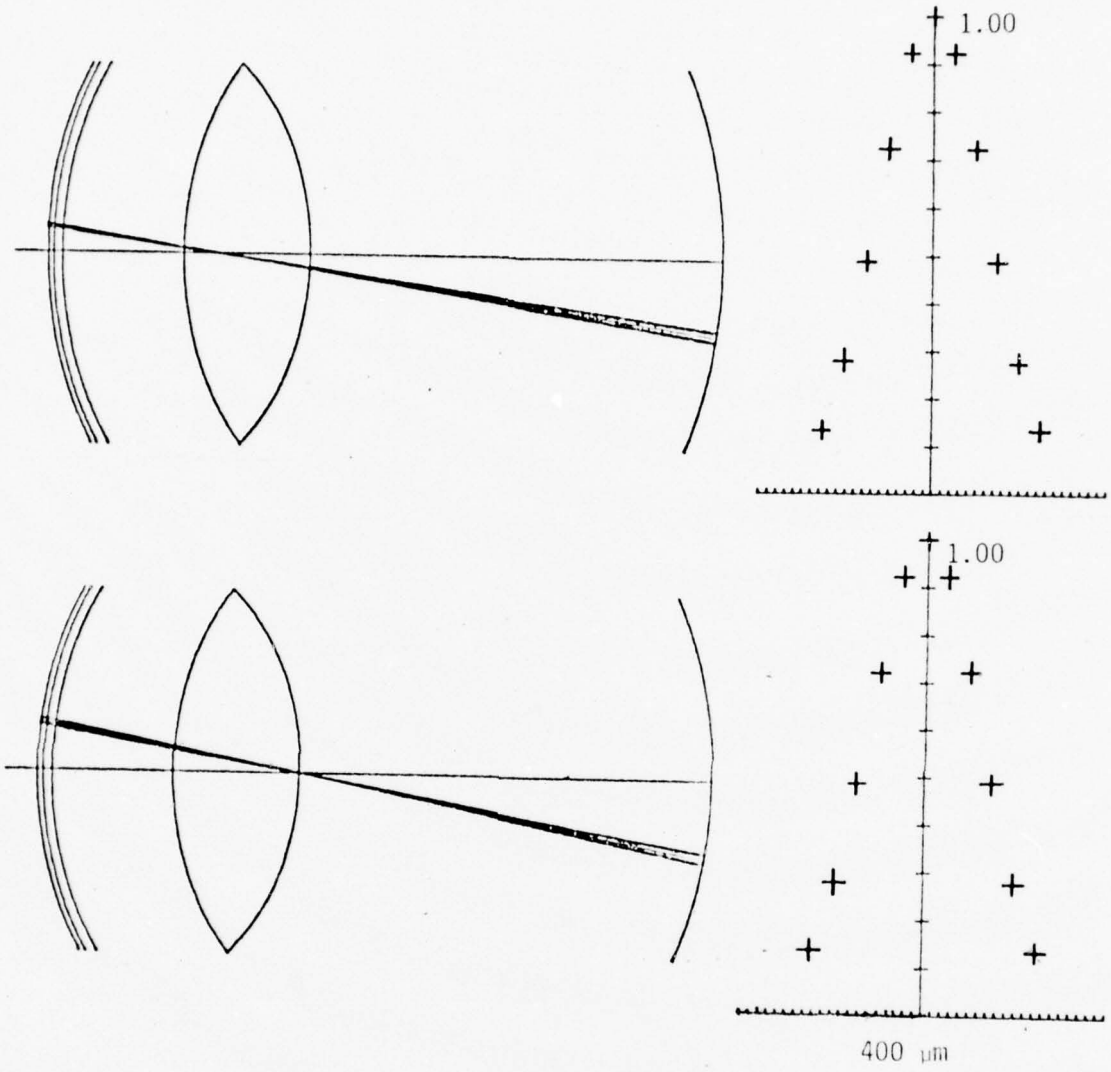

FIGURE 3-3. Predicted Responses to Beam Deflector in Average Eye. At left: ray tracing in horizontal plane of average monkey eye(14), showing successive displacements of focus and sagittal profile of beam entering eye through neutral power contact lens and 250 μm layer of 2.5% methyl cellulose at left, passing through anterior chamber, crystalline lens, and vitreous human, and ending at an assumed spherically curved retina. The upper profile is predicted when the pellicle is at its center position; the lower profile when the pellicle is at an extreme position, -0.5 mm parallel to the axis of the incident laser beam. The finite thickness of cornea and refractive laminations of the crystalline lens are ignored in this eye model. At right: Unit-normalized distributions for respective beam profiles at left.

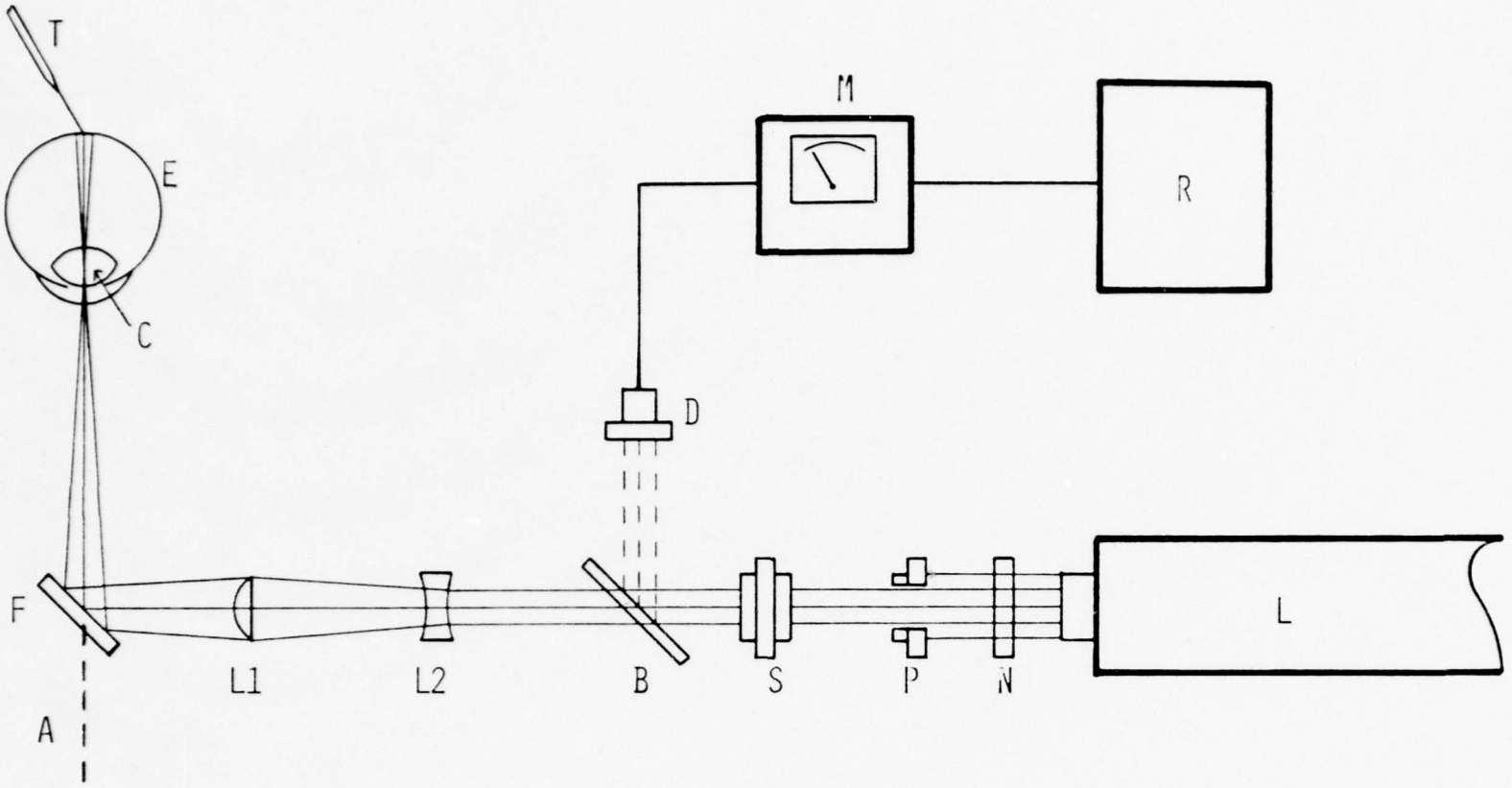

FIGURE 3-4. Schematic Diagram of Experimental Apparatus. L-krypton-ion laser; N-neutral density filter; P-pinhole; S-electro-mechanical shutter; B-beamsplitter; L1,L2-Gallilean lens system; A-optical axis of fundus camera; F-front surface mirror; E-subject eye; C-cross-over point of deflector (coincident with focal point of Gallilean lens system); T-microthermocouple; D-photodiode; M-power meter; R-strip chart recorder.

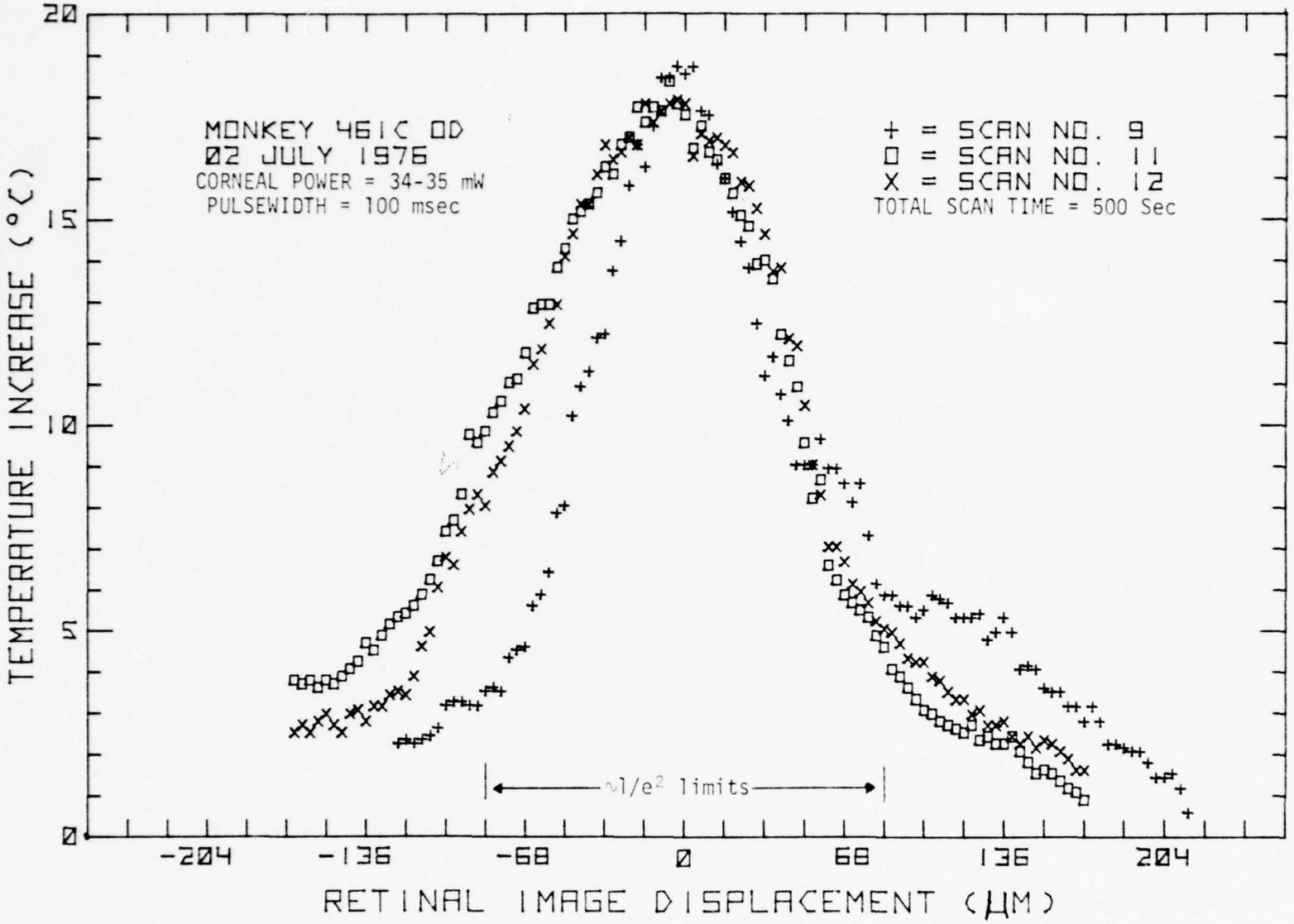

FIGURE 3-5. Results of Three Sequential Scans of Laser-Induced Retinal Temperature Increase. (Wavelength 647.1 nm).

10 msec pulse of 514.5 nm laser radiation incident on a rhesus macula with an image of comparable dimensions (~180 μm $1/e^2$ diameter) using a microthermocouple probe of comparable size (26 μm diameter). Unfortunately the probe depth was not specified in reference 15. At any rate, the average retinal irradiance for their conditions can be estimated as ~94 W/cm^2 which is in quite good agreement with the results quoted above. The agreement is even better if one adjusts the two irradiances for absorption of the two wavelengths[11] in an assumed depth of 5 μm in the PE. Considering that the temperature increase had not reached equilibrium in either case (see Figure 3-6), this agreement is perhaps fortuitous.

Retinal temperature increases were measured as a function of laser power for a range of fixed exposure times (pulsewidths). The subject eye and beam were aligned for maximum probe response and peak temperatures were recorded for the pulsewidths and laser powers listed in Table 3-1. The data are displayed in Figure 3-7. Unfortunately, the beam asymmetry precluded a meaningful estimate of average retinal irradiance and, as before, the depth of the probe tip in the PE was unknown.

Additional experiments were carried out using optical rather than microthermocouple probes. The optical probes consisted of 2 mm quartz rods drawn to fine tips. The experimental setup was similar to that used in the experiments described above but the laser source was a Spectra Physics 125 helium-neon laser with a maximum output of ~50 mW at 632.8 nm. Highly reproducible and symmetric scans were obtained as can be seen in Figure 3-8. The $1/e^2$ retinal image diameter in this case was ~120 μm.

Although not completely successful, the in vivo thermal and optical measurements of the rhesus eye have yielded valuable results. Peak temperature increases were comparable to those obtained by Welch, et al.[15] using similar retinal beam images and probe diameters but different wavelengths. The efforts discussed in this chapter have led to improved surgical procedures, a sophisticated beam deflector design and other modifications in the experimental apparatus required to carry out successful in vivo retinal probe experiments.

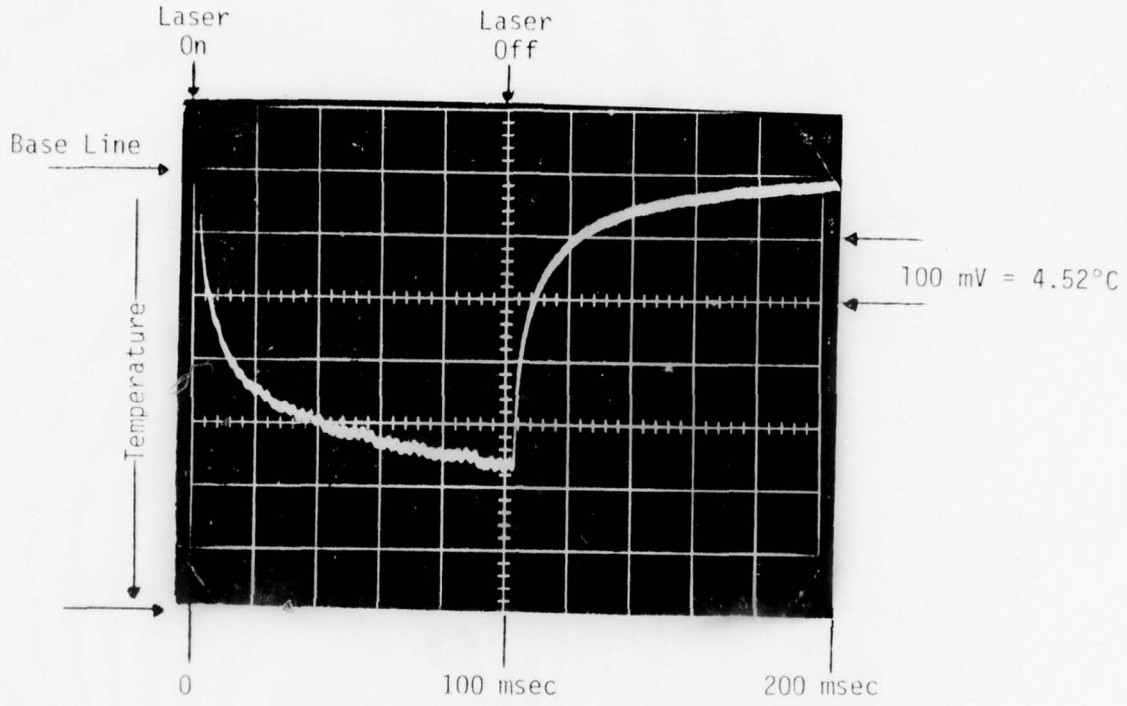

FIGURE 3-6. Oscilloscope Trace of Laser-Induced Retinal Temperature Increase near Center of Retinal Image. Note the near symmetry of the asymptotic approaches to thermal equilibrium at 100 and 200 msec. (Subject 461C, OD; wavelength 647.1 nm; corneal power 35.2 mW; calculated retinal image diameter ∿250 μm at $1/e^2$ limits. Actual image diameter appears closer to ∿180 μm as shown in previous figure).

TABLE 3-1.

PEAK RETINAL TEMPERATURES INDUCED BY VARIOUS LASER PULSEWIDTHS AND CORNEAL POWERS[a,b]

Pulsewidth (sec)	Corneal Power (mW)			
	8.0	12.4	19.2	28.0
0.05	3.19±0.07	1.58±0.09	5.98±0.08	8.74±0.16
0.1	4.61±0.07	3.63±0.22	6.92±0.14	10.83±0.29
0.2	5.29±0.10	4.98±0.05	7.48±0.20	11.44±0.24
0.5	5.82±0.06	7.69±0.21	7.96±0.12	12.46±0.17
1.0	5.91±0.06	7.82	8.55±0.04[c]	13.15±0.09
2.0	5.94±0.02	7.57	8.73±0.05[c]	13.78±0.22[c]
5.0	---	7.68	8.77	13.56
10.0	---	8.09	---	---

(a) Subject 461C, OD. Depth of probe in PE unknown, wavelength = 647.1 nm.

(b) Peak temperature increases in ^{o}C. All temperatures are mean and mean deviation of three successive measurements unless otherwise specified.

(c) Mean of two successive measurements.

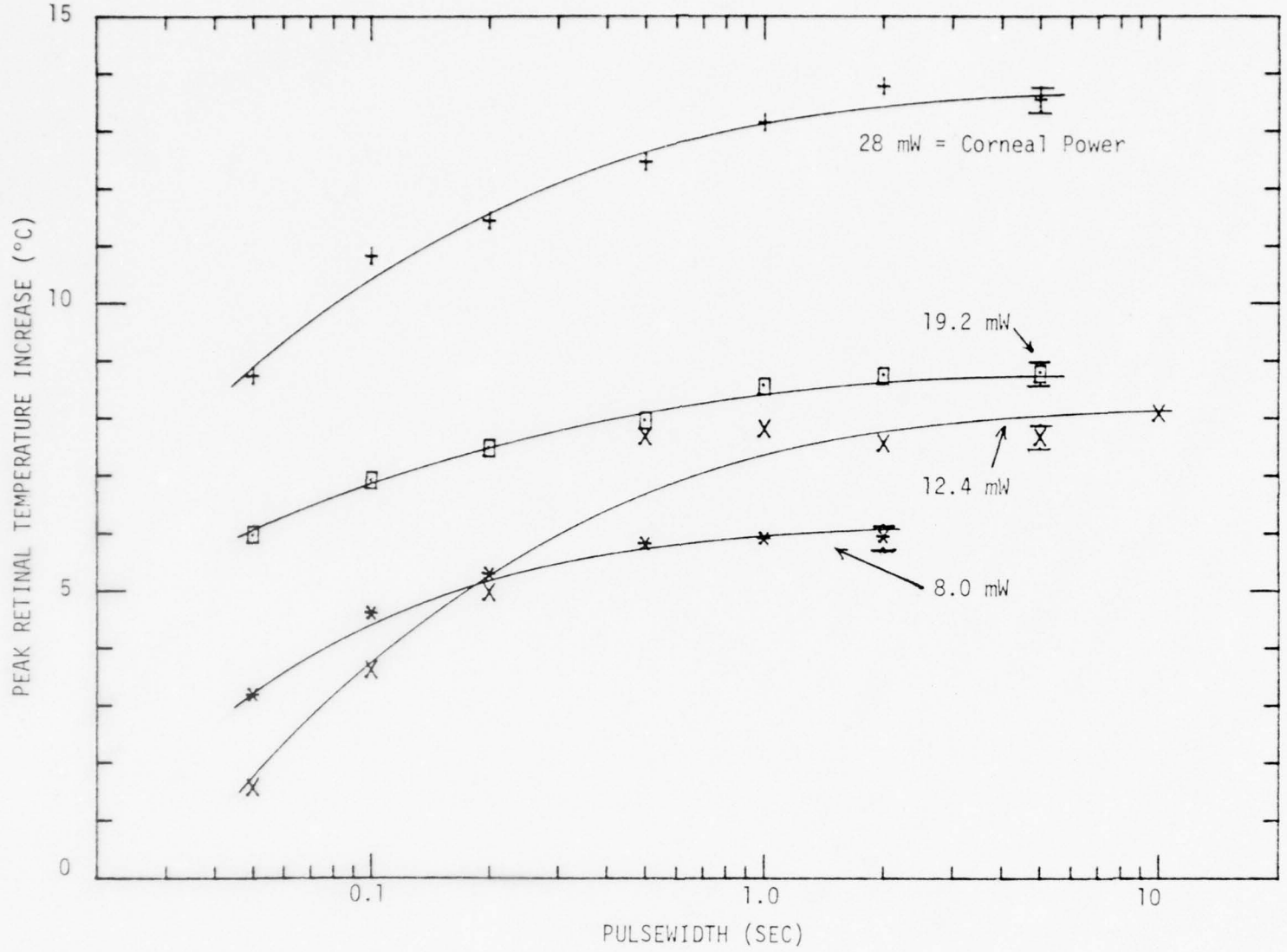

FIGURE 3-7. Dependence of Peak Retinal Temperature Increase with Pulsewidth at Various Corneal Powers. (Subject 461C, OD; wavelength 647.1 nm).

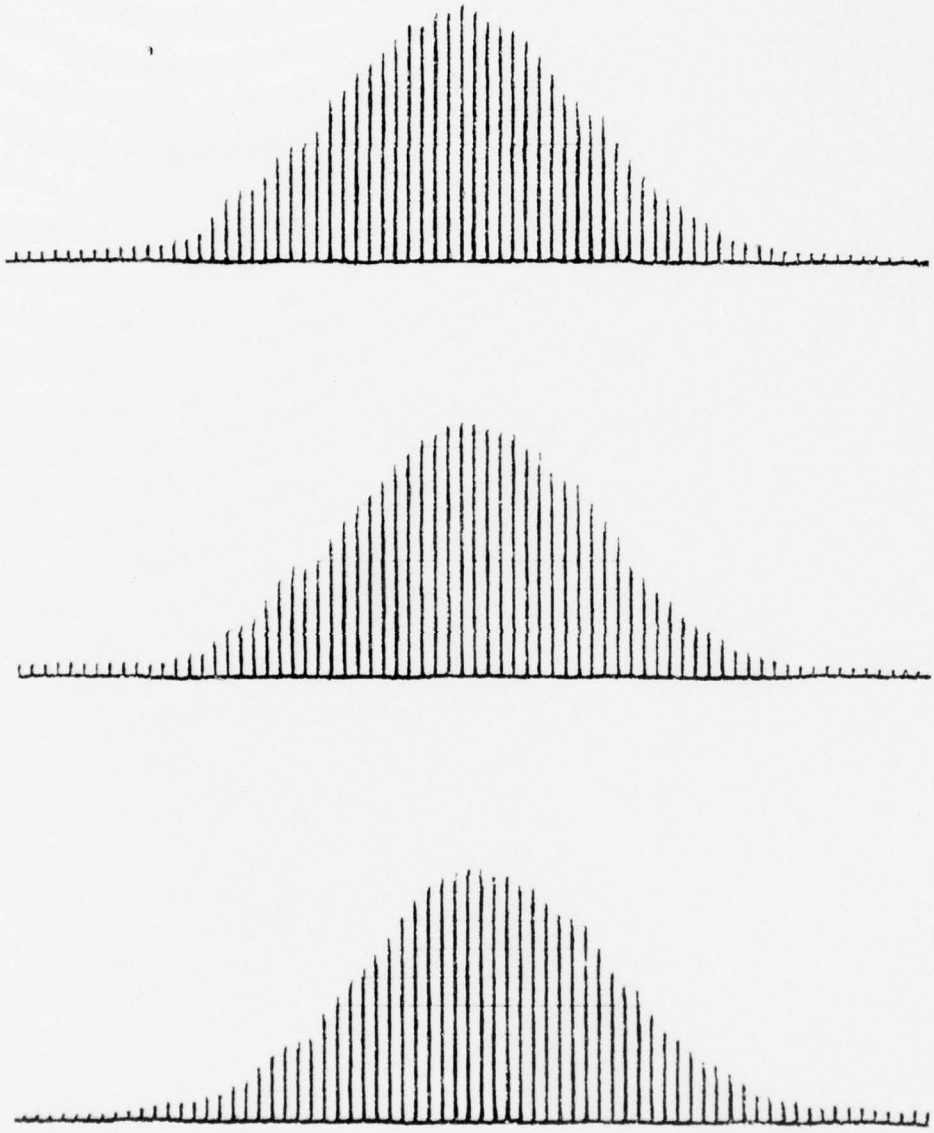

FIGURE 3-8. Representative in vivo Optical Scan Data of Rhesus Retina. Three successive beam scans in chronological order obtained by implanting a quartz optical probe within the distal retina (Subject 312C). Middle scan was obtained in reverse direction of top and bottom scans. The probe tip was 100 μm diameter. Chart speed, 25 mm/min; shutter duration, 0.3 sec; hydraulic driver scanning increment and frequency, 10 μm and 2 Hz respectively.

REFERENCES

1. Hemstreet, H.W., Jr., J.S. Connolly and D.E. Egbert, "Ocular Hazards of Picosecond and Repetitive Pulse Lasers, Volume I", Technology Incorporated, Final Report, Contract F41609-73-C-0016, USAF School of Aerospace Medicine, January 1977.

2. Connolly, J.S., H.W. Hemstreet, Jr. and D.E. Egbert, ibid., Volume II, "Argon-Ion Laser 514.5 nm", January 1977.

3. Geeraets, W.J. and D. Ridgeway, "Retinal Damage from High Intensity Light", Acta. Ophth. Supp. 76:109, 1963.

4. Cain, C.P. and A.J. Welch, "Measured and Predicted Laser-Induced Temperature Rises in the Rabbit Fundus", Invest. Ophth. 13:60, 1974.

5. Welch, A.J., C.P. Cain and L.A. Priebe, "Investigation of Temperature Rise in the Fundus Exposed to Laser Radiation", Final Technical Report, Contract F41609-73-C-0031, USAF School of Aerospace Medicine, May 1974.

6. Reed, R.P., "Thin Film Sensors of Micron Size and Applications in Biothermology", Ph.D. Dissertation, University of Texas, 1966.

7. Cain, C.P., "Dynamic Spatio-Temporal Temperature Measurements in Laser Irradiated Rabbit Eyes", Ph.D. Dissertation, University of Texas, 1972.

8. Welch, A.J. and L.A. Priebe, "Model of Thermal Injury Based on Temperature Rise in Fundus Exposed to Laser Radiation", Interim Technical Report, Contract F41609-74-C-0025, September 1974.

9. White, T.J., M.A. Mainster, J.H.Tips and P.W. Wilson, "Chorioretinal Thermal Behavior", Bull. Math. Biophys. 32:315, 1970.

10. Henriques, F.C., "Studies of Thermal Injury", V. Arch. Path. 43:489, 1947.

11. Takata, A.N., et al., "Thermal Model of Laser-Induced Eye Damage", Illinois Institute of Technology Research Institute, Final Technical Report, Contract F41609-74-C-0005, USAF School of Aerospace Medicine, October 1974.

12. Crum, C.G., "An Experimental Apparatus and Procedure for Obtaining Dynamic Spatio-Temporal Temperature Measurements in Laser Irradiated Monkey Eyes", M.S. Thesis, School of Engineering, USAF Institute of Technology, December 1973.

13. Nawrocki, A.D., et al., in "Research on the Ocular Effects of Laser Radiation", Technology Incorporated, Second Annual Report, Part III, Contract F41609-73-C-0017, USAF School of Aerospace Medicine, February 1975.

14. Gallagher, J.T., "Optical Components", USAF SAM/RAL Project 6301, unpublished results, 1975.

15. Welch, A.J., et al., "Limits of Applicability of Models of Thermal Injury", The University of Texas at Austin, Interim Technical Report, Contract F41609-76-C-0005, USAF School of Aerospace Medicine, May 1976.

CHAPTER 4

EFFECTS OF LASER RADIATION ON RETINAL LIPIDS

Cliffe D. Joel* and William H. Bowie

A. INTRODUCTION

With the continued widespread growth in the use of lasers, it is becoming increasingly important to understand the mechanisms of the damaging effects of laser radiation on ocular tissues as well as threshold levels for damage. It is now well established that lasers can produce readily observable lesions in the primate cornea, lens and retina, but very little is known about the specific biochemical mechanisms underlying ocular lesions produced by laser radiation at various wavelengths[1]. Recent evidence[2-5] strongly suggests that ocular damage produced by near-ultraviolet, repetitive visible pulses or short visible wavelengths occur *via* photochemical rather than strictly thermal mechanisms. Also, it has recently been shown[6] that the primate cornea is more sensitive to laser-induced photochemical damage *in vivo* when it is bathed in an atmosphere of pure oxygen rather than air and is in turn more sensitive in air than in pure nitrogen. This suggests the possibility that at least part of the damage may involve free-radical oxidative damage to tissue components, in particular the highly unsaturated fatty acids.

Fatty acids are long hydrocarbon chains bonded *via* the carboxyl group at one end of a lipid molecule. Cell membranes are composed primarily of lipid and protein molecules in approximately equal proportions. The lipids occur as bimolecular layers with the hydrocarbon portions of the fatty acids buried in the middle and the polar ends of the lipids pointing outward, toward the aqueous phase. The proteins are sometimes on the surface of the lipid bilayer and in other cases embedded partially or fully within the lipid bilayer.

The fatty acids of animal lipids usually have an unbranched chain from 16 to 22 carbon atoms long. They have from 0 to 6 double bonds, and these double bonds are situated at every third carbon. If a fatty acid has one or more double bonds, it is referred to as "unsaturated". The complete structure of a given fatty acid can be specified by a simple abbreviation; for example, 22:6ω3 represents a fatty acid with a chain of 22 carbon atoms containing 6 double bonds beginning on the third carbon from the methyl

* National Science Foundation Faculty Research Participant, Summer 1976. Permanent address: Department of Chemistry, Lawrence University, Appleton, Wisconsin 54911.

(nonpolar) end. The six most common fatty acids in ocular tissues and in many other animal tissues are 16:0, 18:0, 18:1ω9, 18:2ω6, 20:4ω6 and 22:6ω3.

It is known that molecular oxygen can attack the double bond system of unsaturated fatty acids by a free-radical mechanism[7] and that the rate of this so-called "autoxidation" increases markedly with the degree of unsaturation of the fatty acid. The most highly unsaturated fatty acid found in nature is the 22:6ω3 which is so predominant in the retina[24]. It therefore seems reasonable to investigate the possibility that laser induced photochemical damage in the retina might be mediated, at least in part, by the autoxidative destruction of the highly unsaturated fatty acids of the tissue lipids.

Daemen[8] has pointed out that there must be a high *in vivo* oxygen tension in the retinal rod outer segments and suggested that normal renewal of the rod outer segment discs may be necessitated by the gradual irreversible autoxidative destruction of their highly unsaturated fatty acids. Young[9] has observed that the outer segment renewal rate is elevated in both frog and rat when the intensity of retinal illumination is increased. It is also noteworthy that the concentration of vitamin E (α-tocopherol), which acts as an antioxidant and thus partially protects polyunsaturated fatty acids from autoxidation *in vivo*, is unusually high in retinal rod outer segments[8]. Vitamin E is destroyed when it acts as the termination of a free-radical chain reaction, and as soon as it is totally depleted the rate of autoxidative destruction of fatty acid rises sharply[7]. It seems possible that in laser-induced photochemical damage, the threshold level may represent the amount of radiant energy required to deplete the tissue of vitamin E and consequently render the highly unsaturated fatty acids much more susceptible to autoxidative destruction.

In addition to oxidation of unsaturated lipids by molecular oxygen in its ground electronic state, it is also possible that photochemical mechanisms of ocular damage may involve photosensitized formation of the much more reactive singlet ($^1\Delta_g$) molecular oxygen[10,11]. The energy level of this state lies at 7882 cm^{-1} above the ground triplet state and is particularly reactive with respect to oxidation of carbon-carbon double bonds, e.g., in carotenoids[12], cholesterol[13] and vitamin E[14]. Thus, this reactive oxygen species, if formed in sufficiently high concentrations in the vicinity of the ROS lipids, could react with the highly unsaturated fatty acids. However, it should be noted that long-term exposure to low levels of laser radiation in the blue region of the spectrum (442-488 nm) affects para-macular tissue more strongly than the macula[5,15]. Ham[15] has attributed this effect to protection of the macula by xanthophyll which absorbs strongly in this wavelength region. The results presented below support this hypothesis.

B. METHODS

B-1. Laser Exposures

The left eyes of three rhesus monkeys (Macaca mulatta) were irradiated with the 465.8 nm line of a Spectra Physics 170 argon-ion laser. The right eyes of these animals had been enucleated previously for other experiments. The optical arrangement was quite similar to that used to induce large retinal lesions of pre-determined diameter (Chapter 1). In order to ensure exposure of a sufficiently large retinal area for excision and lipid extraction, five overlapping sites were exposed as depicted in Figure 4-1. The calculated retinal image diameter was ∿920 μm between the $1/e^2$ intensity limits. This criterion was employed in order to achieve consistency with the results of Ham, et al.[5,15]. Visual estimates of the beam diameter (700-800 μm) were obtained by viewing the laser image on the fundus of a control animal through a semi-transparent beamsplitter attached to a fundus camera equipped with a calibrated reticle(17).

Similar sets of exposures were made on the retinae of four control eyes as well as on the three experimental eyes, as outlined in Table 4-1. The lowest corneal power employed (∿9.4 mW), was chosen to ensure that each exposure site would receive no less than a threshold energy dose[5] for a non-thermal lesion.

In the case of the control eyes, lesions similar to those observed by Ham, et al.[5,15] were observed at every paramacular site at ∿24 hours post-exposure, but not at one hour, indicating that these lesions were induced by photochemical rather than strictly thermal processes[25]. It was also found, again in agreement with Ham, et al., that the macular sites were markedly lower in sensitivity to these exposure conditions. With one exception, the maculae of these control animals showed no clear evidence of damage. The single exception was observed in animal 666C (OS) in which the macula showed a "bleached", brightly reflecting area which was first observable within a few seconds after exposure and which reached maximum development at ∿20 min post-exposure. This lesion gave the appearance of being somewhat elevated from the macula. Curiously, the lesion appeared as a barely detectable darkened region at one hour post-exposure, but the following day again showed a bleached appearance. Polaroid photographs of the control eyes were taken at periodic intervals following the laser exposures. Examples are shown in Figure 4-2.

The eyes of the three experimental animals were enucleated at ≲1 hour post-exposure and treated as discussed below. As in the case of the control exposures, no clear evidence of retinal damage could be seen ophthalmoscopically so soon after exposure. However, the hypothesized oxidative reaction should be complete well within the first several minutes following irradiation. Presumably, this would give rise to a much slower process leading to gross alteration of membrane structure detectable ophthalmoscopically at ∿24 hours post-exposure. The criterion for sacrifice (≲1 hour) was chosen so as to

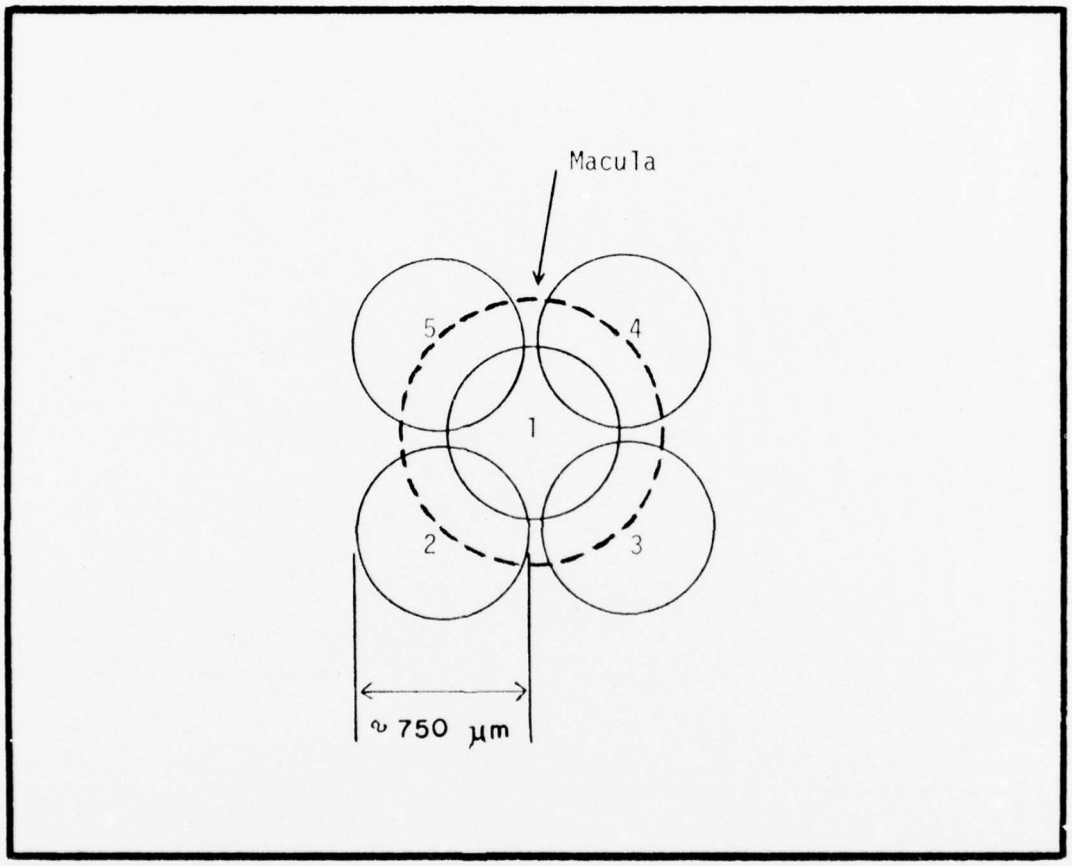

FIGURE 4-1. Diagram Of Retinal Exposures.
Numbers indicate chronological sequence of exposures.

TABLE 4-1.

LASER EXPOSURES OF EXPERIMENTAL AND CONTROL EYES

A. Experimental Eyes (19 August 1976)

Monkey	Corneal Power (mW)	Exposure Time (sec)	Exposure Site[a]	Clock Time at Start of Exposure
522 OS	9.4	120	1	15:22
	9.4	120	2	15:29
	9.4	120	3	15:33
	9.4	120	4	15:38
	9.4	120	5	15:43
			Euthanized	16:48
554 OS	19.4	120	1	16:29
	19.4	120	2	16:43
	19.4	120	3	16:47
	19.4	120	4	16:51
	19.4	120	5	16:56
			Euthanized	17:05
221B OS	39.6	100[b]	1	17:28
	39.6	60	2	17:59
	39.6	60	3	18:02
	39.6	60	4	18:04
	39.6	60	5	18:07
			Euthanized	18:15

(a) See Figure 4-1.

(b) Delivered in five successive exposures of 10 sec each followed by two exposures of 20 and 30 sec, respectively. The exposures were spaced at 1-3 min intervals and the fundus was examined between exposures. No evidence of thermal lesions was detected up to 45 min following the first exposure.

TABLE 4-1 (continued)

B. Control Eyes (8 September 1976)

Monkey	Corneal Power (mW)	Exposure Time (sec)	Exposure Site[a]	Clock Time at Start of Exposure
662C OS	9.4	120	1	10:47
	9.4	120	2	10:53
	9.4	120	3	10:59
	9.4	120	4	11:05
	9.4	120	5	11:12[d]
662C OD	19.4	120	1	11:35
	19.1	120	2	11:43
	19.1	120	3	11:48
	19.8	120	4	11:54
	19.8	120	5	11:58[d]
666C OS	40.7	120	1[b]	14:03
	40.0	120[c]	2	15:13
	40.3	120	3	15:19
	40.7	120	4	15:26
	40.0	120	5	15:30[d]
666C OD	40.0	60	1	14:36
	40.0	60	2	14:41
	39.2	60	3	14:44
	39.2	60	4	14:47
	38.9	60	5	14:51[d]

(a) See Figure 4-1.

(b) Lesion, possibly thermal, noted shortly after exposure (see text).

(c) Delivered in six successive exposures of 20 sec at 20 sec intervals.

(d) No lesions, except as noted above, at ∿1 hour exposure. All paramacular sites showed lesions (∿700 m diameter) at 24 hours post-exposure.

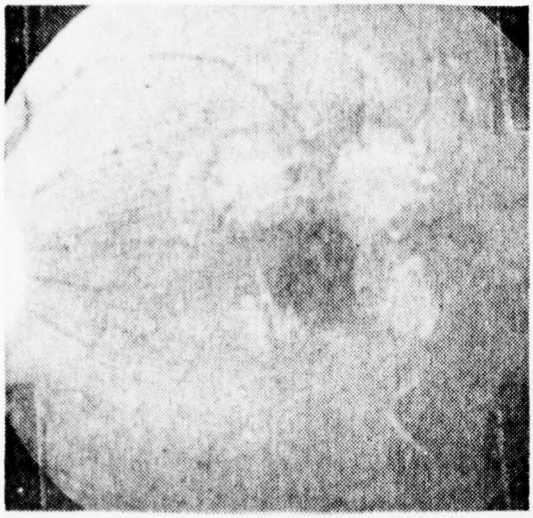

662C OS

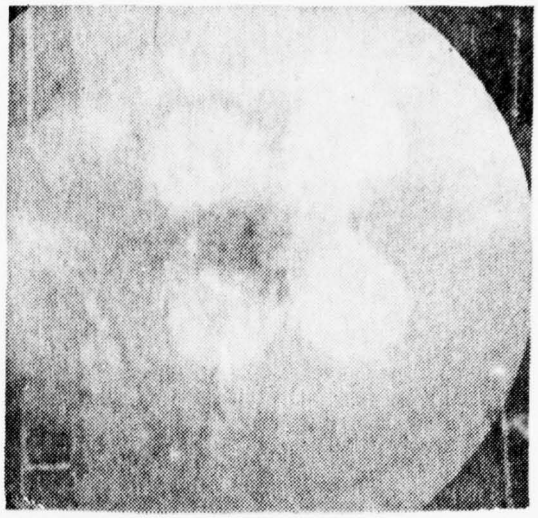

662C OD

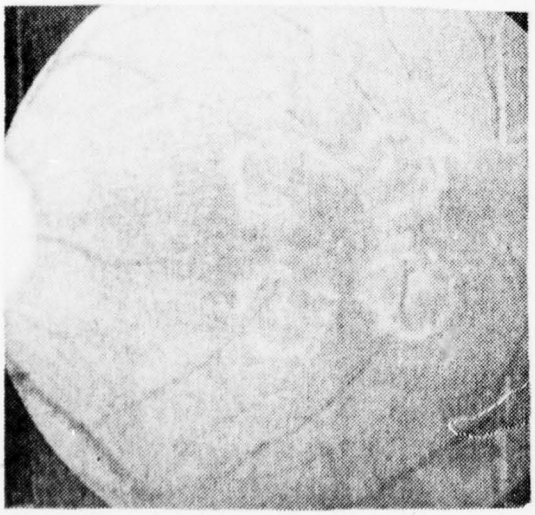

666C OS

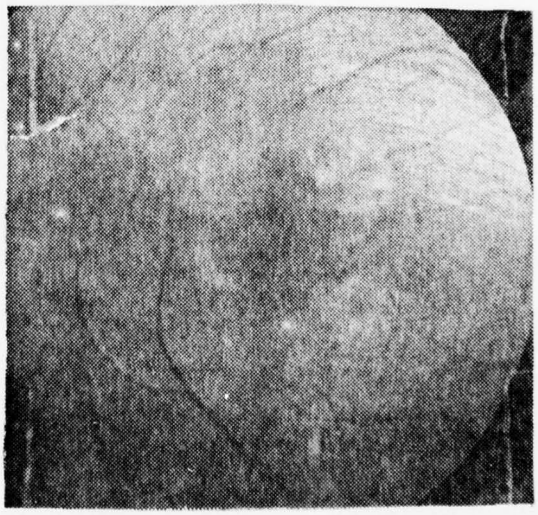

666C OD

FIGURE 4-2. Fundus Photographs of Presumed Photochemical Lesions at One Week Post-exposure.

distinguish between thermal and photochemical lesions. The former would presumably appear during this interval following exposure whereas the latter should not[5,15].

B-2. Removal of Retinal Tissue Samples

Immediately following enucleation, the cornea was carefully removed in a manner designed to avoid any rupture of the chamber containing the vitreous humor. At least three long cuts were then made with scissors through all layers of the eyeball, each cut beginning from the edge of the cornea and extending posteriorally to within ~6mm of the optic nerve. These cuts were located so as to avoid the laser-irradiated or control zone in the region of the macula. Care was taken to avoid retinal detachment. The macula could be located directly at this stage by means of low-power, magnifying binocular spectacles, using as guides the color of the macular pigment as well as the characteristic pattern of the blood vessels around the macula.

The desired zone was then excised with a razor blade, each cut being made through all layers including the sclera. After the desired area was excised, the retina was pulled off, leaving behind the pigment epithelium (PE), choroid, sclera and perhaps some detached rod outer segments interdigitated with the PE. The PE plus choroid could then be scraped off the sclera and taken together as a sample. Due to the adhering vitreous humor, it was not possible to obtain a meaningful measure of the size of the tissue sample by taking the fresh weight. The fresh weights were used, however, to estimate the amount of tissue water introduced into the chloroform-methanol solvent system used to extract the retinal lipids. Additional details of the experimental procedures may be found in an interim report[16].

B-3. Preparation of Tissue Lipids for Gas Chromatography

The total lipids were extracted from the tissue and freed of non-lipid contaminants by a modification of the method of Folch-Pi, et al.[18]. This involved placing the tissue sample in ~19 times its own volume (assuming a tissue density of 1.00 g/ml) of chloroform-methanol (2:1 by volume). The tissue samples can be stored safely in the solvent mixture, which terminates virtually all enzymatic activities. Because of the tendency of molecular oxygen to attack the unsaturated lipids, all operations including storage of samples were carried out, as far as was practicable, under a nitrogen atmosphere. Solvents were freed of dissolved oxygen by bubbling with nitrogen before use, and lipid samples were stored in a freezer at ~-20°C.

The tissue samples were homogenized by hand using a Potter-Elvehjem homogenizer with a glass pestle. Insoluble material was then removed by centrifugation. The supernatant fluid was freed of non-lipid contaminants by shaking with a volume of 0.05% aqueous $CaCl_2$. The resulting two-phase

system was centrifuged in order to produce a clean separation of phases. The upper phase, consisting of most of the methanol and water in the system plus the non-lipid contaminants, was taken off by means of a water aspirator. The resulting washed lipid solution was then either used directly or diluted to a volume of 5.0 ml with 2:1 chloroform-methanol so that several aliquots could be taken.

Since the intact lipid molecules are too large and usually too polar to be volatile enough for gas chromatography, the fatty acids were stripped off the lipid molecules and simultaneously converted to their much more volatile methyl esters. This process of methanolysis was accomplished by a modification[19] of the method of Morrison and Smith[20]. Care was taken to preclude exposure of the lipid sample to atmospheric oxygen, particularly when the sample is kept at 100°C for 90 minutes during the methanolysis reaction.

Finally, the washed solution of methyl esters of the fatty acids was evaporated to dryness under a stream of nitrogen. The residue was dissolved in a small volume of heptane, usually ~40 µl, and an aliquot of 2 to 7 µl, was run through the gas chromatograph for quantitative measurement of the fatty acid pattern.

B-4. Gas Chromatography

The methods used for gas chromatography were essentially those described by Joel, et al.[19]. The instrument employed was a Packard 800 series with hydrogen flame ionization detector. Pyrex columns, 6 mm od x 2 mm id x 10 feet long, were packed with 10% diethylene glycol succinate on 100-200 mesh Chromosorb-WAS (Supelco). The column was filled while tapping it with a metal spatula and simultaneously applying a vacuum to the outlet end after insertion of a glass wool plug 1 cm long. The column packing was compressed by application of air at 45 psi to the inlet end with repeated tapping along the entire length of the column. The column was conditioned at 203°C for 64 hours, after which the packing had settled by 2 cm. Conditioned column packing was added and a 1 cm glass wool plug inserted such that the amount of dead space at the inlet end of the column was as small as possible. During injection of the sample, the tip of the microsyringe needle reached to within 6 mm of the top of the glass wool. The column used for the work described in this report gave 3600 theoretical plates with 16:0 fatty acid (methyl palmitate) and achieved a baseline separation between 18:0 and 18:1ω9.

The gas chromatography conditions were varied in order to establish optimal conditions for the runs. For example, the effect of carrier gas (helium) flow rate on the separation of 18:0 from 18:1ω9 was studied, as well as the effects of hydrogen and air flow rates on the signal-to noise ratio. From these studies, the optimum flow rates were selected on the basis of minimal noise level, maximal detector response to 16:0, maximal separation of 18:0 from 18:1ω9, and minimal time consumed for a complete

chromatographic run. Thus, helium flow was set at 52 ml/min (i.e., the highest possible flow rate using the pressure regulator available), hydrogen flow at 23 ml/min and air flow at 500 ml/min. The system was capable of detecting well under 1 ng of 16:0, but the most quantitatively accurate results were obtained when the total sample consisted of approximately 10 μg or more of a mixture of fatty acid methyl esters. Approximately 4 mm^2 of retina was found to yield more than enough lipid to work at this sample size.

Before the first run of each day, a sample of 30 μg of 20:4ω6 was run through the chromatograph in order to inactivate any sites that might irreversibly bind highly unsaturated fatty acids. A mixture of several known fatty acids including 22:6ω3 was run through the column in order to determine whether or not there were selective losses of any particular types of fatty acids (short-chain or long-chain, saturated or highly saturated). The results appeared to be acceptable.

The column used could achieve a partial separation of 18:0 (the fatty acid methyl ester) from 18:1a (the dimethyl acetal of the fatty aldehyde) to the extent that either could readily be detected in the presence of at least a 20-fold excess of the other. This degree of separation of these two compounds is generally considered to be difficult to achieve.

C. RESULTS AND DISCUSSION

Laser parameters chosen for the experiments coincided with those reported to induce photochemical rather than thermal retinal lesions[5]. Corneal powers, exposure time and retinal image size were calculated to span the range of retinal energy dose from 50 to 800 J/cm^2. The former value is the approximate threshold at this wavelength (465.8 nm) interpolated from the data of Ham, et al.[5] and was based on a "worst case" assumption that the actual retinal image diameter was a factor of two larger than the calculated value. Thus, the retinal dose delivered to each site exceeded the threshold for presumed photochemical damage without inducing thermal damage. Funduscopic examination of the three animals used in this study was carried out immediately prior to euthanization (≤1 hour post-exposure) and, indeed, no evidence of thermal lesions was seen.

The eyes were enucleated immediately (<5 min) after sacrifice and were stored overnight in N_2- saturated, isotonic saline at ~0°C. Severe retinal detachment was noted when the eyes were dissected. Such severe detachment had not been observed in eyes dissected immediately following enucleation.

Due to the severity of the retinal detachment in these three eyes, difficulties were experienced in attempts to dissect usable retinal tissue samples. Thus, the first eye removed (221B) yielded no useful sample of

the irradiated retinal tissue and was used for additional control analyses. Peripheral areas of the other two retinas (552C and 554C) were used for exploratory trials in order to establish procedures for selective dissection of the irradiated retinal sites.

Areas of retina + pigment epithelium + choroid were dissected from 552C and 554C. The first sample taken from 552C included the macula and presumably all of the irradiated area. A second area taken from 552C was between the disc and the irradiated site and was intended to serve as the most suitable control area. Ideally, one would like to obtain the control area from the macular zone of the other eye of the same animal, but these three monkeys were uni-ocular. Finally, an irradiated area similar in location to that taken from 552C was taken from 554C.

The retina + pigment epithelium + choroid were taken together rather than the retinal layer alone because of the possibility that the largest laser effects might occur in the most distal portions of the rod outer segments. These are the oldest portions of the outer segments and thus might have experienced some degree of lipid autoxidation even before laser exposure[8]. Some of the more distal parts of the rod outer segments may become detached and remain with the pigment epithelium into which they protrude. In retrospect, it would appear preferable to analyze the retina separately from the pigment epithelium + choroid in the laser-exposed eyes.

Table 4-2 shows a comparison of the fatty acid patterns of the irradiated zones of monkeys 552C and 554C with that of the control zone of monkey 552C. Clearly there are no striking effects of laser radiation on the fatty acid pattern. There is no indication of any depletion of 22:6ω3 due to laser treatment, nor is there any indication of the appearance of new peaks representing fatty acids with structures altered due to laser radiation. The experiment should be repeated with more appropriate controls as well as with retinas in which the lesions are clearly visible, i.e., at $\sim$24 hours post-exposure.

Table 4-3 shows a comparison between the fatty acid pattern of the retina of monkey 221B and that of the pigment epithelium + choroid of the same eye. The most striking differences are a five-fold higher concentration of 18:2ω6 in the pigment epithelium + choroid and an apparent two-fold higher concentration of 22:6ω3 in the retina. A relatively high content of 22:6ω3 and low content of 18:2ω6 are characteristic of vertebrate central nervous tissue in general[21-23]. Alveldano and Bazán[24] have observed a similar difference in the fatty acid patterns of what they termed "retina plus choroid" in the frog. This is the first known report of the fatty acid pattern of the monkey retina.

Figure 4-3 illustrates the complete gas chromatograph of the fatty acids of the retina of monkey 221B. All but three of the peaks occurring as 1% or more of the total fatty acids could be identified with a great deal of assurance, primarily on the basis of retention time. The three uncertain peaks are relatively minor.

TABLE 4-2.

COMPARISON OF FATTY ACID PATTERNS OF CONTROL AND LASER-TREATED AREAS OF MONKEY RETINA + PIGMENT EPITHELIUM + CHOROID

Tentative Identification of Peak	Amount of Each Fatty Acid Expressed as % of Total Fatty Acids[a]		
	Monkey 552C Control Area	Monkey 552C Irradiated Area	Monkey 554C Irradiated Area
16:0a[b]	1.2	1.7	1.3
16:0	16.3	12.4	15.6
18:0a[b]	2.4	2.5	3.1
18:0	20.8	20.2	21.7
18:1	13.0	12.6	13.9
18:2ω6	4.8	5.1	5.7
20:0	0.8	1.0	1.1
20:3ω6	1.5	1.4	1.4
20:4ω6	12.3	12.3	14.1
Unidentified[c]	1.6	1.5	1.3
22:4ω6	2.0	2.4	2.1
22:5ω6 or 24:0	3.3	3.0	2.2
22:6ω3	16.2	20.0	13.2

(a) The amount of each fatty acid is calculated as the peak height multiplied by its retention time on the column. This gives the percentage of each component by weight. Only fatty acids occurring at a level of at least 1.0% in at least one of the three samples are shown in this table.

(b) "a" designates the dimethylacetal of the fatty aldehyde with no double bonds.

(c) This peak may contain 22:0 and/or a minor contaminant from the chloroform solvent.

AD-A043 457 TECHNOLOGY INC SAN ANTONIO TEX LIFE SCIENCES DIV F/G 6/18
RESEARCH ON THE OCULAR EFFECTS OF LASER RADIATION.(U)
AUG 77 J A ZUCLICH, J T YATES, A D NAWROCKI F41609-73-C-0017
UNCLASSIFIED TI-77-0561-03 NL

2 OF 3
AD A043457

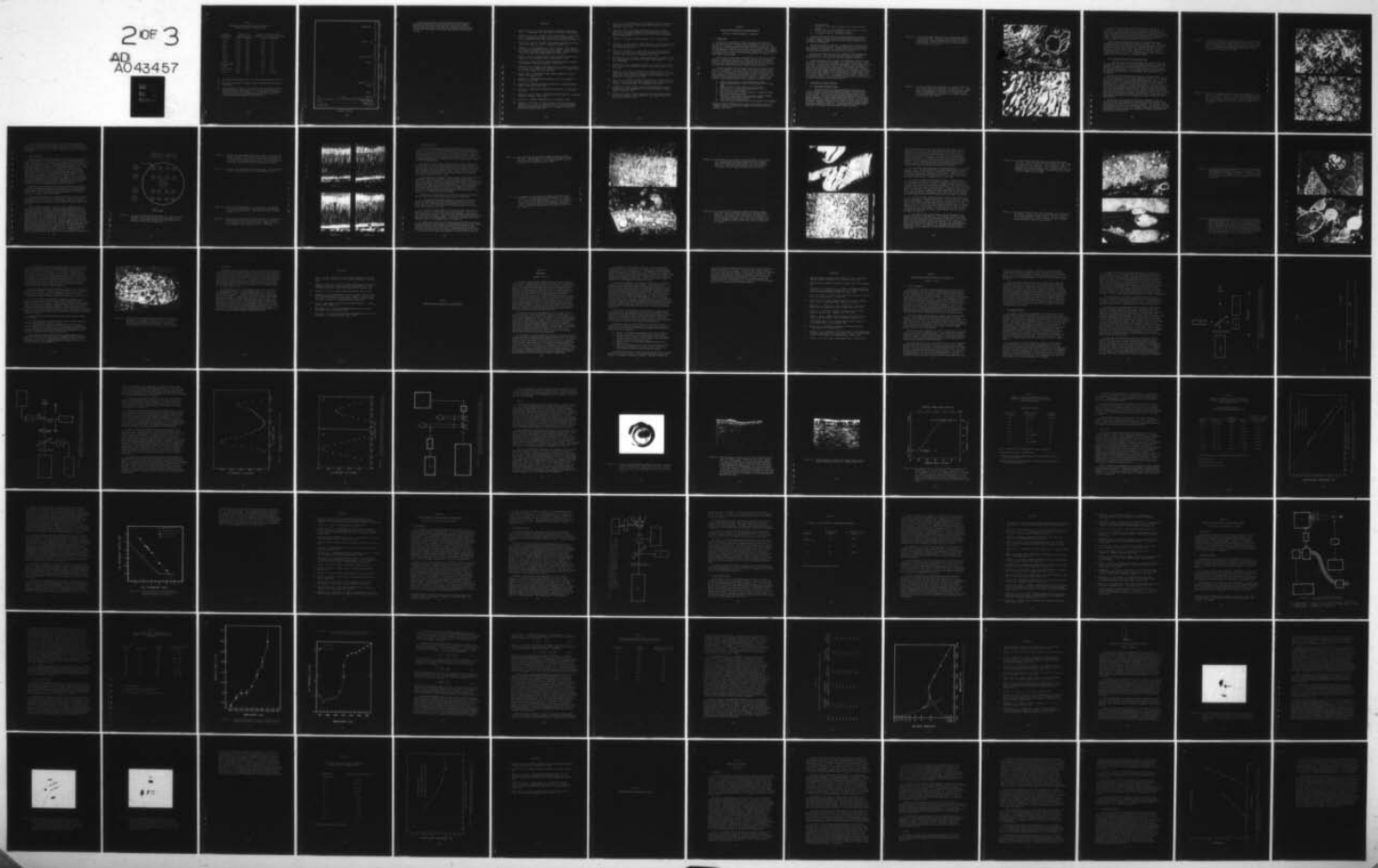

TABLE 4-3.

COMPARISON OF FATTY ACID PATTERNS OF RETINA WITH PIGMENT EPITHELIUM + CHOROID LAYERS

Tentative Identification of Peak	Retention Time Relative to 18:0		Amount of Each Fatty Acid[a] Expressed as % of Total Fatty Acids	
	Retina	PE+Choroid	Retina	PE+Choroid
16:0a	0.45	0.46	1.0	2.4
16:0	0.53	0.53	16.2	16.0
18:0a	0.87	0.88	2.6	2.2
18:0	1.00	1.00	20.0	17.9
18:1	1.12	1.13	14.1	17.7
18:2ω6	1.36	1.37	1.9	10.0
20:0	1.85	1.88	1.2	1.4
20:3ω6	2.84	2.88	1.8	1.1
20:4ω6	3.18	3.22	12.3	14.5
Unidentified[b]	3.49	3.55	0.4	1.3
22:4ω6	5.79	5.88	2.0	2.2
22:5ω6 or 24:0	6.40	6.66	2.7	1.2
22:6ω3	8.44	8.58	22.2	10.2[c]

(a) Data obtained from monkey 221B. For further explanations see Table 4-2.

(b) This peak may contain 22:0 and/or a minor contaminant from the chloroform solvent.

(c) The 22:6ω3 peak for the PE + choroid sample was approximately twice as wide as observed in other samples. This is most likely due to the presence of material other than 22:6ω3. If instead, all the material in the peak were 22:6ω3, then the percentage of 22:6ω3 in the PE + choroid would be approximately 20 rather than 10.2.

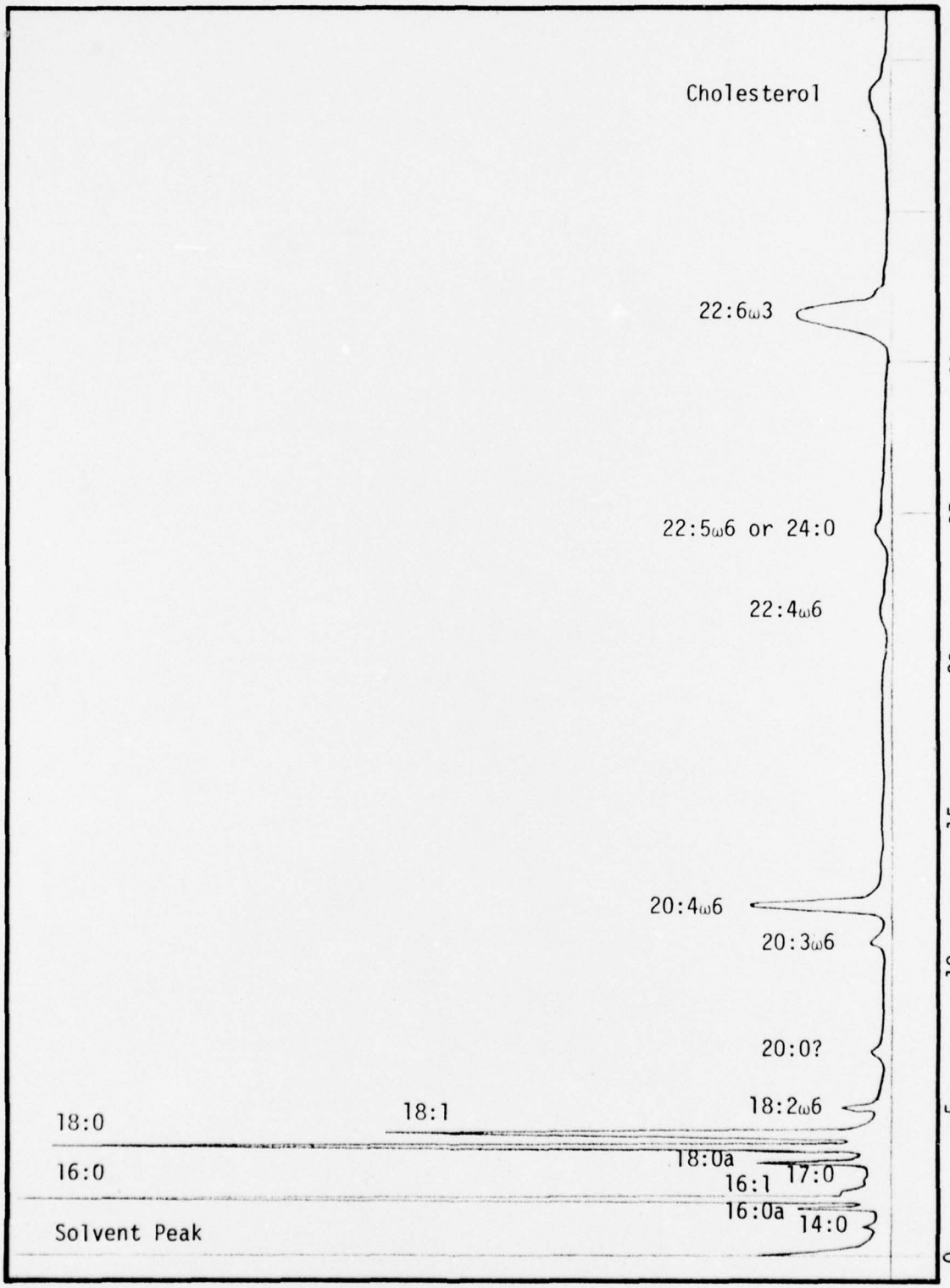

FIGURE 4-3. Gas Chromatogram of Fatty Acids of Monkey Retina.

In conclusion, the major problems regarding the procedures and techniques for obtaining the desired specimens of retina, pigment epithelium and choroid and analyzing their quantitative fatty acid patterns have been solved. The project has reached the stage at which the effects of laser radiation on retinal fatty acids can be assessed directly.

REFERENCES

1. Wolbarsht, M.L., ed., "Laser Applications in Medicine and Biology", Vol. 2, Plenum Press, New York, 1974, and references cited therein.

2. Connolly, J.S., et al., "Research on the Ocular Effects of Laser Radiation", Technology Incorporated, Twelfth Interim Technical Report, Contract F41609-73-C-0017, USAF School of Aerospace Medicine, March 1976.

3. Zuclich, J.A. and J.S. Connolly, "Ocular Damage Induced by Near-Ultraviolet Laser Radiation", Invest. Ophthalmol. 15:760, 1976.

4. Connolly, J.S., H.W. Hemstreet, Jr. and D.E. Egbert, "Ocular Hazards of Picosecond and Repetitive Pulse Lasers, Volume II: Argon-Ion Laser (514.5 nm)", Technology Incorporated, Final Report, Contract F41609-73-C-0016, USAF School of Aerospace Medicine, January 1977.

5. Ham, W.T., Jr., H.A. Mueller and D.H. Sliney, "Retinal Sensitivity to Damage from Short Wavelength Light", Nature 260:153, 1976.

6. Zuclich, J.A. and W.E. Kurtin, "Oxygen Dependence of Near-UV Induced Corneal Damage", Photochem. Photobiol. 25:133, 1977.

7. Holman, R.T., in "Progress in the Chemistry of Fats and Other Lipids", R.T. Holman, W.D. Lundberg and T. Malkin, eds., Vol. 2, Academic Press, New York and Pergamon Press, London, 1954.

8. Daemen, F.H.M., "Vertebrate Rod Outer Segment Membranes", Biochem. Biophys. Acta 300:255, 1973.

9. Young, R.W., "The Renewal of Photoreceptor Cell Outer Segments", J. Cell Biol. 33:61, 1967.

10. Kearns, D.R., "Physical and Chemical Properties of Singlet Molecular Oxygen", Chem. Rev. 71:395, 1971.

11. Foote, C.S., "Mechanisms of Photosensitized Oxidation", Science 162: 963, 1968.

12. Seely, G.R. and T.H. Meyer, "The Photosensitized Oxidation of β-Carotene", Photochem. Photobiol. 13:27, 1971.

13. Lamola, A.A., personal communication to J.S. Connolly, 1974.

14. Stevens, B., R.D. Small, Jr. and S.R. Perez, "Physical and Chemical Quenching of O_2 $^1\Delta_g$ by α-Tocopherol (Vitamin E)", Eleventh Informal Conference on Photochemistry, Abstract 5-3, Vanderbilt University, Nashville, Tennessee, June 1974.

15. Ham. W.T., Jr., presentation at "Laser Bioeffects Meeting", Bureau of Radiological Health, U.S. Food and Drug Administration, Rockville, Maryland, July 13, 1976.

16. Joel, C.D., et al., in "Research on the Ocular Effects of Laser Radiation", Technology Incorporated, Thirteenth Interim Technical Report, Part VI, Contract F41609-73-C-0017, USAF School of Aerospace Medicine, August 1976.

17. Sanders, V.E., ibid., First Annual Report, Part I, February 1974.

18. Folch-Pi, J., M. Lees and G.H. Sloane-Stanley, "A Simple Method for the Isolation and Purification of Total Lipids from Animal Tissues", J. Biol. Chem. 226:497, 1957.

19. Joel, C.D., C.A. Ellis, J.K. Lace, P.B. Joel, M.R. Swanson and J.R. Stroemer, "Stability of the Brain Fatty Acid Pattern in Adult Rats During Extreme Starvation", J. Neurochem. 23:23, 1974.

20. Morrison, W.R. and L.M. Smith, "Preparation of Fatty Acid Methyl Esters and Dimethylacetals from Lipids with Boron Floride-methanol", J. Lipid Res. 5:600, 1964.

21. McMullin, G.F., S.C. Smith and P.A. Wright, "Tissue Fatty Acid Composition in Four Diverse Vertebrate Species", Comp. Biochem. Physiol. 26: 211, 1968.

22. Jerde, R.S., P.B. Joel, J.R. Stroemer, R.O. Haight and C.D. Joel, "A Comparative Study of Nervous Tissue Lipid Fatty Acid Patterns of Various Animal Species with Particular Reference to Docosahexaenoic Acid", Biochem. Soc. Transactions 3:727, 1975.

23. Joel, C.D., R.S. Jerde, P.B. Joel, G. Peterson, J.R. Stroemer and R.O. Haight, "Vertebrate and Invertebrate Central Nervous System Fatty Acid Patterns", Transactions Amer. Soc. Neurochem. 7:128, 1976.

24. Aveldaño, M.I. and N.G. Bazán, "Fatty Acid Composition and Level of Diacylglycerols and Phosphoglycerides in Brain and Retina", Biochem. Biophys. Acta 296:1, 1973.

25. Gibbons, W.D. and R.G. Allen, "Evaluation of Retinal Damage Produced by Long-Term Exposure to Laser Radiation", USAF School of Aerospace Medicine, SAM-TR-75-11, 1975.

CHAPTER 5

OCULAR HISTOPATHOLOGY AND ELECTRON MICROSCOPY

William H. Bowie and Robert V. Blystone*

A. INTRODUCTION

Duties of the histopathology support function of this contract included securing ocular tissues; fixing and embedding tissues in preparation for sectioning; sectioning; and preparation of slides for light microscopy or of unsupported thin sections for electron microscopy. Except for the comparative light and electron microscopy reported in this chapter, all prepared ocular tissues were turned over to pathologists of the USAFSAM Veterinary Science Division, Clinical Pathology Branch for evaluation of laser induced ocular damage.

Ocular tissues (globes) were enucleated directly from freshly killed animals or removed with the aid of a Stryker saw from perfused animals. Methods of preservation included direct immersion of the fresh globe in fixative, whole body perfusion of the subject through the left ventricle, and whole body retrograde perfusion through the descending aorta.

Although equipment for the automatic processing of standard tissue samples was available, it was not suitable for processing ocular tissues due to the uniqueness of the chemicals and time schedules required for these tissues. Consequently, all processing of ocular tissue was accomplished manaually as was staining of mounted sections. The chemical time schedules varied according to the specific task but, in general, were similar to the following outline for the treatment of retinal tissue:

1. immerse entire globe in ~3% gluteraldehyde overnight
2. dissect exposed macula or other area of interest out of fixed globe
3. immerse tissue in fresh fixative for several hours
4. wash tissue in 0.1 M sodium cacodylate buffer (pH 7.3)
5. wash tissue in distilled water
6. post-fix tissue with 1% osmium tetroxide in cacodylate buffer
7. wash tissue in distilled water
8. dehydrate tissue through a series of ethyl alcohol solutions of graded concentrations, ending with 100% alcohol
9. treat tissue with propylene oxide
10. infiltrate tissue overnight with a 50:50 propylene oxide-complete

* National Science Foundation Faculty Research Participant, Summer 1976. Permanent address: Department of Biology, Trinity University, San Antonio, Texas 78284.

plastic mixture

11. infiltrate tissues under vacuum with 100% complete plastic mixture
12. immerse tissue in complete plastic mixture; allow to cure at 45°C-65°C overnight or, preferably, longer
13. trim plastic, mount in microtome and section.

Corneal tissues were processed according to the above schedule or, in some instances, according to a more routine paraffin processing technique. Examples of the latter can be found in any standard manual of histologic techniques[1].

Sectioning methods used employed a standard rotary microtome (AO) or a Porter-Blum Ultramicrotome. Tissues sectioned on the AO instrument were embedded in a paraffin-type compound while those sectioned on the ultramicrotome were embedded in Epon 812 or Spurr plastic.

Stains utilized were toluidine blue, methylene blue and hematoxylin and eosin (H & E). The former two were used on sections embedded in plastic while the H & E was used on sections embedded in paraffin.

During the course of this contract, histopathologic support was used to evaluate laser-induced ocular damage for a number of projects. Among these were: a study of the wavelength dependence of retinal damage induced by visible laser radiation; a study of the chronological development of laser induced retinal lesions; and studies of the location and extent of corneal and retinal damage induced by near-UV laser radiation. Discussions of these and other examples of the contributions of histopathologic evaluation to the overall program can be found elsewhere in this report as well as in earlier reports[2,3]. The remainder of this chapter is devoted to a comparative study of light and electron microscopy (EM) of retinal lesions induced by mode-locked visible laser pulses[4].

B. PRELIMINARY ELECTRON MICROSCOPY

B-1. Previously Prepared Tissues

Tissues mounted in the previously prepared blocks had been fixed by perfusion or whole eye immersion procedures. In some of these tissues, artifacts resulting from the fixative procedure were evident at the EM level. The principal artifact observed was probably due to osmotic imbalance of tissues fixed by whole eye immersion. Specifically, these preparations revealed swollen mitochondria (Figure 5-1), disruption of nuclear envelopes, and swelling or disruption of other membrane-bound organelles. Moreover, immersion in cold ($\leq 4^0$C) fixative produced possible ice crystal formation (Figure 5-2). EM examination of perfused samples revealed tissue profiles with substantially fewer artifacts.

FIGURE 5-1. Electron Micrograph Showing Swollen, Distended Mitochondria (subject 108C, OD). Section was taken from the periphery of a lesion area. These malformations are typical of osmotic shock and were evident in nearly all eyes fixed by immersion (X 27,800, neg. no. 76-352).

FIGURE 5-2. EM View of a Longitudinal Section (i.e., parallel to the optic axis) Through the Pigment Epithelium (subject 39C, OD). Section taken from periphery of lesion area. The white spindle-shaped areas are interpreted as voids due to the formation of ice crystals during whole eye immersion in cold ($\sim 4^{o}C$) fixative (X 15,000, neg. no. 76-363).

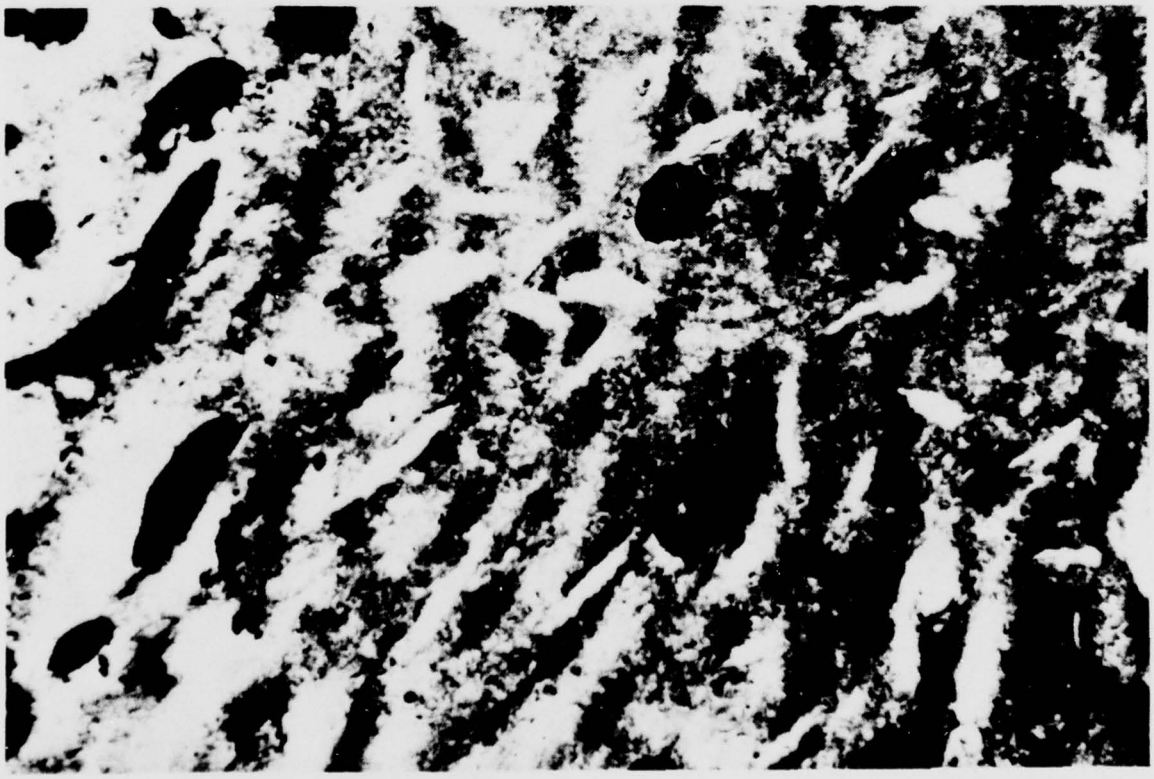

A block of control tissue was aligned and cut perpendicular to the optical axis. In this manner, retinal lesions can be examined as a function of axial depth across the entire diameter of the exposure site. Thus, this approach should allow semi-quantitative estimates of the overall extent of damage as well as the severity of damage within individual retinal layers. Such estimates would provide valuable information needed to validate thermal and non-thermal models of retinal injury.

Examination of transverse sections of this control eye showed structure and detail not apparent in parallel sections. For instance, at low magnification (~100x) the outer limiting membrane appears as a broad circular band as does Bruch's membrane, a portion of which is shown in Figure 5-3 at high magnification. Similarly, the spatial orientation of the photoreceptors is more readily observable in transverse than in longitudinal sections. Figure 5-4 shows a transverse view of the inner segment region of a normal (i.e., unexposed) retina.

B-2. Comparative Light and Electron Microscopy

Both eyes from each of three animals (461C, 511C and 585C) were enucleated for this study. All had been exposed previously in the course of threshold measurements using mode-locked visible laser pulses[4]. In addition, the right eye of No. 461C had been used for an *in vivo* thermal and optical probe experiment. Thus, the eyes from this subject were fixed by immersion whereas both of the other animals were perfused prior to enucleation.

The fixative combinations were the same for all three animals: 3.0 to 3.5% gluteraldehyde in 0.1 M sodium cacodylate buffer (pH 7.3), followed by 1% osmium tetroxide in 0.05 M sodium cacodylate buffer (also at pH 7.3). The major variation in technique tested with animals 511C and 585C was the embedding matrix. Older specimens had been embedded in Luft's Epon[5] which proved to be too soft for large, thin sections. Specimens from 585C (both eyes) were embedded in a modified Mollenhauer Epon-Araldite plastic[6] which also yielded unsatisfactory results. Sections of peripheral retina, saved from 585C and 461C, were later infiltrated with Spurr plastic[7] which proved to be satisfactory. However, the usual thick section stain (toluidine blue) gave less than desirable results in this plastic. Methylene blue in sodium borate was found to be an acceptable stain for sections embedded in Spurr plastic.

The macular areas of both eyes of 461C were embedded in Epon and sectioned from nasal to temporal in increments of 2 μm per section. Some thin sections were taken for EM microscopy, primarily for initial experience in coordination of thick-thin sectioning techniques. The resulting electron micrographs of these tissues did not contain significant information regarding laser induced injury, but they did contribute to a general overview of the ultrastructure of the retina.

FIGURE 5-3. Electron Micrograph of a Transverse Section (i.e., perpendicular to optic axis) Through Bruch's Membrane (subject 199B, OS). The basal enfoldings of the pigment epithelium are seen at the upper right while the choroidal fenestrations are seen at the lower left. Collagen fibers predominate and appear to be randomly arranged (X 12,800, neg. no. 76-396).

FIGURE 5-4. EM View of a Transverse Section Through Inner Segments of Photoreceptors. The central area is a single cone surrounded by rods (subject 199B, OS). Darkly stained mitochondria are predominant. The white vacuolar areas within the cells are probably artifacts due to osmotic damage produced during fixation (X 9,050, neg. no. 76-432).

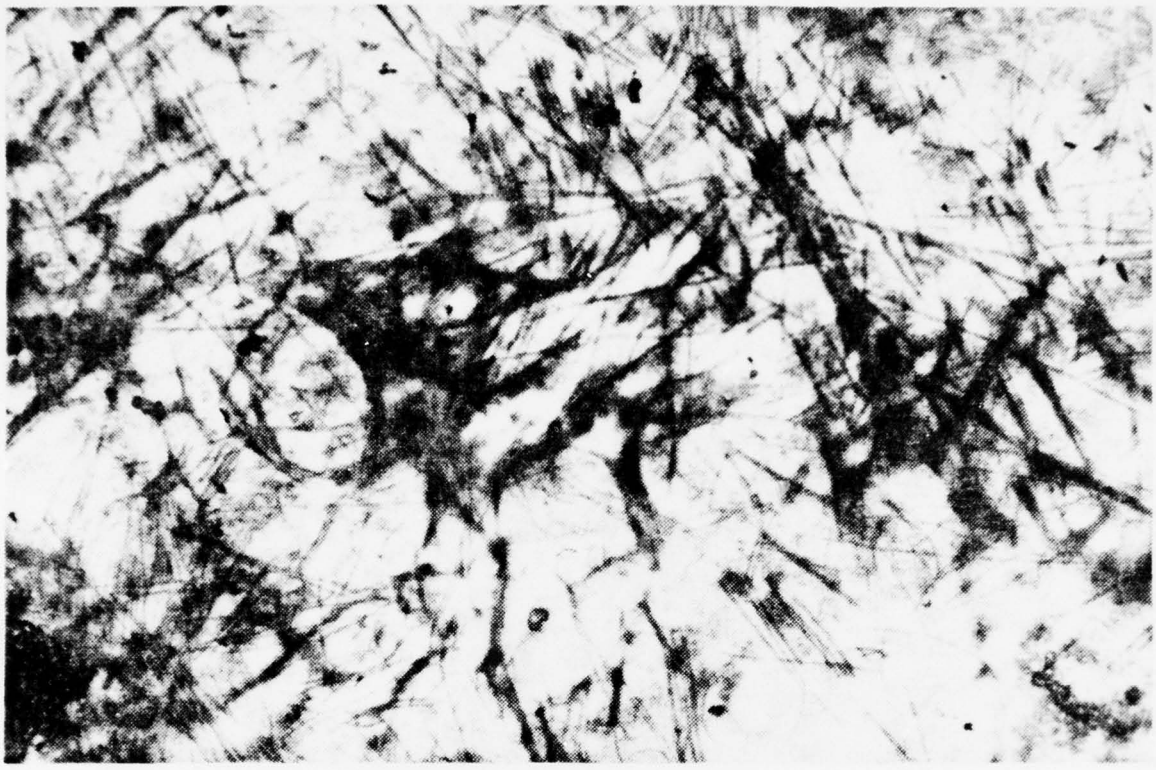

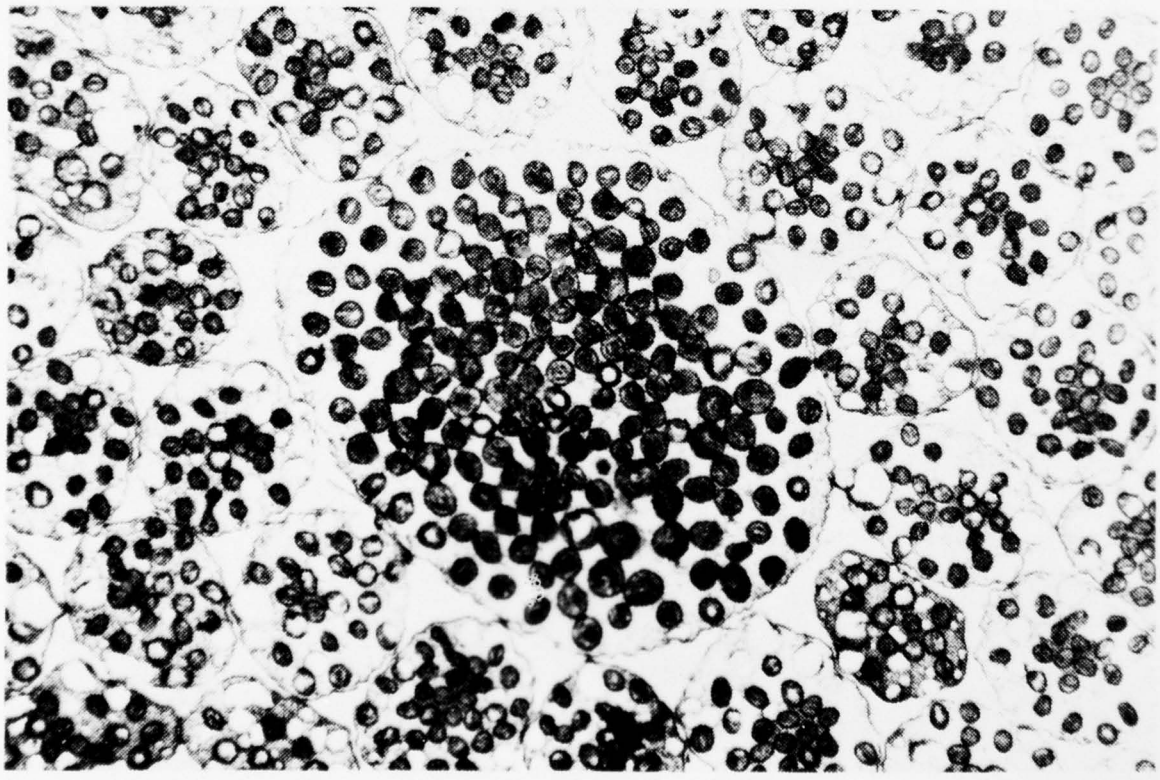

Tissue samples from the right eye of animal 511C were embedded in Spurr plastic and subjected to alternate thick-thin sectioning for light and electron microscopy, respectively. Detailed results of the microscopic examinations are presented in Sections C (light microscopy) and D (electron microscopy).

C. LIGHT MICROSCOPY

The right eye of animal 511C had been exposed to mode-locked, visible laser pulses 6 months prior to sacrifice. A row and column pattern of marker lesions was used to define a 4 x 4 grid of exposure sites within the macula as shown in Figure 5-5. The exposure conditions were as follows: wavelength, 514.5 nm; pulsewidth, ∿250 psec; pulse repetition rate, ∿104 MHz; pulse train duration, 10 msec (see reference 4 for further details). The peak power delivered to each of the 16 exposure sites is indicated in Figure 5-5. For this set of exposure conditions, two threshold levels were determined: at one hour post-exposure, the threshold (ED_{50}) was ∿430 mW peak pulse power, whereas using a 24-hour observation criterion, the peak pulse power ED_{50} was found to be ∿210 mW[4]. Thus, none of the sites in this eye were exposed to powers lower than the 24-hour threshold. Five sites received less than the 1-hour threshold dose and the remaining eleven were exposed to peak power levels ranging from slightly supra-threshold to ∿4 times threshold, based on the 1-hour ED50.

Ophthalmoscopic examination of this eye at one hour, eight days and ∿two weeks post-exposure showed lesions at all sites except those exposed to peak powers lower than 475 mW. At six months (i.e., immediately prior to sacrifice) only six lesions were clearly identifiable, viz., those exposed to peak powers higher than 681 mW.

The eye was sectioned at 2 μm intervals through the vertical markers (M5 through M8) until the first horizontal marker (M4) was identified. After that, serial thick (i.e., 2 μm) sections were taken for light microscopy with thin (i.e. 1200 Å) sections for electron microscopy taken every 10-15 μm.

Three definite experimental lesions, and one probable lesion were identified by light microscopy. These were found approximately 400 μm inferior to the fovea centralis and were therefore assigned to the row of sites defined by M8. All experimental lesions were about 20-30 μm wide and none showed extensive disruption of the pigment epithelium. The area shown in Figure 5-6 is assigned to site 832 and can only be classed as a probable lesion. This classification is based on the absence of pigment spicules on the inner surface of the PE and on the vague disorganization in the microvilli region of this area. The most apparent damage in sites that received ≥832 mW was confined to the inner segments and, to some extent, the PE (Figures 5-7 through 5-9). The outer nuclear layer appeared to be slightly disarranged and depressed towards the PE. The outer limiting membrane was not appreciably thickened. The inner segments showed some disruption, and vacuolation was evident at site 1587 (Figure 5-8). In addition, displaced nuclei were found in the inner segments of some lesions.

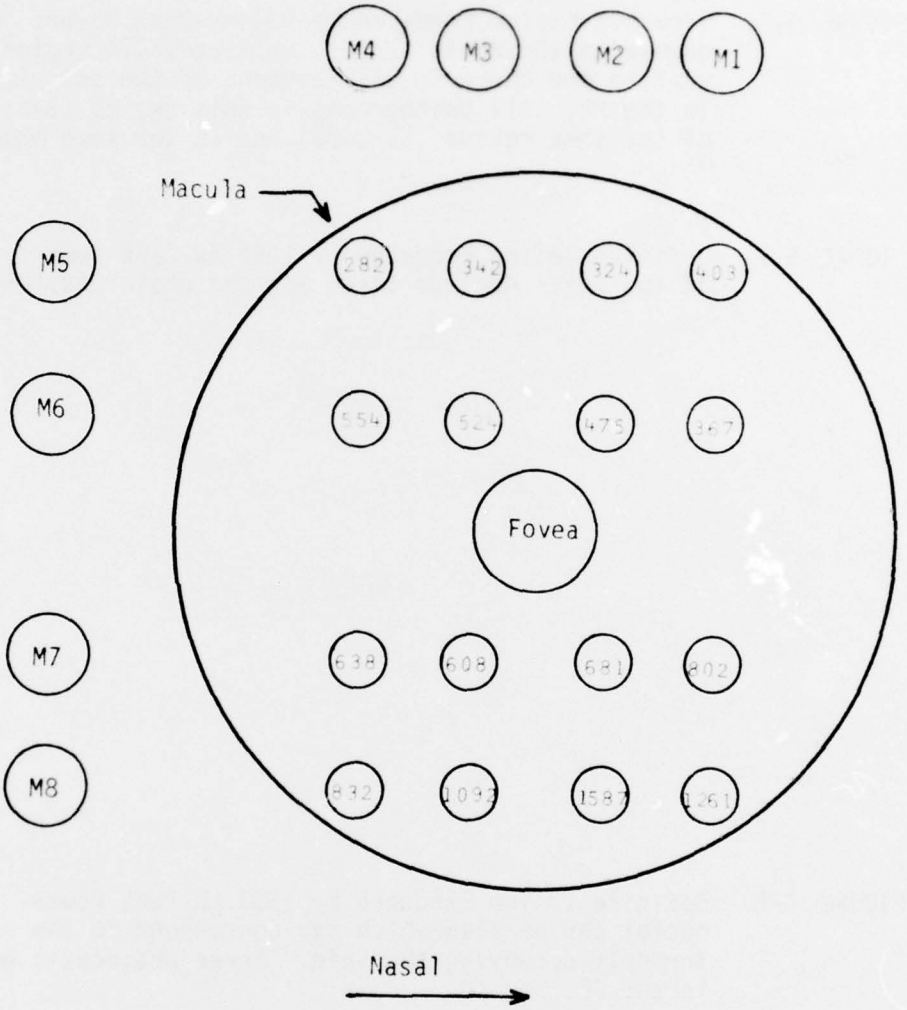

FIGURE 5-5. Diagram of Retinal Exposure Area in 511C OD. The locations of experimental and marker lesions (M) are approximate and not to scale. Experimental exposure sites are labeled with the peak pulse power applied to each site.

FIGURE 5-6. Probable Lesion Produced by 832 mW Peak Power. Only very minor damage to the PE is seen. The microvilli region shows some disruption and there is displacement of the spicules and granules in the PE. All photographs in this series (5-6 through 5-9) are of the same retina (511C OD) and at the same magnification.

FIGURE 5-7. Definite Lesion Produced by 1092 mW Peak Power. Disorganization of the outer nuclear layer and the photoreceptors is seen.

FIGURE 5-8. Definite Lesion Produced by 1587 mW Peak Power. Two pyknotic nuclei can be seen which may correspond to the photoreceptors formerly occupying the void. Three phagocytic bodies are seen in the PE.

FIGURE 5-9. Definite Lesion Produced by 1261 mW Peak Power. Disorganization of the outer nuclear layer and migration of nuclei into the outer segments is seen. The large, lightly shaded area in the PE appeared, when examined by EM, to be a lipid droplet.

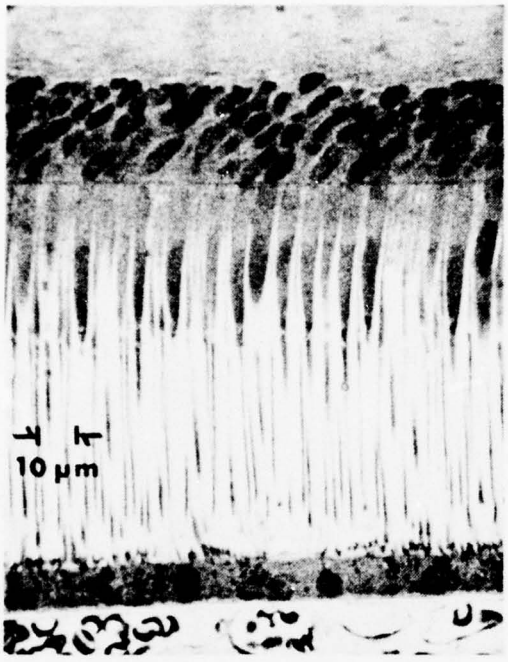

FIGURE 5-6

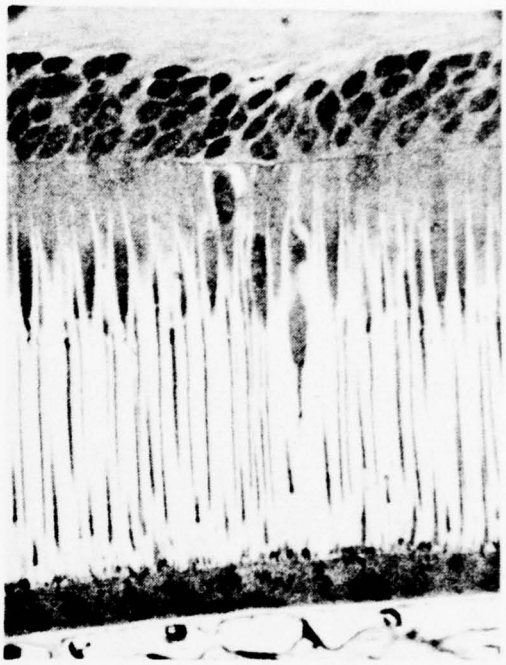

FIGURE 5-7

FIGURE 5-8

FIGURE 5-9

D. ELECTRON MICROSCOPY

The electron microscopy reported here should not be considered as a substitute for histopathology, but rather an extremely powerful adjunct. Light microscopy must be used to identify exposure sites with respect to distances from established landmarks. Correlation of light microscopy at appropriate magnification with electron microscopy of adjacent (thin) tissue sections provides the combination of microscopic techniques required to examine exposure sites for subtle, laser-induced morphological changes of retinal fine structure.

The efforts of this project centered primarily on EM examination of specimen 511C OD. The most prominant experimental lesions (sites 1092, 1587 and 1261, Figure 5-5) together with three marker lesions in the same eye and lesion areas selected from among previously prepared tissue blocks were examined at the ultrastructural level. Figures 5-10 through 5-18 were selected as representative of the nearly 400 electron micrographs taken during the course of this study.

Initial attempts at electron microscopy quickly revealed that the task of locating small, near-threshold lesions is at best tedious and, in most cases, impossible without correlated light microscopy of the suspected sites. Consequently, only tissue areas having experimental lesions previously identified by light microscopy were examined by EM. Several additional suspect lesion sites were also located by EM. However, in the absence of well-defined markers within the macula, distance mapping could not be carried out. Consequently, none of these areas could be assigned to laser exposure sites with any degree of confidence.

Observation of retinal lesions at the EM level led to the following general conclusions regarding the ultrastructure of these areas:

1) The spindle-like pigment granules (i.e., spicules) located in the apical pigment epithelial villi are generally absent in the lesion areas. The villi themselves appear little affected. Also, electron-dense pigment granules are absent from the basal components of the apical villi (see Figure 5-10, -11, -13).

2) Rod outer segments (ROS) in the vicinity of the microvilli are generally atypical or totally absent at lesion epicenters. This effect is more pronounced in the case of the higher power exposures, especially at the sites of marker lesions. Figures 5-11 and 5-12 illustrate ROS disruption typically seen in such damaged areas. In addition, the normal association between ROS and PE is disrupted (Figures 5-10 and 5-11).

3) Some cells of the PE in the area of the lesion show accumulations of what appear to be lipid droplets. The experimental exposure sites appear to contain distinctly more of these droplets than do the marker sites. (Compare Figure 5-13 with Figure 5-11). No determination can be made at this time as to whether the lower droplet count at the marker lesion sites is associated with the higher laser powers or is due to the fact that the

FIGURE 5-10. Longitudinal Section through the Pigment Epithelium (subject 511C, OD). The presence of microvilli with no pigment granules and the scarcity of round or ovoid pigment granules are typical of lesion sites (X 14,900, neg. no. 76-521).

FIGURE 5-11. Longitudinal Section through the Pigment Epithelium (subject 511C, OD). This disorganization was often seen as a result of high energy inputs (marker lesions). The PE is disorganized as are the microvilli and rod outer segments. Some scattered "lipid" droplets are noted just above the basal infoldings, which are themselves exaggerated and distorted (X 10,650, neg. no. 76-501.)

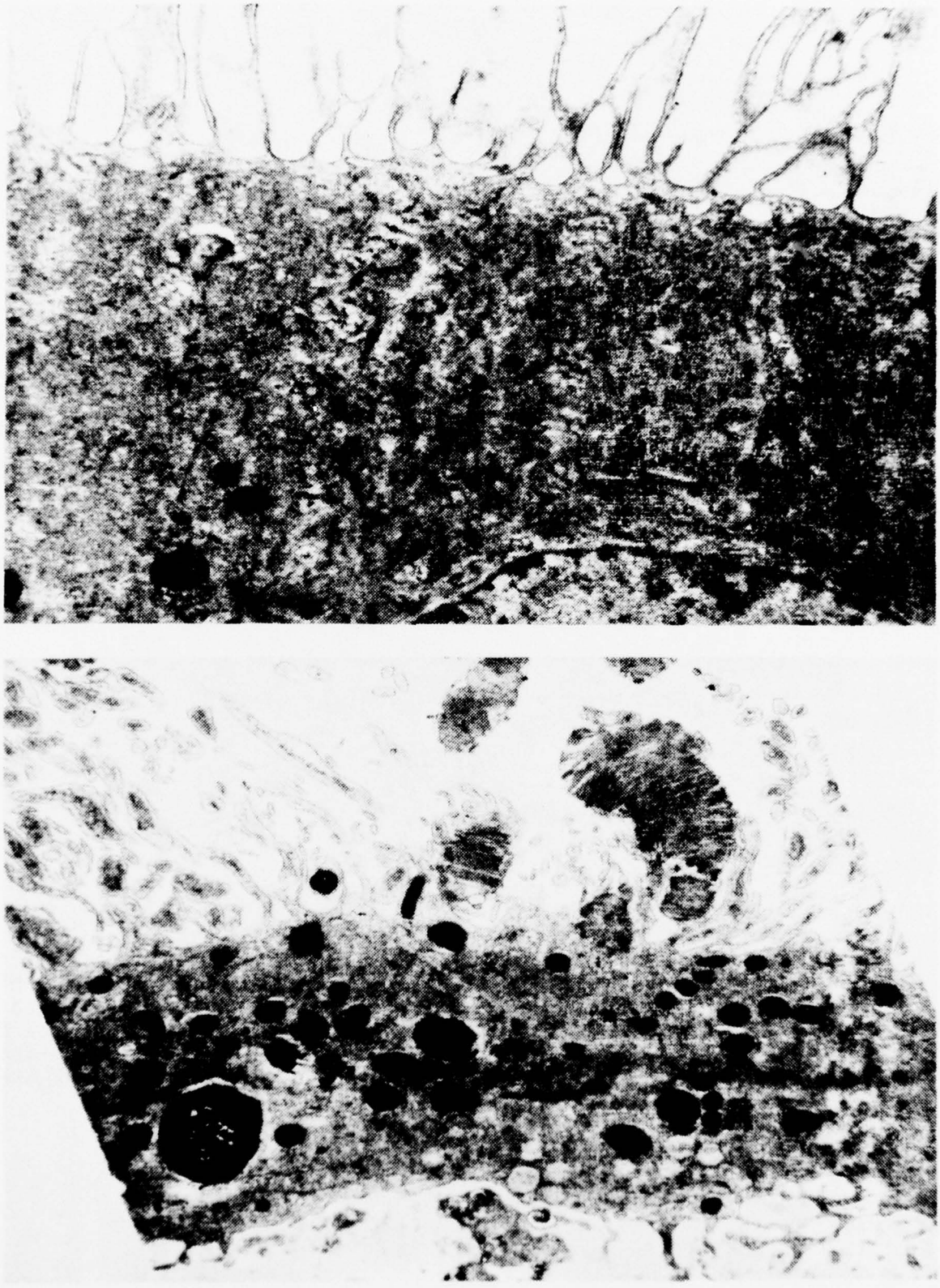

FIGURE 5-12. Longitudinal Section Through a Rod Outer Segment (subject 158B, OD). Section taken from the periphery of a 550 μm diameter, supra-threshold thermal lesion (300 mW, 500 msec exposure at 647.1 nm). Lamellar disorganization of this type is often encountered in lesion areas (X 26,500, neg. no. 76-210).

FIGURE 5-13. Longitudinal Section Through the Pigment Epithelium (subject 511C, OD). The microvilli are shown to the left while Bruch's membrane is seen to the right. The regular, sharply defined ovoid bodies are tentatively identified as lipid droplets. The area is adjacent to a known lesion site. Also note the absence of apical pigment granules in the PE microvilli (X 12,000, neg. no. 76-514).

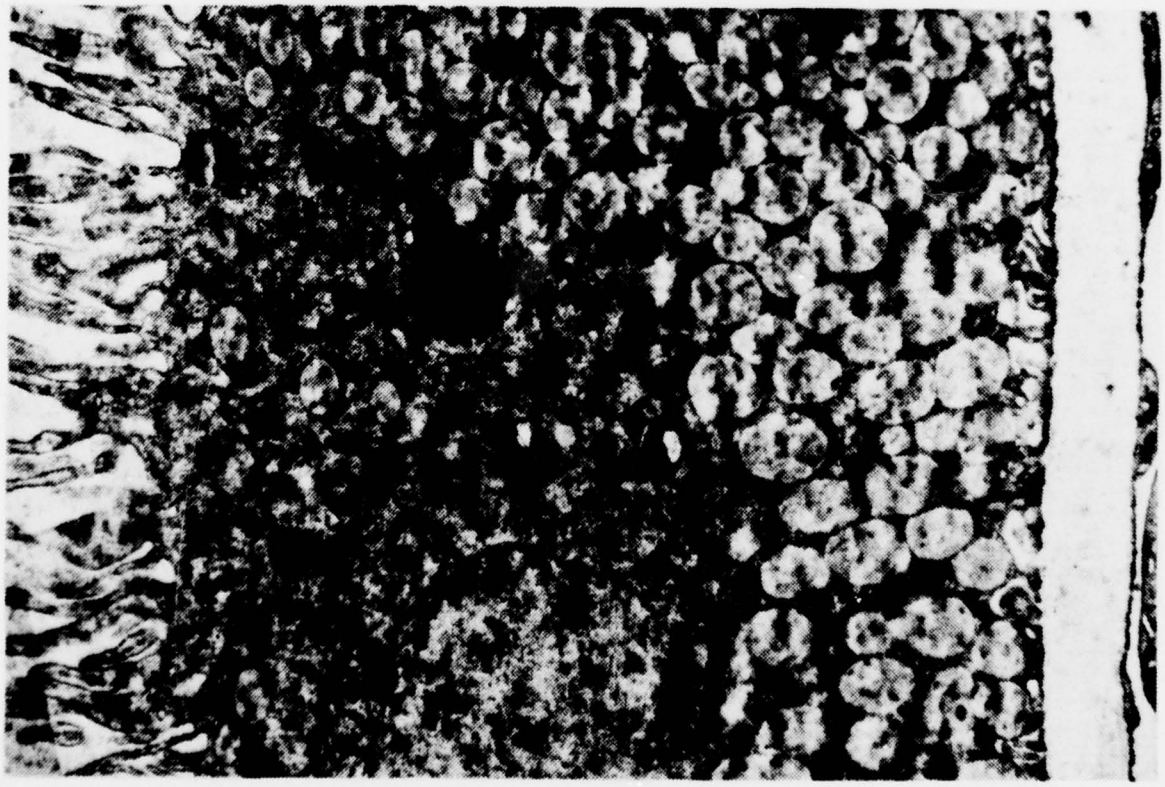

markers are in the paramacular region while the experimental exposure sites are in the macula. The rather preliminary data suggest that the droplets tend to be displaced toward the basal side of the pigment epithelium at experimental sites whereas the marker sites demonstrate a more disperse droplet population. Droplets are rarely encountered more than a few tens of μm removed from lesion sites, which is taken as confirmation that they are directly associated with the laser exposure. However, it must be pointed out that identification of these bodies as lipid is tentative and is based solely on fine structure morphology. Histochemistry must be performed to confirm this assignment.

4) In general, the morphology of the pigment epithelium is disturbed at lesion sites. Neither mitochondria nor other membrane-bound organelle components appear as frequently as in normal tissue. Cytoplasmic pigment components and autophagic components are irregular in their distribution and at times tend to cluster together, especially in cells located toward the edges of the lesions. (Figures 5-10, -11, -13, -14).

5) The relationships of the basal PE to Bruch's membrane and to the choriocapillaris appear to be highly disturbed at marker lesion sites, as illustrated in Figure 5-14. Figure 5-15 shows a pigment-like packet completely enclosed in a thickened Bruch's membrane. These pigment packets resemble elements also seen in normal choroid. Frequently, small cytoplasmic bodies are seen next to the basal infolds of the pigment epithelium (Figure 5-14). This association suggests that these bodies might be extrusions of the pigment epithelium. Experimental lesion sites, in contrast, generally show the pigment epithelium and the choroid with near-normal associations.

6) The most dramatic element that marks readily identifiable lesion sites is the absence, at lesion epicenters, of the inner and outer segments of the photoreceptors. However, this effect is also observable at the lower magnifications accessible with light microscopy (Figure 5-8). The void appears to be filled with a uniformly granular substance together with some membranous debris. This appears to be characteristic of older (~6 months post-exposure), high power lesions. In addition, at the outer limiting membrane, EM reveals that microvilli from the Müller cells may be seen extending into the void.

7) The outer nuclear layer vitread to the void epicenter often demonstrates numerous irregularities. At six months post-exposure some pyknotic nuclei are seen in this lesion area (Figure 5-16). Also, there tend to be fewer than normal nuclei in the outer nuclear layer at lesion sites, resulting in greater internuclear spacings. As a consequence, Müller cell cytoplasm may expand to fill the space left by the destroyed photoreceptor nuclei. This Müller cell cytoplasm often demonstrates elaborate arrays of endoplasmic reticulum which are clearly visible in Figure 5-16.

FIGURE 5-14. Longitudinal Section Through the Pigment Epithelium (subject 511C, OD). Apical microvilli seen in the upper left have formed a secondary layer or infolding. Bruch's membrane is seen in the lower portion of the photograph. The PE adjacent to Bruch's membrane seems to have invaginated and extruded material into and possibly through Bruch's membrane. This area is within a marker lesion (X 14,980, neg. no. H1829).

FIGURE 5-15. Longitudinal Section Through Bruch's Membrane (subject 511C, OD). The membrane is thickened and enlarged and contains two packets, one of which apparently contains pigment. The other seems to contain the remains of a lamellar body of some other membrane-bound structure (X 31,400, neg. no. H1830).

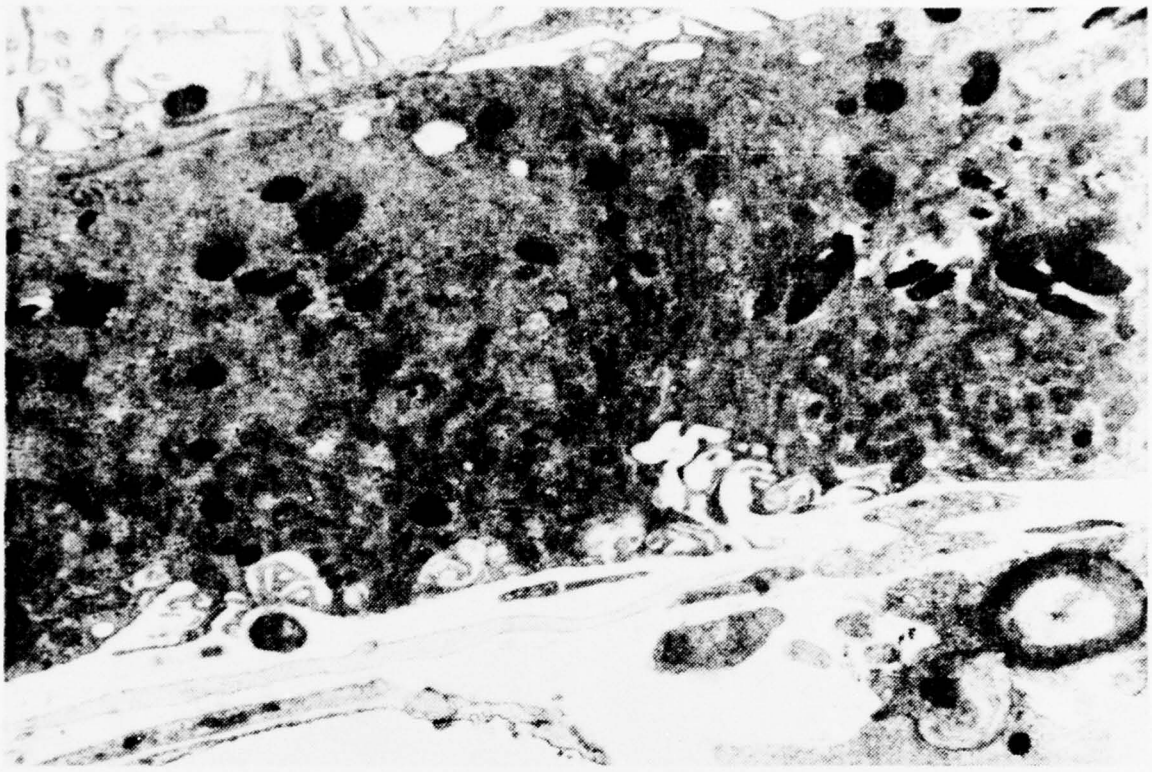

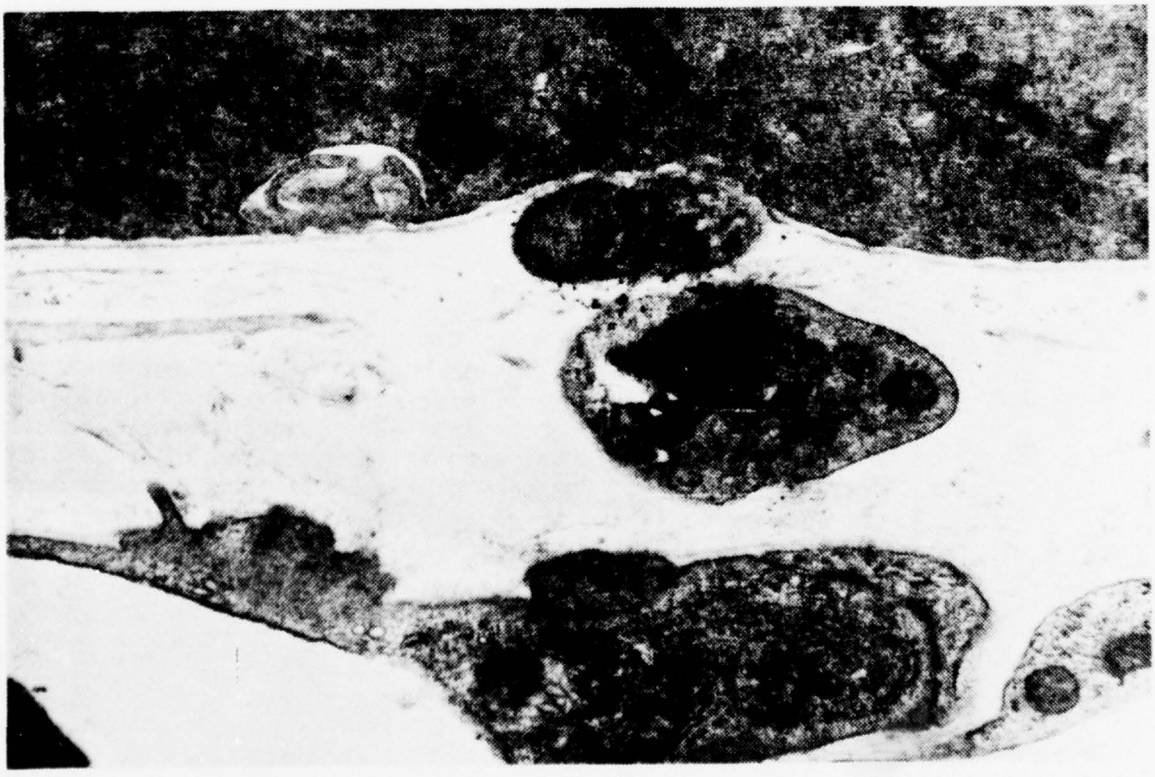

FIGURE 5-16. Longitudinal Section Showing Müller Cell Proliferation Around a Damaged Nucleus (subject 511C, OD). The abundance of Müller cell endoplasmic reticulum is apparently a response to space left by the loss of damaged or dead cells. A pyknotic nucleus is seen at the upper center of the micrograph (X 21,900, neg. no. H1838).

FIGURE 5-17. Longitudinal Section Showing Cross-section of Photoreceptor Axons Between the Outer Nuclear Layer and the Outer Plexiform Layer (subject 461C, OS). Three stages of axon morphology are shown. The overall lighter axons are interpreted as normal. The darker bodies are believed to represent an intermediate stage of necrosis. The very dark axon is thought to be necrotic and may be linked to an injured or destroyed photoreceptor. This area is approximately 150 μm lateral to a lesion site in the outer nuclear layer. (X 23,400, neg. no. 76-463).

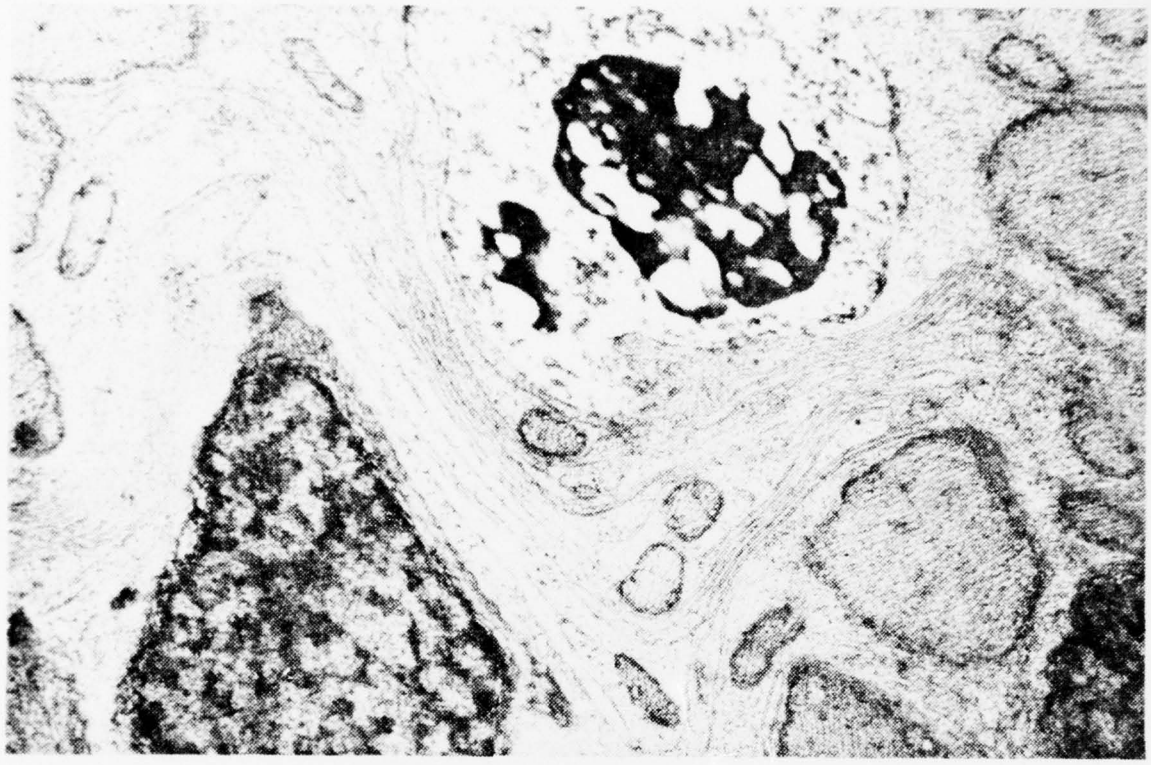

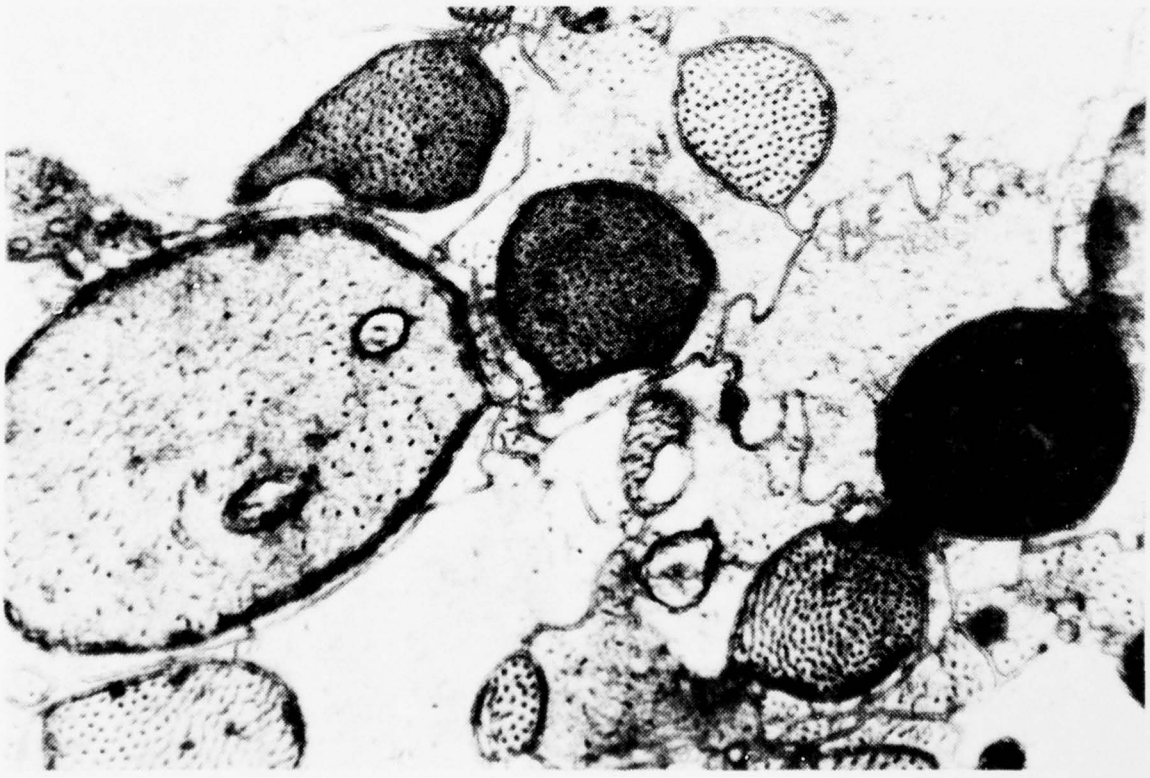

8) At normal as well as laser-exposed retinal sites, the peripheral axons of photoreceptors are oriented at approximately right angles to the optic axis on the vitread side of the outer nuclear layer and extend ∿100-200 μm to the outer plexiform layer. This lateral displacement causes difficulty in tracing lesion effects in this region. However, gaps in axon bundles were in some instances observed vitread and lateral to the PE lesion site. These gaps presumably correlate with missing axons that were originally connected to photoreceptors destroyed by laser irradiation. In addition, electron-dense axons were occasionally noted in the vicinity of the lesion (Figure 5-17). Such axons are interpreted as damaged or necrotic; and may reflect a response to direct injury or to damage or destruction of their associated photoreceptors.

9) Structures similar to that shown in Figure 5-18 were occasionally encountered at the outer plexiform layer, some 200-300 μm from the edge of a lesion. This structure probably represents a collected mass of necrotic cone pedicles and rod spherules. On occasion, patches of missing pre-synaptic termini were also detected laterally in the outer plexiform layer.

Some further comments on electron microscopy of specimen 511C, OD appear to be warranted. This eye had received 16 experimental laser exposures (Figure 5-5) of which all but 5 showed lesions at one hour, eight days and two weeks post-exposure. After six months, only six of the eleven lesions were ophthalmoscopically observable. Four of these, viz., those induced by the highest peak powers, could be located and confirmed by light microscopy but the other lesions could not be seen at this level of examination. However, using EM, several additional areas which may have been laser exposure sites were detected.

Ultrastructural anomalies observed in these suspect areas included the following:

1) Apical pigment was absent from the PE over a lateral region of 10-15 μm and occasionally as much as ∿30 μm;
2) Lipid droplets seemed to be concentrated in the PE within a lateral distance of one or two cells (15-30 μm) of the depigmented area;
3) Occasionally, the photoreceptor inner segments showed more than the usual intercellular spacing at the outer limiting membrane at sites usually coincident with the phenomena noted above.

It is conceivable that relatively low peak power exposures (i.e., near-threshold) may cause the destruction or damage of only a few photo-receptors. This degree of damage would be difficult to detect at six months post-exposure due to apparent expansion of adjacent cells to fill the void left by the destroyed cells.

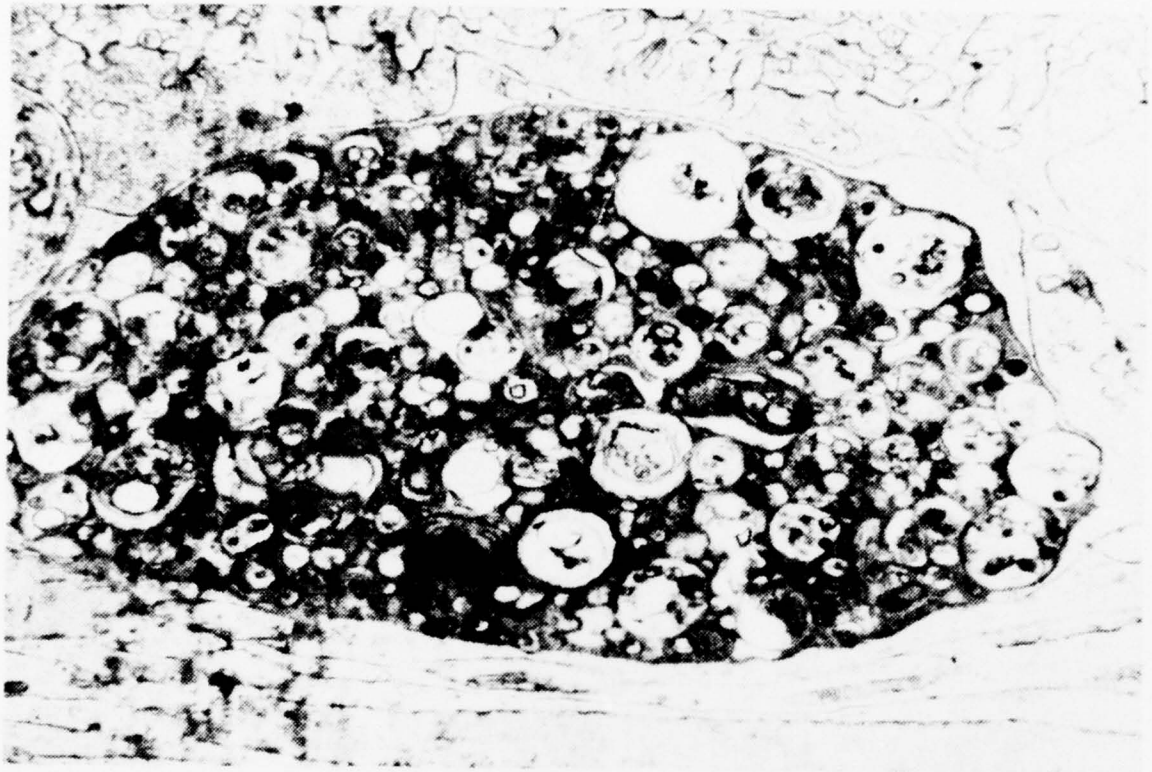

FIGURE 5-18. Longitudinal Section Showing Phagocytized Material Vitread to the Outer Plexiform Layer (subject 511C, OD). This material may be debris of damaged or destroyed cells or organelles including cone pedicles and rod spherules. The structure is ~250 μm lateral to a lesion site (X 11,050, neg. no. 76-532).

E. CONCLUSIONS

As expected, electron microscopy revealed in greater detail morphology observed at the light microscopy level. Ultrastructural studies revealed the formation of lipid droplets presumably resulting from laser exposures or in conjunction with long-term repair processes following laser exposures. Elaboration of Müller cell endoplasmic reticulum was observed in the outer nuclear layer at some lesion sites. The results discussed above indicate that most of the damage observed at six months post-exposure is in the photoreceptors (outer and inner segments) and in the outer nuclear layer. At the higher exposure levels, there is evidence of some damage to the PE but the extent appears minor.

The 1-hour threshold for retinal damage in 511C OD was found to be ~440 mW (peak pulse power), in good agreement with the ED_{50} value of ~420 mW determined by probit analysis using a sample of six eyes, each with 16 exposure sites[4]. In contrast, a 24-hour damage criterion gave an ED_{50} of ~210 mW[4]. Examinations of 511C OD at 8 days and two weeks post-exposure showed no lesions other than those seen at 1 hour. At six months post-exposure, only those retinal sites exposed to peak powers ≥830 mW (i.e., about twice the 1-hour ED_{50}) were clearly visible at the ophthalmoscopic level. Similarly, examination of this same eye by light and electron microscopy revealed clear evidence of damage only for peak powers higher than 830 mW but not at sites exposed to lower powers. Thus, it appears that some degree of repair may have occurred in this retina over the six-month interval between exposure and sacrifice.

REFERENCES

1. Luna, L.G., ed., "Manual of Histologic Staining Methods of the Armed Forces Institute of Pathology", Third Edition, McGraw-Hill, New York, 1968.

2. Sanders, V.E. and J.A. Zuclich, "Research on the Ocular Effects of Laser Radiation," Technology Incorporated, First Annual Report, Contract F41609-73-C-0017, USAF School of Aerospace Medicine, February 1974.

3. Connolly, J.S., et al., ibid, Second Annual Report, February 1975.

4. Connolly, J.S., H.W. Hemstreet, Jr., and D.E. Egbert, "Ocular Hazards of Picosecond and Repetitive Pulse Lasers. Volume II: Argon-Ion Laser (514.5 nm)". Technology Incorporated, Final Report, Contract F41609-73-C-0016, USAF School of Aerospace Medicine, January 1977.

5. Luft, J., "Improvements in Epoxy Resin Embedding Methods", J. Biophys. Biochem. Cytol. 9:409, 1961.

6. Mollenhauer, H.H., "Plastic Embedding Mixtures for Use in Electron Microscopy", Stain Tech. 39:111, 1964.

7. Spurr, A.R., "A Low-viscosity Epoxy Resin Embedding Medium for Electron Microscopy", J. Ultrastructure Res. 26:31, 1969.

PART II

OCULAR EFFECTS OF ULTRAVIOLET LASER RADIATION

CHAPTER 6

BACKGROUND

Joseph A. Zuclich

In the past several years, numerous ultraviolet lasers possessing a wide variety of beam parameters have become commerically available. These include continuous wave (cw) lasers such as argon- and krypton-ion lasers, short pulsewidth, high power units such as nitrogen gas lasers and various solid state and tunable dye lasers which, with frequency doubling, yield wavelengths as short as 250 nm. Existing safety standards[1,2] have not anticipated the wide ranges of beam parameters available with these lasers. The suggested standards for far-UV radiation (200-300 nm) are based, in part, on corneal threshold studies with non-coherent radiation sources[3,4] and thus have some experimental basis. In the near-UV (300-400 nm) range, however, there is a paucity of experimental threshold data even for non-coherent sources and the safety standards appear to be based on the assumption that any corneal damage would be thermal in nature. Permissible exposure levels for the near-UV are quoted only for the cornea and then only for single pulse exposures, with the quoted maximum permissible exposure (MPE) applying to any wavelength in the range of 315-400 nm[1,2].

Recently, several papers have appeared on ocular damage induced by near-UV radiation. Ebbers and Sears[5] reported on corneal damage induced in the rhesus eye by the 325 nm output of a helium-cadmium laser. They, as well as MacKeen, et al.[6], also noted cataract formation induced by the helium-cadmium laser. Further, Zigman, et al.[7,8] have reported pathologies in the lenses and retinae of mice subjected to repeated exposures of non-coherent near-UV radiation. From these studies it is clear that in addition to corneal hazards, there are potential lenticular and retinal hazards from near-UV radiation. Little evidence is available regarding the mechanism for damage at each site and, thus, little experimental support exists for any safety standard which attempts to set MPE levels for wide ranges of beam parameters.

The UV segment of the electromagnetic spectrum is somewhat arbitrarily divided into three wavelength regions commonly referred to as the near-UV (300-400 nm), far-UV (200-300 nm) and vacuum-UV (4-200 nm). This investigation has dealt specifically with ocular hazards of near-UV radiation although many of the mechanistic considerations should apply equally well to the far-UV portion of the spectrum. Radiation in these wavelength regions is absorbed by chromophoric sites normally found in proteins and nucleic acids as well as by numerous minor constituents of the cell [9,10]. The absorbing chromophores belong to the class of aromatic molecules and are characterized by delocalization or sharing of electrons by several chemical bonds resulting in low-lying electronic energy levels.

The energy of a single photon in the near- or far-UV wavelength range is such that it can promote an electron of the absorbing aromatic chromophore to an excited energy level. The transient excited state of the absorbing molecule is highly labile and the molecule can subsequently engage in a number of chemical reactions with its molecular neighbors. The resulting photo-induced products may be incompatible with the normal functioning of the exposed system and may, in time, lead to some biological damage which is observable at the macroscopic level.

In an earlier report(11), the molecular composition and absorption properties of the components of the primate eye were discussed and potential damage sites from 200-400 nm radiation were pointed out. The formulation of a quantitative model for a photochemical damage mechanism was begun through a consideration of the electronic energy level schemes associated with aromatic molecules and the kinetics involved with UV-induced transitions between the energy levels. An approximate solution was presented for the number of photoproducts or "molecular lesions" formed as a function of the laser beam parameters. This solution was valid, however, only in the limit of long pulsewidths (i.e., microseconds or greater), where the differential equations for the populations of the electronic energy levels could be solved in the steady state approximation, and with radiation intensities sufficiently low that only a negligible fraction of the absorbing molecules were found in excited states at any given time.

Realizing that this approximate solution would not suffice for the entire spectrum of beam parameters associated with operational lasers, development of the theoretical model was continued and a general solution derived for a molecular electronic energy level scheme consisting of a ground state and excited singlet and triplet states(12). Numerical examples were presented to illustrate explicity the complicated dependence of photoproduct formation on the laser beam parameters(12).

Although the basic three level electronic energy level scheme is thought to be an adequate representation of the absorbing molecule, the exact formalism to be used for quantitative photochemical predictions in any given case will depend on:

(1) whether the formation of photoproducts proceeds through the excited singlet state, the excited triplet state or both;
(2) whether the final product is formed directly from one or both excited states or if there are intermediate steps (and hence additional transient species) involved:
(3) whether single or multiple-photon absorption processes are involved; and
(4) whether the absorbing species themselves are involved in the photochemical reactions or if there is energy transfer to other molecules which are then the reactive species.

The experimental program carried out concurrently with the theoretical modeling was designed, in part, to distinguish among these various possibilities. The material presented in Chapters 7 through 10 covers the

progress made towards identification of the primary sites and mechanisms of near-UV induced ocular damage. The results have already answered some of the questions posed above and have provided feedback for modifying and refining the theoretical model. In addition, the experiments and theoretical considerations reported here provide a basis for more comprehensive safety standards for the use of UV lasers. Although the detailed theoretical derivations[11,12] are not repeated here, the instances where the experimental results contribute to the model development are fully discussed in the following chapters.

REFERENCES

1. "American National Standard for the Safe Use of Lasers", American National Standards Institute, Inc., Standard Z136.1, 1973.

2. American National Standards Institute, Proposed laser safety standard, 1976.

3. Pitts, D.G., W. R. Bruce and T. J. Tredici, "A Comparative Study on the Effects of Ultraviolet Radiation on the Eye", SAM-TR-70-29, USAF School of Aerospace Medicine, Brooks AFB, Texas, 1970.

4. Pitts, D.G. and T. J. Tredici, "The Effects of Ultraviolet on the Eye", Amer. Ind. Hygiene Assoc. J. 32:235, 1971.

5. Ebbers, R.W. and D. Sears, "Ocular Effects of a 325 nm Ultraviolet Laser", Amer. J. Optom. and Physiol. Optics 52:216, 1975.

6. MacKeen, D., S. Fine and B. S. Fine, "Production of Cataracts in Rabbits with the Ultraviolet Laser", Ophthal. Res. 5:317, 1973.

7. Zigman, S., T. Yulo and J. Schultz, "Cataract Induction in Mice Exposed to Near-UV Light", Ophthal. Res. 6:259, 1974.

8. Zigman, S. and T. Vaughan, "Near-ultraviolet Light Effects on the Lenses and Retinas of Mice", Invest. Ophthalmol. 13:462, 1974.

9. "The Molecular Basis of Life: Readings from Scientific American", W. H. Freeman and Co., San Francisco, 1968.

10. Steiner, R.F., "The Chemical Foundations of Molecular Biology", D. van Nostrand Co., Princeton, 1965.

11. Zuclich, J.A., in "Research on the Ocular Effects of Laser Radiation", Technology Incorporated, First Annual Report, Part II, Contract F41609-73-C-0017, USAF School of Aerospace Medicine, February 1974.

12. Zuclich, J.A., et al., ibid., Second Annual Report, February 1975.

CHAPTER 7

CORNEAL DAMAGE INDUCED BY NEAR-UV LASER RADIATION

Joseph A. Zuclich

A. EARLY EXPERIMENTS

As previously reported[1] corneal damage induced by near-UV laser radiation appears to be the result of a photochemical damage mechanism. Initial experiments were carried out using a krypton-ion laser emitting at 350.7 and 356.4 nm (~3:1 intensity ratio). It was soon discovered that corneal epithelial lesions are induced in rhesus monkeys with incident energy doses of greater than 70 J/cm^2. Slit lamp examinations revealed that slightly supra-threshold lesions appear as well defined spots on the surface of the cornea. The spots have a fairly even texture when the exposure is 10% or more above threshold, but exposures closer to the threshold dose often yield a more "patchy" appearance. There does not appear to be any significant depth associated with threshold lesions. Exposures of 50% or more above threshold cause crater-like effects which apparently penetrate several cellular layers of the epithelium. No scarring of the corneal stroma was noted in any of the exposed animals.

The time following exposure before a corneal lesion becomes visible (with slit lamp observation) depends upon the energy dose delivered relative to the threshold dose. With doses as high as two to three times threshold, the first signs of lesion formation appear within one hour. After several hours, the lesions generally develop a crater-like appearance which may persist for ~24-48 hours. The crater-like lesions, however, do not penetrate below the epithelium and all signs of corneal damage disappear by 48-72 hours post exposure.

With doses closer to threshold, no signs of abnormality are observed in the first 6-8 hours following exposure. The lesions which eventually appear do not reach maximum development until 12-24 hours post exposure and, again, appear to repair within 48-72 hours. Based upon these observations, an 18 hour criterion was established for the determination of corneal lesion formation in threshold studies.

Using the krypton-ion laser (350.7 and 356.4 nm), corneal threshold determinations were carried out for continuous exposures (i.e., single pulses) of 18, 30 and 45 seconds. The exposure energy required to induce corneal lesions was approximately 70 J/cm^2 in each instance. This reciprocity is predicted by a photochemical model[1,2] but is not consistent with expectations for a purely thermal damage mechanism. Thermal model calculations using a version of the IITRI program[3] indicate that irradiated corneal tissue would reach a virtual thermal equilibrium state

after several seconds of continuous irradiation. The predicted peak temperature is directly proportional to the intensity of the radiation source. Thus, the peak temperature increase resulting from the threshold dose of 66 J/cm^2 for 45 sec exposures to 350 nm radiation would be $\sim 8^0$C, whereas that for the threshold dose of 72 J/cm^2 for 18 sec exposures would be $\sim 24^0$C.

Using the results summarized above as a starting point, additional experiments were carried out to: (1) provide further evidence that the observed corneal damage is indeed the result of a photochemical damage mechanism; (2) gain some insight into the molecular nature of the damage mechanism; (3) provide input for further theoretical modeling, especially with regard to wavelength dependence and molecular rate constants required to make quantitative predictions; (4) identify conditions where mechanisms other than photochemical appear to contribute to the observed damage, or where ocular tissues other than the cornea have the greatest sensitivity to UV radiation, thereby establishing limits on the ranges of beam parameters for which any theoretical photochemical model can be reliably used for predictive purpose; and (5) point out instances where existing laser safety standards for the use of UV lasers[4,5] do not appear to provide an adequate margin of safety.

B. EXPERIMENTAL METHODS

The subjects used in these experiments were rhesus monkeys (Macaca mulatta) generally ranging in age from two to three years and in weight from two to four kilograms. The animals were maintained and the experiments conducted in accordance with procedures outlined in the "Guide for Laboratory Animal Facilities and Care", National Academy of Sciences - National Research Council. The pupils were dilated with a topical application of atropine (1% atropine sulfate) administered up to 24 hours prior to exposure. The animals were pre-anesthetized with an intramuscular injection (0.1 cc per kilogram weight) of ketamine hydrochloride (100 mg/ml) and anesthetized with an intravenous injection (0.5-1.00 cc per kilogram) of sodium pentobarbital (50 mg/ml). During exposure and observation the eyelids were held open by a wire speculum. Corneal drying was prevented by periodic irrigation with normal saline. Observations of the corneas and lenses of the subjects were made with a Nikon "Zoom-Photo" slit lamp microscope. Retinal examinations were carried out with a Zeiss fundus camera.

Ultraviolet laser sources used were as follows: Spectra Physics 164-01 krypton-ion laser with cw output simultaneously at 350.7 and 356.4 nm ($\sim$3:1 intensity ratio) and a maximum UV output of $\sim$100 mW; Coherent Radiation 500K krypton-ion laser emitting at the same wavelengths but with a maximum UV output of only $\sim$50 mW; Spectra Physics 170 argon-ion laser with cw output simultaneously at 351.1 and 363.8 nm ($\sim$1:1 intensity ratio) and a maximum UV output of $\sim$1 W; Molectron UV-1000 nitrogen laser emitting at 337.1 nm with a nominal 10 nsec pulsewidth, pulse repetition rate variable to 50 Hz and a peak power of $\sim$1 megawatt.

A schematic diagram for the krypton and argon laser experiments is shown in Figure 7-1. The arrangement for the nitrogen laser experiments was similar but involved focusing of the beam with a quartz lens as discussed below. The subjects were positioned with the aid of a Spectra Physics 155 helium-neon (~0.5 mW) alignment laser arranged so that the beam, after reflection off a beamsplitter, was colinear with the UV laser beam. Intensity profiles were measured with a beam scan apparatus consisting of an EG&G-SGD100A photodiode mounted on a micrometer translation stage driven by a synchronous motor. Spatial resolution of the scans was limited by a 50 μm diameter aperture attached directly to the front face of the photodiode. The voltage output of the photodiode was traced on an X-Y recorder. A typical beam scan obtained in this way is shown in Figure 7-2, the profile being essentially Gaussian in spatial distribution.

The corneal spot size is defined as the beam diameter at the $1/e^2$ points as measured at the appropriate distance from the output mirror of the laser. Usually, a single pulse or train of pulses was delivered to the center of each cornea. Determination of corneal or lenticular lesion formation was made by slit lamp observation at ~18 hours post-exposure.

The power output of the krypton and argon lasers was controlled by varying the current through the plasma tube. Power measurements were made with a Scientech 3600 laser power meter, the output of which was coupled to a Keithley 149 milli-microvoltmeter. The power meter and voltmeter were calibrated as a unit every three months using sources and procedures traceable to NBS standards. Power measurements taken immediately before and after each animal exposure, were usually identical and were averaged. The duration of the exposures was controlled with an electronically triggered mechanical shutter. When required, trains of pulses were generated by triggering the shutter at the desired frequency or, for pulsewidths shorter than one second, by interposing a mechanical chopping wheel between the laser and the subject. In the latter case, the pulsewidth was monitored during the exposure by reflecting ~10% of the chopped beam from the beamsplitter onto a photodiode whose output was coupled to a Monsanto 101C or Systron-Donner 7034 counter/timer. The slots and spokes of the chopping wheel were of equal width so that all pulse train exposures were at 50% duty cycle.

The procedure for monitoring the output of the nitrogen laser was complicated by the short (<10 nsec) pulsewidth and asymmetric beam profile. The beam of the nitrogen laser had dimensions of 6x25 mm at the output aperture of the laser, necessitating the use of a quartz lens (250 mm focal length) to focus the beam at the surface of the cornea of each subject. This is shown in schematic form in Figure 7-3. Intensity profiles were measured in the focal plane using the beam scan apparatus described above. This was accomplished by pulsing the nitrogen laser at 10Hz, monitoring the photodiode output with a fast oscilloscope and recording the relative intensity at 25 or 50 μm intervals of translation.

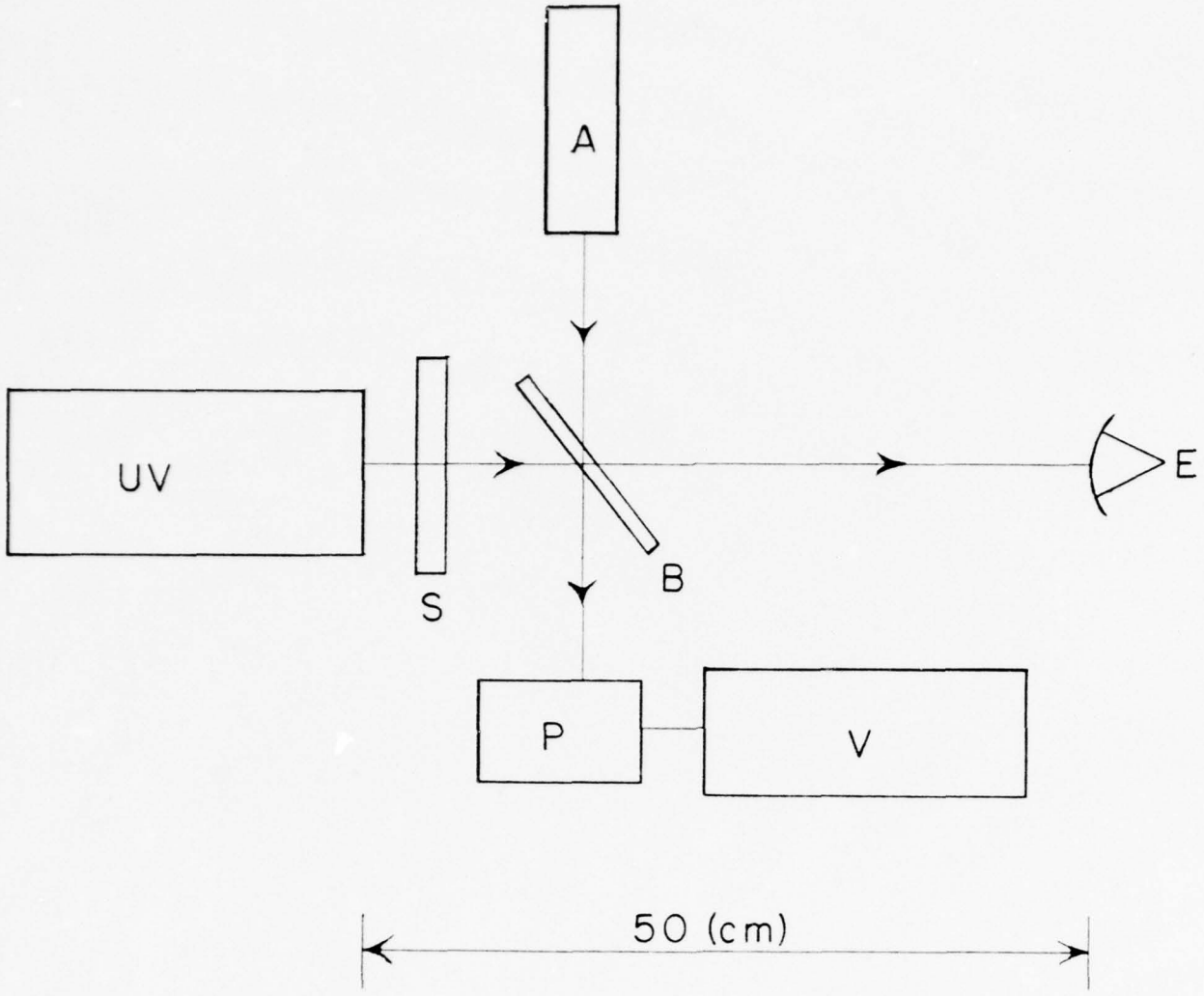

FIGURE 7-1. Block Diagram of Laser Apparatus for Corneal and Lenticular Irradiations. UV-ultraviolet laser source; A-alignment laser; S-shutter; B-beamsplitter; P-laser power meter; V-millimicro-voltmeter; E-subject eye.

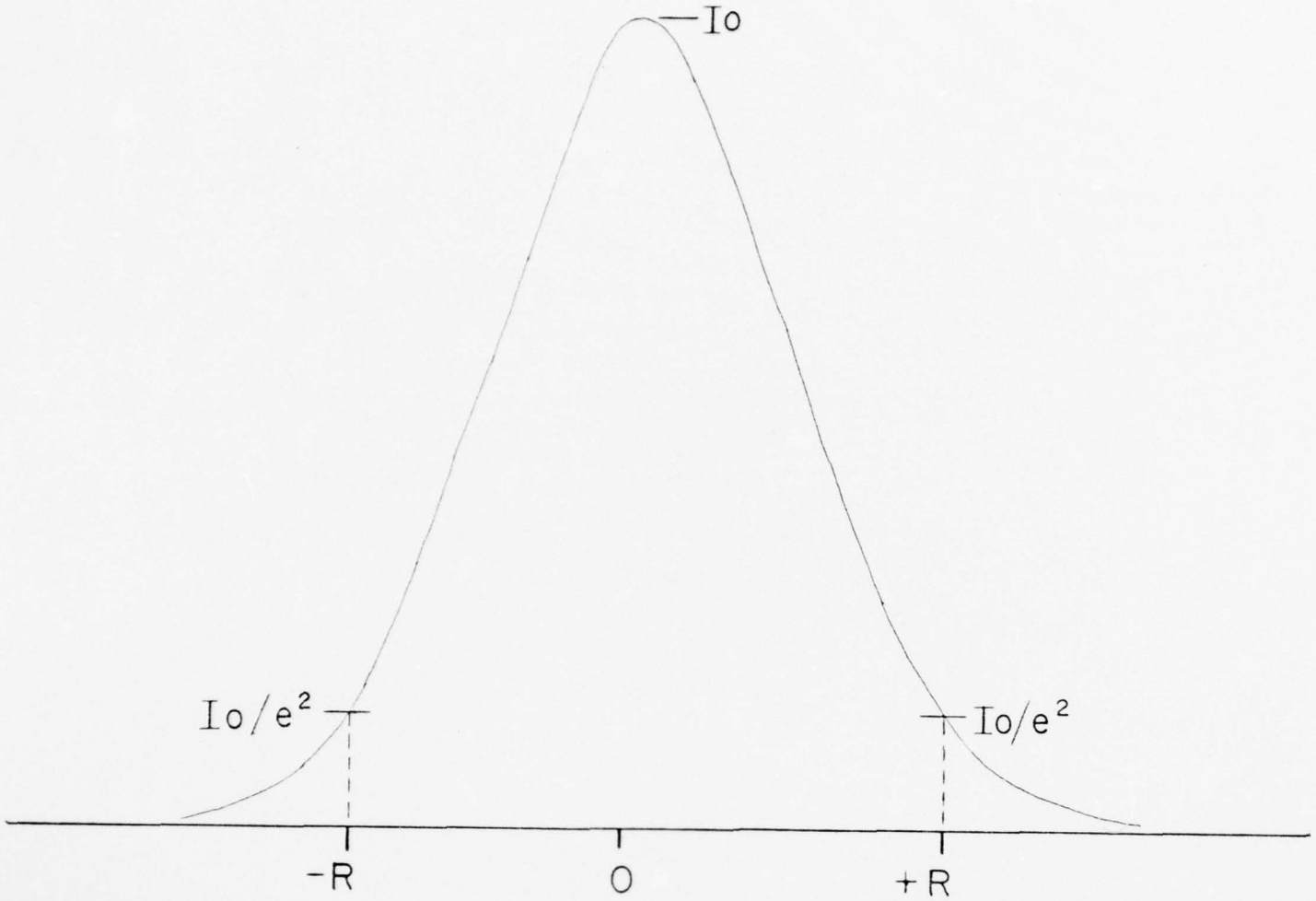

FIGURE 7-2. Horizontal Beam Scan of Near-UV Emission of Krypton Laser. I_0-intensity of beam at center of distribution; 2R-diameter of beam at $1/e^2$ points.

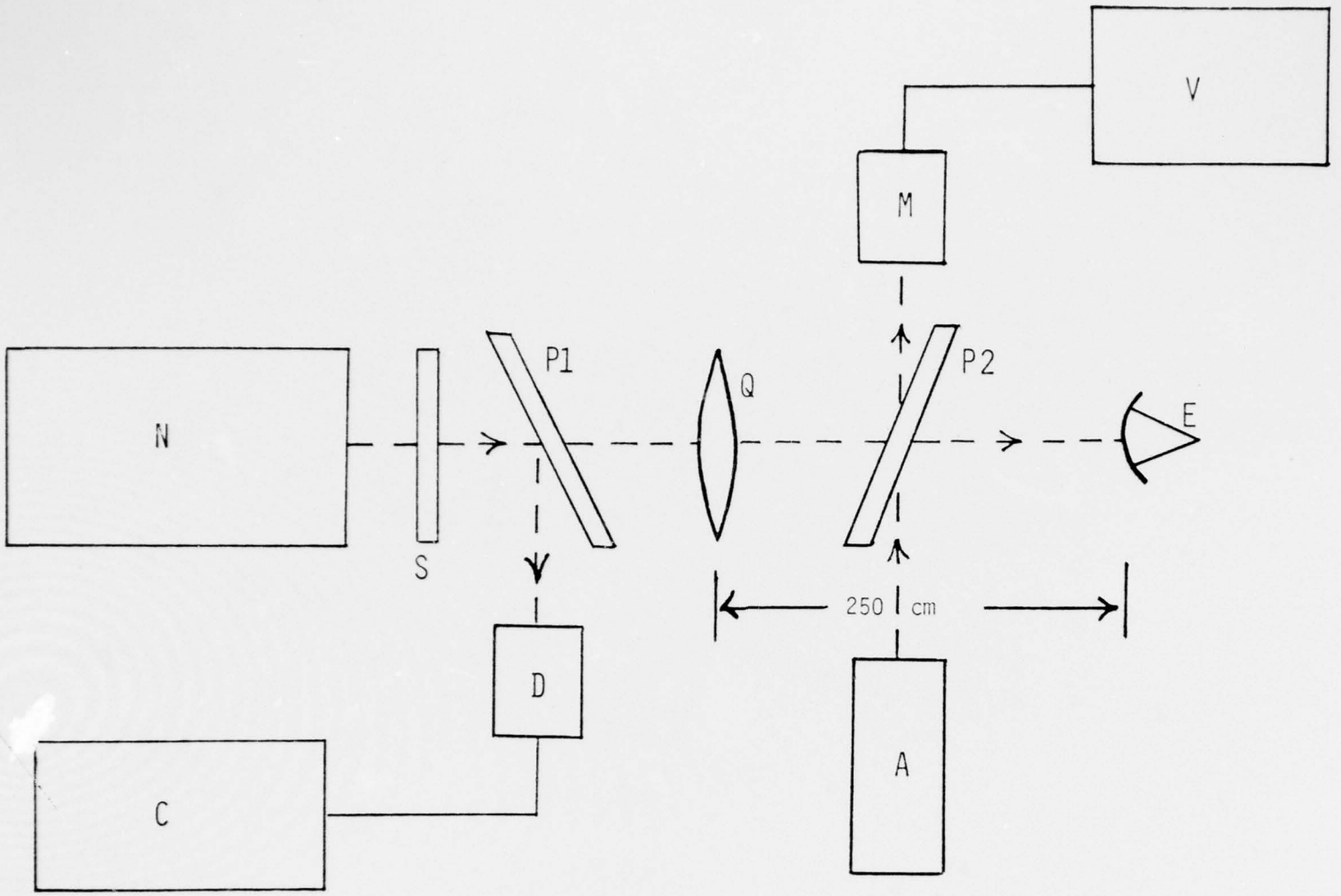

FIGURE 7-3. Experimental Apparatus for Nitrogen Laser Study. N-nitrogen laser; C-counter/timer; S-shutter; D-photodiode; Q-quartz lens; M-laser power meter; V-microvoltmeter; A-alignment laser; P1,P2-pellicles; E-subject eye.

Figure 7-4 illustrates a horizontal beam scan obtained in this manner. It is seen that although the overall beam diameter was ∿2.5 mm, the scan reveals two lobes with a deep trough between. Thus, the cross-sectional profile was composed of two elliptically shaped lobes and corneal doses were averaged over both lobes. Beam scans in the vertical direction through the peak of each lobe are shown in Figure 7-5.

For purposes of defining a corneal spot size, the axial lengths of each ellipse were taken as the $1/e^2$ points of each lobe of Figure 7-4, and the respective vertical scans of Figure 7-5. The areas of the two ellipses were 3×10^{-3} cm^2 and 2×10^{-3} cm^2 (corresponding to the left and right hand lobes of Figure 7-4 respectively). This yields an effective corneal spot size of 5×10^{-3} cm^2.

The pulsewidth and peak power output of the nitrogen laser were essentially constant for all runs. The pulsewidth, as measured with a Spectra Physics 403 high-speed light detector coupled to a Hewlett Packard 184A oscilloscope, was ∿5 nsec at half maximum and ∿10 nsec at the base. For experiments reported here the pulse repetition frequency was fixed at 10 Hz. Threshold data were generated by varying the pulse train length, i.e., the number of pulses delivered to each eye. The average power output of the laser at 10 Hz repetition rate was measured with a calibrated laser power meter, as described above. The number of pulses delivered to the cornea was determined by a photodiode coupled to a counter/timer.

In order to facilitate experiments involving long exposure times (10^3 and 10^4 sec), the optical path of the Coherent Radiation CR-500K krypton-ion laser beam was arranged so that four eyes (two rhesus subjects) could be exposed simultaneously. A schematic diagram of the setup is shown in Figure 7-6. A series of four pellicles (2-8 μm in thickness) deflected a fraction of the beam onto the cornea of each subject eye. The two subjects were positioned so that the optical pathlengths from the laser head to the respective corneal planes were equal. Therefore, equal laser spot sizes (∿1.9 mm diameter) were obtained at each cornea. Despite the invisibility of the UV laser beam, the specific area of the cornea being irradiated was readily identified by the "spot" of visible scattered light emanating from the corneal surface. If the subject eye drifted during the exposure so that a change in the position of the irradiated "spot" relative to the pupil was detected, the data from that eye were discarded.

The intensities of the beam deflected by each of the four pellicles were measured before and after each exposure with a Scientech 3600 laser power meter, the output of which was coupled to a Keithley 150B microvolt/ammeter. During the exposures, the power output of the laser was continuously monitored by measuring the intensity of the beam transmitted through the entire pellicle train using a photodiode connected to a strip-chart recorder. In this way, the calculated energy doses delivered to each cornea could be corrected for any changes in the laser output during the exposures. However, such power drifts were negligible for all experiments reported here.

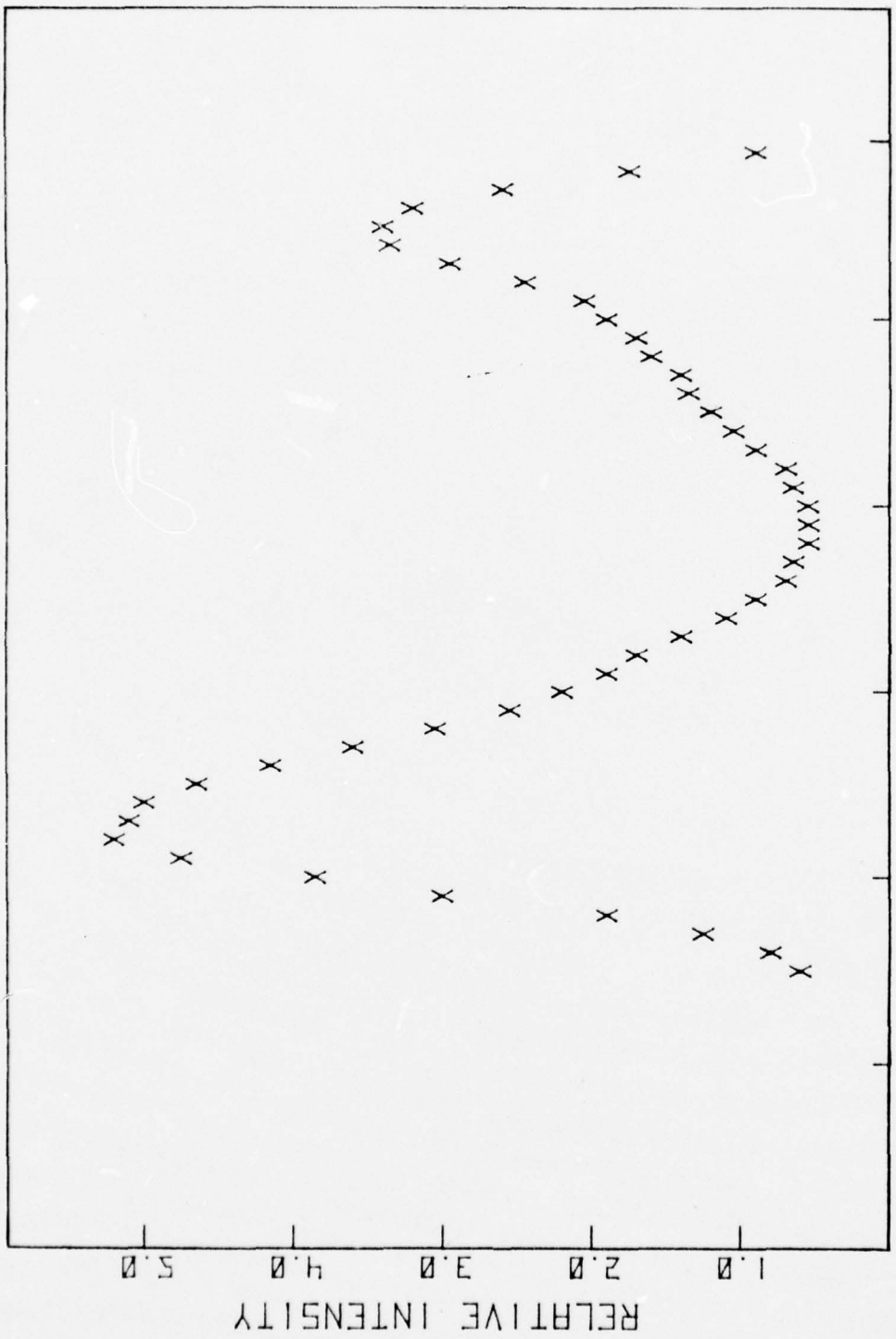

FIGURE 7-4. Beam Scan of Focused Output of Nitrogen Laser; Horizontal Direction.

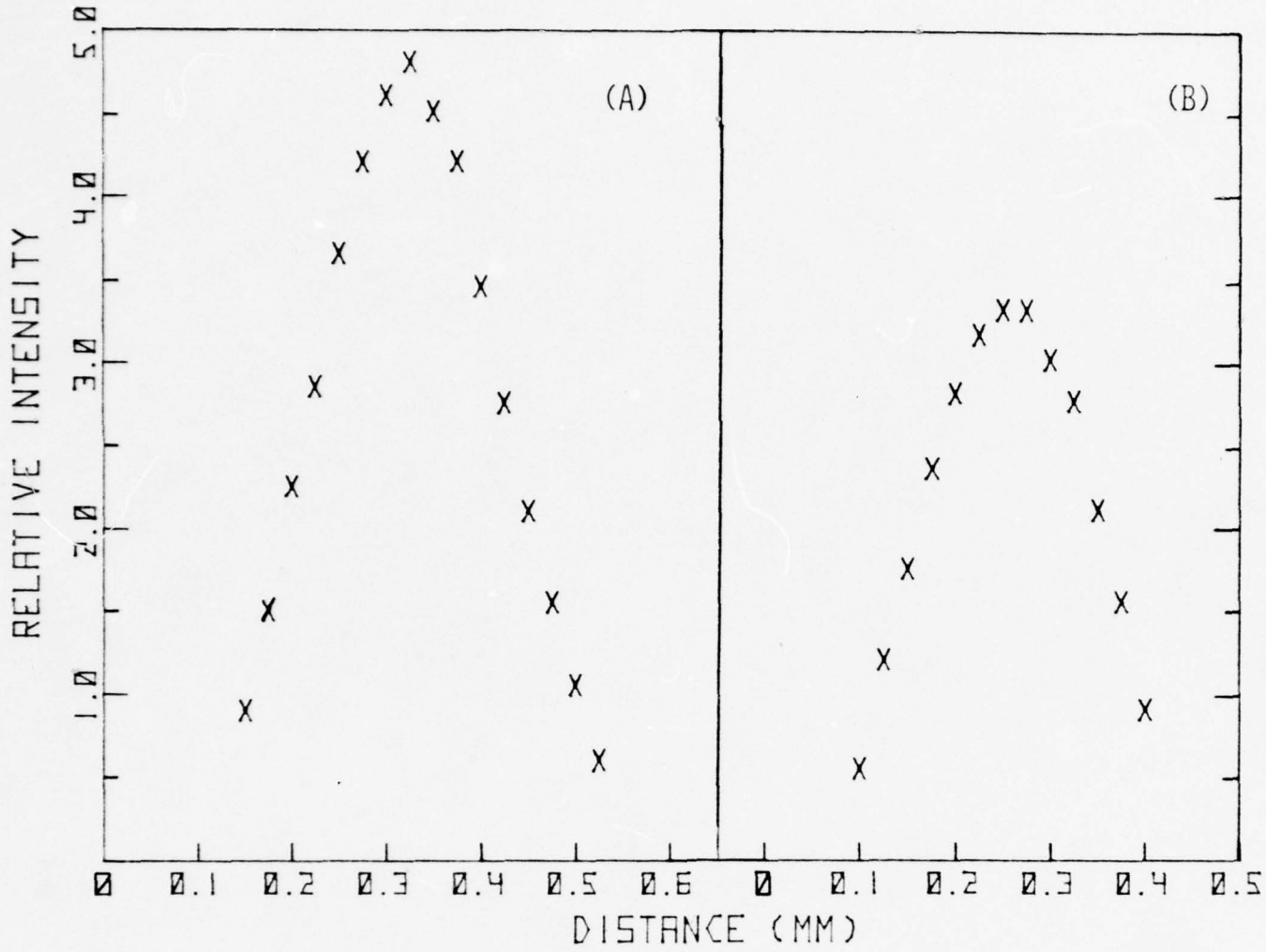

FIGURE 7-5. Beam Scans of Focused Output of Nitrogen Laser; Vertical Direction. (A corresponds to left lobe of Figure 7-4. B corresponds to right lobe).

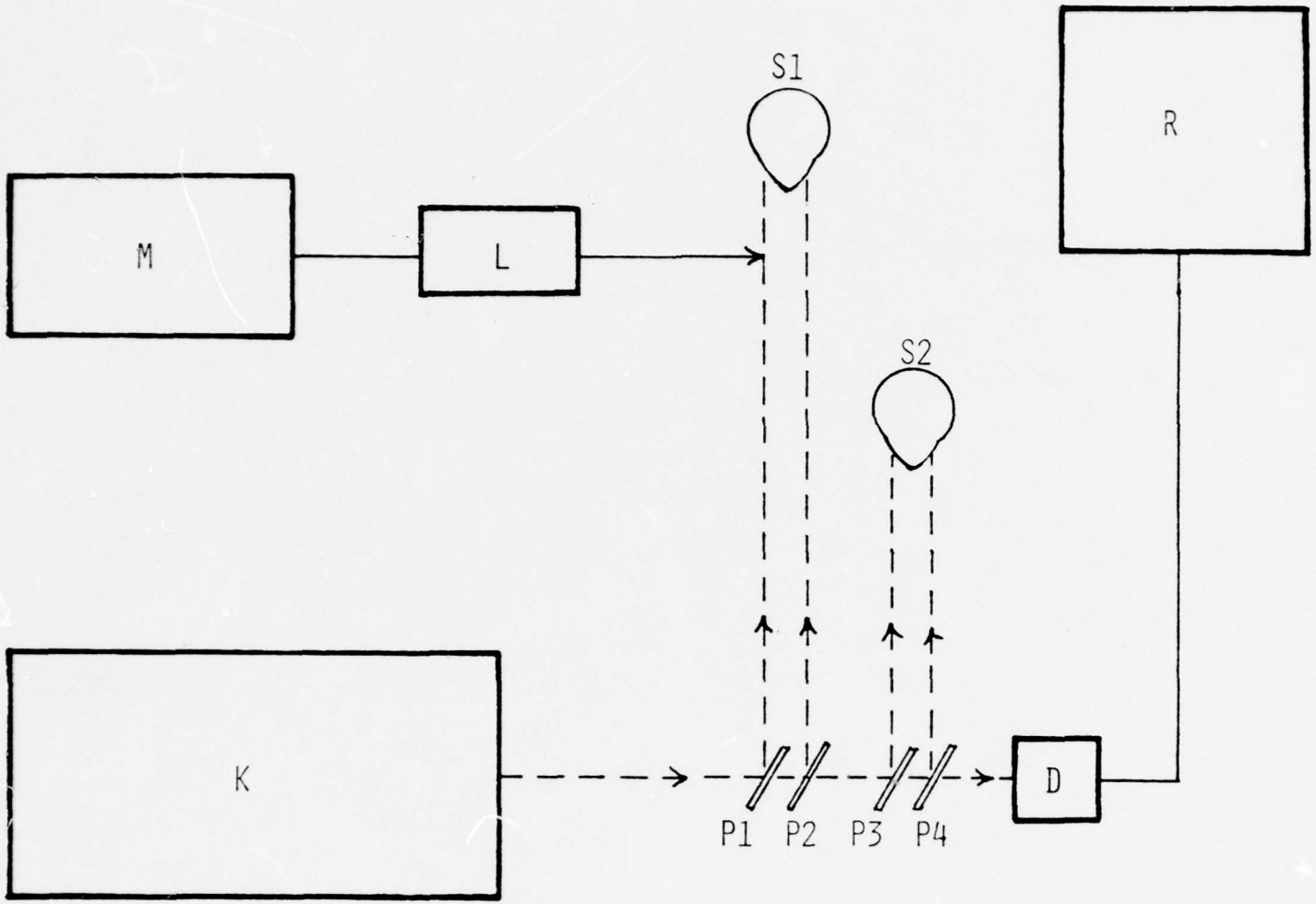

FIGURE 7-6. Experimental Apparatus for Simultaneous Exposure of Four Eyes. K-krypton laser; M-microvoltmeter; L-laser power meter; D-photodiode; R-strip-chart recorder; P1,P2,P3,P4-pellicles; S1,S2-subjects.

During the exposures, a single suture was used to hold back the upper lid. The corneas were irrigated with normal saline at 1-2 minute intervals. In order to minimize the tedium associated with this operation, a syringe delivery system was devised to simultaneously direct streams of saline onto each of the four corneas.

C. RESULTS

A slit lamp photograph of a severe corneal lesion is shown in Figure 7-7. The lesion was photographed at 18 hours following exposure to an energy dose of approximately ten times threshold. In order to examine such lesions at the cellular level, several animals were sacrificed and histopathologic evaluations of the corneal lesions carried out. Figure 7-8 shows the edge of an epithelial lesion in a region of the cornea exposed to a dose of 120 J/cm^2 (i.e., approximately twice threshold). The outer cellular layers in the lesion area were more flattened than in the unirradiated area and the epithelial thickness was reduced considerably compared to normal tissue. Figure 7-9 illustrates a view of the damaged tissue near the center of the lesion area. The cells of the epithelial basal layer were swollen and distorted. The flattened cells of the squamous layer took up much more eosin stain than cells in unirradiated areas of the cornea. Thus, the damage extended through all layers of the corneal epithelium.

Corneal epithelial thresholds were determined for single-pulse exposures to krypton- and argon-ion lasers with varying exposure times. Approximately 25-30 eyes were exposed for each threshold determination. The dose-response plot for the 120 sec data is shown in Figure 7-10 and is typical for this series of experiments in that there is a sharply defined threshold with only a few data points not in accord. Dose-response plots for all other corneal thresholds discussed in this report have been presented in interim reports[1,8-12] and are not reproduced here. The thresholds and confidence limits were calculated by the method of probit analysis[6,7]. The results for single-pulse exposures are summarized in Table 7-1.

The corneal threshold for continuous 30 sec exposures to the argon-ion laser (351.1 and 363.8 nm) was 82 ± 23 J/cm^2, compared to the value of 66 ± 8 J/cm^2 found for a 30 sec exposure to the krypton-ion laser (350.7 and 356.4 nm). When the wavelength dependence of UV-induced corneal damage is taken into account, these two thresholds are found to be in close agreement. This is discussed more fully in Chapter 9. For a 4 second exposure to the argon laser, the threshold was 96 ± 14 J/cm^2. However, under these conditions, cataracts were induced at a slightly lower threshold (see Chapter 10) than corneal damage and, in fact, interfered with the slit lamp observations of the corneal lesions. For 1 sec exposure times the corneal threshold appears to be in the range of 80-90 J/cm^2 whereas the lenticular threshold is significantly lower. Because of the interference by cataracts with corneal observations, a quantitative determination of the corneal thresholds for 1 sec exposures was not attempted.

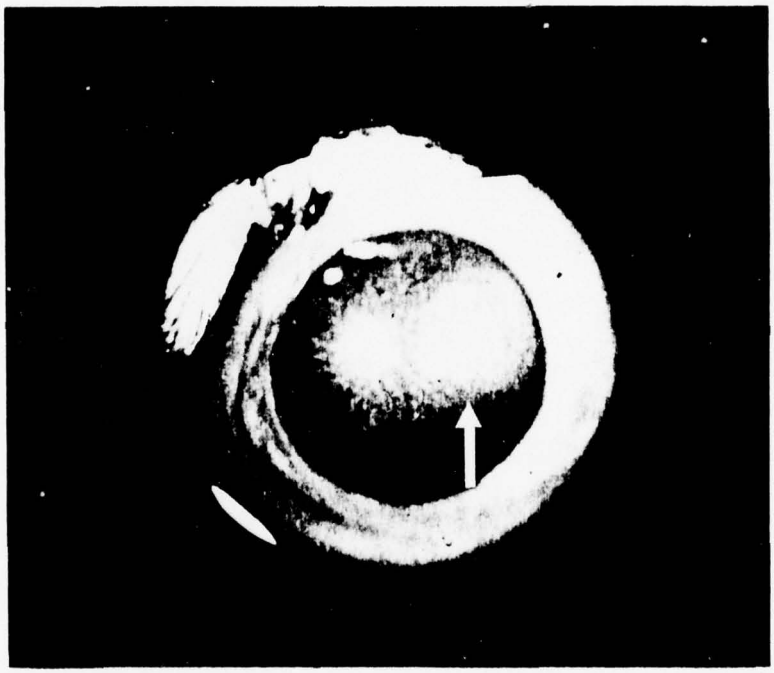

FIGURE 7-7. Slit Lamp Photograph Showing Corneal Lesion Induced by Near-UV Output of Krypton Laser. Energy dose, ~650 J/cm^2. Corneal spot size, ~2 mm. The bright spot to the left of the lesion is the reflection of the slit lamp source from the corneal surface.

FIGURE 7-8. Photomicrograph of Corneal Tissue in Region Exposed to Near-UV Output of Krypton Laser. Corneal dose, 120 J/cm^2. Corneal spot size, 1.3 mm diameter. Tissue fixed in glutaraldehyde in cacodylate buffer and stained with hematoxylin and eosin. Photomicrograph shows edge of lesion area. The tissue shown in the right half of the photograph is in the region exposed to the laser radiation. The epithelial thickness is reduced significantly relative to that of the unirradiated tissue shown at the left edge of the photograph. The debris seen just above the epithelial surface is an artifact of the tissue processing. Magnification, 290X.

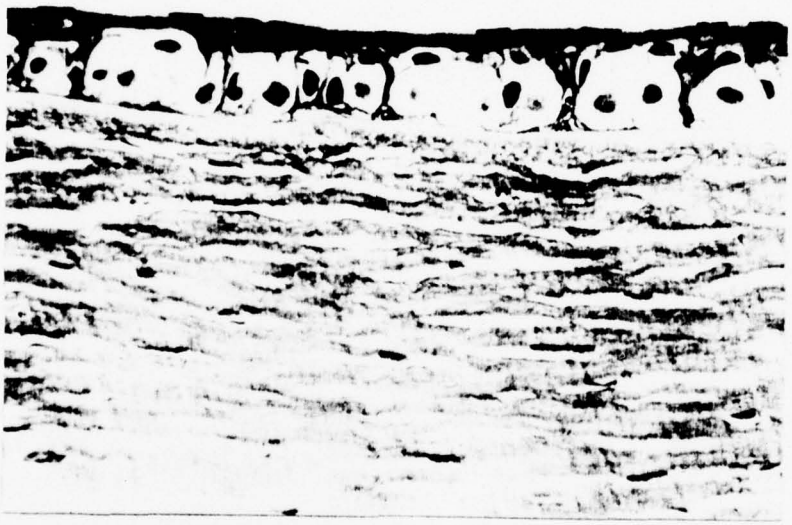

FIGURE 7-9. Photomicrograph of Corneal Tissue Showing Central Area of Lesion Illustrated in Figure 7-8. Magnification, 335X.

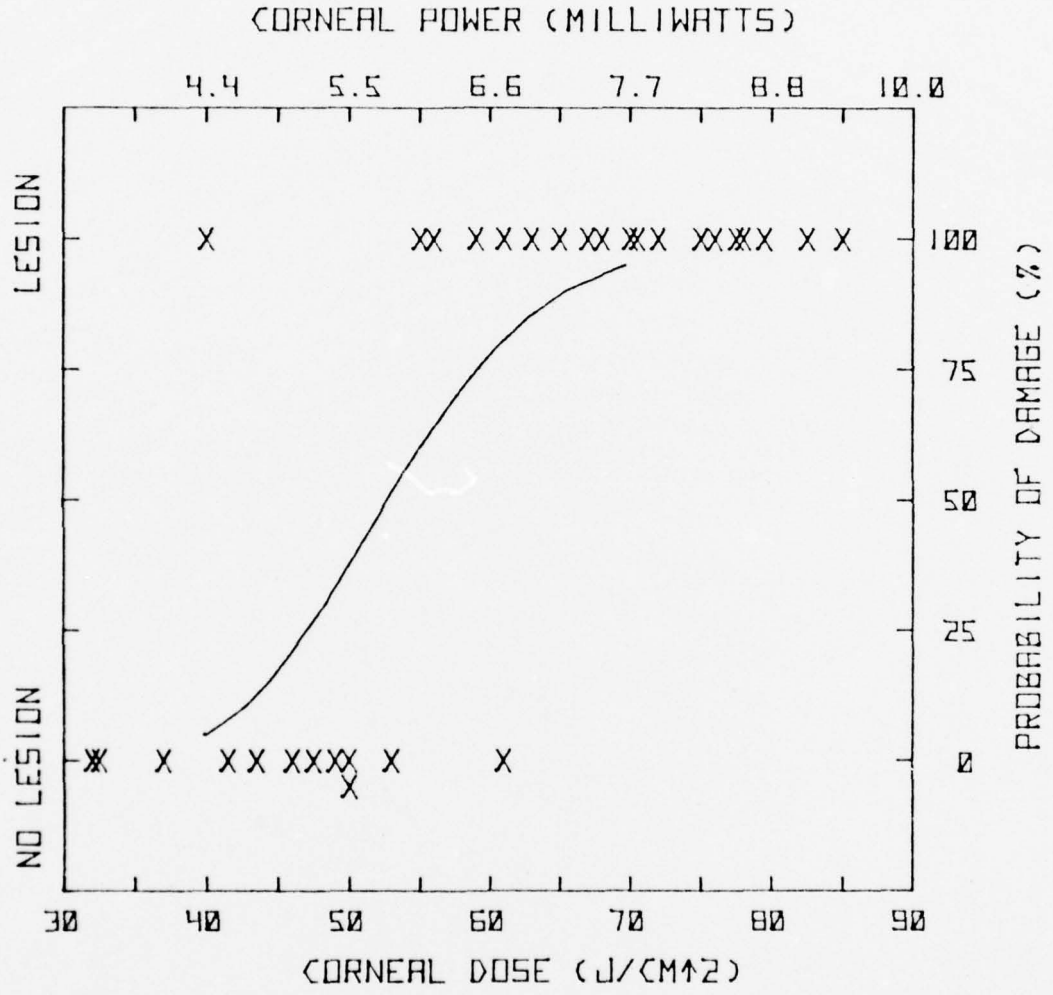

FIGURE 7-10. Dose-response Plot for 120-second Continuous Exposures to the Near-UV Output of a Krypton-ion Laser. Corneal spot size, 1.3 mm diameter; 31 eyes. Each corneal examination is recorded as a lesion or no lesions datum (left hand scale). The solid curve is the probability of damage (right hand scale). The abscissa is calibrated both in terms of energy dose delivered to the cornea (lower) and the laser power incident at the cornea (upper).

TABLE 7-1.

SUMMARY OF THRESHOLD IRRADIANCES FOR CORNEAL EPITHELIAL LESIONS INDUCED BY KRYPTON-ION LASER (350.7 and 356.4 nm)

Single-Pulse Exposures

Exposure Time (sec)	Radiant Exposure (J/cm^2)	Irradiance (W/cm^2)
10^4	26 ± 1[a]	2.6×10^{-3}
10^3	21 ± 4	2.1×10^{-2}
120	53 ± 8	0.44
45	62 ± 6	1.4
30	66 ± 8	2.2
30	82 ± 23[b,c]	2.7
18	66 ± 8	3.6
4	96 ± 14[b,d]	24

(a) 95% confidence limits calculated from slope of probit line.

(b) Argon-ion laser (351.1 and 363.8 nm).

(c) Threshold normalized to wavelengths emitted by krypton-ion laser is 67 J/cm^2 (see Chapter 9).

(d) Threshold normalized to wavelengths emitted by krypton-ion laser is 79 J/cm^2 (see Chapter 9).

The epithelial threshold found for continuous 10^3 sec exposures was 21 ± 4 J/cm^2, a significant decrease from the thresholds listed in Table 7-1 for shorter exposure times. For 10^4 sec exposures, the threshold was 26 ± 0.5 J/cm^2. The experimental apparatus shown in Figure 7-6 was used for these two threshold determinations.

Corneal thresholds were also determined for multiple-pulse krypton laser exposures with pulsewidths ranging from 250 μsec to 1 sec. In each case, the pulse train length was 30 sec at 50% duty cycle. The threshold data are summarized in Table 7-2 which also lists the irradiance per pulse delivered to the cornea and the calculated irradiance which would be required to deliver the respective threshold dose with a single pulse of the same pulsewidth.

The threshold for exposure to trains of 10 nsec pulses from the nitrogen laser (337.1 nm) was found to be 8.4 ± 3.3 J/cm^2. The appearance of the corneal lesions induced by the nitrogen laser is different from those induced by the krypton-ion laser, in that the former show indications of mechanical tearing or fracture of the epithelial layer.

D. DISCUSSION

The corneal epithelial threshold data presented in Tables 7-1 and 7-2 are plotted in Figure 7-11 as single-pulse irradiance vs. pulsewidth. With the exception of the extreme pulsewidths (10^{-8} sec nitrogen threshold, and 10^3 and 10^4 sec krypton thresholds), the data fall very close to a straight line representing an energy dose of ~67 J/cm^2 delivered to the cornea. The fact that the product of threshold intensity and the pulsewidth is a constant (reciprocity relationship) supports the postulate that the corneal epithelial damage mechanism is a photochemical process[1,13]. Moreover, the primary mechanism appears to involve a single photon absorption process since the threshold is linearly dependent on both pulsewidth and intensity. It should be noted that the thresholds for multiple-pulse exposures are in agreement with those for single-pulse exposures. This clearly demonstrates the cumulative effect of repetitive pulses and provides further support for the hypothesis of a photochemical mechanism. These results are in distinct contrast with what would be expected for a thermal damage mechanism since the time between successive pulses (up to 1 sec) should permit considerable thermal relaxation[3] of the irradiated tissue and preclude a cumulative thermal build-up.

Further evidence for the hypothesis of a photochemical damage mechanism is offered by the fact that the damage threshold appears to depend upon the ambient oxygen concentration. Experiments conducted in an oxygen-deficient atmosphere (i.e., flushing the corneas with nitrogen gas) indicate a dramatic increase in the incident energy dose required to produce corneal epithelial lesions (see Chapter 8).

TABLE 7-2.

SUMMARY OF THRESHOLD IRRADIANCES FOR CORNEAL EPITHELIAL LESIONS INDUCED BY KRYPTON-ION LASER (350.7 and 356.4 nm)

Multiple-Pulse Exposures
(30-sec Pulse Trains; 50% Duty Cycle)

Pulsewidth (msec)	Radiant Exposure (J/cm^2)	Irradiance (Per Pulse) (W/cm^2)	Number of Pulses	Calculated Irradiance for Threshold Dose Delivered in Single Pulse (W/cm^2)
10^3	66 ± 9[a]	4.4	15	66
20	67 ± 6	4.4	7.5×10^2	3.3×10^2
5	63 ± 10	4.2	3×10^3	1.3×10^4
2	71 ± 15	4.8	7.5×10^3	3.6×10^4
1	67 ± 12	4.5	1.5×10^4	6.8×10^4
0.5	71 ± 10	4.7	3×10^4	1.4×10^5
0.25	64 ± 12	4.3	6×10^4	2.6×10^5
10^{-5}[b]	8.4 ± 33[c]	1.1×10^8	8[d]	8.8×10^8

(a) 95% confidence limits calculated from slope of probit line.

(b) Duty cycle, 10^{-7}.

(c) Nitrogen laser (337.1 nm).

(d) Pulse train length, 0.9 sec.

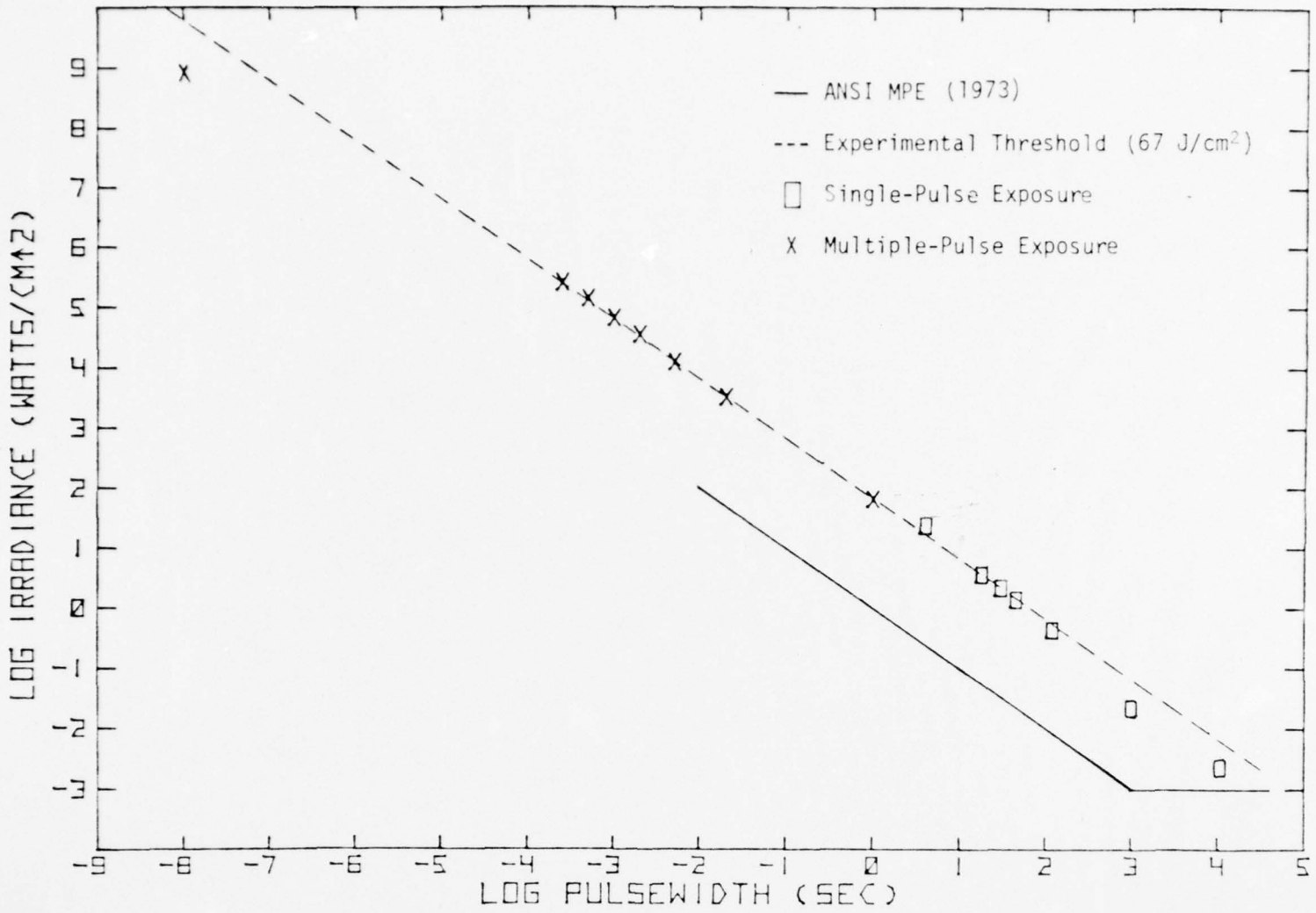

FIGURE 7-11. Comparison of Experimentally Determined Corneal Thresholds with Present ANSI Maximum Permissible Exposures for 315-400 nm Radiation.

Despite the strong evidence for a photochemical damage mechanism, it should not be assumed that the threshold irradiance vs. pulsewidth curve (Fig. 7-11) for single pulses can be extrapolated to exposure times much less than four seconds, since for shorter pulsewidths, it is possible that the higher peak powers would be sufficient for thermal damage to occur with lower energy doses than required to induce photochemical damage. Further, the constant energy relationship would be expected to hold only as long as the exposure times are long compared to the lifetimes of any transient species which may be precursors of the photoproducts[1]. Finally, at very high peak powers, additional processes such as multi-photon absorption, dielectric breakdown or acoustic shock may be involved in the primary damage mechanism. In fact, the threshold for 10 nsec pulses obtained from the nitrogen laser (1 megawatt peak power) is nearly an order of magnitude lower than 67 J/cm^2, indicating that in this case, some other mechanism is more efficient than the presumed photochemical process.

Also shown in Figure 7-11 is the corneal maximum permissible exposure (MPE) suggested by the American National Standards Institute for ~315 to 400 nm radiation[4]. The ANSI standard follows a 1 J/cm^2 line for exposure times up to 1000 sec. For longer exposure times, the presently recommended MPE approaches a constant irradiance of 1 mW/cm^2. This trend is qualitatively consistent with predictions based on thermal damage mechanisms[3,14]. However, our data for long exposure times indicate that UV-induced corneal damage involves a photochemical mechanism and such effects are generally regarded to be cumulative at least over times necessary to effect a repair or replacement of the damaged tissue. In this instance, the only available guidelines that indicate the period of time over which radiation doses may be cumulative are the data presented here on development and repair of the laser-induced corneal lesions and some early work on effects of non-coherent UV radiation by Verhoeff, et al.[15]. Based on these results, it seems prudent to assume that the effects of near-UV radiation on corneal tissue will be cumulative over a period of 24-48 hours.

In any event, the data for 10^3 and 10^4 sec exposures clearly indicate that the threshold irradiance vs. pulsewidth curve does not level off at 10^3 sec as suggested by the ANSI standard. Indeed, close examination reveals that there appears to be a slight decreasing trend of threshold energy dose with increasing exposure time. There does not appear to be any theoretical basis for this trend within the context of a photochemical model. Rather, it is assumed that the detrimental corneal effects which accrue during long exposures with repeated saline irrigations account for the enhanced corneal sensitivity.

The trend of decreasing threshold energy with increasing exposure time can be seen in Figure 7-12 where the long pulsewidth (>1 sec) portion of Figure 7-11 is plotted on an expanded scale. The slope of the experimental curve is steeper than that of an equal energy curve (e.g., the ANSI MPE curve for 1-1000 sec) and intersects the recommended constant irradiance segment of the ANSI curve at ~2×10^4 sec. In contrast, the 67 J/cm^2 curve of Figure 7-11 would intersect the 1 mW/cm^2 ANSI curve at ~9×10^4 sec. Thus,

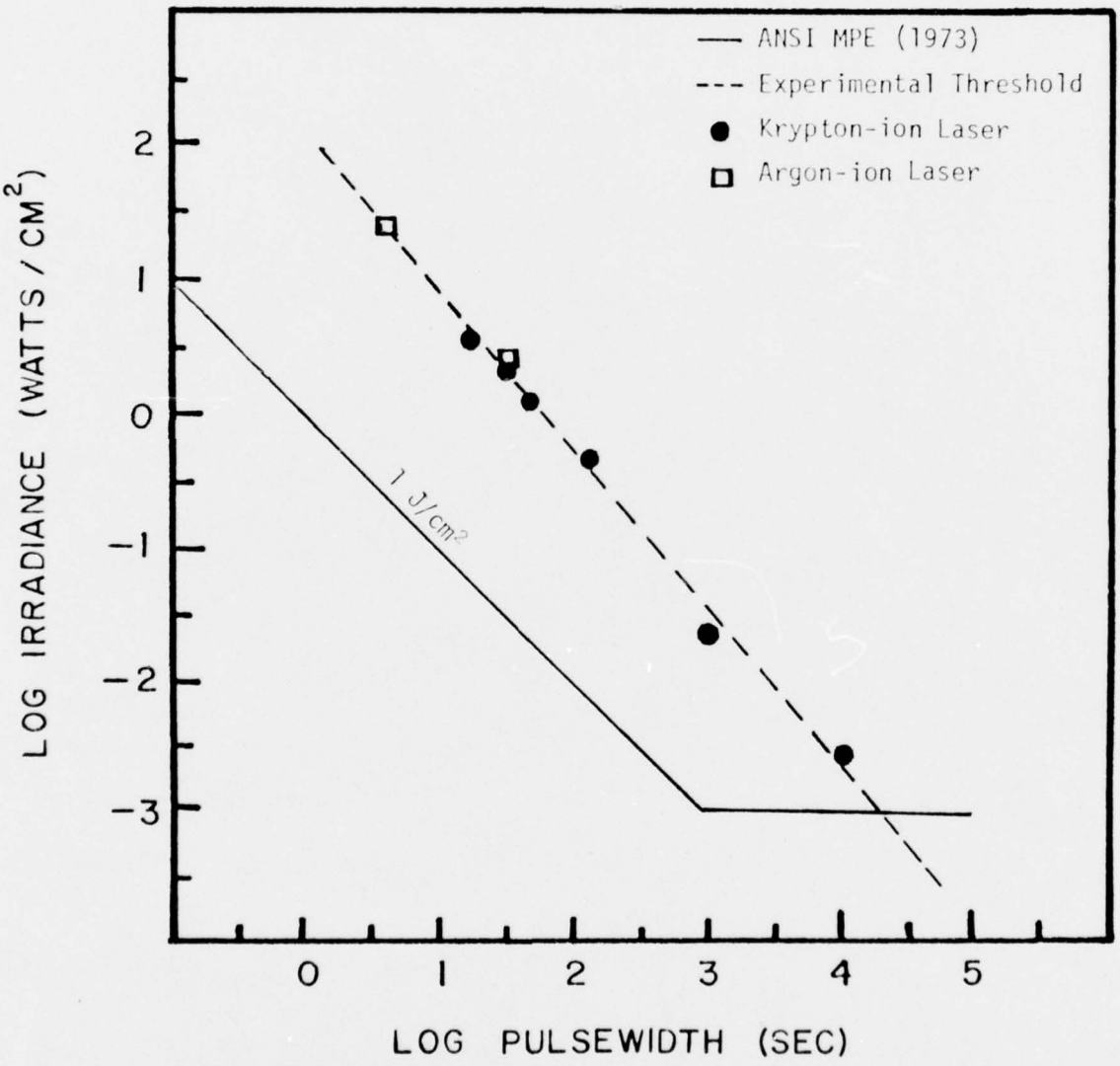

FIGURE 7-12. Comparison of Experimentally Determined Corneal Threshold Data with ANSI Maximum Permissible Exposure for Near-UV.

the experimental results suggest that for exposure times greater than 2×10^4 sec, the ANSI MPE may be higher than the experimental thresholds for corneal epithelial damage. The threshold of 26 J/cm^2 found for 10^4 sec exposures is only a factor of 2.6 above the ANSI corneal MPE for this exposure time. This does not appear to be an adequate margin of safety, especially in view of the significant changes in threshold with wavelength discussed in Chapter 9. Thus, on the basis of near-UV corneal threshold data for exposure times of up to 10^4 sec, it is recommended that the near-UV corneal MPE should be extended along the equal energy curve (1 J/cm^2) to exposure times of at least 10^5 sec.

REFERENCES

1. Zuclich, J.A., et al., in "Research on the Ocular Effects of Laser Radiation", Technology Incorporated, Second Annual Report, Part II, Contract F41609-73-C-0017, USAF School of Aerospace Medicine, February 1975.

2. Zuclich, J.A., ibid., First Annual Report, February 1974.

3. Takata, A.N., et al., "Thermal Model of Laser-Induced Eye Damage", Illinois Institute of Technology Research Institute, Final Technical Report, Contract F41609-74-C-0005, USAF School of Aerospace Medicine, October 1974.

4. "American National Standard for the Safe Use of Lasers," American National Standards Institute, Inc., Standard Z136.1, 1973.

5. American National Standards Institute, proposed laser safety standard, 1976.

6. Finney, D. J., "Probit Analysis", 2nd Ed., Cambridge University Press, Cambridge, England, 1952.

7. Natrella, M.T., "Experimental Statistics", NBS Handbook 91, U. S. Department of Commerce, National Bureau of Standards, 1963.

8. Zuclich, J.A., in "Research on the Ocular Effects of Laser Radiation", Technology Incorporated, Ninth Quarterly Report, Part II, Contract F41609-73-C-0017, USAF School of Aerospace Medicine, May 1975.

9. Zuclich, J.A., et al., ibid., Tenth Quarterly Report, August 1975.

10. Zuclich, J.A. and J.S. Connolly, ibid., Eleventh Quarterly Report, November 1975.

11. Zuclich, J.A., ibid., Twelfth Interim Technical Report, March 1976.

12. Zuclich, J.A. and W. E. Kurtin, ibid., Thirteenth Interim Technical Report, August 1976.

13. Zuclich, J.A. and J.S. Connolly, "Ocular Damage Induced by Near-Ultraviolet Laser Radiation", Invest. Ophthal. 15:760, 1976.

14. Mainster, M.A., et al., "Transient Thermal Behavior in Biological Systems", Bull. Math. Biophys. 32:303, 1970.

15. Verhoeff, F.H., L. Bell and C. B. Walker, "The Pathologic Effects of Radiant Energy on the Eye", Proc. Amer.Acad. Arts and Sci. 51:630, 1916.

CHAPTER 8

OXYGEN DEPENDENCE OF NEAR-UV INDUCED CORNEAL DAMAGE

Joseph A. Zuclich and William E. Kurtin*

A. INTRODUCTION

Harmful effects of near-ultraviolet (320-400 nm) radiation on cells have been widely reported in recent years[1-3]. Such studies have generally dealt with strains of bacteria and have used end points such as percentage of cell lethality[4] or mutagenicity[5,6] to define the nature and extent of the damage. Aside from the work discussed in this volume, reports on the effects of near-UV radiation on ocular tissues are few in number, and primarily involved exposure to low-intensity broad-band light sources over prolonged periods[7,8]. However, two recent papers have discussed corneal and lenticular damage induced by 325 nm radiation from helium-cadmium lasers[9,10]. The work reported here is concerned with ocular hazards of near-UV argon-ion laser radiation in primates. In particular, the most sensitive ocular tissue for the exposure parameters of interest has been found to be the epithelial layer of the cornea (Chapter 7). The end point used to define damage is the observation of a macroscopic corneal lesion (analogous to a skin erythema), although in some instances histopathologic examination has been carried out to describe the damage at the microscopic level. The lesions appear as opacities on the surface of the cornea, the shape of the lesion being characteristic of the laser beam dimensions.

Chapter 7 of this report discussed the induction of corneal epithelial damage in rhesus monkeys exposed to the near-UV output (350.7 and 356.4 nm) of a krypton-ion laser. A corneal irradiance of 2.2 W/cm^2 is sufficient to induce observable lesions with 30 sec exposures. When the exposure duration is varied, the threshold irradiance correspondingly changes in such a way that the total energy dose remains at ~60-70 J/cm^2. This reciprocity relationship between laser intensity and pulsewidth is taken as evidence that the observed damage is the result of a single-photon photochemical process. This hypothesis is further supported by the fact that the effects of repetitive exposures are cumulative while the threshold energy dose remains constant over wide ranges of pulsewidths and pulse repetition rates. Threshold data were obtained for multiple-pulse exposures with pulsewidths ranging from 250 μsec to 1 sec as well as single-pulse exposures with durations of 4 to 10^4 sec. The threshold dose is essentially constant over this range of pulsewidths with an average value of 67 J/cm^2. This value is of the same order of magnitude as observed breaks in survival curves of cell cultures exposed to 365 nm radiation[11,12].

* National Science Foundation Faculty Research Participant, Summer 1975. Permanent address: Department of Chemistry, Trinity University, San Antonio, Texas, 78284.

In order to further elucidate the nature of the photo-induced damage in the epithelial cells, the effect of oxygen concentration at the corneal surface has been investigated. A marked oxygen enhancement in the photo-inactivation of bacterial cells by near-UV light has been reported[4]. A similar oxygen dependence of near-UV lethality was recently reported for two mammalian cell lines[13]. The experiments described below were designed to test for a possible oxygen dependence of the production of corneal epithelial lesions.

B. EXPERIMENTAL METHODS

The subjects used in these experiments were rhesus monkeys (Macaca mulatta) generally ranging in age from two to three years and in weight from two to four kilograms. The animals were maintained and the experiments conducted in accordance with procedures outlined in the "Guide for Laboratory Animal Facilities and Care", National Academy of Sciences - National Research Council.

The animals were anesthetized with an intravenous injection (0.5-1.0 cc per kilogram) of sodium pentobarbital (50 mg/ml) following preanesthetic sedation with an intramuscular injection (0.1 cc per kilogram) of ketamine hydrochloride (100 mg/ml). The pupils were dilated with a topical application of atropine (1% atropine sulfate) administered ∿24 hours prior to exposure. The corneas and lenses of the anesthetized animals were examined with a Nikon "Zoom-Photo" slit lamp microscope. The acceptable subjects were fitted with a set of goggles containing vent tubes for introducing flowing gas over the eyes. Oxygen, nitrogen, or ambient air was passed through the goggles at a flow rate of ∿0.4 l/min for 15 min prior to exposure. The eyelids were then retracted by means of sutures, without disturbing the goggles, and the corneas were exposed to the near-UV laser radiation. The gas flow was terminated and the goggles and sutures removed immediately following the exposure. The subjects were kept in single cages without further treatment until the post-exposure corneal examinations. They were then sedated with ketamine hydrochloride and examined with the slit lamp microscope. The conscious subjects did not exhibit any recognizable symptoms of eye irritation at any time following the exposure.

A schematic representation of the experimental set-up is shown in Figure 8-1. The UV source was a Spectra Physics 170 argon-ion laser equipped with optics to yield UV output simultaneously at 351.1 and 363.8 nm (intensity ratio ∿1:1). No attempt was made to separate these two wavelengths for the experiments reported here. The subjects were positioned with the aid of a Spectra Physics 155 helium-neon alignment laser (∿0.5 mW) arranged so that the beam, after reflecting off a beamsplitter, was colinear with the UV laser beam. Intensity profiles were measured with a beam scan apparatus consisting of an EG&G-SGD 100 photodiode mounted on a micrometer translation stage driven by a synchronous motor. Spatial resolution of the scans was limited by a 50 μm diameter aperture attached directly to the front face of the photodiode. The voltage output of the photodiode

FIGURE 8-1. Schematic Diagram of Laser Apparatus for Corneal Irradiation Under a Controlled Atmosphere. UV - ultraviolet laser source; A - helium-neon alignment laser; S - shutter; B - beamsplitter; P - laser power meter; V - microvoltmeter; G - gas source; F - flowmeter; E - subject eye with fitted goggles.

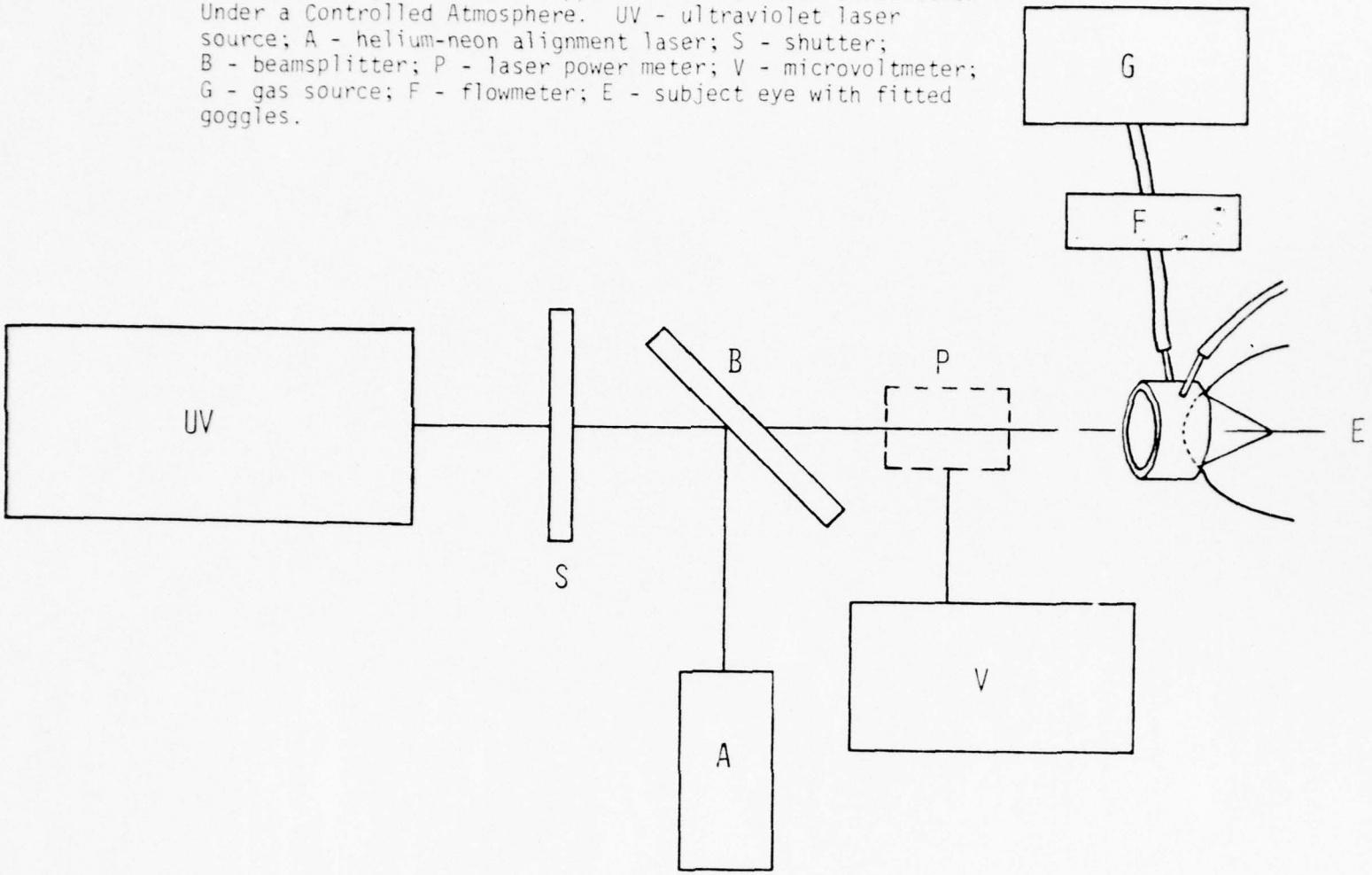

was traced on an X-Y recorder. The beam scan profile was essentially Gaussian in shape. The corneal spot size was defined as the beam diameter at the $1/e^2$ points as measured at the appropriate distance from the output mirror of the laser.

The power output of the argon-ion laser was controlled by varying the current through the plasma tube. Power measurements were made with a Scientech 3600 laser power meter, the output of which was coupled to a Keithley 149 milli-microvoltmeter. The power meter and the voltmeter were calibrated as a unit using sources and procedures traceable to NBS standards.

The duration of the exposures was controlled with an electronically triggered mechanical shutter. For the experiments reported here, each cornea was exposed to the UV laser radiation for 30 sec. The laser power output was varied in order to deliver the desired dose to the cornea.

The corneas of the exposed eyes were re-examined with the slit lamp at 18 hours post-exposure and lesion formation was noted at this time. The 18 hour criterion was established by earlier work which indicated that the near-UV induced corneal lesions reach maximal development at 12 to 24 hours following exposure (Chapter 7). Slightly supra-threshold lesions appeared as well-defined spots on the surface of the cornea, being more reflective to the slit lamp light source than unexposed areas of the cornea. The spots had a fairly even texture if the exposure was 10% or more above threshold but exposures closer to the threshold dose often yielded lesions with a "patchy" appearance. There did not appear to be any significant depth associated with threshold lesions. However, exposures of 50% or more above threshold caused crater-like effects which apparently penetrated the epithelial layer of the cornea but did not affect the underlying stromal layer.

The damage threshold was defined as the energy dose for which 50% of the exposures would produce a lesion. Threshold energies and 95% confidence limits were calculated by probit analysis[14,15]. A minimum of 25 eyes was used for each threshold determination.

C. RESULTS AND DISCUSSION

The thresholds for eyes flushed with oxygen, nitrogen, and normal atmosphere (control eyes) are summarized in Table 8-1. Dose-response plots of the raw data were presented in interim reports[16,17]. It is seen that the threshold for nitrogen flushed eyes markedly increases relative to the control, and is roughly twice that for eyes in an oxygen-enriched atmosphere. However, the dependence on oxygen concentration is actually more dramatic than this factor of two when the extent of damage is considered. For eyes flushed with nitrogen, the corneal lesions induced by doses of as high as 180-200 J/cm^2 generally appeared as minimal or barely visible lesions. Eyes flushed with oxygen showed relatively severe lesions with doses only slightly in excess of the threshold value of 66 J/cm^2.

TABLE 8-1.

CORNEAL EPITHELIAL THRESHOLDS UNDER VARIOUS ATMOSPHERES

Atmosphere	Threshold Dose (J/cm^2)	95% Confidence Limits* (J/cm^2)
Air (control eyes)	82	58-104
O_2	66	56-77
N_2	133	116-155

*Calculated from the slope of probit line.

Studies by Smelser[18], Takahashi, et al.[19] and Hill and Fatt[20] indicate that flushing with nitrogen gas is effective in diminishing the oxygen tension within the epithelial cells. Measurements of the exact oxygen tension in these cells under a nitrogen atmosphere have not been made. If the rate at which the cells consume oxygen remains constant as the oxygen pressure is reduced, the cells would become anoxic at low oxygen pressures. However, there is evidence from other biological systems for an oxygen-tension dependent oxygen consumption rate[21]. If this is the case, then even at zero oxygen pressure the epithelial cells may still have a small oxygen tension, determined by the rate at which oxygen could be delivered to the cornea from the aqueous humor. We have no quantitative indication that the corneal surface cells become anoxic after only 15 min exposure to a nitrogen atmosphere. It is possible that the threshold would be higher than 133 J/cm^2 with further deprivation of normal oxygen concentrations. Similarly, with prolonged exposure to an enriched oxygen atmosphere, the hazard from near-UV radiation may be even greater than that reflected by the threshold of 66 J/cm^2 obtained in this work.

The molecular targets for the oxygen dependent near-UV inactivation of mammalian cells are not known. Our results may be interpreted as evidence for a photodynamic effect[22,23], but do not distinguish between several prossiblities such as damage to the DNA template, to DNA repair processes or to RNA metabolic processes[24]. It is also possible that the effect is due to direct photo-oxidation not involving damage to the genetic machinery[25].

It is interesting to note that an earlier report of near-UV lethality in mammalian cells[26] was later shown to involve the production of toxic photoproducts in the tissue culture medium[27]. The more recent work of Danpure and Tyrrell[13] demonstrated the oxygen dependence of near-UV lethality in mammalian cell lines by irradiating the cells while suspended in an inorganic buffer rather than in tissue culture medium. The approach used in this work has the advantage of observing the oxygen dependence of near-UV lethality in mammalian cells <u>in situ</u>.

From the viewpoint of laser hazards, these experiments should be pursued in order to determine the extent of enhancement of near-UV sensitivity for subjects in an enriched oxygen atmosphere for prolonged periods and to measure the degree of protection from near-UV radiation which may be afforded to subjects whose corneas are shielded from atmospheric oxygen. In particular, the effect of contact lens use on the corneal threshold could be investigated. Additional experiments along this line would further elucidate the nature of the involvement of molecular oxygen in the UV-induced corneal damage mechanism. Discovery of the fact that oxygen is intimately involved in the formation of epithelial lesions induced by near-UV laser radiation is an important step towards specification of a molecular mechanism in sufficient detail to yield a working quantitative model.

REFERENCES

1. Eisenstark, A., "Sensitivity of Salmonella Typhimurium Recombinationless (*rec*) Mutants to Visible and Near-Visible Light", Mutation Res. 10:1, 1970.

2. Peak, M.J., "Some Observations on the Lethal Effects of Near-Ultraviolet Light on *Escherichia coli*, Compared with the Lethal Effects of Far-Ultraviolet Light", Photochem. Photobiol. 12:1, 1970.

3. Pollard, E.C., "Cellular and Molecular Effects of Solar Ultraviolet Radiation", Photochem. Photobiol. 20:301, 1974.

4. Webb, R.B. and J.R. Lorenz, "Oxygen Dependence and Repair of Lethal Effects of Near Ultraviolet and Visible Light", Photochem. Photobiol. 12:283, 1970.

5. Kubitschek, H.E., "Mutagenesis by Near-Visible Light", Science 155:1545, 1967.

6. Webb, R.B. and M.M. Malina, "Mutagenesis in Escherichia coli by Visible Light", Science 156:1104, 1967.

7. Zigman, S., T. Yulo and J. Schultz, "Cataract Induction in Mice Exposed to Near-UV Light", Ophthal. Res. 6:259, 1974.

8. Zigman, S. and T. Vaughan, "Near-Ultraviolet Light Effects on the Lenses and Retinas of Mice", Invest. Ophthalmol. 13:462, 1974.

9. MacKeen, D., S. Fine and B.S. Fine, "Production of Cataracts in Rabbits with the Ultraviolet Laser", Ophthal. Res. 5:317, 1973.

10. Ebbers, R.W. and D. Sears, "Ocular Effects of a 325 nm Ultraviolet Laser", Amer. J. Optom. and Physiol. Optics 52:216, 1975.

11. Tyrrell, R.M., "Induction of Pyrimidine Dimers in Bacterial DNA by 365 nm Radiation", Photochem. Photobiol. 17:69, 1973.

12. Tyrrell, R.M., "REC A^+ - Dependent Synergism Between 365 nm and Ionizing Radiation in Log-Phase *Escherichia coli*: A Model for Oxygen-Dependent Near-UV Inactivation by Disruption of DNA Repair", Photochem. Photobiol. 23:13, 1976.

13. Danpure, H.J. and R.M. Tyrrell, "Oxygen-Dependence of Near-UV (365 nm) Lethality and the Interaction of Near-UV and X-rays in Two Mammalian Cell Lines", Photochem. Photobiol. 23:171, 1976.

14. Finney, D.J., "Probit Analysis", Second Edition, Cambridge University Press, New York, 1952.

15. Natrella, M.G., "Experimental Statistics", NBS Handbook 91, U.S. Department of Commerce, National Bureau of Standards, Washington, D.C., 1963.

16. Zuclich, J.A., et al., "Research on the Ocular Effects of Laser Radiation", Technology Incorporated, Tenth Quarterly Report, Part II, Contract F41609-73-C-0017, USAF School of Aerospace Medicine, August 1975.

17. Zuclich, J.A., ibid., Twelfth Interim Technical Report, March 1976.

18. Smelser, G.K., "Relation of Factors Involved in Maintenance of Optical Properties of Cornea to Contact Lens Wear", A.M.A. Arch. Ophthalmol. 47:328, 1952.

19. Takahashi, G.H., I. Fatt and T.K. Goldstick, "Oxygen Consumption Rate of Tissue Measured by a Micropolarographic Method", J. Gen. Physiol 50:317, 1966.

20. Hill, R.M. and I. Fatt, "Oxygen Uptake from a Reservoir of Limited Volume by the Human Cornea in vivo", Science 142:1295, 1963.

21. Maurice, D.M. and M.V. Riley, in "Biochemistry of the Eye", C. N. Graymore ed., Academic Press, New York, 1970.

22. Spikes, J.D. and C.A. Ghiron, in "Physical Processes in Radiation Biology", L.G. Augenstein, R. Mason and B. Rosenberg, eds., Academic Press, New York, 1964.

23. Spikes, J.D. and R.S. Livingston, "The Molecular Biology of Photodynamic Action: Sensitized Photoautoxidations in Biological Systems", Adv. Radiation Biol. 3:29, 1969.

24. Ramabhadran, T.V., "Effects of Near-Ultraviolet and Violet Radiations (315-405 nm) on DNA, RNA and Protein Syntehsis in E. coli B/r: Implications for Growth Delay", Photochem. Photobiol. 22:117, 1975.

25. McCormick, J.P., J.R. Fischer, J.P. Packlatko and A. Eisenstark, "Characterization of a Cell-Lethal Product from the Photooxidation of Tryptophan: Hydrogen Perioxide", Science 191:468, 1976.

26. Wang, R.J., J.D. Stoien and F. Landa, "Lethal Effects of Near-Ultraviolet Irradiation on Mammalian Cells in Culture", Nature 247:43, 1974.

27. Stoien, J.D. and R.J. Wang, "Effect of Near-Ultraviolet and Visible Light on Mammalian Cells in Culture II. Formation of Toxic Photoproducts in Tissue Culture Medium by Blacklight", Proc. Natl. Acad. Sci. U.S. 71:3961, 1974.

CHAPTER 9

ACTION SPECTRUM FOR NEAR-UV INDUCED CORNEAL DAMAGE

Joseph A. Zuclich and William E. Kurtin*

A. INTRODUCTION

Photochemical mechanisms for near-UV induced damage in the corneal epithelium have been discussed at length in Chapters 7 and 8. The dependence of threshold dose on the intensity and pulsewidth of the radiation source together with the cumulative effects of repetitive pulses now appear to be well understood. However, no information was previously available regarding the wavelength dependence of the corneal threshold. Since the ANSI standard quotes a single MPE for the entire wavelength range 315-400 nm[1,2], it is necessary to determine the wavelength dependence within this range in order to assure an adequate margin of safety for all exposure parameters.

B. EXPERIMENTAL METHODS

Several near-UV emitting lasers were available, but the specific wavelengths emitted were not sufficient for determining an action spectrum over the wavelength range of interest. Therefore, a xenon arc lamp with relatively uniform output throughout the near-UV was used as the radiation source. A schematic diagram of the experimental apparatus is shown in Figure 9-1.

The lamp was a Hanovia 1000 W xenon arc lamp mounted in an Oriel 6140 housing and powered by an Oriel C-72-50 power supply with external ignitor. An adapter placed on the exhaust port of the lamp housing allowed 4" flexible tubing to be connected between the housing and an external blower which vented the exhaust outside of the laboratory. External venting was required because of the high levels of ozone generated by the arc lamp.

After passing through a water cell (15 cm pathlength), the lamp output was directed through a Bausch & Lomb 500 mm, UV-visible monochromator (Model 33-86-45) fitted with a 1200 groove/mm grating blazed at 500 nm. The reciprocal dispersion was 16.5 Å/mm. The slits were set at 6 mm so that the bandwidth (full width at halfmaximum) for all exposures was ~10 nm.

---

* National Science Foundation Faculty Research Participant, Summer 1976. Permanent address: Department of Chemistry, Trinity University, San Antonio, Texas 78284.

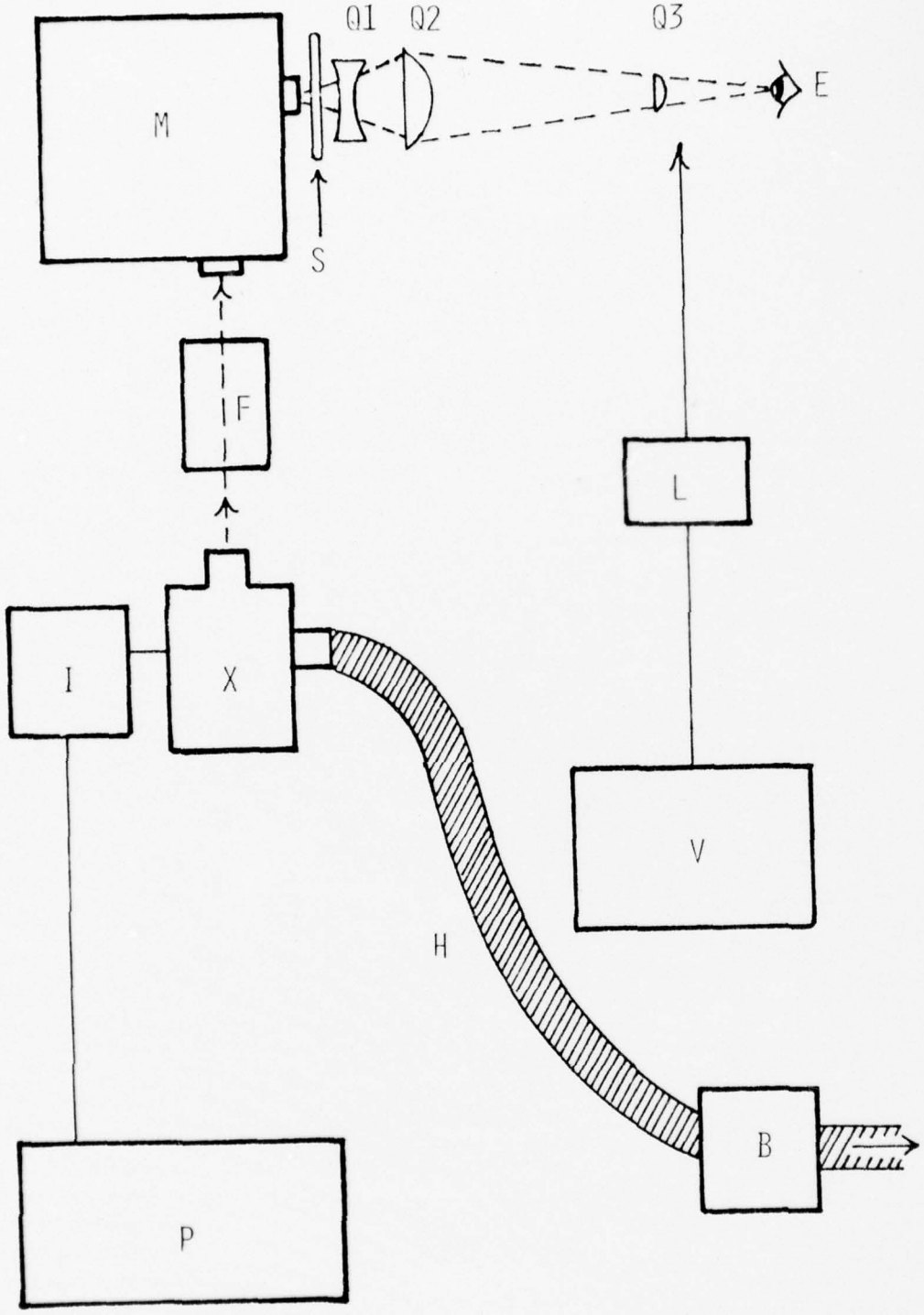

FIGURE 9-1. Experimental Apparatus for Inducing Corneal Lesions with Xenon Arc Lamp.

M - monochromator; S - shutter; Q1, Q2, Q3 - quartz lenses; F - filter cell; X - xenon arc lamp; I - ignitor; P - power supply; H - flexible hose; B - blower; V - microvoltmeter; L - power meter; E - subject eye.

After exiting the monochromator the near-UV beam passed through a series of three quartz lenses, the last of which focused the beam onto the corneal surface of the subject. The quartz lenses were chosen so that the focused image of the slit was as small as possible while still maintaining the necessary working distance (>1.5") between the last lens and the surface of the cornea. These lenses were selected empirically from available supplies and were fixed in place at optimum positions along an optical bench, the position of which was fixed with respect to the monochromator. Thus, the focal plane of the optical system was fixed in space and each subject was placed on a mount with translation stages that allowed positioning of the corneal surface in the focal plane. The focused spot had a trapezoidal shape reflecting the shape of the monochromator output slit. Beam scans in the horizontal and vertical direction yielded average dimensions of 1.36 mm and 1.48 mm, respectively. However, intensity profiles were not uniform and therefore these dimensions are not necessarily indicative of the magnitude of the exposed area. In order to maintain consistency in the definition of spot size (for comparison of the corneal thresholds with those obtained using laser sources) the periphery of the image was defined as the $1/e^2$ intensity coutour. The area of the focused image thus determined was 0.016 cm^2, which is equivalent to a circular spot with a diameter of ~1.4 mm.

Power measurements were made with a Scientech 3600 laser power meter, the output of which was coupled to a Keithley 150B microvolt/ammeter. The duration of the exposures was controlled with an electronically triggered mechanical shutter. Animal preparation and handling procedures were identical to those previously described for corneal threshold determinations using UV laser radiation (Chapter 7).

C. RESULTS AND DISCUSSION

Corneal thresholds were determined at 10 nm intervals over the wavelength range of 320-390 nm. Since the power output of the xenon arc lamp was not readily adjustable over a wide range, thresholds were obtained by varying the exposure time at a given constant intensity at each wavelength. Dose-response plots for each threshold determination are included in an appendix in Reference 3. The threshold data are summarized in Table 9-1 and are plotted as threshold vs. wavelength in Figure 9-2.

As seen in this figure, the threshold increases monotonically with wavelength but with a pronounced shoulder in the 340-350 nm region. The corneal threshold for wavelengths shorter than ~340 nm apparently reflects involvement of the photochemical damage mechanism which accounts for the sensitivity of epithelial cells to far-UV radiation. As shown by Pitts, et al.[4,5], the epithelial cells exhibit maximum UV sensitivity at 270 nm where the threshold is ~0.004 J/cm^2. On passing to longer wavelengths, the corneal sensitivity decreases rapidly up to about 320-330 nm at which point the rate of decrease begins to fall off, as indicated in Figure 9-3. As discussed below, this trend may reflect involvement of different damage mechanisms for far- and near-UV irradiation of corneal tissues.

TABLE 9-1

WAVELENGTH DEPENDENCE OF THRESHOLDS (ED50) FOR CORNEAL LESIONS INDUCED BY NONCOHERENT NEAR-UV RADIATION

WAVELENGTH[a] (nm)	NO. OF EYES	THRESHOLD (J/cm^2)	95% CONFIDENCE LIMITS[b] (J/cm^2)
320	22	9.6	8.5 - 10.7
330	27	41.1	35.3 - 47.7
340	33	58.3	51.6 - 65.8
350	26	61.5	55.0 - 68.5
360	24	88.4	(c)
370	25	130	116 - 147
380	25	179	157 - 205
390	29	258	230 - 288

(a) 10 nm bandwidth

(b) Calculated from slope of probit line

(c) No overlap of "Lesion" and "No Lesion" data

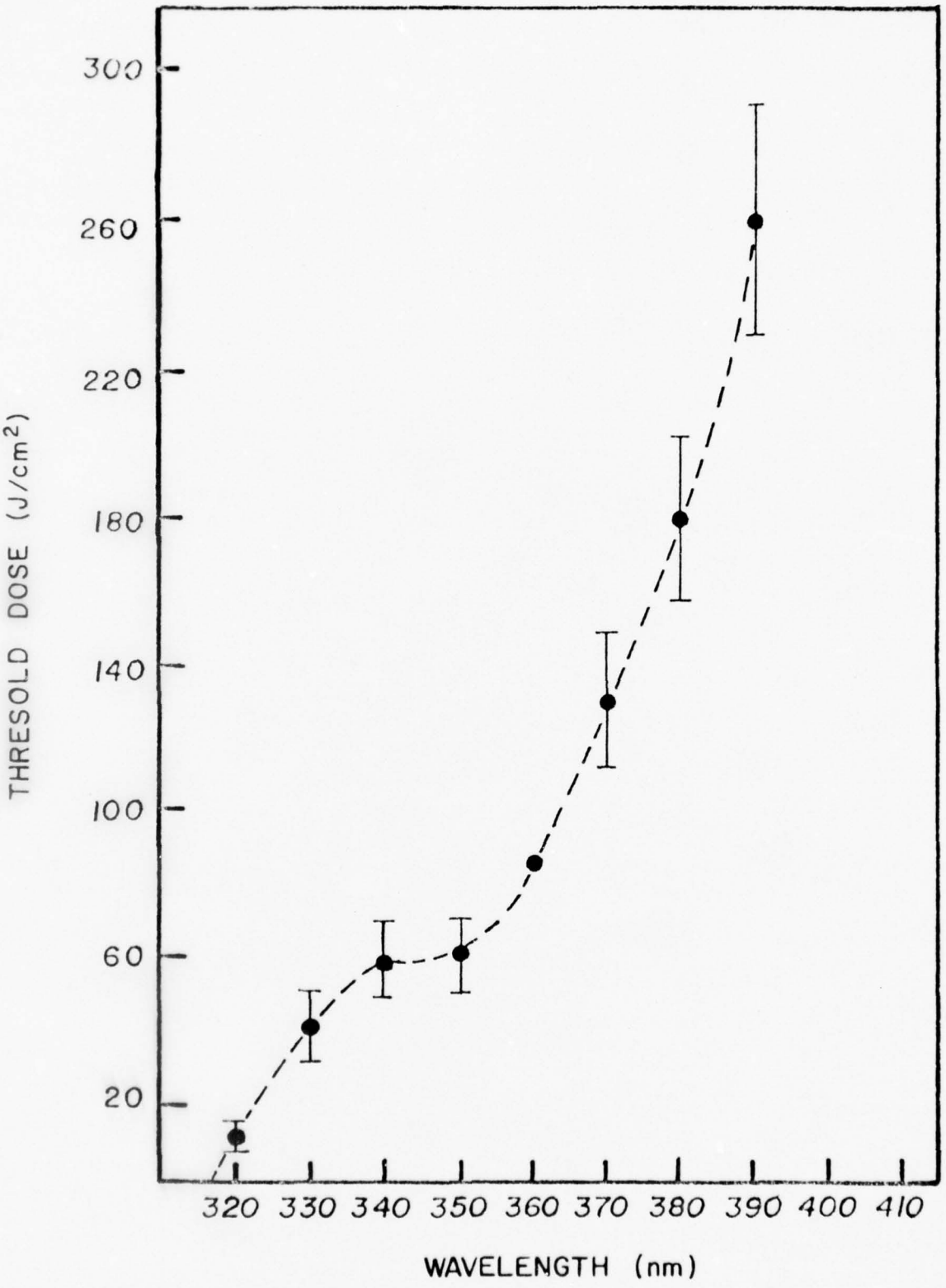

FIGURE 9-2. Experimental Thresholds for Corneal Epithelial Lesions Induced by Monochromatic, Noncoherent Near-UV Radiation.

FIGURE 9-3. Experimental Threshold for Corneal Epithelial Lesions Induced by Noncoherent UV Radiation.

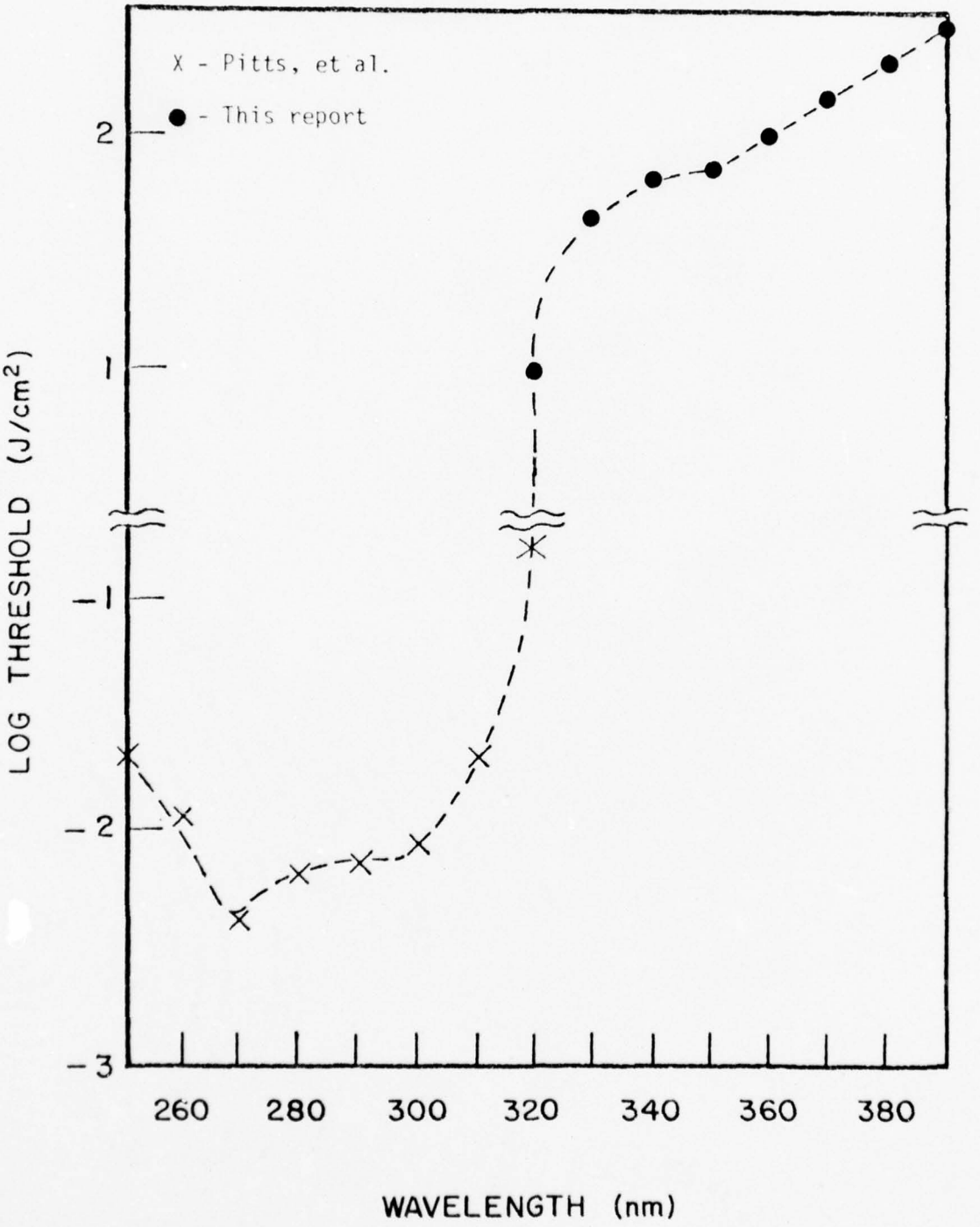

The variation of corneal threshold with wavelength displayed in Figure 9-2 is consistent with threshold determinations obtained using several different lasers with near-UV output. For instance, the threshold of 32 J/cm^2 reported[6] for exposure to 325 nm radiation from a helium-cadmium laser agrees closely with the value of ~30 J/cm^2 which can be readily interpolated from Figure 9-2.

The thresholds observed with the near-UV outputs of krypton- and argon-ion lasers require further analysis since each of these lasers emits two near-UV wavelengths. The observed threshold, $T(\lambda_1,\lambda_2)$, for a source emitting at two wavelengths λ_1 and λ_2 can be related to the thresholds $T(\lambda_1)$ and $T(\lambda_2)$ at λ_1 and λ_2, respectively by the equation:

$$\frac{1}{T(\lambda_1,\lambda_2)} = \frac{f(\lambda_1)}{T(\lambda_1)} + \frac{f(\lambda_2)}{T(\lambda_2)} \qquad (9\text{-}1)$$

where $f(\lambda_1)$ and $f(\lambda_2)$ are the respective fractional intensities of λ_1 and λ_2 radiation in the mixed wavelength source. Thus, for krypton laser radiation (350.7 nm and 356.4 nm, intensity ratio 3:1) the predicted threshold, T, is given by:

$$\frac{1}{T} = \frac{.75}{63.4} + \frac{.25}{78.7} \qquad (9\text{-}2)$$

where the thresholds $T(\lambda_1)$ and $T(\lambda_2)$ were obtained by linear interpolation of the data shown in Table 9-1. The above expression yields a predicted threshold of 66.6 J/cm^2. Similarly, for argon laser radiation (351.1 nm and 363.8 nm, intensity ratio 1:1):

$$\frac{1}{T} = \frac{.50}{64.5} + \frac{.50}{104} \qquad (9\text{-}3)$$

which gives a predicted threshold of 80 J/cm^2. These results are in close agreement with the observed thresholds of 66 J/cm^2 and 82 J/cm^2 found for 30 sec exposures to krypton and argon near-UV radiation, respectively. Thus, the apparent discrepancy between the two observed thresholds is completely explained by the wavelength dependence illustrated in Figure 9-2.

This wavelength dependence may be used to derive an empirical absorption spectrum for the molecular species involved in the near-UV photochemical damage mechanism even though the species remains unidentified. For the purpose of obtaining a quantitative photochemical model, however, one need only consider the corneal threshold dose and not the fraction of the incident energy actually absorbed by the cornea (more specifically by the corneal epithelium) or the fraction of the absorbed energy directly absorbed by or transferred to the molecular species involved in the damage mechanism. It has been shown[7,8] that for the case where the photoproduct is formed directly from an excited state of the absorbing species (assuming a single-photon absorption process), the number of molecular lesions, P, induced

by an exposure to radiation of intensity, I, and wavelength, λ, for an exposure time, τ, is directly proportional to the product of the molecular extinction coefficient, $C(\lambda)$ with $I\tau$. Thus:

$$P \propto C(\lambda)\ I\tau = C(\lambda)\ E \qquad (9\text{-}4)$$

where E is the incident energy dose. The number of molecular lesions necessary to yield observable macroscopic corneal damage, P_{Th}, is presumed to be independent of the exposure parameters. Therefore:

$$P_{Th} \propto C(\lambda)\ E_{Th}(\lambda) = \text{constant} \qquad (9\text{-}5)$$

where $E_{Th}(\lambda)$ is the threshold energy dose at wavelength λ. Using this expression and the threshold data of Table 9-1, the effective near-UV molecular extinction coefficient can be normalized to any desired wavelength. The most reliable and reproducible near-UV threshold data available appear to be the results reported in Chapter 7 for krypton laser radiation. The corneal threshold approximates 67 J/cm^2 for wide ranges of beam parameters. Thus, if $C(\lambda)$ is arbitrarily set equal to unity for λ = 352 nm (the effective wavelength of the krypton-ion laser emitting at 350.7 and 356.4 nm with an intensity ratio of 3:1), the extinction coefficient for any other wavelength follows from Equation (9-5). The results for 320-390 nm are shown in Table 9-2.

The unspecified proportionality constant in Equations (9-4) and (9-5) involves rate constants for population and depopulation of the excited singlet and triplet states of the absorbing molecule. The expressions are valid only when the pulsewidth, τ, is long compared to the excited state lifetimes (so that the differential equations for the populations of the energy levels can be solved in the steady state) and when the intensity, I, is sufficiently low that only a negligible fraction of the absorbing molecules populate the excited state at any given time[8]. These conditions are not stringent for cases of interest here and are undoubtedly satisfied for all corneal threshold data discussed in this report save possibly for the experiments involving 10 nsec pulses with $\sim$1 megawatt peak power levels from a nitrogen laser. Therefore, the data of Table 9-2 can be used together with the known dependence of corneal damage on radiation intensity and pulsewidth to predict thresholds for laser systems emitting in the near-UV for wide ranges of beam parameters; i.e., for varying wavelengths, pulsewidths and intensities as well as for varying pulse repetition rates and train lengths when multiple-pulse exposures are considered. The results, of course, would still be normalized relative to the observed threshold for krypton laser radiation or to any other suitable reference which was chosen. Further development of a quantitative photochemical model for prediction of absolute thresholds must rely on determination of the molecular rate constants referred to above.

The curves shown in Figures 9-2 and 9-3 represent the energy doses incident on the cornea necessary to induce visible damage in the epithelium. In order to extract a useful action spectrum for comparison with absorption

TABLE 9-2.

MOLECULAR EXTINCTION COEFFICIENTS FOR ABSORPTION
OF NEAR-UV RADIATION BY THE CORNEAL EPITHELIUM

Wavelength (nm)	Threshold (J/cm^2)	Extinction Coefficient (Normalized to 352 nm)
320	9.6	7.0
330	41.1	1.63
340	58.3	1.15
350	61.5	1.09
352	67.0	1.00
360	88.4	0.76
370	130	0.52
380	179	0.37
390	258	0.26

spectra of cellular constituents, it is necessary to consider the number of quanta absorbed at each wavelength rather than the intensity of the incident radiation. This conversion is carried out in Table 9-3. The first two columns list the wavelength and threshold energy dose, respectively. The third column lists the experimental thresholds expressed in terms of incident quanta/cm^2. Multiplying each of these values by the corneal absorption[9] (i.e., 1 - transmission) yields the absorbed threshold photon density, N', also in units of quanta/cm^2. Finally, the relative sensitivity, R, of the absorbing tissue is inversely proportional to the corrected threshold dose, N', and is shown normalized to 320 nm (the wavelength of highest sensitivity) in the last column.

By plotting these values vs. wavelength, a "true" action spectrum, i.e., corrected for total corneal absorption is obtained as shown in Figure 9-4. This spectrum exhibits somewhat more pronounced structure in the 340-350 nm region than the uncorrected action spectra shown in Figures 9-2 and 9-3. As suggested by the dashed lines in Figure 9-4, this spectrum may represent the superposition of an absorption tail of cellular constituents involved in far-UV photochemical damage and a second, rather broad curve representing near-UV absorbing cellular constituents. The latter with its apparent maximum at $\sim$350 nm agrees quite well with the absorption spectrum of 4-thiouridine, a nucleic acid base found in certain transfer-RNA molecules. Jagger and co-workers[10,11] have presented formidable evidence suggesting that 4-thiouridine is the target for near-UV induced damage in E. coli cells. However, there is no evidence that the target for near-UV action in mammalian cells is the same as that in bacterial cells. Furthermore, there are several other cellular constituents which have broad absorption bands centered at $\sim$350 nm and which could be regarded as potential near-UV targets in mammalian cells[10]. Examples of these are reduced nicotinamide adenine dinucleotide (NADH) and the isoprenoid benzo- and naphtho-quinones of the electron transport system. Thus, it is obvious that additional studies are required in order to identify the molecular species involved in the near-UV photochemistry in epithelial cells. However, the action spectrum reported here together with the previously reported oxygen dependence of near-UV induced epithelial damage (Chapter 8) has narrowed the field of potential candidates.

Finally, in view of the wavelength dependence of the corneal threshold discussed above together with observations of thresholds for long single-pulse exposures (Chapter 7), it is obvious that for certain combinations of near-UV exposure parameters, the ANSI[1,2] standard does not provide an adequate margin of safety. Decreasing the corneal MPE for 315-400 nm by a sufficient margin will, of course, lead to a safety standard with an adequate safety margin for all exposure parameters. However, such a standard may be unnecessarily restrictive for certain exposure parameters (e.g., for wavelengths $>$360 nm and exposure times $<10^3$ sec). Therefore, it may be desirable to divide the 315-400 nm wavelength range into two or more regions and to quote an appropriate MPE for each region.

TABLE 9-3.

WAVELENGTH DEPENDENCE OF RELATIVE SENSITIVITY (R) OF CORNEAL TISSUE

λ (nm)	Experimental Threshold (J/cm^2)	Experimental Threshold (Quanta/cm^2 x10^{-19})	Corneal Absorption[9]	N'=Absorbed Threshold Dose (Quanta/cm^2 x10^{-19})	R=1/N' (Normalized to 320 nm)
320	9.57	1.54	.523	.806	1.00
330	41.1	6.83	.440	3.05	.265
340	58.3	9.98	.388	3.87	.208
350	61.5	10.8	.340	3.68	.219
360	88.4	16.0	.295	4.72	.171
370	130	24.2	.253	6.13	.132
380	178	34.1	.228	7.76	.104
390	258	50.7	.209	10.60	.076

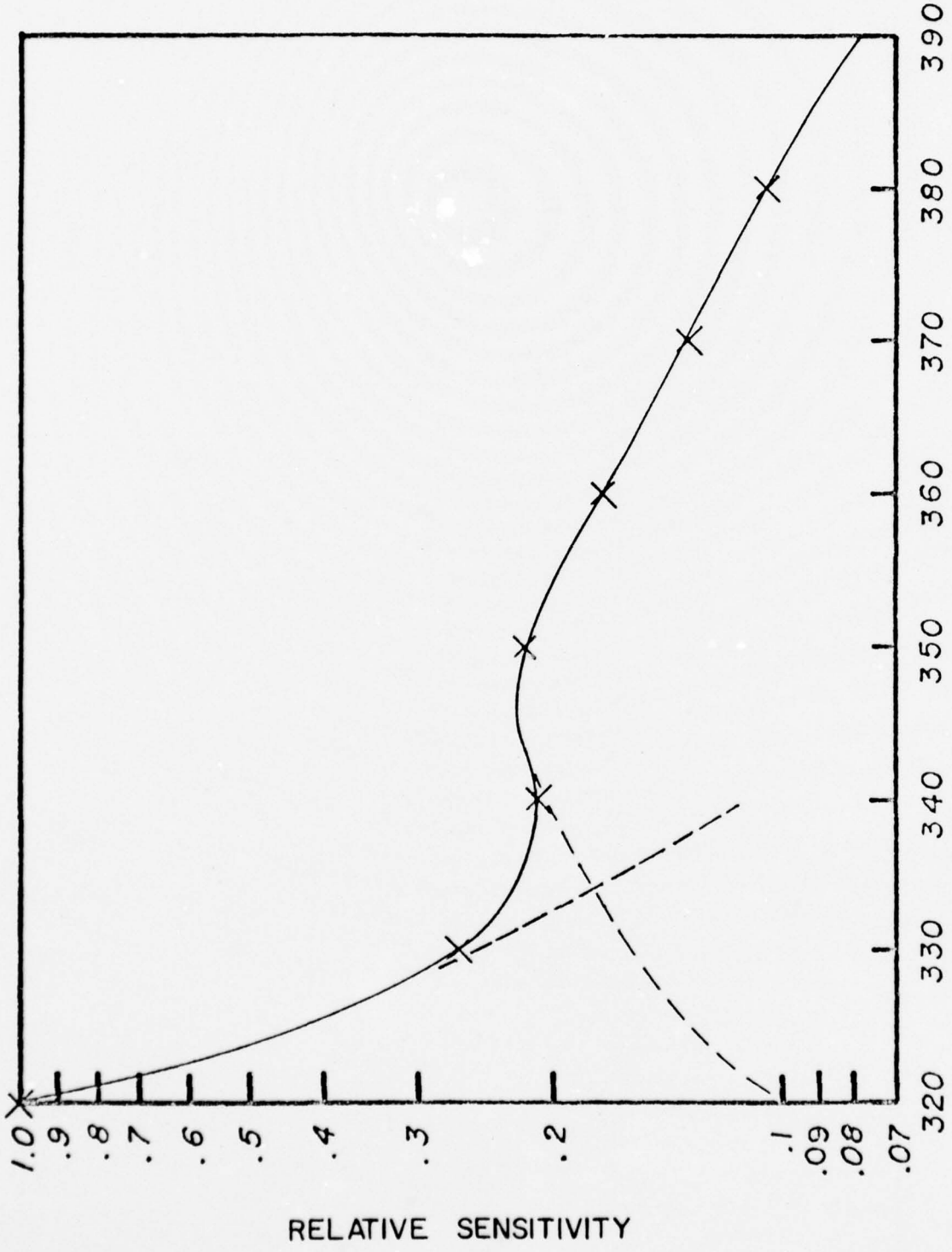

FIGURE 9-4. Relative Sensitivity of Corneal Epithelium to Absorbed Near-UV Radiation.

REFERENCES

1. "American National Standard for the Safe Use of Lasers", American National Standards Institute, Inc. Standard Z136.1, 1973.

2. American National Standards Institute, proposed laser safety standard, 1976.

3. Zuclich, J.A. and W. E. Kurtin, in "Research on the Ocular Effects of Laser Radiation", Technology Incorporated, Thirteenth Interim Technical Report, Part II, Contract F41609-73-C-0017, USAF School of Aerospace Medicine, August 1976.

4. Pitts, D.G., W.R. Bruce and T.J. Tredici, "A Comparative Study on the Effects of Ultraviolet Radiation on the Eye", SAM-TR-70-28, USAF School of Aerospace Medicine, Brooks AFB, Texas 1970.

5. Pitts, D.G. and T.J. Tredici, "The Effects of Ultraviolet on the Eye", Amer. Ind. Hygiene Assoc. J. 32:235, 1971.

6. Ebbers, R.W. and D. Sears, "Ocular Effects of a 325 nm Ultraviolet Laser", Amer. J. Optom. and Physiol. Optics 52:216, 1975.

7. Zucilch, J.A., et al., in "Research on the Ocular Effects of Laser Radiation", Technology Incorporated, Second Annual Report, Part II, Contract F41609-73-C-0017, USAF School of Aerospace Medicine, February 1975.

8. Zuclich, J.A., ibid., First Annual Report, February 1974.

9. Boettner, E.A. and D. Dankovic, "Ocular Absorption of Laser Radiation for Calculating Personnel Hazards", University of Michigan, Final Report, Contract F41609-74-C-0008, USAF School of Aerospace Medicine, Brooks AFB, Texas, October 1974.

10. Ramabhadran, T.V., "Near-UV Effects on Synthesis in E. coli B/r", Photochem. Photobiol. 22:117, 1975.

11. Ramabhadran, T.V., T. Fossum and J. Jagger, "In Vivo Induction of 4-Thiouridine-Cytidine Adducts in t-RNA of E. coli B/r by Near-Ultraviolet Radiation", Photochem. Photobiol. 23:315, 1976.

CHAPTER 10

LENTICULAR EFFECTS OF NEAR-UV LASER RADIATION

Joseph A. Zuclich

The question of a corneal maximum permissible exposure (MPE) for a given set of beam parameters as quoted by the ANSI standard[1,2] is evidently of little consequence if other ocular tissues are more sensitive than the cornea. This work has revealed certain conditions where this is indeed the case. A discussion of retinal lesions induced by near-UV laser radiation was presented in Reference 3 along with a brief description of preliminary observations of reversible lenticular clouding which resulted from certain laser exposures. More recent work has revealed conditions where permanent lenticular opacities are induced with energy doses less than those required to cause corneal damage. These experiments which utilized the near-UV emissions of argon-ion and nitrogen lasers are described below. Experimental techniques were essentially identical to those reported for corneal damage experiments in Chapter 7. Lenticular observations were made with the same slit lamp microscope used for the corneal work.

The krypton-ion laser experiments discussed in Chapter 7 did not lead to permanent lenticular lesions in any subject regardless of exposure time. However, doses of an order of magnitude or more greater than the corneal epithelial threshold did cause reversible clouding on the anterior surface of the lenses. The clouding could be observed with the slit lamp after the corneal lesions had repaired (two to three days post-exposure). In every case, this lenticular clouding completely cleared within one month. Animals which exhibited the reversible clouding were monitored for up to nine months following the exposures but no further lenticular anomalies developed.

With the high powers (up to 1W) of continuous UV output (351.1 and 363.8 nm, intensity ratio ~1:1) available from the Spectra Physics 170 argon-ion laser, cataracts could be induced with relatively short exposure times, and under some conditions are observable immediately following the exposure.

Figure 10-1 shows a cataract induced by a 1 sec exposure to 500 mW of near-UV laser radiation at a corneal dose of 21 J/cm^2. The picture was taken less than five minutes following exposure. For exposures just above lenticular threshold, the opacity may take some time to develop and may not be visible until several hours post-exposure. An 18 hour criterion was arbitrarily chosen for lesion determination, chiefly because this conforms with the protocol for corneal lesion determinations (Chapter 7).

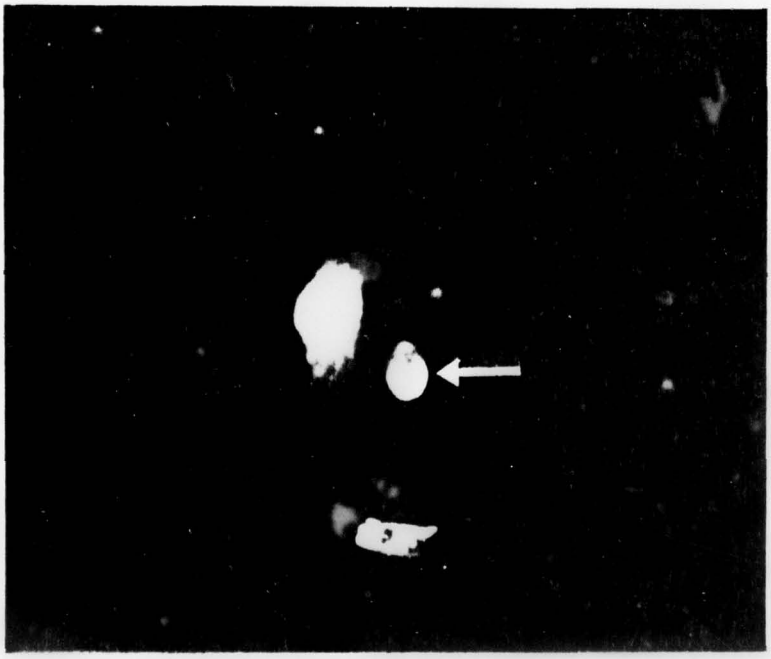

FIGURE 10-1. Slit Lamp Photograph of Cataract Induced by Near-UV Output of Argon Laser. Corneal dose, 21 J/cm^2. The egg-shaped cataract (arrow) is seen to the right of the source reflection from the corneal surface. A reflection from the lid is seen below the cataract.

The lenticular threshold for 4 sec exposures to argon laser radiation is 76.4 J/cm^2 incident at the cornea, equivalent to a corneal irradiance of 19 W/cm^2. For 1 sec exposures, the threshold dose is 18.7 ± 1.8 J/cm^2, again equal to an irradiance of ∿19 W/cm^2. In this case, the threshold dose is only ∿25% of the expected corneal threshold.

Lenticular opacities were also induced by the 337 nm emission of the Molectron UV-1000 nitrogen laser. A single ∿10 nsec pulse focused onto the cornea (peak power output ∿1 megawatt to yield a corneal irradiance of 1.1 J/cm^2) was sufficient to cause a barely visible clouding on the anterior surface of the lens. Trains of two or more pulses induced distinct cataracts visible immediately following the exposure. Figure 10-2 illustrates two nitrogen laser-induced cataracts resulting from doses of 120 J/cm^2 (upper) and 56 J/cm^2 (lower), observed at less than five minutes post-exposure. In at least one case, there was some progression of such cataracts with time. Figure 10-3 shows a rhesus eye with two nitrogen laser-induced cataracts observed at three months post-exposure. Initially, the appearance of these lesions was similar to those shown in Figure 10-2, but after three months there was evidently some further degeneration of the tissue surrounding each lesion. However, the majority of the UV laser-induced cataracts did not change in appearance for periods of up to one year following exposure.

Some of the less severe lenticular lesions have shown some fading and apparent diminution after several months. In contrast, in one case where no lenticular lesion was found immediately or at 18 hours post-exposure, a distinct cataract was observed in the exposed area at two months post-exposure.

In view of these conflicting preliminary observations, it is clear that further long-term (up to several years) studies will be required to decide if there is, in fact, any danger of eventual cataract development from single or repeated exposures to doses less than those required to cause immediate lenticular opacities. Similar studies will be required to decide if there is danger of further progression of those cataracts which are found immediately following exposure, or if there is some chance of eventual attrition of these opacities.

Although the lenticular data are at present too sparse to draw any conclusions regarding the damage mechanism, the deviations from an equal energy dose seem significant and it is obvious that a photochemical mechanism such as that operative in the corneal epithelium is not involved here. As noted above, the lenticular thresholds for 1 sec and 4 sec exposures are both equivalent to a corneal irradiance of ∿19 W/cm^2. Further, the maximum output of the unfocused krypton beam (∿5 W/cm^2 incident at the cornea) is not sufficient to induce cataracts even with exposure durations of several minutes. Both of these facts suggest a peak power phenomenon which in turn could imply a thermal damage mechanism. In order to obtain further support for this hypothesis, the IITRI thermal model[4] was used to calculate lenticular thresholds for 350 nm radiation for a wide range of pulsewidths.

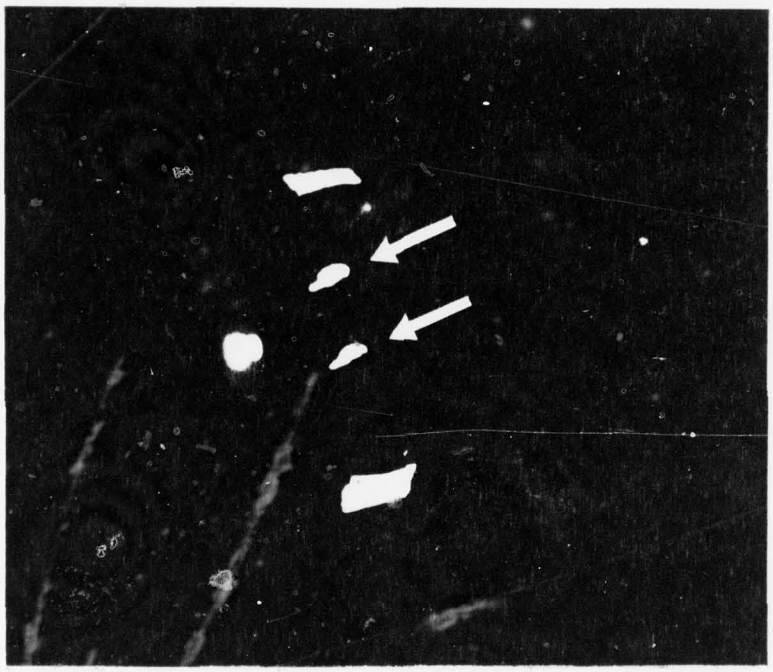

FIGURE 10-2. Slit Lamp Photograph of Cataracts Induced by Trains of 10 Nanosecond Pulses from Nitrogen Laser. Corneal doses, ~120 J/cm^2 (upper cataract) and ~60 J/cm^2 (lower cataract). A reflection of the slit lamp source form the corneal surface is seen to the left of the cataracts (arrows). Reflections from the lids are seen above and below the cataracts. Photograph taken less than five minutes post-exposure.

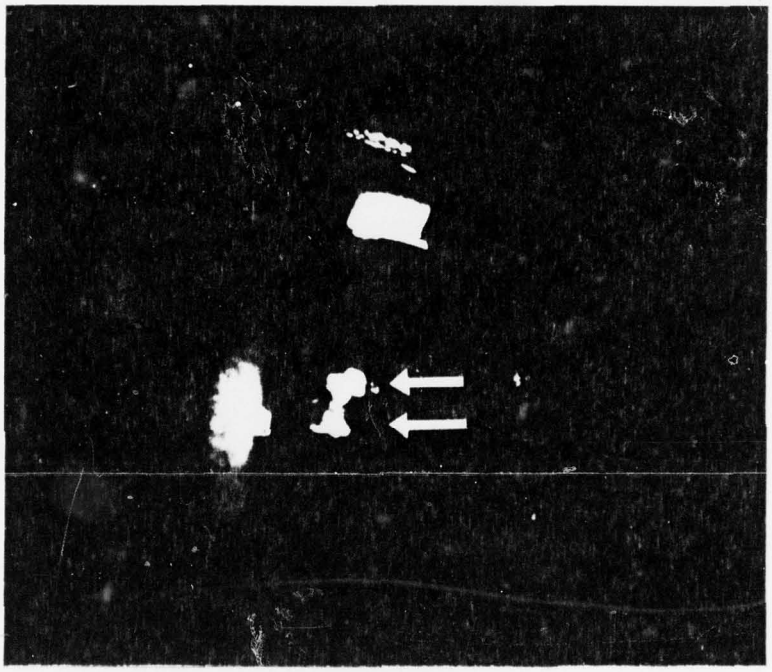

FIGURE 10-3. Slit Lamp Photograph of Cataracts Induced by Trains of 10 Nanosecond Pulses from Nitrogen Laser. Corneal doses, ∿120 J/cm^2 (upper cataract) and ∿60 J/cm^2 (lower cataract). A reflection of the slit lamp source from the corneal surface is seen to the left of the cataracts (arrows). A reflection from the lid is seen above the cataracts. Photograph taken ∿3 months post-exposure.

The predicted thresholds for exposure times ranging from 10^{-5} to 10^{4} sec are shown in Table 10-1. The data are plotted as an irradiance vs. pulsewidth curve in Figure 10-4. Also plotted in Figure 10-4 are the experimental argon laser lenticular thresholds for 1 and 4 sec exposure times, the approximate threshold (1.1 J/cm^2) for cataracts induced by 10 nsec pulses from the 337 nm radiation from a nitrogen laser, and the lenticular threshold reported by Ebbers and Sears[5] for 325 nm radiation from a helium-cadmium laser. It is seen that the trend of the limited experimental data is parallel with the predicted curve and, in any case, is clearly not in accord with the equal energy dose curve found for corneal thresholds. It should be pointed out, however, that although the thermal model has proven to be reliable in predicting retinal damage thresholds over wide ranges of beam parameters[4] there has been no previous opportunity to test the success of the model in predicting lenticular thresholds.

TABLE 10-1.

LENTICULAR THRESHOLDS FOR 350 nm RADIATION.
PREDICTED BY IITRI THERMAL MODEL[4]

Pulsewidth (sec)	Threshold Irradiance (W/cm^2)
10^{-6} and less	*
10^{-5}	8.2×10^5
10^{-4}	7.9×10^4
10^{-3}	7.4×10^3
10^{-2}	7.2×10^2
10^{-1}	77
1	13.4
2	9.2
4	7.4
10	5.85
10^2	3.75
10^3	2.55
10^4	1.73

*Outside normal precision of program.

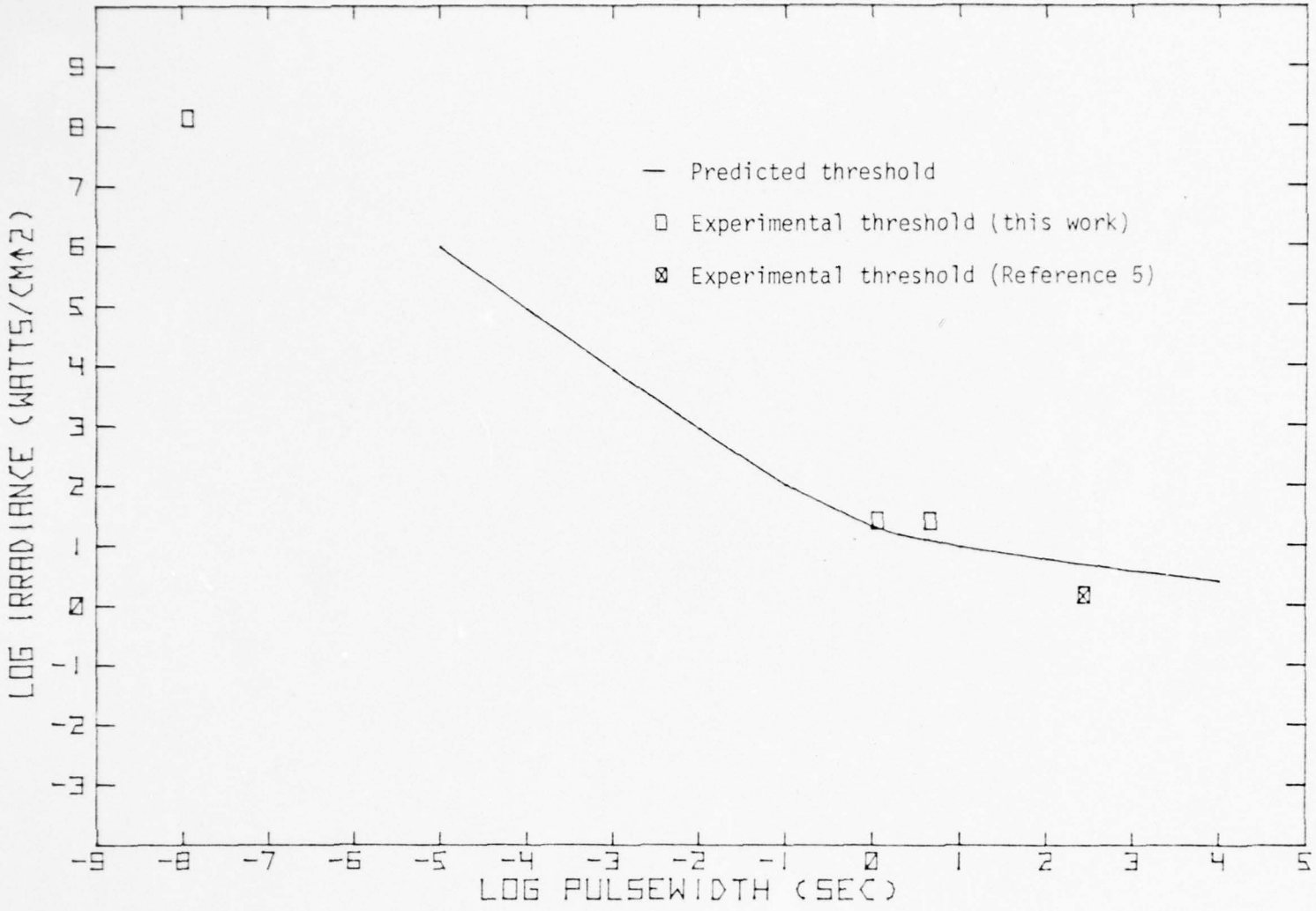

FIGURE 10-4. Comparison of Experimentally Determined Lenticular Thresholds with Thresholds Predicted by Thermal Model Calculations.

REFERENCES

1. "American National Standard for the Safe Use of Lasers,"American National Standards Institute, Inc. Standard Z136.1, 1973.

2. American National Standards Institute, proposed laser safety standard, 1976.

3. Zuclich, J.A., et al., in "Research on the Ocular Effects of Laser Radiation", Technology Incorporated, Second Annual Report, Part II, Contract F41609-73-C-0017, USAF School of Aerospace Medicine, February 1975.

4. Takata, A.N., et al., "Thermal Model of Laser-Induced Eye Damage", Illinois Institute of Technology Research Institute, Final Technical Report, Contract F41609-74-C-0005, USAF School of Aerospace Medicine, October 1974.

5. Ebbers, R.W. and D. Sears, "Ocular Effects of a 325 nm Ultraviolet Laser", Amer. J. Optom. and Physiol. Optics 52:216, 1975.

PART III

NEUROPHYSIOLOGY AND PHYSIOLOGICAL OPTICS

CHAPTER 11

VISUAL EVOKED RESPONSE

J. Terry Yates

A. BACKGROUND

The preceding chapters of this report discuss macroscopically observable changes in the rhesus monkey eye following exposure to high intensity laser radiation. These studies, while quite important for the assessment of the extent of ocular damage, say little about the loss of visual function that follows such insult. Of more concern is the possibility that a functional loss has occurred in the visual system, even though the injury is not macroscopically observable. It would seem that the ultimate factor determining the classification of laser systems and the specification of laser safety standards must rest upon the assessment of loss of visual function, whether such loss is long term or immediate. For this reason, a program was initiated to develop neurophysiological procedures for estimating damage to the visual nervous system.

The spatial resolving power of the visual system can be investigated by using spatial sine wave gratings as stimuli. An observer's ability to discriminate a grating pattern of this kind is a function of the modulation depth (contrast) and the spatial frequency (cycles per degree of visual angle) of the grating. In recent visual system investigations, modulation transfer functions (MTF's) have been obtained which describe the minimum stimulus contrast needed for (threshold) detection at varying spatial frequencies. An MTF may be briefly described as the loss in contrast (modulation depth) in an image plane as a function of spatial frequency in an object plane. It should be noted that the applicability of linear systems analysis to visual information is valid at threshold, where the system is known to behave in a linear fashion[1,2]. Recent reports give credence to the notion that the system is also linear when operating on chromatic spatial stimuli and at suprathreshold levels[3]. Perhaps the primary benefit of using sine wave grating stimuli is that they can be used in neurophysiological investigations as well as psychophysical studies. As a consequence of using the same type of stimulus in these otherwise separate investigative procedures, meaningful comparisons can be made between an organism's ability to discriminate spatial detail and the underlying neurophysiology.

There is little doubt that the cortically represented visual system of primates is organized in large part to extract pattern information. Hubel and Wiesel have demonstrated the binocular convergence of information in the visual cortex, the columnar organization within areas 17 and 18, and the salient details of feature extraction by simple, complex and hypercomplex cells within those cortices[4-7].

A recent investigation limited solely to the foveal projection of area striata found changes in chromatic information processing within the laminae of the foveal cortex which parallel changes in pattern information processing[8]. Indeed, if the proper "feature detectors" of such cells were not carefully "tuned", it was not possible to extract chromatically selective responses. For example, if a cell were of the complex type of Hubel and Wiesel[4] it was found essential that the light stimulus be made the proper width, oriented at the proper angle and swept across the receptive field at an optimal velocity in order for it to be activated.

The cells of area striata may be conceived of as an aggregate of tuned harmonic resonators. A sinusoidal luminance distribution (grating) will selectively activate some of those resonators. By means of a suitably coarse electrode, an electrical signal may be recorded from the brain, the amplitude of which is linearly related to the logarithm of stimulus contrast[9]. It has been shown in man and cat that the (extrapolated) zero value of the signal occurs at a stimulus contrast that corresponds to the psychophysical threshold. Simply put, when the stimulus can not be seen, the cortical cells do not respond. The importance of the observation, of course, is that a biological signal exists that can be related to behavioral data and that can be used to predict behavior. The savings in training time for animal psychophysics is potentially very great.

Although the visual system is responsible for the analysis of an impressive number of attributes of a visual scene, perhaps the most noticeable and devastating losses are those which impair the capacity of that system to resolve spatial detail. It was for this reason, and the fact that recent developments in theory and data analysis procedures have taken a quantum jump in sophistication, that the visual dimension related to spatial resolving power was chosen as a starting point for these studies.

A variety of scalp recorded evoked responses have been categorized as visual evoked responses (VER's). For that reason, some confusion exists about the nature of the cortically evoked electrical events in any VER experiment. In studies of this sort, the a priori intention is to isolate a stimulus dimension and manipulate it as an independent variable while eliminating the influence of other attributes either by holding their influence constant or by removing the attribute from the stimulus situation.

Two major sorts of VER have been described and will be briefly mentioned here. The best investigated sort of VER is that arising from a stimulus that may be described as a spatially-unstructured field. These are large area, usually flash activated, stimuli that are most aptly used to investigate the temporal visual system or alternatively in clinical settings to provide a continuity check between retina and brain. Quite different is the VER related to the spatial structure of the stimulus field. Careful control of stimulus parameters permit a transfer function to be established describing the relationship between the relevant stimulus dimension and the organism's behavior with concommitant knowledge of the underlying electrical events. To be able to obtain all of these estimates in one experimental paradigm is most unusual.

As typically carried out, the process is described as steady state stimulation since a repeating stimulus is continuously presented, and it is assumed that the visual system has "adapted" to a number of other stimuli and test conditions. The nervous sytem will, more or less, produce a stream of stimulus dependent potentials at a constant amplitude and frequency related in some way to the stimulus. The neurophysiological task is to analyze that stream of electrical events and determine the quantitative nature of the neurophysiological parallelism with the stimulus. In the specific case of steady state, pattern evoked VER's, the task is simplified by the nature of the stimulus.

It may be argued that gratings which temporally alternate in counter-phase (180^0 phase reversal) while spatial frequency is held constant primarily activate spatially tuned cells. Brightness is constant due to temporal integration and can have no effect. If a suitable biological signal which is bandwidth-limited at the temporal alternation rate, is derived by filtering techniques, one may imagine that only events that are related to spatial variables are being sampled, since only the spatial stimulus parameter is varying. It was this technique that was successfully utilized in man and cat to estimate behavioral contrast sensitivity thresholds, and therefore was proposed for use with monkey.

Estimates of the transfer function (MTF) of the rhesus monkey eye exist(10) together with estimates of the combined performance of retina-brain and eyeball optics. The latter take the form of contrast sensitivity functions obtained during animal psychophysics experiments(11). It should prove possible to correlate biological signals derived from the monkey visual cortex with those known behavioral and optical properties of the rhesus monkey spatial visual system.

Laser exposures below the threshold for tissue damage constitute a special case of a more general paradigm in visual science known as transient adaptation. A rapid luminance change perturbs the system and adaptation consequently changes. Differences in spatial, chromatic, temporal and binocular resolving power have been reported. Perhaps the least well investigated changes are those which occur in the spatial achromatic and spatial chromatic systems.

B. METHOD

A variety of special purpose devices was necessary in order that a spatial sinusoidal luminance pattern could be generated on a CRT "face" and that appropriate 180^0 phase shifts could be introduced periodically and at will.

A simplified CRT display system was designed, built and calibrated. A high frequency (60 KHz) triangular wave was applied to the vertical input of a conventional oscilloscope to provide a "raster-like" display. Modulation of the oscilloscope z-axis with a sinusoid results in an illuminance distribution whose intensity varies sinusoidally across the extent of the tube face. The contrast of the display may be varied by changing the z-axis input voltage and analogously the spatial frequency (number of sinusoids per degree of visual angle) may be varied by changing the modulation frequency. In order to alternate stripes in counterphase (180^0 phase reversal), a special circuit was devised so that, when triggered, phase coherent sine wave bursts could be generated at one of two phase angles: either at a reference phase, which we shall describe as phase 0, or at 180^0 with respect to the reference. At regular intervals, but always at the start of an oscilloscope sweep, a phase reversal is introduced. A reversal frequency of 8 or 16 Hz may be selected. Additional circuitry makes it possible to maintain constant space averaged luminance (luminance integrated over the target area) while contrast is varied. (See Appendix 11-A).

Contrasts were evaluated by means of a microphotometer. A square wave was used to modulate the z-axis of the display in order to ascertain the intensities of the maxima and minima of the luminance profile. It can be demonstrated that that procedure gives values equivalent to those obtained from direct measurement of sine wave peak and trough intensities. The possibility of sampling errors due to the use of a fixed spatial sampling aperture is thus avoided. Average luminance was evaluated with a telephotometer and was maintained at a 1 fC level. Due to the variability in luminous output of the available oscilloscope and to the ease of disturbing control settings, a "spot" check of important parameters was carried out before each experimental run.

Sintered silver/silver chloride surface electrodes were applied to the scalp of an observer following the usual cleansing and decornification procedures. Seventy percent methanol was used to remove surface oil and tissue debris. Electrodes were affixed over the inion and 2.5 cm lateral to that placement. A reference electrode was attached to an ear lobe. Electrodes were held in place by a commerical adhesive tab routinely used for that purpose. A standard electrolyte paste was applied to the scalp-electrode interface.

Differential amplification was used throughout. A gain of $1x10^7$ to $1x10^8$ was necessary since the relevant biological signal is approximately 0.1 to 1 μV, whereas the signal processing unit requires peak voltages close to ± 5 V to achieve full digital resolution. Data were tape recorded on FM tape along with suitable synchronization signals for later processing.

Recorded data were narrow band filtered at 16 Hz by means of a band-pass filter centered to capture responses related to the stimulus counter-phase alternation frequency of 8 Hz. It should be noted that an alternation frequency of 16 Hz actually corresponds to twice that rate since the stimulus changes phase at 1/2 cycle intervals. This frequency was chosen because it

is well above the band of frequencies characteristic of endogenous brain activity (especially alpha rhythm) and the resultant filtered waveform was found to be approximately sinusoidal in form. Alternation rates substantially higher cause non-sinusoidal data to be recorded, while slower rates produce data that are contaminated by the spontaneous rhythms of the brain.

A filter of Butterworth design with 12 db per octave "skirts" was fabricated for this purpose. The gain of the filter was such that the 1 V dynamic range of the magnetic tape unit could be boosted to the required level.

One thousand responses to a sine wave stimulus were averaged by conventional procedures. A variety of stimuli were presented covering the contrast range of interest as well as two baseline conditions. In one condition data were obtained with the subject's eyes closed and the oscilloscope occluded. In another condition the subject viewed a glowing, but patternless, oscilloscope. The former assesses the magnitude of spectral components from brain rhythms other than those of interest. The latter gives an indication of any effects due to diffuse field luminance interruptions.

Data were collected from an emmetropic observer with natural pupils under free viewing conditions. The only instructions to the subject were to "relax" (this process reduces the likelihood of recording unwanted muscle potential artifacts) and to "look at" the display screen. No specific instructions were given regarding eye fixation.

C. RESULTS AND DISCUSSION

Figure 11-1 is a graphical representation of the data collected for two spatial frequencies. As is frequently the case in sensory systems, the measured attribute (microvolts of visual evoked response) is proportional to the logarithm of stimulus intensity (Michelson contrast). A linear regression was performed for each of the two data sets. Coefficients of determination of 0.89 and 0.99 were found for stimulus conditions of 15 Hz/deg and 5 Hz/deg (visual angle) respectively. This relationship implies that a remarkable amount of the variance in the measured attribute may be accounted for by changes in the independent variable. Extrapolation of the fitted line through the abscissa has been previously shown to give an estimate of the contrast value necessary to just see a grating[5]. There is a strong dependency between the derived physiological potential and behavioral estimates of contrast sensitivity. For a 15 Hz/deg stimulus, the estimated threshold contrast was 0.145 and similarly for a 5 Hz/deg target, the value was 0.0075. These values clearly indicate a lesser sensitivity of the spatial visual nervous system to higher spatial frequencies. The obtained values are well within the range of known behavioral threshold values for targets of this luminance and size and for these presentation conditions[9].

FIGURE 11-1. Summed Evoked Response Amplitude vs. Contrast for Two Spatial Frequencies. Open squares indicate a stimulus stripe pattern with 15 Hz/degree. Crosses are for a 5 Hz/degree target.

It seems clear that the visual cortex with its highly specialized pattern processing capabilities is highly activated by the pattern stimuli used as targets. A useable signal of biological origin can be extracted to estimate spatial visual functioning. The methodology employed needs a better quantitative base. The implementation of more sophisticated spectral analysis techniques would, of course, help clarify the measurement problem. It should be noted that equipment limitations would not permit estimation of the rapidity and reliability with which measures could be obtained nor was it possible to investigate and obtain optimal electrode placement.

The narrow band filtering process used is only one of several processes that may be used to extract signal from noise. As such, it behaves in a fashion analogous to a comb filter. The frequency of interest is contained in a narrow frequency band which passed through the filter. All other frequencies, whether biological in origin or otherwise, may be thought of as "noise". Fourier analysis may be thought of as representing the ultimate case of a comb filter. Each frequency in the spectrum may be analyzed in total isolation from any other frequency. By analogy, a filter centered at exactly the frequency of interest, and exactly 1 Hz wide with infinite rejection of unwanted frequencies is realizable. As would be predicted for the Fourier analysis of a sinusoid buried in band limited noise, a line spectrum was seen at the alternation frequency and significantly lower spectral components were seen elsewhere. In general, the amplitude of the spectral data line was large for high contrast stimuli and smaller for low contrast stimuli, but in all cases was orders of magnitude larger than EEG noise components such as the alpha rhythm. This analysis technique holds great promise for isolating contrast specific components of evoked brain activity and should afford better noise reduction than techniques whose spectral resolving power is based on broader bandwidths.

AD-A043 457 TECHNOLOGY INC SAN ANTONIO TEX LIFE SCIENCES DIV F/G 6/18
RESEARCH ON THE OCULAR EFFECTS OF LASER RADIATION.(U)
AUG 77 J A ZUCLICH, J T YATES, A D NAWROCKI F41609-73-C-0017
UNCLASSIFIED TI-77-0561-03 NL

3 OF 3
AD A043457

END
DATE FILMED
9 -77
DDC

REFERENCES

1. Campbell, F.W., R.H.S. Carpenter and J.Z. Levinson, "Visibility of Aperiodic Patterns Compared with That of Sinusoidal Gratings", J. Physiol. Lond. 204:283, 1969.

2. Campbell, F.W. and J.G. Robson, "Application of Fourier Analysis to the Visibility of Gratings", J. Physiol. Lond. 197:551, 1968.

3. Regan, P., "Colour Coding of Pattern Responses in Man Investigated by Evoked Potential Feedback and Direct Plot Techniques", Vis. Res. 15:175, 1975.

4. Hubel, D.H. and T.N. Wiesel, "Receptive Fields of Single Neurons in the Cat's Striate Cortex", J. Physiol. 148:574, 1959.

5. Hubel, D.H. and T.N. Wiesel, "Receptive Field, Binocular Interaction and Functional Architecture in the Cat's Visual Cortex", J. Physiol. 160: 105, 1962.

6. Hubel, D.H. and T.N. Wiesel, "Shape and Arrangement of Columns in Cat's Striate Cortex", J. Physiol. 165:559, 1963.

7. Hubel, D.H. and T.N. Wiesel, "Receptive Fields and Functional Architecture of Monkey Striate Cortex", J. Physiol. 195:215, 1974.

8. Yates, J.T., "Chromatic Information Processing in the Foveal Projection area striata of Unanesthetized Primate", Vis. Res. 14:163, 1974.

9. Campbell, F.W. and L. Maffei, "Electrophysiological Evidence for the Existence of Orientation and Size Detectors in the Human Visual System", J. Physiol. Lond. 207:635, 1970.

10. Yates, J.T. and T.H. Harding, "Monkey Spatial Vision: Physiological Optics Evaluation", Vis. Res., in press, 1977.

11. Yates, J.T. and T.H. Harding, "Monkey Spatial Vision Psychophysical Studies", Vis. Res., in press, 1977.

APPENDIX 11-A

COUNTERPHASE GRATING STIMULATOR

A special purpose circuit was constructed to interface with a cathode ray tube display in order that counterphase spatial sinusoidal gratings could be displayed and a wide range of experimental parameters adjusted at will.

Principle of Operation

A pulse generator serves as the master time base for the system and is initially set to provide a 1 KHz repetition rate. The pulses serve to trigger two devices, an integrator (ramp generator) and a binary ripple counter. The former serves to drive the x-axis of the display. The latter determines the number of sweep repetitions generated before a phase change is initiated. A binary thrumbwheel switch selects a submultiple of the base frequency from the master time base after division by the ripple counter. In this fashion, n, n/2, n/4, n/8, n/16, ..., N rates are obtainable, where n = the base rate and $N = n/2^X$ = division by powers of two. The extreme range of possible rate division coupled with a precise but variable time base offer unusual flexibility in control of grating alternation frequencies.

The output of the ripple counter is a logic level that must be scaled to achieve +1 volts when asserted and -1 volts when false. An operational amplifier (labeled "scaler" in Figure 11-A-1) performs that function.

The critical element in this system is an analog multiplier (labeled "multiplier" in Figure 11-A-1). In this application, a phase coherent sinusoid derived by triggering a Wavetek model 116 oscillator from the master time base is multiplied by either +1 or -1 by the multiplier. A sinusoid when cross multiplied by +1 volts will result in an unchanged multiplicand, whereas a -1 volt multiplier will result in a 180^0 phase shift of the multiplicand.

Many display oscilloscopes change the dc level at which the z-axis input operates as increasing frequencies are applied. Since the modulating signal arising from the multiplier circuit must be applied to the z-axis, a brightness adjustment circuit has been provided. Any change in luminance that is frequency dependent may be nulled by suitable manipulation of the brightness control circuit.

The ramp generating circuitry is somewhat unique and deserves further comment. The circuit is an operational amplifier based integrator. In the absence of an input, FET transistor (3N141) behaves as a closed switch

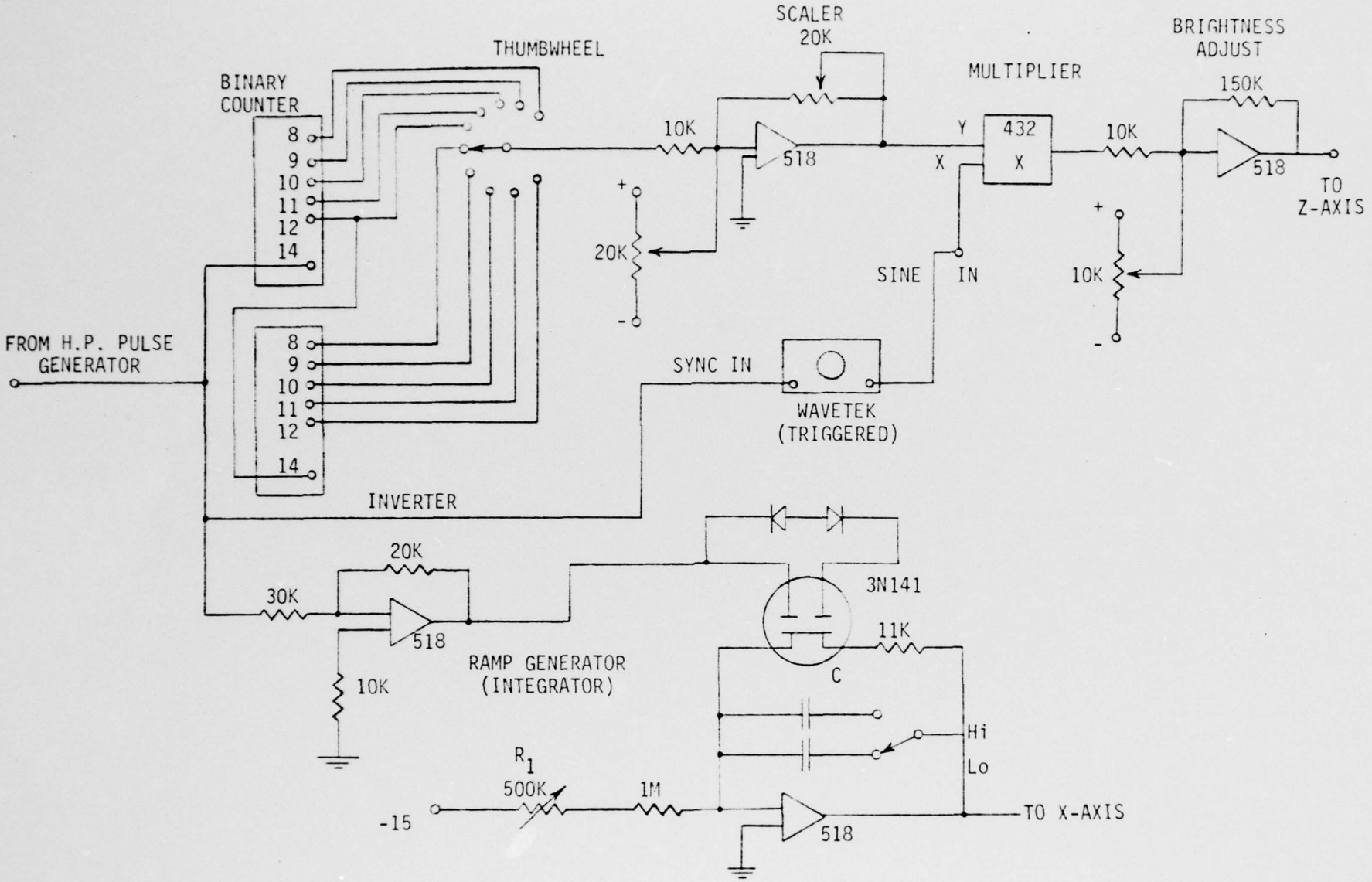

FIGURE 11-A-1. Diagram of a Spatial Sinusoidal Grating Stimulus Generator.

and the integrator capacitors are shorted; therefore, no integration will occur. Upon gating by the inverting amplifier (see Figure 11-A-1), the feedback capacitor is free to charge and integration begins at a rate determined by R_2 and C, such that the integrators bandpass frequency = $1/2\pi RC$. By changing the capacitor of integration (switch selectable) a different bandpass may be obtained. When the gate signal is removed, the transistor switch closes, the capacitor is discharged and the integrator is reset. This process occurs once per "tick" of the master time base.

Sequence of Events

The master time base/ripple counter combination determines the number of oscilloscope sweeps during which the spatial sine wave pattern is presented at a reference phase of 0^0. For most applications, a 1 KHz time base rate is selected and a counter rate of 64 counts is thumbwheel switch selected. After 64 counts of 1 msec, the phase of the grating is reversed to phase 180^0 with respect to reference phase by means of the multiplier circuit previously described. Since 1/64 msec = 15.625 Hz, the selected rate will produce a reversal rate of approximately 16 Hz. Obviously, a thumbwheel selected division of 128 and a 1 KHz time base rate will double the time alloted and result in a 1/128 msec = 7.8125 Hz rate.

The y-axis of the display must be supplied with a high frequency triangular waveform in order that the display's "face" appears to be flooded and to glow uniformly.

The timing circuitry provided may be bypassed by means of the calibrate switch and the display will not change phase. The fixed sine wave pattern may then be calibrated by standard photometric means.

CHAPTER 12

PHYSIOLOGICAL OPTICS

J. Terry Yates and Fred M. Loxsom*

A. INTRODUCTION

Any complete understanding of the spatial visual process must include estimates of the influence of the dioptric apparatus on image processing. Perhaps the best estimates of the eye's dioptrics are obtained from application of methodologies derived from Fourier optics. Modern procedures began with Lambert, Higgins and Wolfe, who used a thin luminous line as an object and photoelectrically evaluated its image(1). That image was degraded in sharpness into a smooth luminance distribution termed the linespread function. The magnitudes of the Fourier transformation of the linespread function provide information about the processing of contrast information by the system. The result is an optical modulation transfer function (MTF). The linespread and the MTF are Fourier transforms of each other(2-4). The linespread methodology has been applied to the human eye(5), cat eye(6) and monkey eye(7). In most cases, the reflected fundal image was broader than would be predicted if the only influence on image quality were diffraction effects from the bending of rays as they traversed the eyeball's pupil. The source of further degradation was thought to be due to chromatic and spherical aberration.

It has been known for some time that the eye is substantially aberrant with respect to visible wavelengths, being myopic for "blue" light, hyperopic for "red" light and in focus for midspectral hues. It is remarkable that the accommodative apparatus attempts to cope dynamically with the three diopter change of focus required to keep images at the spectral extremes in focus. That such chromatic differences are apparent can be seen by the fact that subjective (psychophysical) and objective (electro-optical) evaluations of human chromatic aberration are in good agreement, a fact that has only recently been appreciated(8).

Since so much emphasis has been placed on retinal thresholds for laser damage for data obtained from the cycloplegic, mydriatic eye of the rhesus monkey, it is desirable, if not necessary, to obtain estimates of the change in focus in that eye as the wavelength is varied. The rhesus eye is remarkably similar to the eye of human when suitable estimates of ocular size (and the resulting dioptric differences) are considered(7). In general, the same sorts of focus errors seen in the human eye would be expected; only quantitative differences would occur.

* National Science Foundation Faculty Research Participant, Summer 1976. Permanent address: Department of Physics, Trinity University, San Antonio, Texas, 78284.

Most efforts to measure chromatic focusing errors in the human have employed subjective methods, usually those in which some estimate of the quality of focus of a chromatic target is made by an observer[9]. Although such procedures are plausible with primates, the elaborate training and laborious testing involved would have been prohibitive. Instead, the objective method of photoelectric scanning of a fundal image was selected. A design change was required so that the apparatus previously used by Yates[7] and others[5] to investigate imaging of white light in the primate eye could be used for this purpose. In the traditional apparatus, a bright, narrow, luminous slit is brought to focus on the retina, and an image reflected from the fundus is captured by a photomultiplier after it is swept by a sampling slit. When lights other than a "white" source are to be used, the apparatus must be modified.

B. APPARATUS

The required apparatus includes a continuously variable dioptric correcting device that is common to both the entrance and exit paths of the optic fundus (see Appendix 12-A). Lenses L1 and L2 in Figure 12-1 comprise the basic correcting device. Lens L1 can be moved by a precise micrometer screw with respect to lens L2 in order to provide a range of dioptric powers between +1 and -1 diopters. A 1 mm movement of lens L1 corresponds to 0.05 diopters. Therefore, the system resolution is considerably better than that used by most refractionists. A standard trial lens set, for example, has as its smallest increment a 0.125 diopter lens. Lens L3 serves as a "range-change" device to bring the system under examination within range of the more refined corrector composed of lenses L1 and L2. The extent to which the measurement system itself is chromatically aberrant was unknown and was therefore calibrated. A high quality, first-surface mirror was substituted for the ocular fundus and wavelengths between 400 and 700 nm were tested. The source was a 150 W xenon arc with narrow band ($\sim$10 nm half-bandwidth) interference filters interposed. Good agreement was found between the calculated curves and those predicted from geometric optics (simple thin-lens formulae).

C. EXPERIMENTAL PROCEDURES

Several days before experimentation, animal subjects were keratometered so that good contact lens fits could be obtained. The apparatus was constrained to examine only left eyes due to the interposition of a fundus camera-pellicle system (see below). Animals were selected for evaluation if they were free from corneal defects and if a contact lens was available that fit within $\pm$0.02 mm (radius of base curve). Severe image distortion has been found to result from lenses that deviate from these tolerances.

On the day of an experiment, the appropriate animal was pre-anesthetically tranquilized with ketamine hydrochloride. An indwelling catheter was inserted in the saphenous vein of the right hindlimb and an anesthetic dose of sodium

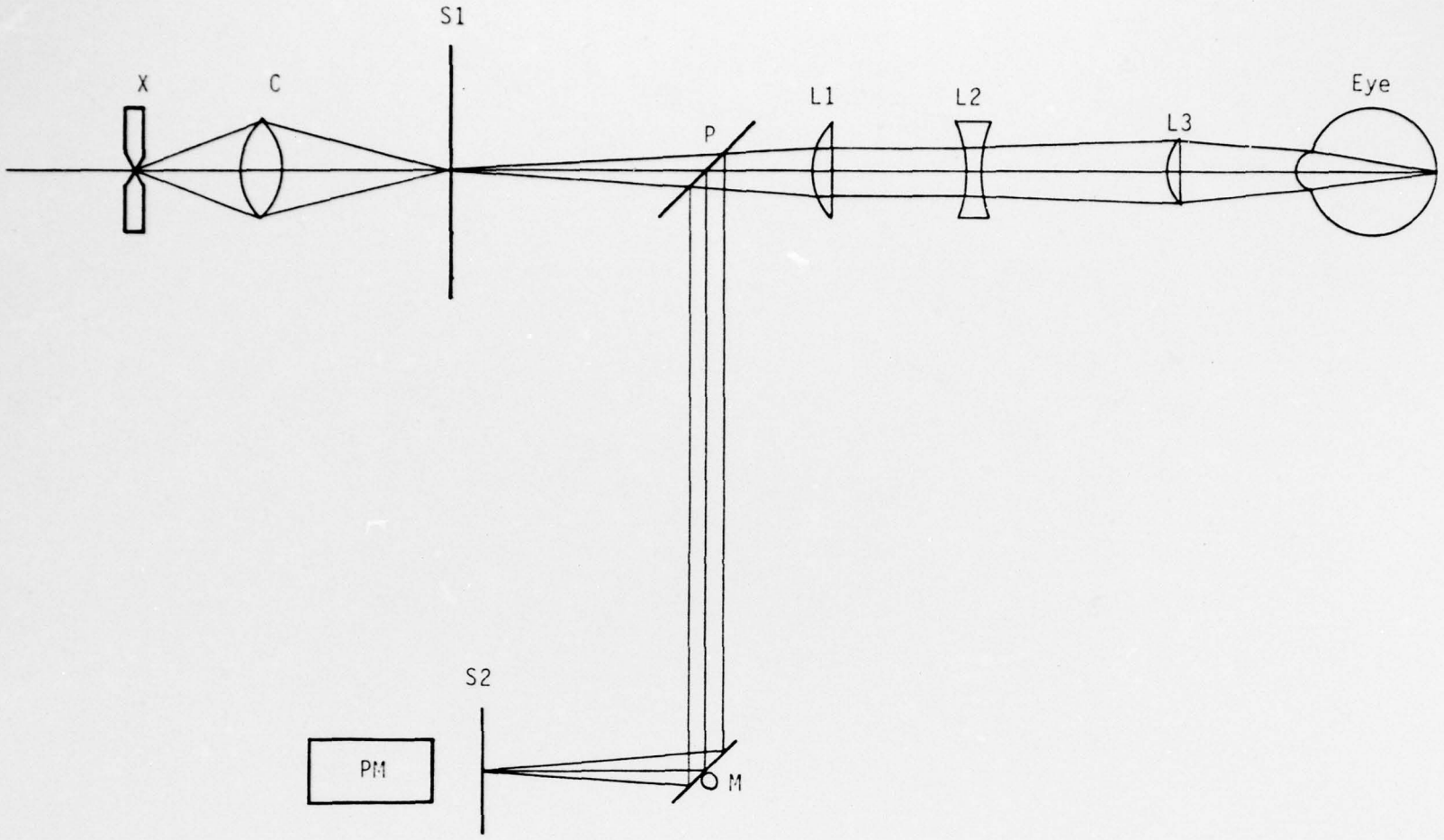

FIGURE 12-1. Schematic Optical System. X = xenon source; S1 = source slit; S2 = analyzer slit; C = condenser lens; L1,L2,L3 = continuous corrector; P = pellicle; M = moving mirror; PM = photomultiplier.

pentobarbital was administered. Anesthesia was maintained at a deep surgical level by continuous infusion of 6 mg/kg/hr of supplemental pentobarbital. Pre-anesthetic atropine sulfate provided some mydriasis and cycloplegia. To insure that complete intrinsic muscle paralysis was obtained, cyclopentophthlate (2%) was double instilled into the conjunctival sac. In addition, 10% phenylephrine hydrochloride was administered to produce maximal mydriasis. Additional instillation of the latter two agents was carried out as needed.

After insertion of a blepharostat, the appropriate contact lens was put in place over the freshly irrigated cornea. The irrigant was normal saline. The previously mentioned corneal surface measurements yielded good contact lens fits, and clear, undistorted "eye grounds" were always present even after 12 hours of experimentation. Conventional streak retinoscopy was carried out for the vertical axis (the axis of the target slit). Estimates were attempted for an accurancy of ±0.125 diopters. A cross check of the refraction by optometrists revealed no discrepancies of more than 0.25 diopters between refractionists. Any severe errors would, of course, have been revealed in the process of experimentation. The apparatus used may be regarded as a high-resolution, static retinoscope.

The anesthetized animal had a rectal thermistor probe used in combination with a water jacket to maintain core temperature at 38.5^{0}C. The animal was positioned in a standard monkey mount, the target beam was crudely aligned with respect to the cornea and the fundus camera was interposed. After suitable manipulation, the fundus was visualized and the target beam was positioned over the center of the *macula lutea*, usually over the *fovea centralis*. On several occasions, the accuracy of the placements were verified by experienced observers.

The procedures previously described by Yates[7] were used to align the photomultiplier. A suitable current-to-voltage device was built to read the anode current of the photoelectric scanner. A 100 μm slit was positioned in front of the detector to sample the reflected chromatic source image, which was that of a 50 μm slit. Both slits were obtained from a high quality monochromator. Ten wavelengths at ∿33 nm intervals in the range from 400 to 700 nm were available for test purposes. Since the primate fundus is a diffuse reflector of low efficiency, and since the electronic system available was noisy, some wavelengths required signal averaging. The spectral extremes proved most troublesome in this regard. Data were FM tape recorded at a suitable bandwidth (usually ten times the highest frequency of interest) for later analysis. The absence of an on-line data reduction device necessitated excessive bracketing of experimental values.

D. RESULTS

Taped data were digitized, signal-averaged, normalized, plotted, and occasionally smoothed (three point quadratic fit) using methods described previously by Yates and Harding[7]. Widths of linespread functions at half amplitude were obtained and comprise the major portion of the data discussed below. It was found after some of the data had been analyzed that the area under the spread function obtained by simple numerical integration was a more simple but equivalent artifice. The location of the narrowest (i.e., best focused) spread function for any particular wavelength was simplified when it was discovered that curves of regular shape were obtained when the full width at half amplitude or the integrated area of the spread function was plotted vs. correcting power (see Figure 12-2).

Figure 12-3 is a plot of composite data for three animals. Several aspects of these data should be noted. First, there is remarkable similarity between the rhesus monkey data and data obtained under similar conditions for the human (see Figure 12-4), demonstrating that the monkey is indeed chromatically aberrant in the same fashion as human. For all wavelengths tested, however, the monkey showed more severe focusing errors than did human. They were, as predicted, more blue myopic and more red hyperopic than their homanid counterparts. It may be inferred that the shorter focal length optical system of rhesus monkey results in this general chromatic aberration trend. Construction of an improved schematic eye for the rhesus should clarify the role of the various dioptric components of the system.

The observation has been made for other lens systems that much of the chromatic blurring is due to edge rays rather than central rays. Attempts to use artificial pupils to elucidate the magnitudes of such effects were not productive owing to the detector sensitivity problem already mentioned.

It should be noted that during the period when these data were being collected, an evaluation of the chromatic aberration in a single human fundus was evaluated[8]. Subjective measures and the objective measure used here compare quite favorably. The utility of the procedure has thus been greatly reinforced.

It is concluded that the technique discussed above represents a sensitive and moderately simple method for in vivo evaluation of chromatic images. Further, the similarity between macaque and human eye has been better elaborated for a new dimension. It has also been demonstrated that any attempt to produce chromatic fundal images for any of a variety of purposes must take into consideration the substantial, longitudinal chromatic focusing error that the rhesus monkey eye possesses.

Finally, these data only hold for situations in which relaxed accomodation is known to exist. In the human, near point accomodation produces a different profile of chromatic aberration than that seen for the cycloplegic eye.

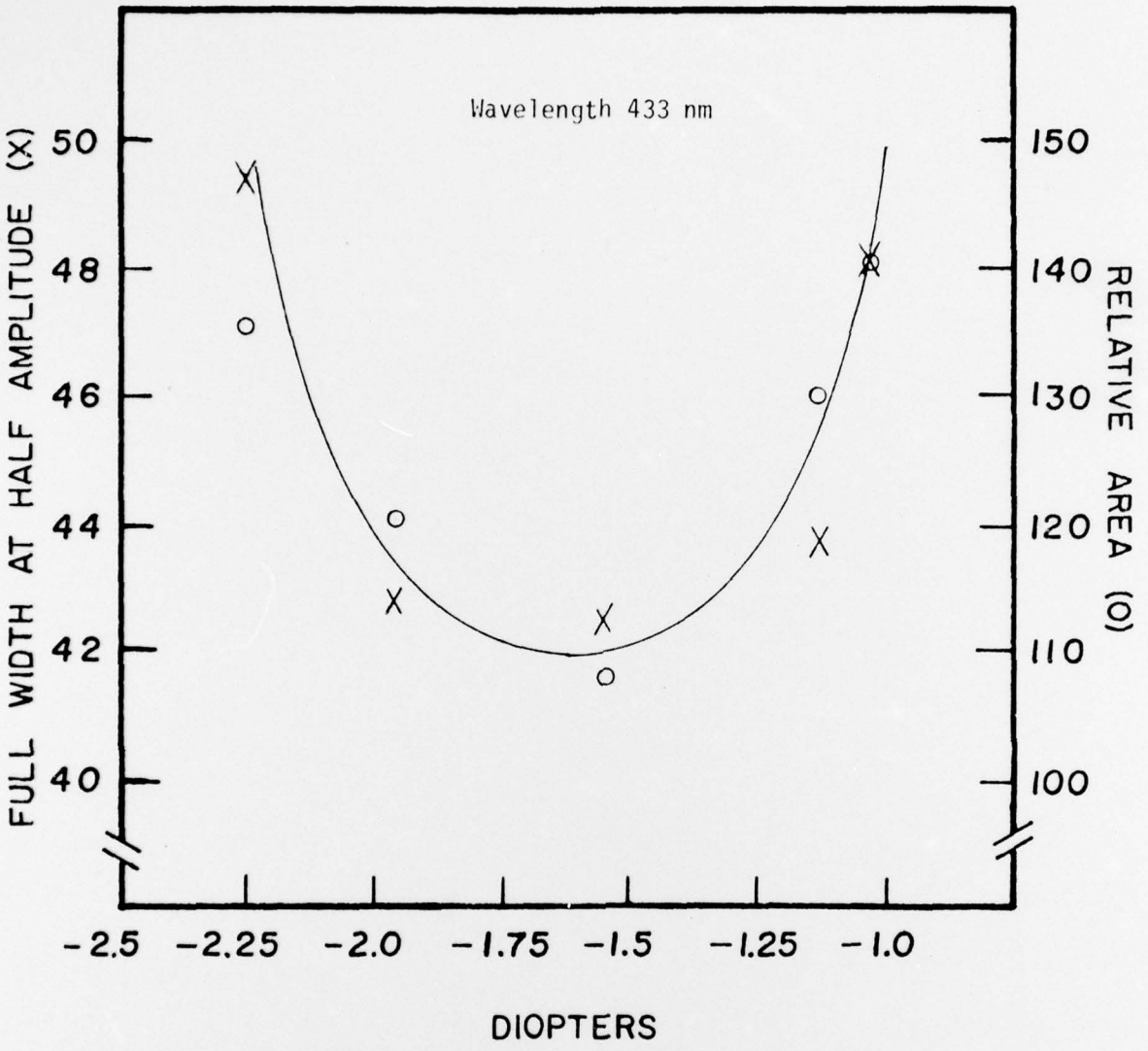

FIGURE 12-2. Comparison of Two Methods of Determining Best Focus for a Line Target Imaged on the Rhesus Monkey Fundus. Equivalent results were obtained when either the width of the normalized line spread function or the area under the normalized spread function was evaluated. The shape and character of the obtained curve is predictable from geometric optics considerations.

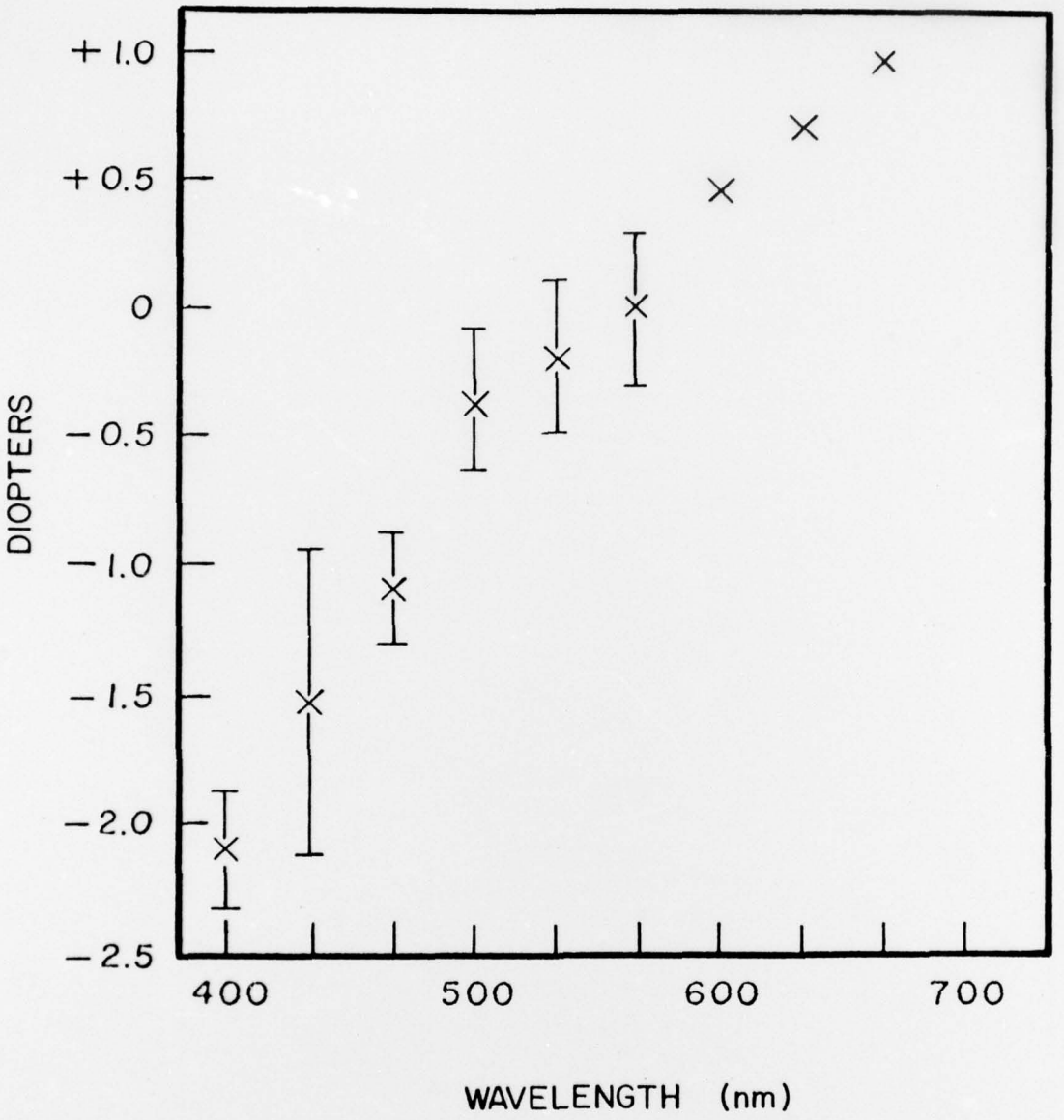

FIGURE 12-3. Normalized Chromatic Aberration For the Eye of Rhesus Monkey. Error bars are one standard error and are inflated due to the small number of observations available to date. The absence of error information for 600 nm and beyond reflects single observations for those wavelengths.

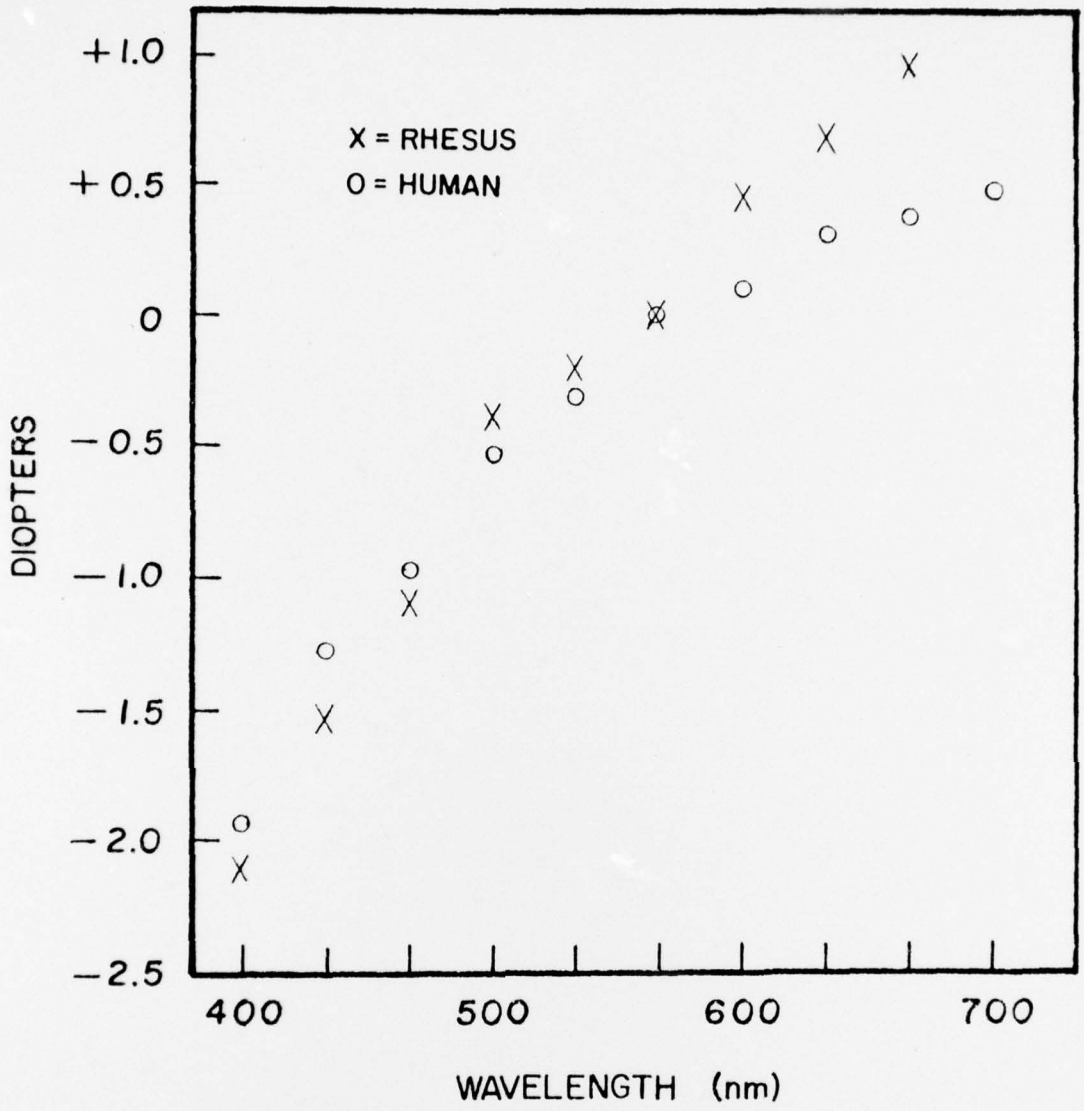

FIGURE 12-4. Comparison of Primate vs. Human Chromatic Aberration as Measured by Similar Electro-Optical Scanning Techniques. Human data were taken from Charman and Jennings(8). Rhesus monkey axial chromatic aberration is generally more severe than that observed in human. The striking similarity between the two dioptric systems is evident.

REFERENCES

1. Lambert, R.L., G.C. Higgins and R.N. Wolfe, "Measurement and Analysis of the Distribution of Energy in Optical Images", J. Opt. Soc. Am. 48: 487, 1958.

2. Duffieux, P.M., "L'integrale de Fourier et ses Applications a L'optique", (Besancon) Privately printed, 1946.

3. Hopkins, H.H., 21st Thomas Young Oration, "The Application of Frequency Response Techniques in Optics", Proc. Phys. Soc., Lond. 79:889, 1962.

4. Linfoot, E.H., "Fourier Methods for Optical Image Evaluation", The Focal Press, London and New York, 1964.

5. Campbell, F.W. and R.W. Gubisch, "Optical Quality of the Human Eye", J. Physiol. 186:558, 1966.

6. Robson, J.G. and C. Enroth-Cugell, "Scattered Light in the Cat Eye", Abstract 102-3, Association for Research in Vision and Ophthalmology, Spring Meeting, Sarasota, Florida, April 28-May 2, 1975.

7. Yates, J.T. and T.H. Harding, "Monkey Spatial Vision: Physiological Optics Evaluation", Vis. Res., in press, 1977.

8. Charman, W.A. and J.A.N. Jennings, "Objective Measurements of the Longitudinal Chromatic Aberration of the Human Eye", Vis. Res. 16:999, 1967.

9. Wald, G. and D.R. Griffin, "The Change in Refractive Power of the Human Eye in Dim and Bright Light", J. Opt. Soc. Am. 37:321, 1947.

APPENDIX 12-A

Figure 12-A-1 schematically represents the continuous dioptric corrector. Lens L1 has an object distance of:

$$S_1 = 0.81 - X \text{ meters.}$$

The resultant image distance is:

$$S_1' = \frac{F_1 S_1}{S_1 f_1}, \text{ where } f_1 = \text{focal length of L1.}$$

The object distance for L2 follows thus:

$$S_2 = 0.06 + X - S_1'.$$

The image distance becomes:

$$S_2' = \frac{F_2 S_2}{S_2 f_2}, \text{ where } f_2 = \text{focal length of L2.}$$

The distance of the resultant image from the eye is then:

$$S_e = 0.13 - S_2',$$

and the corrective power of the two-lens system is given by:

$$P_c = -1/S_e.$$

To account for the chromatic aberration of the lenses used, a correction factor (z) was employed for each wavelength such that:

$$p' = p(1+z),$$

where z was experimentally fitted for each wavelength.

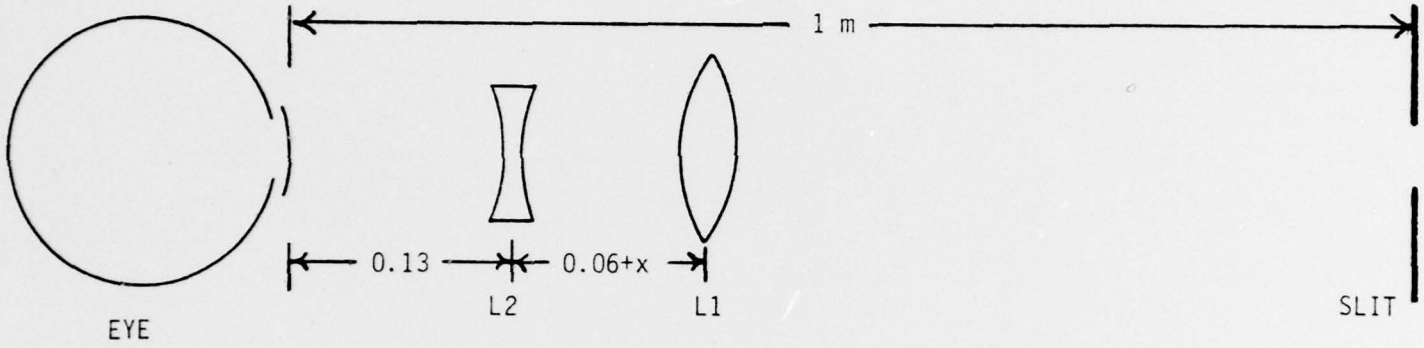

FIGURE 12-A-1. Schematic Lens System for the Major Components of the Continuous Dioptric Corrector System. Distances are in meters. L1 = +6D; L2 = -8D. L2 was fixed in place and L1 could be continuously positioned by a micrometer screw.